COMPUTATIONAL SIMULATION AND ANALYTICAL DEVELOPMENT OF BUCKLING RESISTANT STEEL PLATE SHEAR WALL (BR-SPSW)

Abhilasha Maurya

Thesis submitted to the faculty of the Virginia Polytechnic Institute and State University in partial fulfillment of the requirements for the degree of

Master of Science
In
Department of Civil and Environmental Engineering

Matthew R. Eatherton, Committee Chair
Cristopher D. Moen
Carin L. Roberts-Wollmann

August 06, 2012
Blacksburg, Virginia

Keywords: Steel Plate Shear Wall, hysteretic damping, plate buckling, seismic behavior, finite element modeling

COMPUTATIONAL SIMULATION AND ANALYTICAL DEVELOPMENT OF BUCKLING RESISTANT STEEL PLATE SHEAR WALL (BR-SPSW)

Abhilasha Maurya

ABSTRACT

Steel plate shear walls (SPSWs) are an attractive option for lateral load resisting systems for both new and retrofit construction. They, however, present various challenges that can result in very thin web plates and excessively large boundary elements with moment connections, neither of which is economically desirable. Moreover, SPSW also suffers from buckling at small loads which results in highly pinched hysteretic behavior, low stiffness, and limited energy dissipation. To mitigate these shortcomings, a new type of SPSW has been developed and investigated. The buckling resistant steel plate shear wall (BR-SPSW) utilizes a unique pattern of cut-outs to reduce buckling. Also, it allows the use of simple shear beam-column connections and lends tunability to the shear wall system. A brief discussion of the concept behind the BR-SPSW is presented. A detailed parametric study is presented that investigates the sensitivity of the local and global system behavior to the geometric design variables using finite element models as the main tool. The key output parameters which define the system response are discussed in detail. Analytical solutions for some output parameters like strength and stiffness have been derived and resulting equations are proposed. Finally, preliminary suggestions have been made about how this system can be implemented in practice to improve the seismic resistance of the buildings. The proposed BR-SPSW system was found to exhibit relatively fuller hysteretic behavior with high resistance during the load reversals, without the use of moment connections.

ACKNOWLEDGEMENTS

The two years which I have spent at Virginia Tech has been truly nourishing. My experiences have enriched me socially, professionally, and intellectually, and I am grateful to have the opportunity to acknowledge the people and organizations who have contributed to all aspects of my life.

First and foremost, I would like to thank my advisor, Dr. Matthew R. Eatherton for the valuable guidance and advice. Under his influence, I have grown as an engineer, researcher, and technical writer. I would also like to thank Dr. Christopher Moen and Dr. Carin L.Roberts-Wollmann for their invaluable support and feedback as my advisory committee.

The entire Structures group at Virginia Tech has been a tremendous resource for me. I am grateful for the research discussions within and beyond my research group and for the thorough and high quality lectures that the faculty provides.

My tuition and research were funded in part by the American Institute of Steel Construction (AISC) Milek Faculty Fellowship. This support is sincerely appreciated.

Finally, and most importantly, I'd like to thank my parents, roommates and wonderful friends who have supported me throughout my graduate studies. I am indebted to you all for the completion of this thesis.

TABLE OF CONTENTS

LIST OF FIGURES

LIST OF TABLES

CHAPTER 1
INTRODUCTION

1.1. MOTIVATION FOR THE STUDY

Steel plate shear walls (SPSWs) have been investigated in numerous research projects, and implemented in quite a few buildings (Sabelli and Bruneau, 2006). SPSWs designed in the U.S. and Canada generally use thin plates that are allowed to buckle. Previous studies have shown that SPSWs exhibit significant post-buckling capacity and energy dissipation takes place as the web plate yields in the inclined tension field direction.

A typical steel plate shear wall (SPSW) consists of a thin steel plate, referred to as the web plate, bounded at the sides by columns, also referred to as vertical boundary elements (VBE), and at the floor levels by beams, also referred to as horizontal boundary elements (HBE). This arrangement is shown in Figure 1. Web plates, adequately anchored by the boundary elements, buckle in shear and form a diagonal tension field to resist lateral loads. The basic design process of a SPSW requires the sizing of the web plate such that it can resist the entire base shear. Additionally, HBEs and VBEs must be designed to elastically resist the development of the full expected tensile capacity of the web plate to ensure that the web plate can yield in tension prior to the plastic hinging of the boundary elements. (AISC 341-10). The force-displacement behavior of a typical steel plate shear wall system (Berman and Bruneau, 2005) is shown in Figure 2. The experimental setup was designed such that the boundary elements were connected through a rigid moment connections. The hysteretic behavior shown in Figure 2 is therefore due to the moment frame and the web plate. The hysteretic behavior is stable, but suffers substantial pinching. This pinching in the hysteresis curve aggravates when the force-deformation behavior of the web plate alone is considered as shown in Figure 3. This behavior is due to the fact that the web plate acting in tension field is like tension-only bracing. Tension-only bracing is not allowed in seismic zones because there is no lateral load resistance during load reversal which is similar to the force-deformation behavior of the web plate (refer Figure 3). Moreover, the highly pinched hysteretic behavior of SPSW web plate results in much lower energy dissipation. Early buckling of the web plate also causes reduction in the wall stiffness.

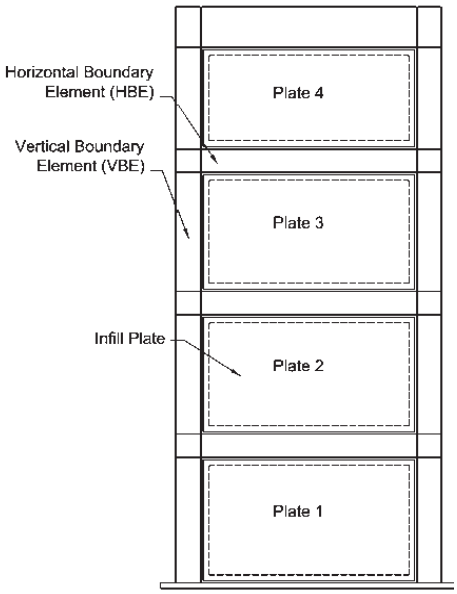

Figure 1: A four-story SPSW system [from (Berman and Bruneau, 2004)]

Current U.S. building codes require SPSW to employ beam-to-column moment connections in conjunction with the SPSW to resist lateral loads during load reversals, increase stiffness, and improve energy dissipation. The inclusion of moment connections requires larger column sections and additional connection cost. The substantial increase in the lateral load resistance during load reversals is shown in Figure 2 as compared to Figure 3, where the difference is the effect of the moment frame. Additionally, to reduce the buckling of the SPSWs and increase the stiffness, there is often a need to increase the thickness of the web plate. This, however, results in added load demand on the boundary elements associated with the anchoring of the tension field which demands larger boundary elements. Research work done by Berman (2011) shows that web-plates as thin as 3/16 in. requires massive columns such as W36x800 in a fourteen story building. Additionally, depending on the load demand, the thickness of the web plate may need to be thinner than 1/16 in. In short, a typical SPSW design methodology results in very thin plates and boundary elements that are significantly larger than comparable braced frames.

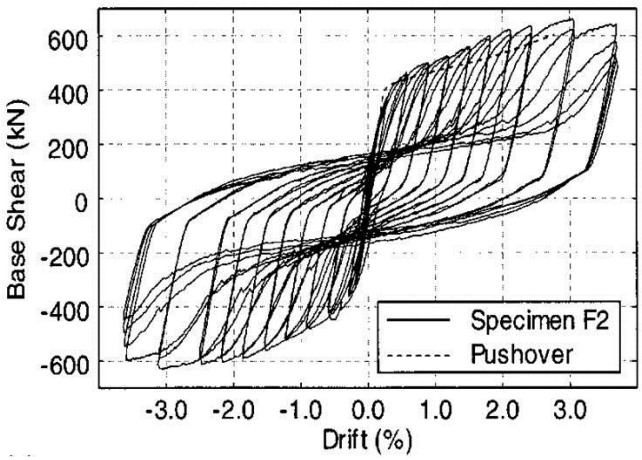

Figure 2: Force-displacement plot for a typical steel plate shear wall system [from (Berman, Celik and Bruneau 2005)]

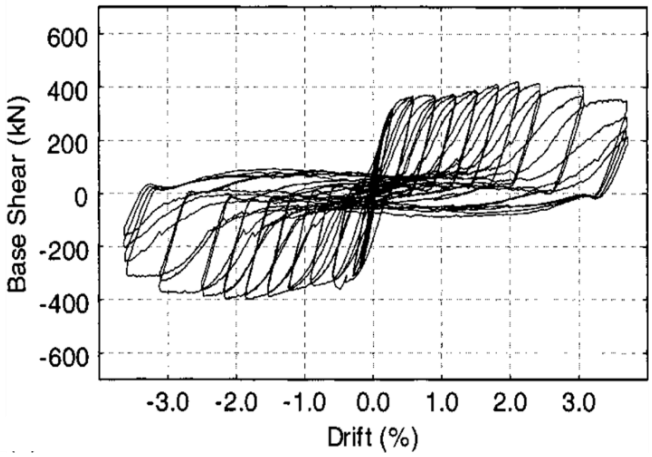

Figure 3: Force-displacement plot for a shear wall web plate [from (Berman, Celik and Bruneau 2005)]

The purpose of this study is to develop a new type of SPSW that reduces buckling by utilizing a unique pattern of cut-outs. Additionally, this type of resilient buckling resistant steel shear wall would also exhibit fuller energy-absorbing hysteresis loops without requiring moment connections. Furthermore, as compared to a standard SPSW which has one primary variable being the plate thickness, this SPSW, with a pattern of cut-outs would allow the selection of more independent variables which can be varied to separately tune the strength, stiffness and ductility of the shear wall system. Thus, this specially designed SPSW would lend tunability to the system. It is therefore expected to be a more efficient and better performing alternative to the currently used SPSW.

The concept behind the resilient buckling resistant steel shear wall is to reduce the out-of plane buckling of shear walls by exploiting a unique characteristic of the ring-type cut-outs. The basic configuration of the buckling resistant steel plate shear wall (BR-SPSW) and the ring shaped cut-outs, which form the basic unit of the full-wall, are shown in Figure 4. When the wall is subjected to lateral forces, this basic ring unit deforms into an ellipse. The transverse and longitudinal deformations of a circular ring that is being stretched into an ellipse are nearly equal. This implies that for a SPSW made of rings, in the direction perpendicular to the tension field, the slack in the compression diagonal direction will be removed. The removal of slack in the compression diagonal will lead to an almost immediate development of tension field action in the opposite direction upon load reversal. In other words, the BR-SPSW reduces buckling due to the fact that the elongation of the ring in one radial direction will be compensated by the shortening of the ring in the perpendicular radial direction, thus reducing out-of-plane deformation. These concepts are further examined in Chapter 3.

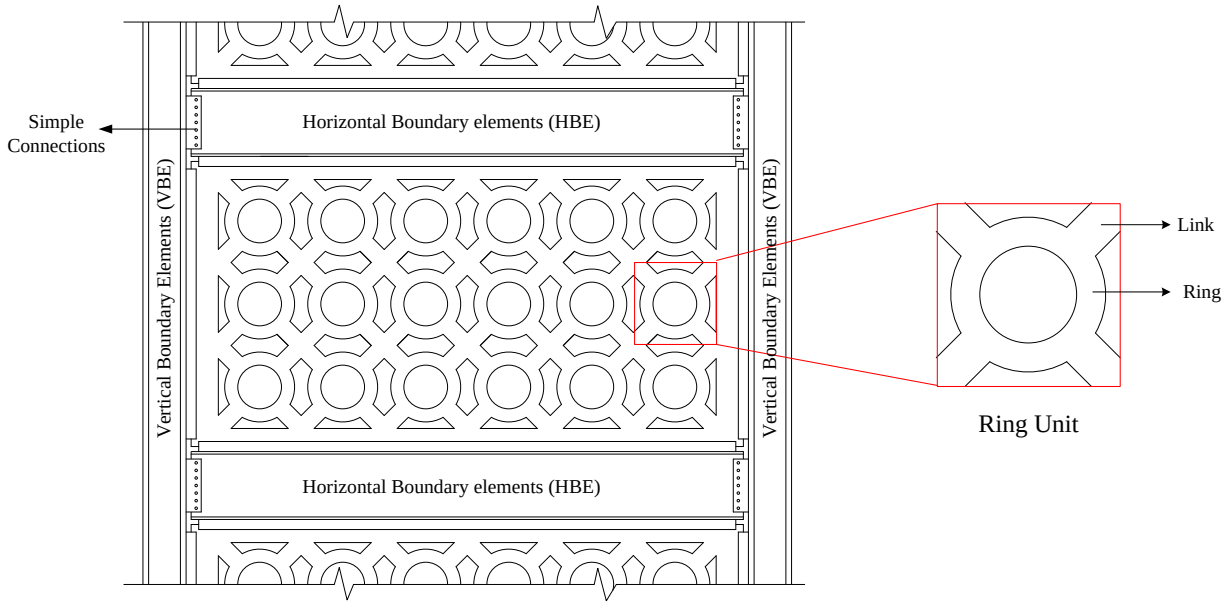

Figure 4: Buckling resistant steel plate shear wall and a basic ring unit

1.2. OBJECTIVES AND SCOPE

The main aim of this report is to develop a more efficient and high performance shear wall system. The concept behind BR-SPSW is new and hence should be extensively explored before it is used for practical purposes. To achieve this goal, global and local behavior of BR-SPSW has

been investigated thoroughly using computational and analytical methods. Additionally, an attempt has been made to devise means (analytical equations and trend plots) to aid the design of BR-SPSW.

This report is organized around six objectives outlined below:

- Proposing the BR-SPSW concept: Propose the idealized concept behind BR-SPSW and how the new system will reduce buckling of the web plate as compared to a typical SPSW system.
- Preliminary investigation of the BR-SPSW concept: As mentioned previously the idea behind BR-SPSW is new and thus requires some preliminary validation through carefully designed models. This type of investigation is required to prove that the proposed concept works more efficiently than a typical SPSW. This exercise also paves the way for a more exhaustive parametric study.
- Developing mathematical models for system behavior: Understanding the deformation mechanics of the ring units in a full wall and developing analytical and empirical solutions for major system response (strength and stiffness) needs to be done. The results from these models must then be compared to the computational results from the preliminary study and the parametric study to determine the efficacy of the proposed equations.
- Performing parametric study: Developing a set of computational models to study the influence of the geometric features of the plate on the overall system response is necessary to conduct the parametric study using ABAQUS (ABAQUS Version 6.10 Documentation) as the finite element analysis tool. Analyzing the results of the analysis and demonstrating the system behavior using suitable plots is a major objective of this research. The buckling behavior of the web-plate is also studied.
- Understanding fracture behavior: The rings in BR-SPSW may be prone to fracture due to their intricate shapes and reentrant corners. Methods to analyze the initiation and propagation of cracks in the ring have therefore been investigated.
- Proposing experimental program: Development of a set of experimental specimens and test set-up for experimentation is required. The behavior of the panels needs to be predicted using the analytical tools developed.

1.3. ORGANIZATION OF THE THESIS

The report is divided into eleven chapters, including this introduction, and four appendices.

Chapter 2 briefly summarizes the research work done in the field of steel plate shear walls. It focusses on the numerous variations of SPSW that have been investigated in the past. Additionally, some energy dissipating devices which work on similar grounds as the ring units have been discussed in this chapter.

Chapter 3 demonstrates the idealized concept behind BR-SPSW. Mathematical tools have been used to show how the use of ring-like cutouts in BR-SPSW help in reducing buckling.

Chapter 4 describes the preliminary investigation of the BR-SPSW concept. Four full scale models with different configurations and ring sizes have been analyzed using ABAQUS as the finite element analysis tool. Additionally, two ring units with different boundary conditions were analyzed to understand the deformation behavior of the rings.

Chapter 5 focuses on understanding the deformation mechanics of the rings to develop an analytical solution for the strength of the ring units. This solution is then translated to the strength of the full wall.

On a similar ground as Chapter 5, Chapter 6 uses the single ring models developed in Chapter 4 to derive analytical and empirical equations for the stiffness of the full wall.

Chapter 7 investigates the effect of initial imperfections of the web-plate on the overall system behavior. Random imperfections and imperfections in the shape of buckling modes of the web plate were studied and necessary conclusions on the influence of initial imperfection are presented.

Chapter 8 summarizes the parametric study done to build on the work done in Chapter 4. This chapter tabulates the model sets carefully designed to thoroughly understand the sensitivity of the system behavior on the geometric features of BR-SPSW followed by the detailed finite element analysis results and conclusions.

Chapter 9 discusses the various techniques that can be used to predict fracture in BR-SPSW using analytical models proposed by various researchers. This discussion is backed up by relevant literature review. Additionally, extended FEM (XFEM) technique has been used to model crack in a single ring model. Recommendations have been made on future work in fracture prediction and modeling.

Chapter 10 outlines the experimental program that is being conducted at Virginia Tech to validate the concept of BR-SPSW. A set of eight specimens have been proposed and behavior related predictions have been made using the computational and analytical techniques developed through the course of this research.

Chapter 11 summarizes the work presented in this report and provides a compilation of conclusions.

CHAPTER 2
LITERATURE REVIEW

This chapter summarizes the previous research work done on steel plate shear walls with a focus on system behavior obtained from previous experiments. The latter part of the section reviews the work done on some dissipative devices also known as yielding frames which may be considered as an inspiration for the development of buckling resistant steel plate shear walls.

2.1. SOLID PANELS

2.1.1. Solid panel with normal strength steel

Thorburn, Kulak and Montgomery (1983) recognized that thin plate shear walls have significant post-buckling strength and developed a method of analysis on this basis. An analytical model was designed to study the shear resistance provided by the buckled plate, wherein the tension zone developed in a buckled plate is represented as a series of inclined planar truss members, capable of transmitting only tension loads. This model, based on the work of Wagner (1931), was used to investigate transfer of forces and the resulting stress redistribution in thin plate walls. The analysis was conducted assuming that the boundary elements were stiff and allowed the development of tension field in the web plate. The investigation of the post-buckling strength of a panel was not done for cyclic loads. Using the analytical model, parametric studies were done to determine the influence of column stiffness and plate thickness and aspect ratio on the overall stiffness and strength of the shear wall panels. It was concluded that increasing web thickness and column stiffness have positive effects on panel shear capacity. Also, panel stiffness increases linearly as the panel length increases. It was noted that the angle of inclination of the diagonal tension forces in a shear wall is a function of the column and beam moments of inertia, panel dimensions and the plate thickness. Also, as column flexibility increases, variation of tensile forces across the plate increases. Maximum stresses occur at mid-plate and they decrease towards the plate edges. Finally, some recommendations were made to improve the analytical model and to compare this study with experimental data.

Timler and Kulak (1983) tested a large-scale single story steel shear wall test specimen to verify the analytical work done by Thorburn et al. (1983). The beam-to-column connection was pin-

jointed for exterior connections and continuous for interior connections. The 5 mm infill panel was welded to the boundary frame by means of a 6mm thick "fish plate" The specimen was tested under monotonically increasing loading to the serviceability drift limit, followed by the final loading excursion until the failure of the structural system. No gravity loads were applied to the system. The test results were then compared with the predicted results. It was noted that there was good agreement between predicted and actual principle stresses in the plate and axial stresses in the frame members. The angle of inclination of the principle stresses was found to be between 46.6^{o} and 53.2^{o}. The predicted angle was 51.0^{o}. Accurate prediction of the entire load-displacement curve was obtained. However, the bending strains in the frame members were over-estimated in each case. Thus, the analytical method put forward by Thorburn, et al. (1983) was found to be a satisfactory approach.

Tromposch and Kulak (1987) verified the analytical model developed by Thorburn, et al. (1983), on a specimen subjected to cyclic loading. The specimen consisted of two panels arranged so that opposing tension fields would form. It had story height of 2200 mm, a bay width of 2750 mm and a panel thickness of 3.25 mm. The boundary members were joined by bolted connections. The steel panels were connected to the frame by using 5mm fish plates. The columns in the frame were axially preloaded to simulate the effect of gravity loads. The specimen was subjected to two loading phases: a cyclic loading phase (28 cycles) and a monotonic loading phase. During the cyclic phase, a maximum load of 4000 kN was applied and a maximum centerline deflection of 17 mm (0.8% drift) was reached. The hysteresis loops were stable, but pinching was observed after 8th cycle. The displacement ductility achieved was about 4.3 for compression cycle and 6.8 for tension cycle. Weld tearing at several corners was observed at the end of this phase. After completing this phase, the specimen was loaded monotonically to a maximum load of 6000 kN. The maximum deflection achieved was 71mm (3.2% drift).The axial loads measured in the frame members produced a good correlation with those predicted by the inclined tension bar model. The measured orientation of the principal strains was close to the predicted value of 44.0^{o}. It was noted that hysteretic behavior of an unstiffened steel plate can be predicted with a reasonable accuracy by the analytical method proposed by Thorburn, et al (1983). It was also recommended that welds between the panel and the boundary members should be designed to carry the ultimate design capacity of the plate material. Finally, it was concluded that inclined

tension model bar can be used with confidence to evaluate the strength and capacity of the steel plate shear wall.

Cassese et al. (1993) investigated the seismic behavior of unstiffened thin steel- plate shear walls. The main aim of the research was to assess the feasibility of thin plate shear walls and to develop new design methods to result in more optimal designs. Eight quarter-scale single-bay three-story specimens were tested. These specimens varied in the beam-to-column connections (moment and shear connections). Three plate thicknesses (gage 22, 14 and 12) were used. The infill plates were welded to the frame elements. One of the specimens used was just a frame without any infill plate. The test results showed that as compared to the frame with no plates, the specimen with gage 22 plate (0.76 mm thickness) was initially nine times stiffer. The thickening of the plates did not result in a substantial increase in the stiffness. With respect to the strength of the plate, it was found that thinnest plate shear wall (gage 22) was 2.8 times stronger than frame with no infill plate. Also, a two-fold increase in strength is observed when a specimen with gage 22 plates is compared with gage 14 plate (1.87 mm thickness). It was also noted that in slender specimens, the plate yielded long before inelastic behavior is observed in the column which is a desirable characteristics. As anticipated, in thicker plates failure was governed by inelastic instability of the column. It was observed that the beam-to-column connection did not have a major effect on the frame behavior. However, this observation was attributed to the fact that the plates are continuously welded to the frame elements so the beam-to-column connection ended up behaving like a moment connection, even when the beam flanges were not welded to the column flanges. However, for more slender members, moment connections have positive effect on initial stiffness and strength. Lastly, energy dissipation of the thicker specimen was found to be almost 2.5 times that of the slender specimen.

Elgaaly (1998) performed a series of tests on thin steel plate shear walls under cyclic loading. An analytical model to determine the behavior of the shear walls was also presented. The model was capable of predicting the behavior for plates with both welded and bolted connection. The tests were conducted in two phases. Eight quarter scale single bay three story specimens were tested in Phase I. These specimens varied in the beam-to-column connections (moment and shear connections) and plate thickness. The plate-to-frame connection was welded in nature for all the specimens. A detailed summary of results and conclusions for Phase 1 tests has been presented in

a paper by Caccese et al. (1993). Phase II tests were performed on seven one third scale single bay two story specimen. Gage 13 (0.0897 in.) plates were used in these tests and the plate-to-beam connection was bolted in all the specimens except one. The columns in all the elements except for one were subjected to compressive axial force. Shear connection detailing was done between the beam and the column of the frame. Also, the bolt spacings were varied in the specimen to determine the optimum bolt spacing. Most of the tests in Phase II had to be stopped prematurely due to either buckling of the column or connection failure. The specimen tested with all the planned cycles reached a drift of 2.39%. A number of conclusions were drawn from Phase II tests. Firstly, it was concluded that bolt spacing did not affect the mode of failure. Also, it was noted that absence of column axial compressive loads does not change the behavior of the wall substantially. The author has recommended that the columns of the bay should be strong enough to allow the plate panels to develop full tension fields and yield without any premature failure of the columns. It was also concluded from the tests that welded plates exhibited higher elastic stiffness and initial yielding load compared to the bolted specimens. However, the ultimate capacity of welded and bolted walls is comparable. One of the most significant contributions from this work is the development of an analytical model using equivalent truss elements which is able to depict the test results to a good degree of accuracy.

Lubell, Prion, Ventura and Rezai (2000) studied the performance of single and multi-story unstiffened steel shear walls subject to cyclic quasi-static loading. One four-story and two single-story steel plate shear wall specimens were tested. Each specimen had unstiffened infill panels having aspect ratio of 1:1 thickness of 1.5mm (gage16) and yield stress of 46 ksi (320 MPa). Full moment connections were provided at all beam-column joints by continuous fillet-welds. For the four-story specimen, each horizontal load was applied at each floor. Gravity loading of this specimen was simulated by means of steel masses attached at each story level. For single story specimens, no gravity loading was applied. It was observed that the column of the multistory frame yielded before significant inelastic action occurred in the infill plate. Also, significant pull-in of the columns caused by the tension field in the infill plates, resulted in an hour-glass deformation mode of all the specimens. It is therefore recommended as a necessary step that capacity design of the bounding columns in a steel plate shear wall is done to ensure that the infill panels yield prior to column hinging and to minimize pull-in of the columns. It was also noted that flexurally stiff beams at the top and bottom of the shear wall are important to prevent

the formation of plastic hinges and to avoid the decrease of out-of-plane stability of the frame. Further, it was observed that the multi-story specimen was more flexible that the single-story specimen because the influence of the overturning moment is more significant as the height of the structure increases. A series of numerical models using strip models was employed to validate the results of the experiments and in all cases the results obtained were fairly accurate with the exception that the elastic stiffnesses of the single story specimens were over predicted by the numerical models. Note that the strip model, shown in Figure 5, represents SPSWs as a series of inclined strip elements, capable of transmitting tension forces only, and oriented in the same direction as the average principal tensile stresses in the panel.

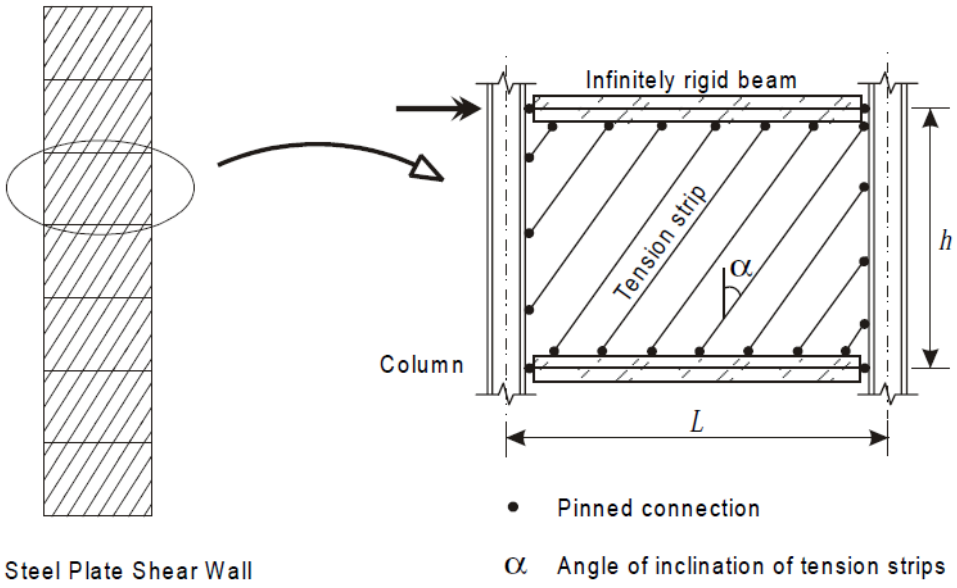

Figure 5: Diagrammatic representation of Strip Model [from (Lubell et al. 2000)]

As observed by Lubell et al. (2000), the code prescribed strip models over predicted the elastic stiffness of the test specimens. Rezai, Ventura and Prion (2000) therefore did numerical analysis using various strip models and compared them with test results of experiments performed on two single story and one four-story specimens by Lubell et al. (2000). An improved model as shown in Figure 6 was then proposed that utilized discrete strips placed at different angles as opposed to one constant angle (e.g. 45^{o}) in the conventional approaches. This variation was introduced in the model to account for the fact that the degree of magnification and inclination of the infill plate principal tension stresses are different at various locations in the plate, for example the corners of an infill steel panel are connected to the relatively stiff beam-to-column joints so they attract a

considerable portion of the steel plate membrane forces. This multi-angle strip model along with three parallel strip models inclined at 37°, 45° and 55° respectively, was employed to numerically analyze the specimens. After a thorough comparison of the analysis results with the experimental results, it was concluded that the multi-angle strip model gave fairly accurate results for single-story specimens and the first story of the four-story specimen. However, it was noticed that none of the models could accurately predict the stiffness and strength of the fourth story. This was attributed to the fact that due to the small overall aspect ratio of the four-story specimen there was an increase in moment to base shear ratio, which resulted in a dominance of flexural deformation compared to shear behavior. This effect can be significant for shear walls with relatively light perimeter framing members which was the case for the specimens tested. It was thus recommended that an improvement be made in the modeling technique to better capture the behavior of multi-story structure at higher stories.

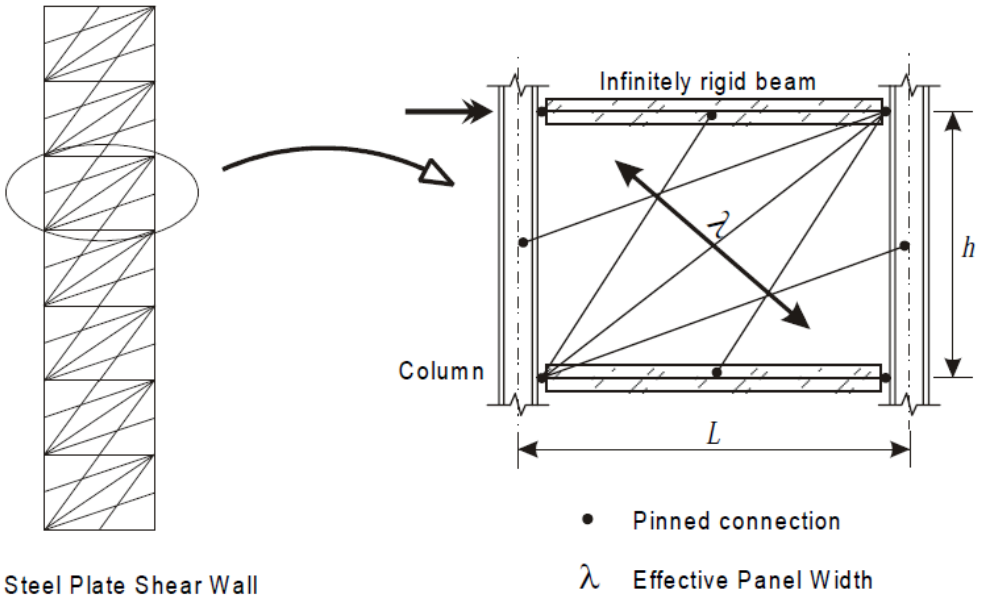

Figure 6: Diagrammatic representation of multi-angle strip model [from (Lubell et al. 2000)]

Schumacher, Grondin and Kulak (1999) investigated the behavior of unstiffened steel plate shear wall panels at their connection to the adjacent beams and columns. Different kinds of infill panel connections were tested and their behavior was compared. In Figure 7, Detail A infill plate was welded directly to the boundary members. Detail B was designed such that fish plates were welded to each of the boundary members and the infill plate then lapped over the fish plates and

welded. Finally, in Detail C, fish plate was welded to only one boundary member and then the infill plate was welded directly to the other boundary member and lapped and welded onto the fish plate. A fourth detail was a modified version of Detail B where two fish plates with a corner cut-out were welded to the boundary members and the infill plate was then lapped asymmetrically over the fish plates and welded. The cutout was made to reduce stress at corners. The four details tested are shown in Figure 7**.** The loading strategy was adopted from ATC-24 (Applied Technology Council 1992) for experiments using quasi-static cyclic loading. Test results concluded that each of the four infill connection performed satisfactorily under the quasi-static loading. Cyclic inelastic response and energy dissipation capacity of all specimens was comparable. It was also observed that the infill plate connection detail welded directly to the boundary members was less susceptible to tearing than were the details that used fish plates. However, due to the impracticality of such connections it cannot be used widely. It was found that although modified Detail B connection delayed significant tearing of the corner detail, it did not substantially improve the load-deformation behavior of the panel.

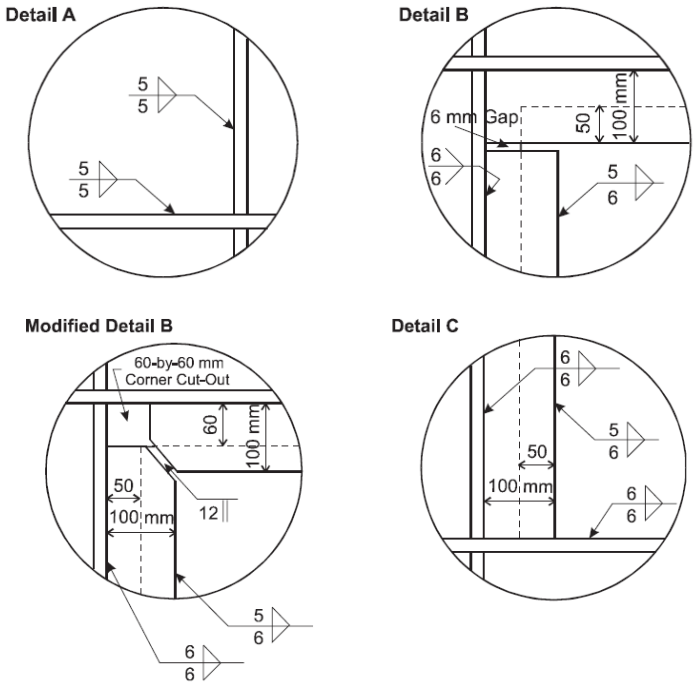

Figure 7: Infill panel connection details tested [from (Schumacher, Grondin and Kulak 1999)]

Berman, Celik and Bruneau (2005) performed cyclic testing on six frames. The main aim of their experiments was to compare hysteretic behavior of light gauge steel plate shear walls and braced

frames. The aim was to design shear walls/ bracing systems that were strong enough to resist necessary lateral forces and yet light enough to keep the existing structural elements from further reinforcement. The flat infill plate (FP) was ASTM A1008 and had a thickness of 1.0 mm and the boundary frame aspect ratio was 2.0. Continuous welded connection was used to connect the infill plate to the boundary frame. Quasi-static testing was performed on the specimen in accordance with the ATC-24 testing protocol. Specimen FP exhibited linear behavior during the first six cycles of the testing. Buckling of the specimen started at 0.29% drift. The specimen was successfully tested up to a drift of 3.7%, after which the testing had to be stopped due to extensive damage to the plate. Overall, behavior of the specimen was ductile and stable up to large drift levels, although pinching is also apparent from the hysteresis. Further analysis showed that 90% of the initial stiffness of the system was due to the infill plate. Almost 50% of the energy dissipated by the system was due to the infill plate. Also, the entire plate contributed to the energy dissipation process. Another specimen on which the test was performed was a corrugated infill plate specimen. The test setup and the load-deformation behavior of the SPSW are shown in Figure 8.

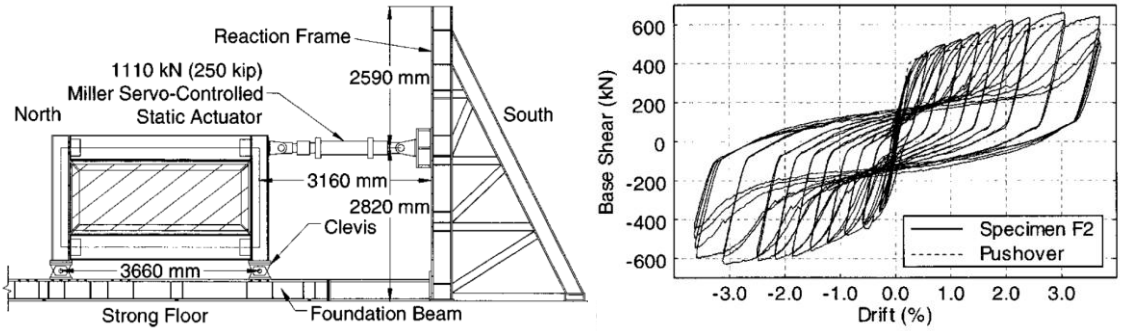

a. Test Setup
(from Berman and Bruneau 2005)

b. Load Deformation Behavior of SPSW
(from Berman and Bruneau 2005)

Figure 8: Test conducted by Berman and Bruneau (2005) demonstrating SPSW behavior

The research work done on solid steel panels with normal strength steel can thus be broadly categorized into two groups. The first group includes the work done by Thorburn, et al. (1983), Elgaaly (1998), Rezai et al.(2000) and others in developing the analytical and numerical models (e.g. the tensile bar model, multi angle strip model and other variations to the conventional strip models) to predict the behavior of steel shear walls under various loading protocols and boundary conditions. The second group includes the work done by Timler and Kulak (1983),

Tromposch and Kulak (1987), Berman et al. (2005), Cassese et al. (1993) and Lubell et al. (2000) in verifying the proposed models and putting forward recommendations for better design of steel plate shear walls through extensive experimentation. The major conclusions that can be drawn from all the experiments performed on the steel plates walls are briefly summarized in the following paragraphs.

Steel plate shear walls perform better than moment frames with no panels. As compared to the moment frame with no plates, the specimen with 22 gage plate was initially nine times stiffer and 2.8 times stronger (Cassese et al.1993). The infill panels also performed better than most of the singly braced frames as is clear from the experiments performed by Berman et al. (2005). The infill plates could achieve a maximum drift of up to 3.7% in cases where the boundary members or connections did not fail prior to the failure of the plates. Almost all the experiments performed exhibited ductile and stable hysteresis behavior up to large drift levels. Experiments conducted by Berman et al. (2005) concluded that almost 90% of the initial stiffness of the system was due to the infill plate and about half of the total energy dissipation of the system was due to the infill plate. It was also concluded that almost the entire plate contributed in dissipating energy, which was another desirable characteristic of this system. Further, it was observed from the experiments done by Tromposch and Kulak (1987) that these infill plate systems could achieve a displacement ductility up to 6.8 which was later reaffirmed by the research done by Berman et al. (2005), wherein he could achieve a displacement ductility of 12.

Although, the use of solid steel panels in the structural frames has advantages as compared to bracing systems, the system also had a few shortcomings and the researchers faced some challenges in implementing the concept. One of the major challenges faced was the failure of the boundary members and the bolt/weld connections before the plates could reach their full capacity. It is clear that the boundary members should elastically resist the moments associated with plate tension and thus, it has been recommended that the boundary members be able to resist the yield capacity of the plate acting at the inclined tension field angle. Experiments performed by Tromposch et al. (1987) and Berman et al. (2005) brought out the fact that the plates start to buckle at very low drifts of almost 0.29% which results in significant loss of stiffness and leads to pinching of hysteresis curve. Also, it was observed in the experiments performed by Berman et al. (2005) that buckling base shear for singly braced and X-braced

frames is higher under similar conditions. Also, post-buckling stiffness for plate walls is considerably less than braced frames. Also, as the thickness of the steel plates decrease, it becomes difficult to connect it to the boundary elements (Eatherton 2006).

2.1.2. Solid panel with Low Yield Strength (LYS) steel

Bruneau and Bhagwagar (2002) conducted non-linear analyses to investigate how structural behavior is affected when thin infills of steel are used to seismically retrofit steel frames located in regions of low and high seismicity. A typical three-bay frame extracted from an actual 20-story hospital building in New York City was considered for this purpose. For loading purpose, synthetic seismic ground excitation time histories were generated. Fully rigid and perfectly flexible frame connection rigidities were considered to capture the extremes of frame behavior. It was concluded from the study that the use of steel or any other ductile material as infill panels can significantly reduce story drifts by as much as 200%. Also, this reduction in story drift can be achieved without any significant increase in floor accelerations. It was also concluded that the low yield strength steel infills behave slightly better (higher ductility ratio and lower story drifts) than standard constructional grade steel under extreme seismic conditions but at the cost of some extra material. It was noted that frames with LYS100 infills reached a maximum ductility ratio of six which is about three times the ductility exhibited by frames having ordinary steel infills for almost the same story drifts. They also exhibited lower fundamental vibration period. Further, it was noted that steel plate shear walls may not be very effective in frames with aspect ratio greater than three.

Vian and Bruneau (2005) investigated a set of three specimens: a solid steel infill panel (S2), panel with twenty 200-mm-diameter (7.9 in.) holes (P) and a panel with quarter circle cut-outs at the top corners (CR). LYS steel infill panels with reduced beam section (RBS) beam-to-column connections at the top and bottom HBE was used. RBS was introduced in the beam design to ensure sufficient ductility in the moment connections. It was observed that RBS reduced the end plastic moment to 60.2% of the span plastic moment. A frame with an aspect ratio of 2:1 was used for experimentation and 7 mm thick fish plates were used to connect the steel panel to the boundary members. The infill panel thickness was 2.6 mm. A stable S-shape hysteretic curve was achieved for specimen S2. The elastic stiffness was found to be 130 kN/mm. Elastic buckling of the specimen started early at a drift of 0.1%, followed by initiation of yielding at

0.2%. Buckling folds were observed to be at an angle of about 27-35^{o}. Finally, the test had to be discontinued at a drift of 3%. The end of the test was marked by cracks in the bottom beam flange at RBS, severe twisting of the columns, tension yielding of the panels with cracks in the corner. Maximum base shear strength was found to be 2115 kN and high displacement ductility of 10 was achieved. Finally, finite element analysis was done using ABAQUS to analyze the specimens. Good agreement in the overall behavior was seen between the test results and the FEM analysis.

Chen and Jhang (2011) investigated the behavior of low yield point (LYP) steel web plates in single and multi-story frames. Four specimens with the width-to-thickness ratio varying from 50 to 150 were selected for the single-story frame test. Plate-type stiffeners were provided in the first two specimens only. All the specimens in this test reached drift angles of about 4-5% without significant decay in their strengths. The buckling started at a drift of about 2-3% for specimens with b/t ratio less than or equal to 80, whereas for specimen with b/t larger than 80, it started as early as 1% drift. Therefore to delay the onset of buckling, a b/t ratio less than 80 is desirable. The maximum shear buckling strength was observed in the specimen with a b/t ratio of 80 and with no stiffeners. It was argued that the boundary elements provided much stronger restraints as compared to conventional plate-type stiffeners. It was concluded that relatively low b/t ratio result in higher buckling strength.

The experimental data was compared to the theoretical values obtained from inelastic buckling stress equation given by Galambos (1987). The difference between the experimental and the theoretical data was found to be less that 14%. For the multi-story frame test, two steel panel specimens were chosen. Beam-to-column connection was a rigid moment type for the first specimen, while for the second specimen, a simple shear type connection was adopted. Both of the specimens displayed stable hysteretic behavior up to a large drift of 5% and significant inelastic tension field was developed at their ultimate strength. It was observed that the frame with moment connections displayed higher stiffness than the one with shear connection. This difference exceeds 30% after the onset of yielding, but gradually reduces at higher drifts. Also, it was noted that moment connections enhanced the strength and energy dissipation capacity of the frame by 28% and 18% respectively. Both the specimens reached a maximum drift of about 6%. It was concluded that the pinching behavior that is usually observed in conventional thin steel

shear walls under in-plane load, could be alleviated due to the use of LYP web plates. The LYP steel also has superior elongation capacity and display significant strain-hardening in the post yield stage.

2.2. PANEL WITH CORRUGATED PLATES

Berman and Bruneau (2005) conducted experiments to study the hysteretic behavior of braced frames and frames with steel infill plates. As mentioned previously, one of these specimens consisted of a corrugated infill plate (cold formed steel deck). The corrugations were inclined at 45^{o} from the horizontal. This was done to force the inclination angle of the tension field to be 45°. The corrugated plate was sandwiched between two angles that were bolted to the boundary frame. The plate was connected to the angles through epoxy. The infill plate consisting of four pieces was fastened together using 1.6 mm diameter steel pop-rivets. The hysteretic behavior was elastic in the first three cycles. Buckling started at about 0.44% drift. The failure of pop-rivets and cracking in epoxy was observed at about yield displacement. The specimen was successfully tested to a maximum displacement of 40.6 mm (2.2% drift). Failure of the specimen was from fractures of the infill plate at locations of repeated local buckling. As anticipated, the hysteresis of the specimen was one-sided because the tension-field action only took place when the corrugations were in tension. The infill contributed to about 90% of the initial stiffness of the system. A displacement ductility of 3 was achieved. It was observed that more than 67% of the total energy dissipated was due to the infill plate. However, total energy dissipated was less than one-fifth of that achieved by solid steel panel.

Stojadinovic and Tipping (2008) proposed a shear wall system that utilized a low profile metal deck as sheathing which was fastened to light-framed cold-formed steel framing with screws. The term “corrugated sheet steel shear wall” or CSSSW was used to describe thissystem. The main purpose of this research was to provide the practicing engineers with a stronger, stiffer and less expensive lateral bracing system. Cyclic loading tests were performed on 44 specimens. The six design variables that were varied during the test were: gauge of the corrugated sheet steel (22 gauge, 20 gauge and 18 gauge), gauge of the studs and tracks, fastener type/size, fastener spacing for attachment of corrugated sheet steel, inclusion of gypsum board on one side and application of the corrugated sheet steel on one or both sides of a wall specimen. For connections, note that the sheathing (corrugated plates) was fastened to the stud and the stud in turn was fastened to the

boundary elements. To facilitate installation and removal of the specimens from the test frame, attachment plates were fastened to the perimeter of the specimens with self-drilling sheet metal screws. These plates, in turn, were fastened to the test frame with High Strength bolts. Test results showed that in all the cases the failure mode of the specimen was the popping out of the screws due to warping of the corrugated plates. In all cases, the first screws to pop out were located in the boundary members. Further, the comparison of the results showed that using of gypsum board had little effect on the strength and stiffness of the CSSSW. To determine the effect of adding the corrugated sheet steel to both sides of a specimen, two specimens were tested. It was concluded that double sided walls can achieve double the shear strength.

2.3. PERFORATED STEEL PLATE SHEAR WALLS

Perforated steel plate shear walls such as shown in Figure 9, are shear walls with single or multiple circular holes. These shear walls were developed by the researchers to allow for utility access. These perforations also served as a method of reducing the panel strength and in turn the demand on the reducing frame. This characteristic was believed to be beneficial in markets that do not have low yield strength (LYS) steel readily available.

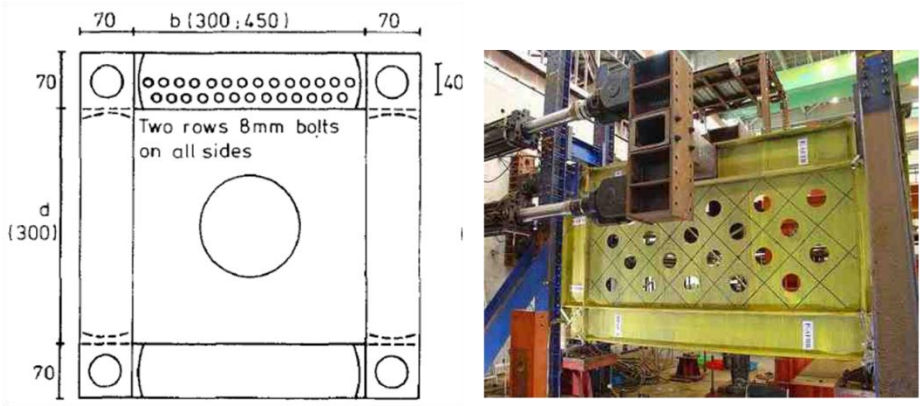

(a) Single perforation panels (Roberts and Sabouri-Ghomi, 1992)

(b) Multiple perforations panel (Vian and Bruneau, 2005)

Figure 9: Perforated steel plate shear walls [from (Roberts et al. 1992 and Vian et al. 2005)]

Roberts and Sabouri-Ghomi (1992) performed a series of sixteen quasi-static cyclic loading tests on unstiffened steel shear walls with centrally placed circular openings of varying diameters. Panels with aspect b/d ratio of 1 and 1.5, thicknesses of 0.83mm and 1.23 mm and circular opening diameter ranging from 0 to 150 mm were used. The plates were clamped between rigid pin-joined frame elements. Experiment results demonstrated that all the panels tested exhibited stable hysteresis loops. All the panels exhibited adequate ductility for the first four loading cycles without significant loss in the load-carrying capacity. It was observed that the stiffness and the ultimate strength of the panels reduced linearly with the increase in the diameter of the circular openings. Roberts and Sabouri-Ghomi (1992), therefore suggested that the strength and the stiffness of a perforated plated can be approximated conservatively by applying a reduction factor of (1-D/d) (where, *D* is the perforation diameter and *d* is the height of the panel) to the strength and the stiffness of a similar un-perforated plate. In another paper, Roberts and Sabouri-Ghomi (1991) developed an analytical model to predict the hysteretic behavior of the unstiffened steel shear walls. This model was modified using the reduction factor and the results were compared with the experimental data. Using a reduction factor of (1-D/d) implied completely neglecting the contribution of steel of width equal to the diameter of the opening along the diagonal. Therefore, as anticipated it was found that the model gave conservative values. Other factors which lead to conservative results were that strain hardening was neglected and the plate boundaries were treated as simply supported, thus underestimating the critical load.

Vian and Bruneau (2005) conducted experiments to investigate the efficiency of steel infill panels with circular openings. They came up with an effective reduction factor to account for reduced stiffness and strength of panels with multiple circular holes. The test set-up and the specimen (specimen CR) dimensions were identical to those mentioned in the previous section. After considering a number of options for the hole diameter and spacings, the final design of the infill panel had 20 circular openings staggered to be aligned diagonally at 45^{o}, with a diameter of 200 mm and horizontal/vertical spacing of 300 mm. This pattern of circular openings would reduce the stiffness of the panel by 17% as predicted by the reduction factors developed by Vian et al.(2005) The specimen displayed stable S-shaped hysteresis loops with little pinching. Observed elastic stiffness was 115 kN/mm. Yielding was first observed at a drift of 0.3%. At 1.2% drift, the RBS connection started yielding at the top beam connection. At 2.5% drift, yielding and buckling of the fish plate was observed in addition to the web local buckling at the

bottom beam RBS connection. The test was finally stopped at 3% drift when a column continuity plate fractured. Although the web panel had not fractured at this drift, severe damage and distortions to the panel had made it impractical to continue testing. The elastic strength and elastic stiffness of the specimen were found to be 85.5% and 81.5% respectively, as compared to a solid panel of same dimensions. This was in good agreement with the value predicted earlier. The maximum base shear achieved was 1790 kN. A displacement ductility of 10 was achieved when the test stopped.

Moghimi and Driver (2011) investigated the influence of perforations on steel plate shear walls by comparing them with similar SPSW systems with no perforations in their infill plates. For the purpose of this study, a set of three four-story walls were chosen. Set A consisted of solid walls whereas set B and C consisted of walls with circular opening. They had 18 openings each on the top-most story. For the other three stories, set B had 22 openings as opposed to set C which had 23 openings. All the openings were regularly spaced vertically and horizontally (at a distance of 280 mm) over the entire area of the infill plates. Note that each set consisted of two specimens which were identical to each other, but employed different beam-to-column connection- moment and shear connections. According to the perforation patterns, it was predicted that the shear resistance of the perforated wall should be 0.6 times that of a solid wall. The pushover analysis showed that a reduction factor of 0.6 was a conservative evaluation. The most notable finding of the paper was associated with the force demand of the shear walls. It was found that, although the perforations reduce the shear capacity of the infill plate considerably, they may not reduce the force demands on the columns, especially at the upper stories where the perforations make the design strength ratios worse. These results are in contrast the main idea behind the development of this system and also highlight an inherent uncertainty in the response of the perforated plates.

2.4. PANEL WITH QUARTER-CIRCLE CUTOUTS

As a continuation of the experiments performed by Vian and Bruneau (2005) on LYS steel panels, tests were done on a specimen with quarter-circle cutouts at the four corners of the web plate. The main purpose of the cutouts was to provide access to utilities. Also, the corner cutouts are a favorable feature because they provide more flexibility to accommodate angle change at the frame corners during sway. This results in lower end moments along the length of the arc. An arc

section 160mm wide and 19mm thick was chosen after preliminary calculations. The other plate dimensions were identical to the ones mentioned in Section 2.1.2.The hysteresis curve obtained was stable with little pinching. As observed in other specimens tested by Vian and Bruneau, buckling of the panel started at a drift of 0.1% and yielding initiated at 0.3% drift. The fish plate started buckling at 1.5% drift. At about 3% drift fractures of the beam RBS was observed in addition to the fractures in the infill plates. At about 4% drift, a loud bang was heard, followed by a reduction in the strength of about 24-35% in the subsequent cycle of the same amplitude. At this drift, the test had to be stopped due to safety issues. The infill plate could have resisted loading to larger deflections, but the testing had to be concluded to prevent lateral support damage. The end of the test was marked by local buckling of the fish plates, severe tears in the panel interior, weld tears in the top bam top flange continuity plates and twisting of the columns. The maximum base shear strength was noted as 2050 kN which was quite comparable to that of an identical panel with no cutouts. An elastic stiffness of 140kN/mm and a displacement ductility of 13.33 were achieved by the specimen.

2.5. SLIT STEEL PLATE SHEAR WALLS AND RELATED SHEAR FUSE PLATES

2.5.1. Panel with rectangular slits

Panels with rectangular slits such as shown in are steel shear walls with vertical slits equally spaced, forming columns of links. When subjected to lateral loading, these links behave as beams in double curvature, dissipating energy in flexural. Numerous variations in these types of panels have been investigated in the past.

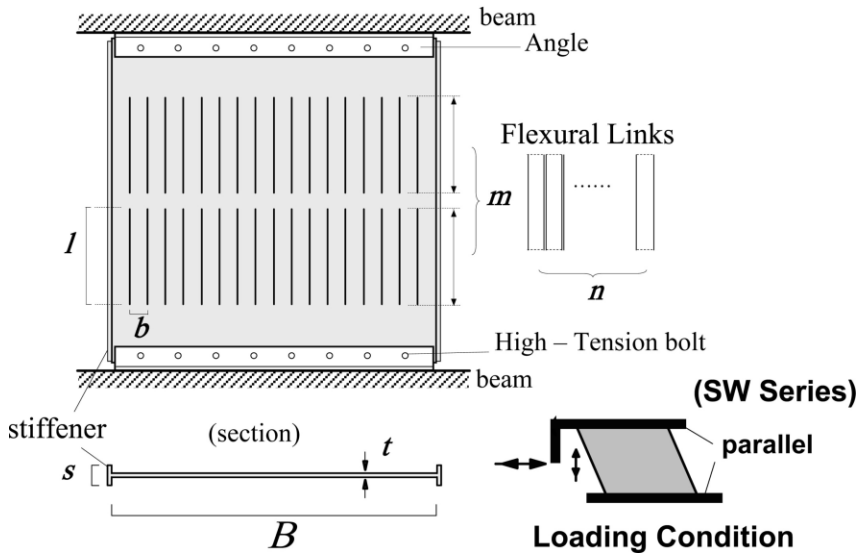

Figure 10: Steel plate walls with rectangular slits [from (Hitaka et al. 2006)]

Hitaka, Matsui, Tsuda and Sadakane (2000) conducted experiments on slit panel shear walls with beam-to-column rigidity ratio and the strength/stiffness of the shear wall as the test parameters. The main aim of the test was to bring out the mutual effects of the wall and the frame when attached to each other. Three sets of frames were used: one with beam-column rigidity ratio larger than 1 and the other, less than 1. In the other set of frames two kinds of shear walls; one stronger and stiffer than the other. Last set of two frames did not have any shear wall. Stiffeners were welded at both sides of the wall to prevent out-of-plane deformation. All the specimens showed stable hysteresis with little or no pinching. A maximum drift of more than 4% was observed in all the specimens. As compared to the frames with infinite stiffness, the behavior of these specimens was relatively unstable. It was noted that the wall contributes greatly to increase the stiffness of the structure. Also, there is a modest increase in the frame stiffness with the addition of shear wall. It was also noted that for the same story drift, the vertical force transferred from beam to the shear wall is smaller in the case where the beams are not infinitely rigid. With respect to energy absorption capacity, it was observed that the shear wall contributed to almost 70-80% of the total energy absorption capacity of the system.

Hitaka and Matsui (2003) introduced the steel plate shear walls with vertical slits. In this system, the segments between the slits formed a series of flexural link and provided a fairly ductile response. Hitaka and Matsui came up with equations to predict the initial stiffness and the

ultimate strength of the slit panels. Also, a series of four tests (A, B, C, D) were conducted on a total of 42 specimens. Test series A and B focused on the behavior of shear walls with varied slit parameters (b/t, L/t, number of slits in a row, number of rows). The objective of the Series C was to study the transverse behavior of the slit walls with and without transverse stiffening. Series D tests examined the shear wall behavior under different loading protocols. Steel panels for all specimens had the dimensions of 800 mm by 800 mm by 34.5 mm, which is about one-quarter to one-third of the full scale applications. All the specimens other than the Series C specimens were stiffener stiffened.

Except for a few, all specimens underwent story drift of more than 3% without initiation of cracks or abrupt strength degradation. The response was pretty linear until the force reached one-third of its maximum, after which the response softened until reaching the maximum strength. At about 5% drift, all the specimens experienced transverse deformation which resulted in post-peak strength degradation. In general, this post peak strength degradation was stable for almost all the elements. At about 2% drift some specimens saw initiation of cracks at slit ends. These cracks propagated further and led to the ductile fractures in some specimens at 4% drift which in turn resulted in substantial strength degradation. It was however concluded that the main cause of strength degradation was transverse buckling of the plate, rather than the ductile fractures.

With respect to the parametric design, b/t ratio of the flexural link was found to be most influential parameter. A major observation to back up this idea was that all the specimens with b/t ratio of 10 did not display any transverse deformation up to a drift of 2.5%, whereas all the other specimens this deformation took place before a drift of 2%. By comparing specimens with equal plastic strength, it was noted that specimens with higher β ratio (ratio of total link length to the wall height) displayed higher ultimate strength. Regarding the out-of plane deformations, a few major conclusions could be drawn. Firstly, Stiffening enhances the maximum strength of a specimen and the drift at which it experiences an increase in out-of-plane deformation. In stiffener-stiffened specimens, it was observed that specimens with relatively large b/t and L/b ratios suffered pinching when inner links deformed out of plane. Contrary to this, specimens with relatively large b/t ratios and smaller L/b ratios, experienced out-of plane deformation of the entire panel. This behavior was similar to panels buckling in shear which eventually led to pinching of the hysteresis curves. It was also noted that controlling the b/t, L/t and L/b ratios can

help restraining the links from flexural torsional buckling. The aspect ratios of the links were thus concluded to be of paramount importance in the behavior of the panels.

Cortes and Liu (2008) discuss the behavior of steel slit panels (SSP) as an independent unit and as a part of lateral force resisting system (LFRS) and put forward the idea of three different SSPs that may be used for the system. The SSPs discussed here differ from the panels tested by Hitaka and Matsui (2000, 2003) in that the aspect ratio of the panel is 1:2 instead of 1:1. Also, the main objective of the design of SSPs was to resist the entire base shear in the SSP instead of just a fraction. In general, the behavior of panels tested by Hitaka and Matsui was similar to SSPs, but the global behavior of a frame with SSP is quite different. Cortes and Liu have suggested the consideration of gravity loads while analyzing the SSP designs. Panel strength and frame stiffness have been pointed out as important factors that influence behavior of LFRS. A flexible beam will result in the reduced stiffness of a Steel Slit Panel Frame (SSPF). Also, the stiffness provided by a panel also depends on the story in which it is located. It has also been noted that the stiffness of the SSP depends on the shear stiffness of the zones above, below, and between links and the shear and flexural stiffness of the links. Finally, three designs for SSPs have been presented (Panel T1, T2 and BR). The first panel (T1) had three rows of nine links. It is simple to fabricate and dissipates great amount of energy. Panel T2 had two rows of eight links and was stiffer than T1. T2 employs stiff stub beams at the top and bottom of the panel which is capable of increasing the overall stiffness. Finally, Panel BR had the same dimensions as Panel T1, however a brace was provided over the links to reduce their buckling. Panel T1 and BR had bolted connections to the loading frame in addition to the edge stiffeners to provide extra stiffening. The experimental results for this panel have been discussed in the next section.

Tests were performed on panel T1 with two different thicknesses. The hysteresis curves obtained from both the tests were flat and stable up to large drifts. The test results showed that both the specimens first yielded at 0.125% drift. Although both specimens suffered lateral torsional buckling, for the thicker T1 panel this type of buckling was observed at 4% drift, as opposed to its counterpart, where it was observed at 2% drift. Both the specimens experienced failure of flexural links at the end of 7% drift, which led to the conclusion of the test. The thicker panel could resist a maximum load of 28.8 kips as opposed to the thinner plate which could only resist a maximum load of 19.8 kips. As anticipated the thicker plate had a higher initial stiffness of

72.6 k/in as compared to the thin panel which had stiffness of 50.6 k/in. Another test was performed on Panel type T2, with a panel thickness of 3/16''. This panel exhibited shear buckling a tension field action at a drift of about 2%. Two main factors that are believed to have caused the tension field action and the shear buckling are the boundary conditions and the aspect ratio of the panel. This panel was welded to the stub beams along its entire width. This created more rigid boundary conditions as compared to the other specimens which had bolted connections. For the panels with bolted connections, the distance from the edge stiffener to the first bolt was not restrained, allowing some rotation to take place. This small rotation proved beneficial in preventing the tension diagonals or shear buckling from occurring. In addition, the width to height aspect ratio of this panel was approximately 0.6. This panel was relatively wider than all other panels which had an aspect ratio of approximately 0.4.

These conditions, found exclusively in this panel, were the main cause for the generation of the apparent tension field action and shear buckling of the panel. Apart from this, lateral torsional buckling of the panel was also observed at a drift of 1.5%. The test had to be concluded early at 5% drift due to fracture in the links. The specimen however has a comparable maximum strength of 24.4 kips and a high stiffness of 80 k/in. the main problem with Panel T2 was the difficulty in installation. The height of the panel was detailed to be the same height as the frame, thus very little space, if any, was available. It was therefore recommended that if this panel was to be specified for use in a building, it would be necessary to leave some space for constructability purposes.

Cortes and Liu (2009) discussed the advantage of steel slit panels as lateral force resisting system. Their work focused on the design aspect of the slit panels. The main parameters to be considered when designing a steel slit panel (SSP) are: α (length to width ratio of the link), β (fraction of panel height that is composed of the links) and the links cross-section aspect ratio b/t. The b/t ratio is important as it influences the buckling of the links and should be ideally between 10 and 15. The geometry of the panel was chosen according to the load demand. The number of panels on each story was decided according to the strength of each story. Once the geometry and the number of panels were decided, the stiffness and the strength of the panel were obtained as the sum of shear forces acting on the links when they reach the plastic moment. The designer must also ensure that global lateral-torsional buckling of the panels do not occur at an early

stage. After the design of the panel, the seismic frame was designed. The stiffness of the frame members is highly influential in the performance of the panel. Also, the story at which the panel is placed affects its behavior. The beam in the frame should be designed to remain elastic and should satisfy a deflection limit of L/500 for gravity loads. Panels must be connected to the frame using fin plate connection. The connection should be checked for all limit states required by AISC. When all the members are designed, finite element modeling should be done to analyze the frame and check the inter-story drift.

2.5.2. Rectangular fuse with buckling restrained channels

Borchers, Peña, Krawinkler, and Deierlein (2010) conducted experiments on rectangular fuse with buckling restrained channels to reduce the buckling in longer links. The behavior of this specimen was then compared to that of a specimen without these channels. The behavior of the two specimens was almost the same prior to reaching 4% drift. However, after this point buckling was observed in the specimen without channels, whereas, since buckling was restrained in the main specimen, strength kept on increasing. After a few cycles, cracks initiated in both the specimens but the strength of the restrained specimen plummeted and within the next three cycles, five of its links totally fractured. Specimen without the channels could sustain 4% more deformation. Two major conclusions were drawn from the test. Firstly, the buckling restrained channels tend to delay strength degradation. Second and more importantly, restraining the links affect low-cycle fatigue. Since the links cannot buckle to distribute deformation, stress concentration is severe at the link ends. Consequently, once the cracks initiate the fuse experiences very brittle failure which is definitely undesirable.

Cortes and Liu (2008) performed experiments on slit fuse with buckling restraint channels (Panel BR) as mentioned in the previous section. The hysteresis loops obtained from the experimental data were generally stable and full. There was minimal pinching and flattening of the loop up to a drift of 4%. The panel did not exhibit any out-of-plane deformation up to a drift of 3%. After that, global twisting and lateral torsional buckling of the panel was observed. The test was finally stopped at a drift of 7% when a majority of the links fractured. The overall behavior of the panel was better than Panel T1 with same dimensions but without any restraint channels. Panel BR was 35% stiffer and exhibited 41% higher strength.

2.6. BUTTERFLYFUSE

2.6.1. Panels with butterfly fuse

The experiments conducted by Borchers, Peña, Krawinkler, and Deierlein (2010) at Stanford University were focused on the behavior of slit fuse and butterfly fuse panels. Figure 11 shows one on the butterfly fuse panels tested. The major of the test specimens were the L, b, t, b/t, L/t, w_s (diameter of the rounded slit ends) and a/b ratio in case of butterfly fuse. A total of six specimens were tested.

The test results showed that unlike the rectangular slit fuse panels where the yielding initiated at the slit edge, butterfly fuse panels had yielding concentrated at around the quarter height of the panel. As the deformation increased, it got distributed along the edge of the slit indicating a proper distribution of yielding. Near the end, buckling became so severe that the links turned 90 degrees and became perpendicular to the loading direction. However, it was observed that butterfly fuse could sustain more deformation and was able to withstand higher load at large drifts.

Two main reasons were brought up for this kind of behavior. First, the uniform yielding along the edge of the link in the butterfly fuse reduced strain concentration at a particular point on the link and thus, delayed crack initiation. Second, since the plastic hinge formation took place at quarter height sections in the butterfly link, the effective length of the link in tension was shorter as compared to the links in slit fuse where the hinges are formed at the slit ends. Due to shorter length of the tension portion, it could contribute more to the lateral strength. Another butterfly fuse which had a relatively larger L/t ratio was tested. It was found that buckling in this specimen was delayed. This differences was however not very significant and it was be concluded that L/t ratio is not very influential in butterfly-fuse performance. Test results of a specimen with a very small b/t ratio (=6) showed that thick fuses can sustain stable hysteretic behavior up to much larger drifts. Buckling was also delayed. This in turn increased the total energy dissipation. The ultimate deformation however was similar. It was thus concluded that a smaller b/t ratio improved stability and energy dissipation. Another specimen with a still smaller b/t ratio (=2) was tested. It was found that very thick butterfly fuse exhibited stable hysteresis behavior throughout the test. Due to strain hardening, the ultimate strength exceeded twice the design

strength. The main findings of this test was that when the fuse is thick enough, buckling can be prevented which implies more energy dissipation. However, their over-strength due to strain hardening might be an undesirable after-effect. Overall, all the butterfly fuses acted in a more ductile manner as compared to the slit fuse panel.

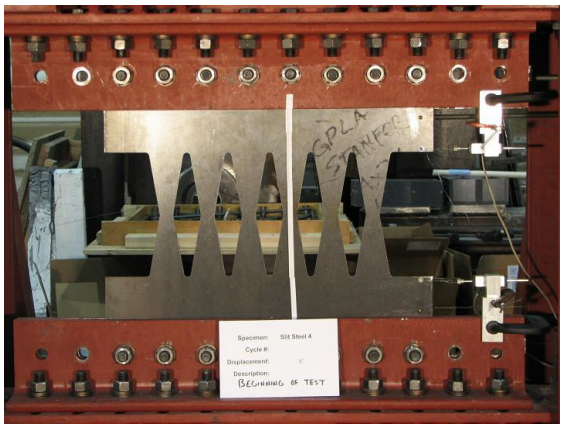

Figure 11: Panel with butterfly fuse [from (Borchers, Peña, Krawinkler, and Deierlein 2010)]

2.6.2. Panels with butterfly fuse attached to a backing plate

Borchers, Peña, Krawinkler, and Deierlein (2010) conducted experiments on butterfly panels with backing plate connection. The results obtained from these specimens were then compared to the ones where no backing plate was provided. It was found that they behaved the same up to a drift of 2.4%. However, after buckling, there was more decrease in strength of the panel without backing plate. After the formation of the tension field, the strength in the fuse with backing plate is 5-10% higher due to the friction between the fuse and the backing plate. The fatigue behavior was also quite different for both the fuses. B10-36W did not show any signs of cracks until a drift of 20% as compared to a drift of 14% in the unrestrained fuse. This was because in the unrestrained fuse, the links formed a hinge in the middle due to compression which incurred a lot of repeated rotation in addition to tension deformation. These conditions led to the fracture of this fuse at such locations. When a thick butterfly fuse (b/t=7) was used with backing plate connection, the most important finding which came out was the damage to the fuse due to over-strength as previously mentioned. At a drift of about 17%, the strength of the fuse exceeded 1.5 times the design strength. The weld was not designed to take up this kind of load and it failed causing the strength to drop down drastically. It was therefore of extreme importance that the connections in slit and butterfly fuses are designed to account for the over-strength due to a

combined effect of tension and strain-hardening. If adequately accounted for this idea, backing plate is a viable connection detail.

2.7. DISSIPATIVE DEVICES EMPLOYING THE RING-LINK SYSTEM

R.G. Tyler (1985) described the tests on a dissipative device carried out by David Smith and Robert Henry in Auckland, New Zealand in 1970s. This device, also known as yielding frames, dissipate energy through the yielding of the round bars which constitute them. The yielding frame shown in Figure 12 is geometrically similar to the framework in which it was incorporated.

When subjected to lateral loading, this device deforms into a parallelogram and develops no slack along the diagonals, as experienced by conventional cross-bracing systems when subjected to racking deformations. The yielding frame thus exhibits stable cyclic behavior. Cyclic tests on bracing systems incorporating the yielding frames showed that many hundreds of cycles can be completed without the development of much slack in the braces. Thus, the proposed bracing system was proved to be reliable in providing stable earthquake resistance.

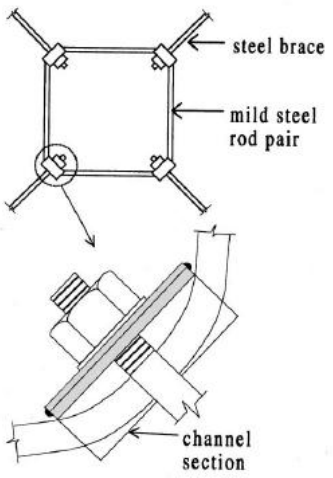

Figure 12: Yielding frame with constant cross-section [from (Tyler 1985)]

Ciampi and Samuelli-Ferretti (1990) also proposed a class of dissipating devices based on flexural yielding of steel. As mentioned above, these yielding frames are geometrically similar to the main framework and connected to its joints through tension-only braces. Under lateral cyclic

loading, the yielding frame deforms inelastically while keeping both the connecting braces in tension. This results in a fully dissipative hysteretic response.

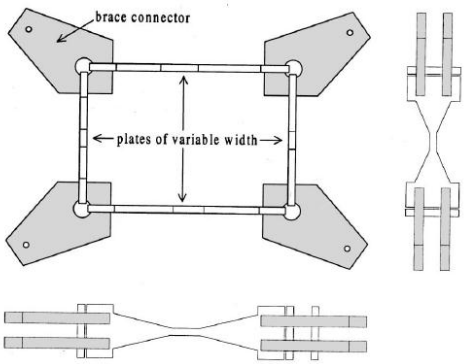

Figure 13: Yielding frame with varying width [from (Ciampi and Samuelli-Ferretti 1990)]

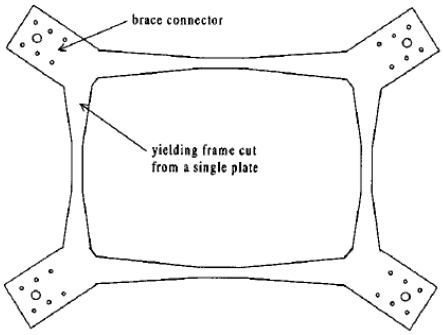

Figure 14: Yielding frame with varying depth [from (Ciampi and Samuelli-Ferretti 1990)]

The energy yielding frame is cut out from a thick steel plate. Unlike the system presented by Tyler (1985), the cross-section of the yielding frame has a tapered shape which is anti-symmetric to the flexural moment distribution that develops in it during the lateral displacement of the whole system. Two variations to this device were proposed-one with linearly variable width as shown in Figure 13 and the other with linearly variable depth shown in Figure 14. This type of varying cross-section ensures that the device experiences uniform distribution of plastic deformation.

This device was tested separately as well as in the form of one-bay one-story frame system. In all cases, the system was efficient and exhibited good dissipation capacity and long cyclic life. However, these devices exhibited undesirable expansion as a result of excessive plastic deformation. In real applications, this kind of expansion may have adverse effects on the

behavior of the entire bracing system. Ciampi and Samuelli-Ferretti (1990), then suggested the use of pinned steel plates parallel to the edges of the yielding frame, as shown in Figure 15. These plates were designed to resist only axial forces and remain elastic, thus ensuring that the plastic deformation in the yielding frame is primarily due to bending.

The modified device was incorporated in one of the buildings of the Laboratories of the National Research Council in Frascati, Italy. As compared to the conventional bracing system, this modified dissipative bracing showed lower inter-story drifts and base shears.

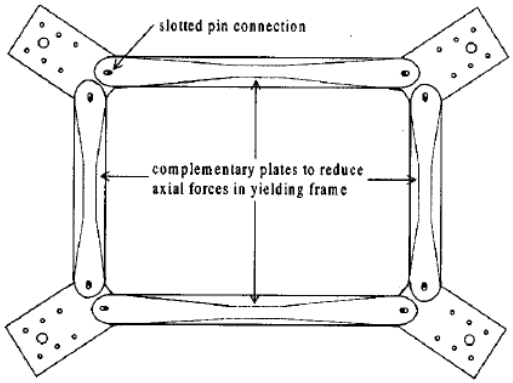

Figure 15: Yielding frame with complementary plates [from (Ciampi and Samuelli-Ferretti 1990)]

Colin Rogers and Tom Morrison (2011) developed a ring fuse system for the rehabilitation of existing structures. The purpose of the ring fuse, shown in Figure 16, was to reduce the tension capacity of the brace below the capacity of the connections. This would ensure that the failure mode of the system is ductile.

The ring fuse was cut out from a steel plate with the help of plasma cutters and was developed to work in tension only. The major advantage of the ring fuse is its tunability. Thus, slight modifications in the geometrical features of the fuse can result in efficient control over the fuse-brace system behavior (like strength, stiffness etc.). This feature of the ring fuse increases its ability to satisfy a wide range of system requirements. Additionally, it also has large deformation capacity.

Several reduced scale tests (both tension-only cyclic loads and reverse cyclic loads) were performed with the ring fuses assembled in the intersection of the braces. Their capacity was tuned below the capacity of the connections. The response of the brace-fuse system was then

compared to the original system without the fuse. As anticipated, the brace-fuse system demonstrated much higher ductility. Finite element models were also generated and the results obtained from them were found to be in good agreement with the tested models.

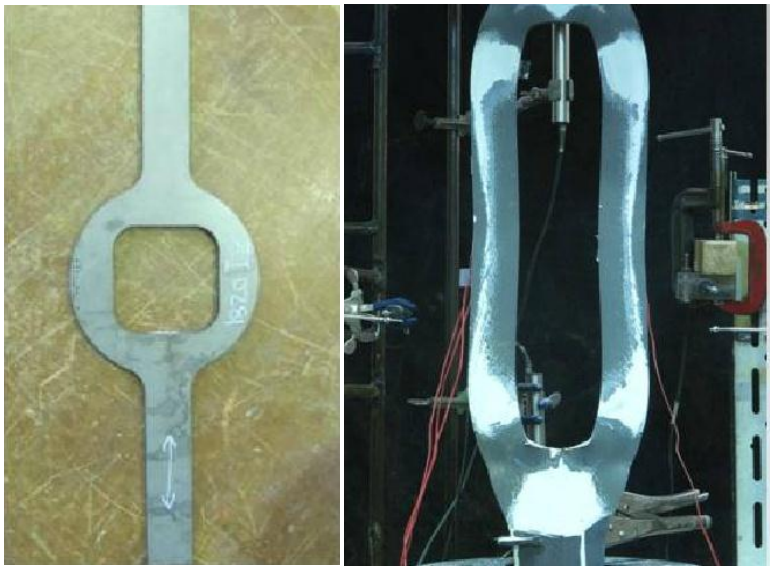

Figure 16: Ring fuse [from (Rogers and Morrison 2011)]

CHAPTER 3

BUCKLING RESISTANT STEEL PLATE SHEAR WALL (BR-SPSW) CONCEPT

The motivation for the use of rings as the basic unit of the shear wall is to improve the energy dissipation capacity and resistance during load reversals of the steel plate shear wall. In the BR-SPSW, this has been accomplished by using ring shaped cutouts as shown in Figure 4. Also mentioned in Chapter 1 was the fact that when the ring shape deforms into an ellipse, the elongation of the ring in one radial direction is compensated by approximately equal shortening of the ring in the perpendicular radial direction. This section elaborates the analytical proof of this concept and how this "ring-effect" translates into reduced buckling of the full wall, higher energy dissipation, and good force resistance during load reversals.

Consider a single ring, as shown in Figure 17 that is stretched by an amount δ_1. In this figure, the stretching is shown to occur in the horizontal direction for clarity, but represents the stretch along the inclined direction of the tension field. For a circle of radius ***r***, the transverse deformation of the circle δ_2 is derived, assuming the perimeter, P, remains constant as the ring is stretched in the longitudinal direction by an amount, δ_1. The definition of geometric parameters for the circle and the ellipse is shown in Figure 17.

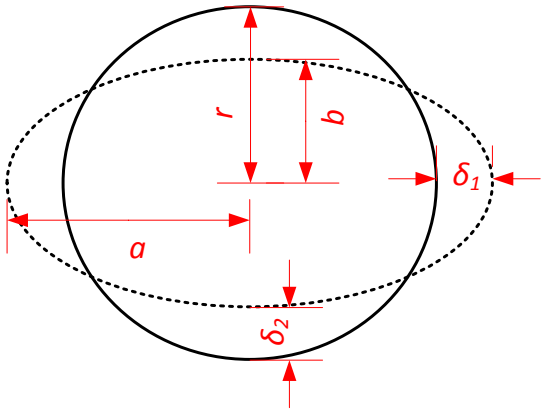

Figure 17: Geometry of the circle and the deformed ellipse

The approximate perimeter of an ellipse, $P_{ellipse}$, is given by Equation 3.1, where *a* and *b* are the major and minor radii of the ellipse, respectively as shown in Figure 12.

$$P_{ellipse} \approx 2\pi\sqrt{\frac{a^2+b^2}{2}} \tag{3.1}$$

The perimeter of the circle, P_{ring}, is given by Equation 3.2.

$$P_{ring} = 2\pi r \tag{3.2}$$

Equating the two perimeters results in Equation 3.3,

$$2\pi\sqrt{\frac{a^2+b^2}{2}} = 2\pi r \tag{3.3}$$

The values for *a* and *b* can be related to the radius and deformations as given in Equation 3.4

$$a = r+\delta_1 \text{and} b = r-\delta_2 \tag{3.4}$$

Substituting these values in the Equation 3.3 and squaring both the sides gives:

$$\frac{(r+\delta 1)^2+(r-\delta 2)^2}{2} = r^2 \tag{3.5}$$

Expanding the terms and solving the quadratic equation for $\delta_2$results Equation 3.6.

$$\delta_2 = r - \frac{1}{2}\sqrt{4r^2 - 4\delta_1^2 - 8r\delta_1} \tag{3.6}$$

The variation in transverse deformation, δ_2, resulting from longitudinal stretching, δ_1, is shown in Figure 18. The plot highlights several key points relevant to the BR-SPSW concept. The curve labeled "Ring" in the plot shows that for small applied deformations, the longitudinal and transverse deformations are nearly equal in magnitude. If the ratio of transverse deformation to the longitudinal deformation (δ_2/δ_1) is thought of as an effective Poisson's ratio of the ring unit, the slope of the "Ring" curve would give the effective Poisson's ratio. For small deformations this ratio is nearly unity. In a steel plate shear wall, an effective Poisson's ratio close to unity is desirable because it implies that when a material is subjected to longitudinal stretching, the plate would experience negligible slack in the transverse direction. To understand how this effect translates into a full scale shear wall system, consider an idealized BR-SPSW model subjected to

a small story drift Δ, as shown in Figure 19. The rings along the tension diagonal will elongate by a similar amount (L+Δ) as the compression diagonal is shortening (L-Δ), essentially pulling the plate taught in the transverse direction, thus resisting the tendency for the plate to buckle.

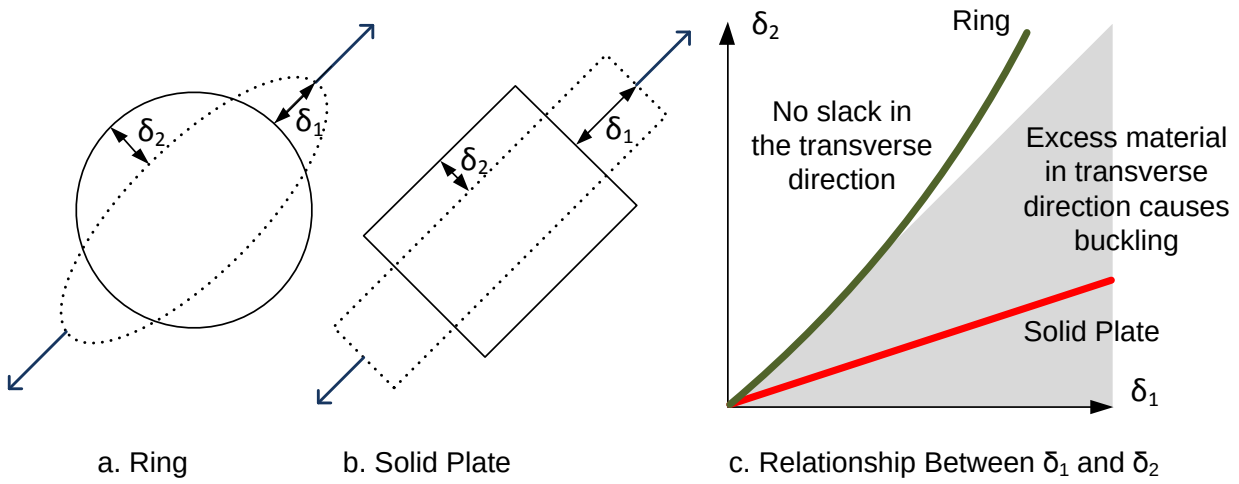

Figure 18: Concept showing how the ring eliminates slack in the direction transverse to the tension diagonal

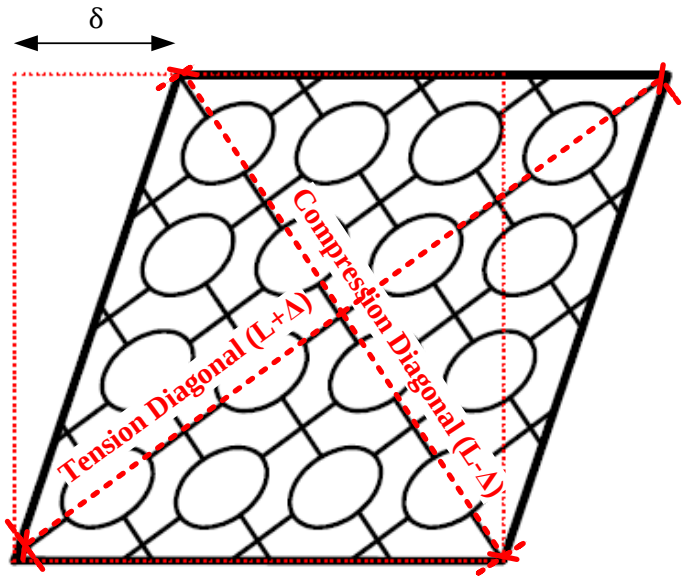

δ: Interstory Drift
L: Initial length of the diagonal

Figure 19: BR-SPSW subjected to lateral load

When compared to a standard SPSW wall, which exhibits an approximate Poisson's ratio equal to the Poisson's ratio of the steel material used (generally 0.3), this is a great improvement because an effective Poisson's ratio of 0.3 would mean that shortening of the solid plate material in the transverse direction is approximately 30% of the elongation in the longitudinal direction. This results in a slack due to excess material in the transverse direction which causes the buckling of the solid plate.

CHAPTER 4

VALIDATION OF THE BR-SPSWCONCEPT AND PRELIMINARY INVESTIGATIONS

This chapter describes and summarizes the analysis of a few selected finite element models (analyzed using ABAQUS (Version 6.10 Documentation)) to prove the concept behind BR-SPSW. Finite element models using shell elements have been used in the past to model SPSW (Vian and Bruneau, 2005). These computational models have been shown to capture wall behavior with good accuracy.

In addition to the validation of the BR-SPSW concept, the preliminary investigations were intended to give insight into the behavior of the BR-SPSW. This was instrumental in developing the parametric study test sets for the more comprehensive understanding of BR-SPSW. Moreover, the preliminary analysis was crucial to understand the deformation mechanics of ring units and the full wall. This information in conjunction with the preliminary analyses results helped the overall development of the analytical solutions for the system behavior (strength and stiffness) presented in Chapter 5 and 6.

As a part of the preliminary investigation, the following models were studied;

- Single story, one bay panel was investigated to analyze the performance of the full wall incorporating the ring units.
- Single story, one bay panel with varying ring diameters were analyzed for preliminary understanding of the influence of ring size on the system behavior (strength, stiffness and buckling mode)
- Unconstrained and constrained ring models were studied to understand the deformation mechanics of the ring units in the full wall. Unconstrained model was a single ring with two links subjected to pure tension along its axis (refer Figure 28). The constrained model as shown in Figure 33, was also a single ring model but with four links subjected to shear (with the base fixed). These models were developed to capture the two extremities in terms of boundary conditions, which were expected to bracket the boundary conditions of a ring unit in the full wall. These models further supported the

strength prediction of the full wall while allowing comparisons to equations predicting the panel strength based on ideal boundary conditions. Both shell and beam elements for finite element modeling

- Single story, one bay panel with staggered configuration was developed with the rings aligned at 45°. This model was investigated as an alternative to the aligned-ring model.

Before presenting the models, key geometric parameters used to define the SPSW rings are defined. Figure 20 defines the design parameters that are used in the subsequent sections.

Table 1 tabulates the notations used in this document associated with the plate geometry.

Table 1: Notations for the geometric features of BR-SPSW

t or t_w	Thickness of the web plate
R_o	Outer ring radius
R_i	Inner ring radius
w_c	Width of the ring
w_l	Width of the link
L_l	Length of the link
N_r	Number of rings in a row
N_c	Number of rings in a column
W	Width of the web-plate (horizontal dim.)
L	Length of the web-plate (Vertical dim.)

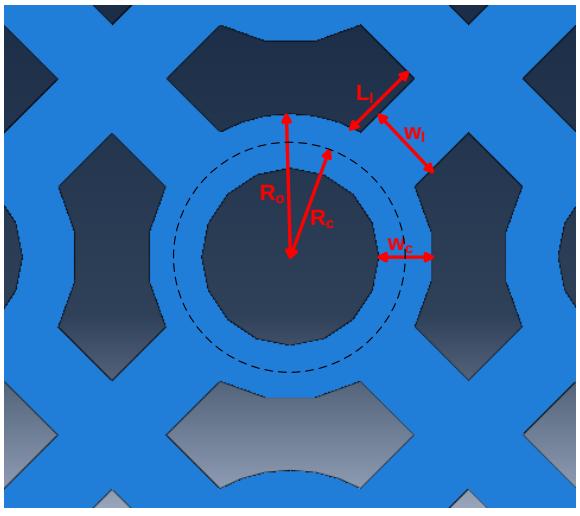

Figure 20: Geometric parameters of the SPSW rings

4.1. SINGLE STORY, ONE BAY PANEL: ALIGNED-RING MODEL

Firstly, the performance of the full panel incorporating ring units was analyzed using ABAQUS (Version 6.10 Documentation) as subjected to cyclic loading. The main modeling parameters used and the analysis results obtained are presented in this section. Figure 21 shows the modeling parameters of the panel.

4.1.1. Modeling features and parameters

For the material properties, stress-strain behavior of a typical 1/4in. thick A36 steel plate obtained from a test conducted in University of Illinois, Urbana-Champaign was used (Tanamal, et al. 2009). Several points were taken from the stress-strain curve shown in Figure 22 and were used as an input in ABAQUS. These points have been tabulated in

Table 2 along with the equivalent true stress and plastic strain values that were inputted in ABAQUS. Isotropic hardening was used to simulate hardening in the material model.

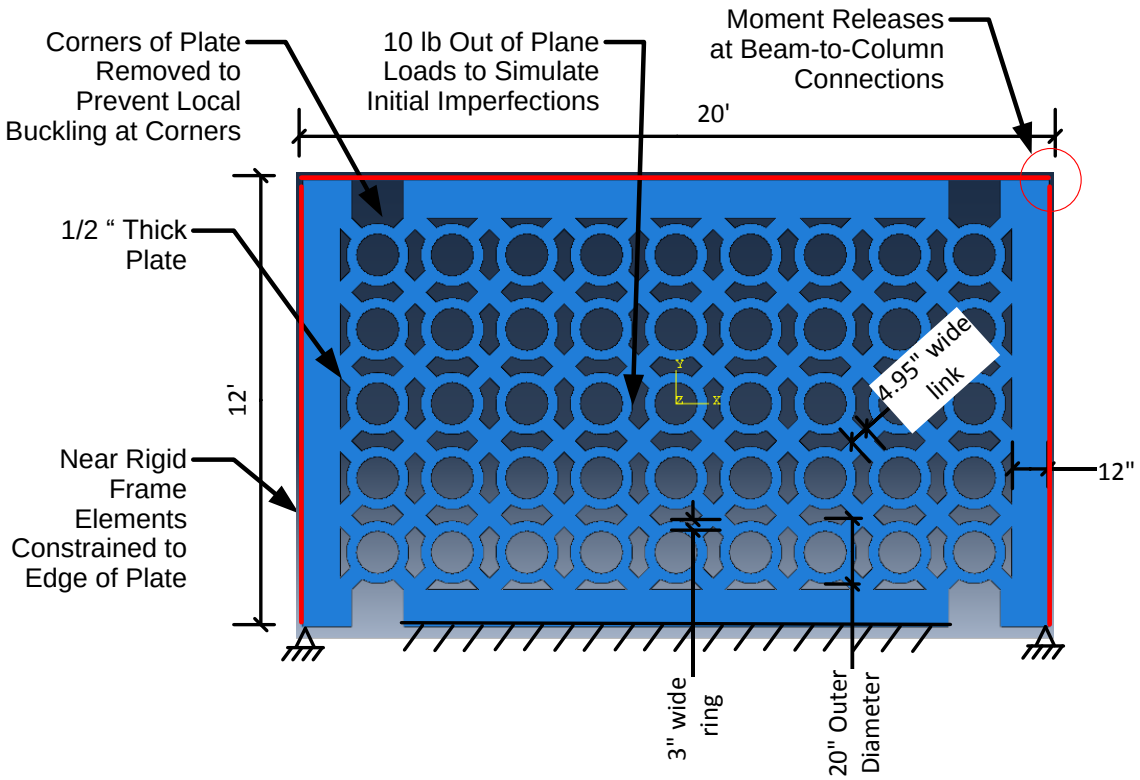

Figure 21: Modeling features of the SPSW panel

Table 2: Engineering and true stress and strain values used for steel

Engineering Stress (ksi)	Engineering Strain(%)	True stress(ksi)	Plastic Strain (%)
40	0.35	40.14	0
40	0.8	40.32	0.65
47	2	47.94	1.81
50	3	57.5	2.77
61.4	15	70.61	13.73

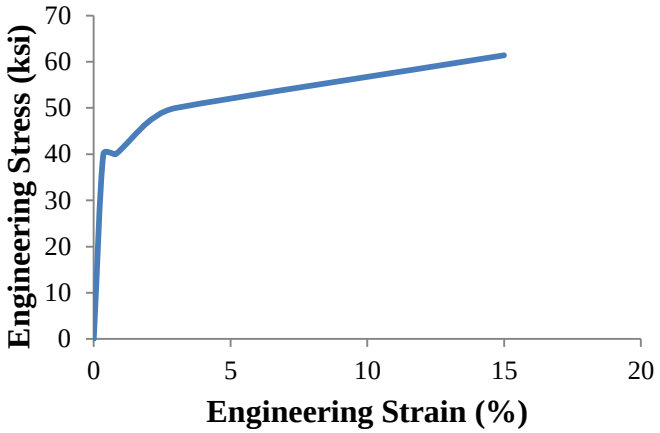

Figure 22: Stress-strain behavior of the steel used for analysis

The Young's Modulus (E) and the Poisson's ratio for the steel has been taken as 29000 ksi and 0.3 respectively. The boundary elements have been modeled near rigid ($A_{cross\text{-}section}$= 5000 in^{2}and I=25e06 in^4) with pinned connections to isolate the behavior of the shear wall. For meshing, four node reduced integration (S4R) shell elements have been used and the meshing has been done using an automatic meshing technique. A global approximate seeding size of 1.5 has been used. To account for imperfections in the panel, several out-of-plane loads of 5 and 10 pounds were applied to the panel at alternate rings on each row. Different types of boundary conditions were applied on different sections of the model. Presented below is a brief description of all the boundary conditions used.

- The base of the plate was pinned.

- The bases of the columns were pinned.
- The connections between the beams and columns were simulated using a multi-point constraint (the coupling option in ABAQUS) fixing all degrees of freedom except in plane rotation (i.e. pinned connection).
- The beam and the edge of the panel have been tied together using a multi-point constraint ("tie" constraint in ABAQUS) which constrains the translational degrees of freedom.
- The top beam was constrained against out-of-plane translation.

Horizontal displacement was applied to the right end of the beam in the form of steps. These displacements were cyclic in nature and went up to 4.5 in (≈3% drift). The loading protocol used for the analysis is shown in Figure 23. The analysis was run including consideration of geometric non-linearities, as large deformations were expected due to buckling.

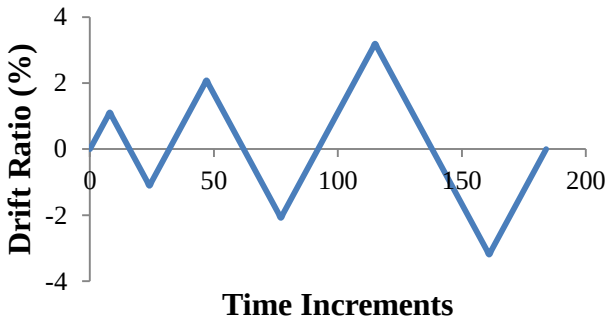

Figure 23: Loading Protocol used in the ABAQUS analysis

4.1.2. Analysis Results

The load-deformation curve for the panel was generated and is shown in Figure 24. The strength of the panel obtained from the ABAQUS modeling is about 204 kips. To obtain the strength of the model, it was subjected to a monotonic loading. An approximate lateral load when the load-displacement curve starts to plateau was recorded as the strength of the specimen. As anticipated, the panel displays a relatively fuller hysteresis curve as compared to the SPSW tested by Berman and Bruneau (2005), as shown in Chapter 1. The pinching behavior of the hysteresis has almost been eliminated. The reduction in strength and stiffness of the panel after each loading cycle is

minimal. Additionally, it can be observed from the hysteresis plot shown in Figure 24 that in the first two cycles, there is a negligible lag in the lateral load resistance as the tension field reverses direction, which is significantly less than that observed in a typical SPSW. The lag in the lateral load resistance at the end of the third cycle is due to the plastic axial deformation of the rings and links not dissimilar to the plastic axial deformations experienced in tests by Ciampi and Samuelli-Ferretti (1990). It is expected that the plastic axial deformations and the resulting lag in hysteretic behavior can be mitigated by adjusting the plate geometry. This will be investigated as part of the parametric study.

Buckling observed in the plate deformed shape was consistent with global tension field type buckling as shown in Figure 25. A small number of the rings experienced local lateral torsional buckling. The maximum out-of-plane deformation at the end of the third cycle was recorded as 5 inches.

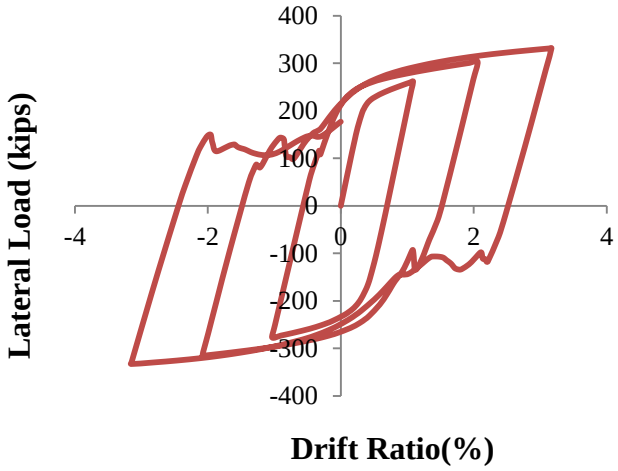

Figure 24: Hysteresis curve for the single story, one-bay panel.

The deformed shape of the panel and the stresses in the panel at 2% drift is shown in the Figure 25. A few important observations can be made from this figure. Note that the red color represents yielded regions and the blue color represents regions below 35 ksi stress.

First, as noted earlier, a few links connecting the ring units are yielding. It is expected that yielding of these links can be minimized by changing the plate geometry. Second, each ring appears to develop four plastic hinges. This arrangement of plastic hinges forms the basis of the plastic mechanisms derived in the next chapter to predict the strength of individual ring units.

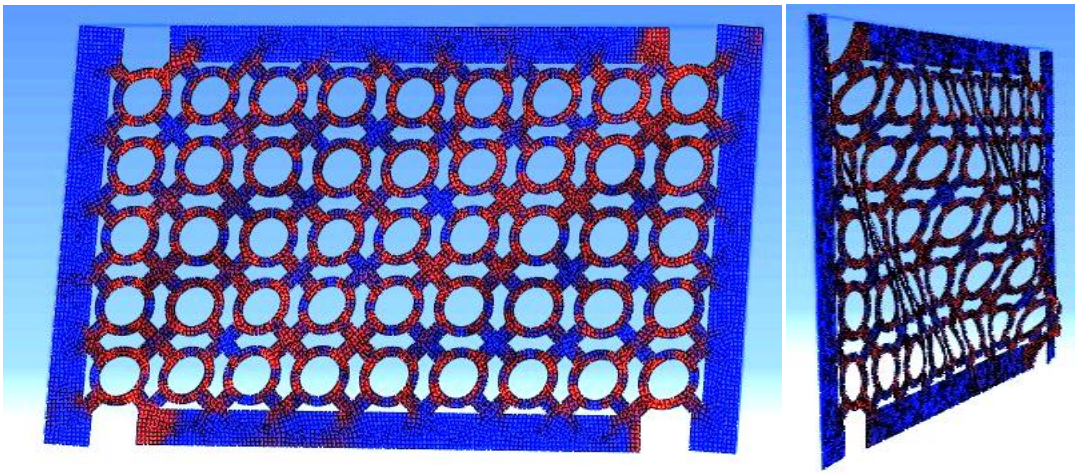

Figure 25: One bay, one story aligned ring panel at the 2% drift

4.2. SINGLE STORY, ONE-BAY PANEL: INFLUENCE OF DIAMETER OF THE RINGS

To study the performance of the panel when the diameter of the rings is varied, two more models were created in ABAQUS and their respective hysteresis curves were generated. Note that this section describes a preliminary investigation of the effect of the ring diameter. A more rigorous study is included in the later chapter on the parametric study.

Although BR-SPSW reduces the amount of buckling as compared to conventional steel plate shear wall systems, it still buckles to some extent. In addition to the wall behavior (strength and stiffness), this section also summarizes the preliminary investigation of the effect of ring diameter on BR-SPSW buckling modes. This issue has been investigated in-depth in the parametric study.

The basic ring unit dimensions of the panels tested as a part of this study is summarized in Table 3. All the other modeling parameters were identical to the model discussed in Section 4.1.

Table 3: Geometrical features of the panels to test the influence of the diameter

	R_o	W_c	W_l
Panel 1	8 in.	2.4 in.	4.24 in.
Panel 2	16 in.	6 in.	9.9 in.

The hysteresis curves obtained from the analysis of Panel 1 are shown in Figure 26. As observed from the hysteresis curve, Panel 1 exhibits stable and full hysteretic behavior up to the second

cycle. In the third cycle, the panel lags in lateral load resistance on tension field reversals, a phenomenon also experienced by the previous panel. The strength for the panel was recorded as 212kips. Buckling of the panel was observed to be majorly global tension field buckling as shown in Figure 26.

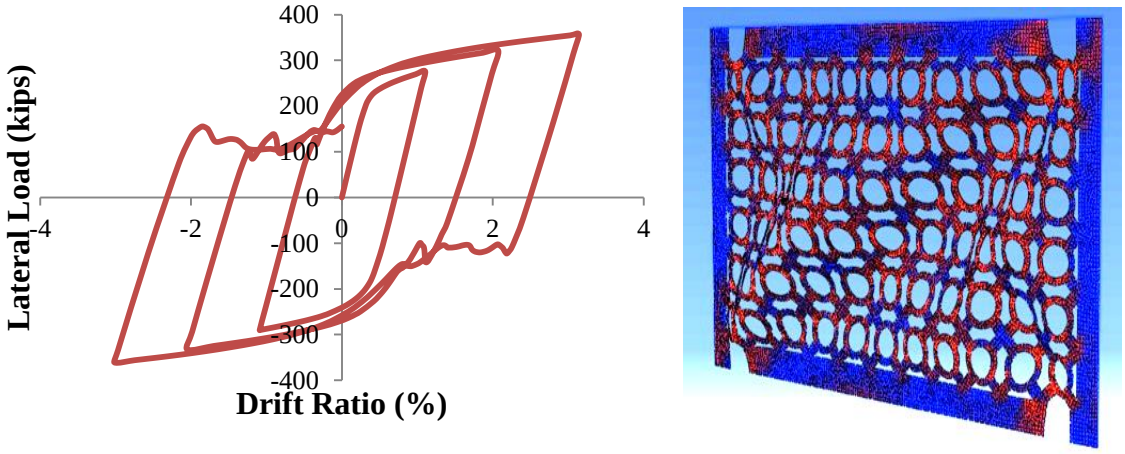

Figure 26: Hysteresis curve and out-of-plane deformation for Panel 1

Next, the hysteretic behavior of Panel 2 as captured and recorded in Figure 27. The panel exhibits a full hysteretic behavior only up to 1% drift. Thereafter, some pinching can be observed in the hysteresis curve. The strength of the panel was recorded as 359kips. Buckling of the panel was mostly in the form of local lateral torsional buckling of the rings as shown in Figure 27.

A preliminary conclusion is that changing the diameter of the rings had a major effect on not only the strength and the stiffness of the panel, but also on its buckling behavior. Ring size thus appears to be a key geometrical feature of BR-SPSW. Additionally, two major modes of buckling were identified: global tension field buckling and lateral torsional buckling of the rings. The panels with larger radii were shown to exhibit a combination of the two modes and the panels with smaller radii prominently exhibited global tension field buckling. It can also be noted that a panel with a smaller diameter may result in a better hysteretic response with reduced pinching.

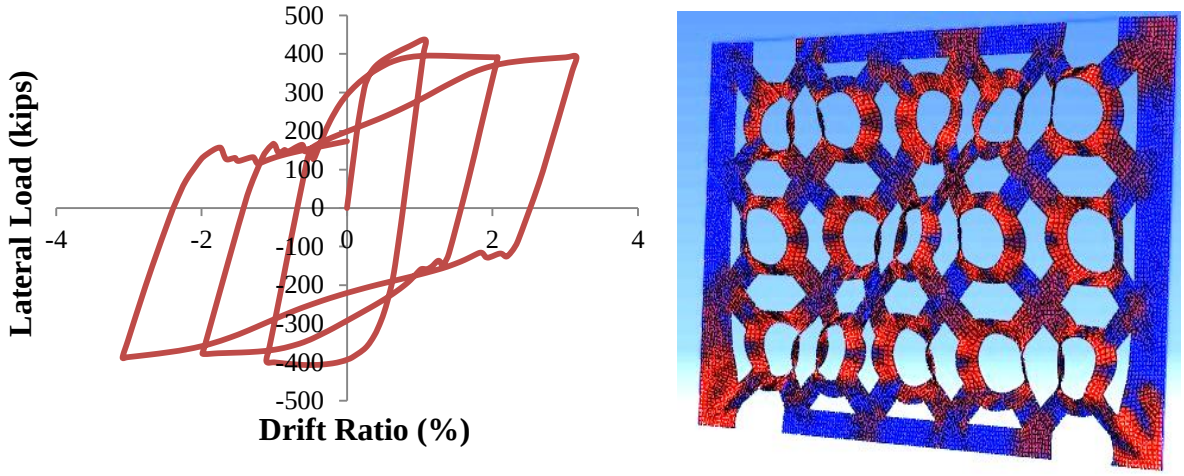

Figure 27: Hysteresis curve and out-of-plane deformation for Panel 2

This preliminary study on the influence of a parameter on the overall panel behavior was used to inform the design of the parametric computational study, which is discussed in detail in Chapter 8.

4.3. UNCONSTRAINED RING MODEL

The unconstrained single ring configuration is used to isolate the smallest unit of BR-SPSW with one end fixed and the other end subjected to horizontal displacement of up to 10 in. This model was developed to capture the ring in its most unconstrained configuration in terms of boundary conditions in the full wall. Figure 28 shows the unconstrained ring model with the boundary conditions and applied displacement. This type of boundary condition was applied to models using both shell and beam elements. The analysis results and conclusions are presented in the subsequent sections.

4.3.1. Shell Model

The shell model was created using S4R elements in ABAQUS as shown in Figure 28. Outer radius of the ring (R_o) for this model was chosen as 10 in. with a ring width (w_c) of 3 inches. Width of the link (w_l) was set as 4.95 in. and thickness of the plate used was 0.5 in. Note that all the material properties and the meshing techniques used were identical to that of the full wall.

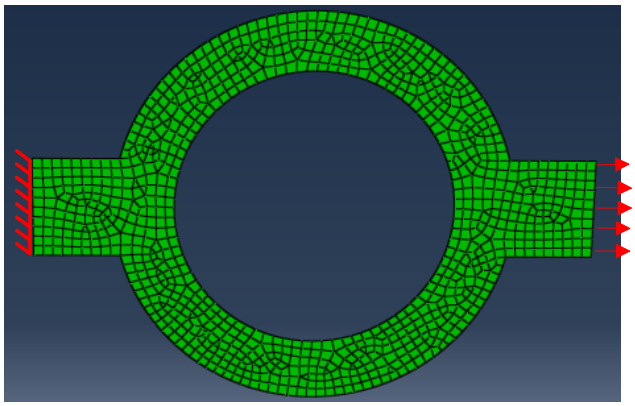

Figure 28: Unconstrained ring model

The load - displacement curve obtained from the analysis is shown in Figure 29. The yield strength predicted by the ABAQUS model is approximately 27 kips, as observed in the load-deformation response by the sharp change in stiffness. The ring, however, exhibits increasing post-yield strength which is a result of the geometric stiffening effect due to the forces in the rings transitioning from flexural to axial at large deformations. This effect could be captured because geometrical non-linearities were included in the analysis.

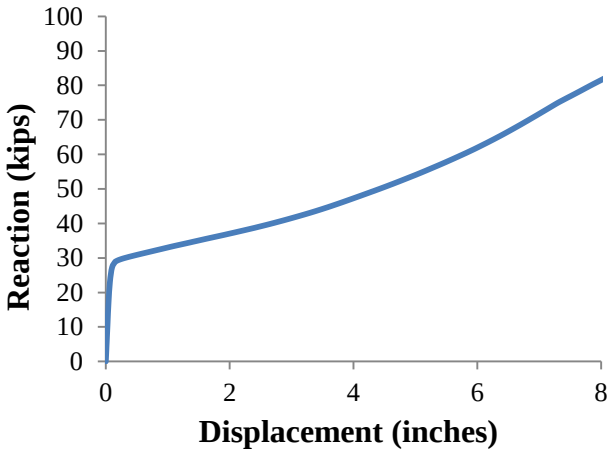

Figure 29: Load-displacement relationship for unconstrained ring shell model

To validate the results obtained from the mathematical solution regarding the transverse shortening of the single ring unit, the elongation and shortening of the ring in the radial directions were recorded. The results are plotted in

Figure 30, along with value of the transverse shortening predicted analytically in Section 3.

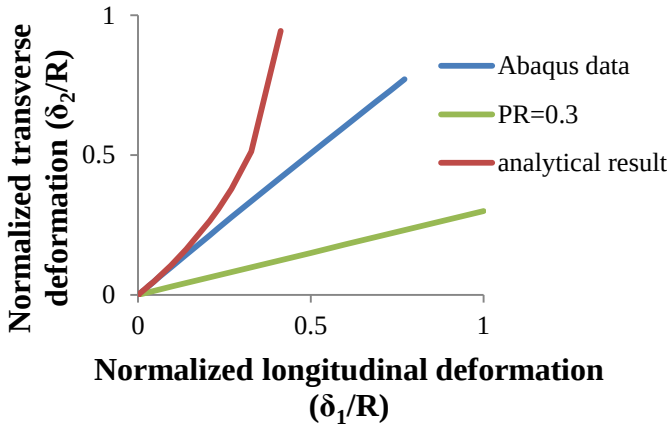

Figure 30: Comparison of effective Poisson's ratio of the single ring unit

It is clear from the above plot that the ring has an effective Poisson's ratio (PR) approximately equal to 1.0 for small deformations which reinforces the fact that when a ring deforms into an ellipse the longitudinal and transverse deformations are nearly same.

Note that the result obtained from ABAQUS is in agreement with the derivation done in Section 3 up to an elongation of 20% of the ring diameter (δ_1/R=0.2). Under increasing elongation, the ring behavior diverges from the analytical solution. It is expected that this is due to the inelastic axial deformation which causes the perimeter of the ellipse to be larger than the original ring perimeter.

4.3.2. Beam Model

The similar model using frame elements was created because it provides a more simplified measurement of strength, as it eliminates the effect of the spread of plasticity through the width of the ring. The model was created as a line model as shown in Figure 31, with a radius of 8.5 in. Note that this is the centerline radius of the unconstrained ring model. The cross-sectional and material properties assigned to the line model were identical to that used for shell element model (t = 0.5 in., w_c = 3 in., w_l = 4.95 in.). Linear two node beam elements were used (B21 elements in ABAQUS).

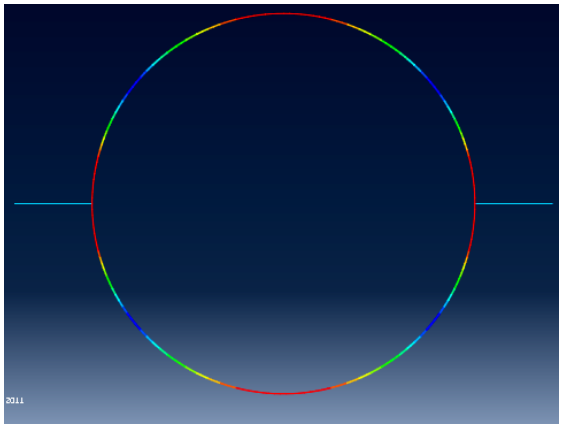

Figure 31: Beam model for unconstrained configuration

The load- displacement plot for the beam model is as shown in Figure 32.The strength obtained by the AQABUS model is 21.5 kips. The reason for choosing the analysis of beam model for the unconstrained configuration will be explained in more detail in a subsequent section in which the results obtained from this model will be compared to the results from the derived equations.

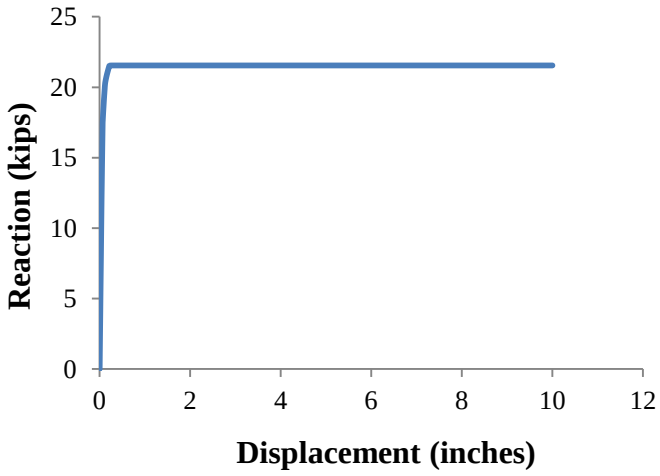

Figure 32: Force-displacement curve for unconstrained beam model

4.4. CONSTRAINED RING MODEL

The constrained ring model was investigated because the boundary conditions for a single ring in the full SPSW panel are not exactly simulated by the unconstrained ring model. It is hypothesized that if the diameter of the rings is increased and the number of rings in the full

panel is decreased, the boundary conditions will be similar to the constrained ring configuration described in this section. Also, it is expected that this type of configuration closely imitates the level of constraint that the rings in corners of the full size panel experiences. It was therefore important to investigate the behavior of the constrained ring configuration.

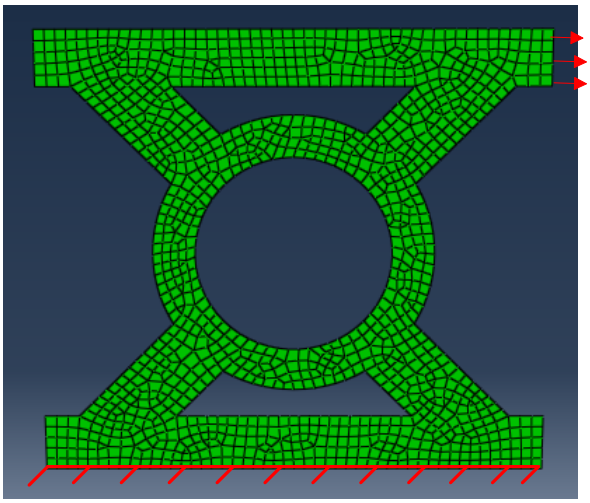

Figure 33: Constrained ring model

The dimensions of the ring and the material properties of the model are identical to the un-constrained model discussed earlier. The material properties and meshing are also similar to those of the full panel. The load -displacement curve for the constrained ring model is shown in Figure 34.

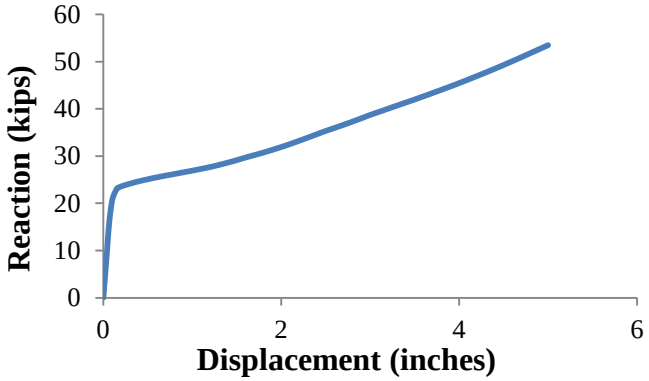

Figure 34: Load-displacement curve for constrained ring model

From the plot above, the strength of the constrained ring model is about 23 kips. Not unlike the unconstrained model, this model also experiences stiffening at large displacements, which is evident from the increase in strength after a displacement of 0.2 in.

4.5. SINGLE STORY, ONE BAY PANEL: STAGGERED CONFIGURATION

The full-size panel with rings can also be built with a staggered configuration as opposed to the aligned configuration discussed previously. The ring units have been staggered to 45^{o} in each row as shown in Figure 35. The staggering in the ring units potentially allows for reduction in link lengths and link intersections as in the aligned-ring models.

The basic dimensions of ring units in this staggered panel are identical to ring units in the full-size panel discussed in Section 4.1. (Except for the link lengths, which are different because of the difference in the distance between each ring). The overall dimension of the panel is also same. The deformation and the stress distribution in the panel at the end of the test are shown in Figure 35.Note that the red color represents the yielded region whereas the blue color represents the region below 35 ksi stress.

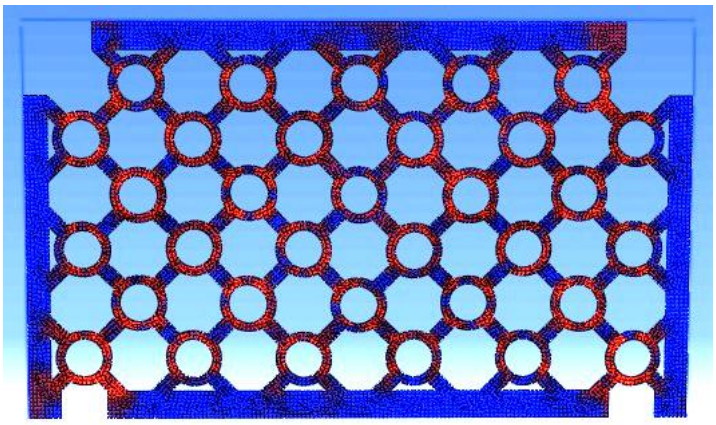

Figure 35: Deformation and stress distribution of the staggered full-size panel at the end of the test

The load vs drift plot for the staggered panel as compared to the aligned-ring panel is shown in Figure 36. The strength of the panel obtained from the ABAQUS analysis is approximately 129 kips. The strength using was calculated using the technique previously described in Section 4.1.

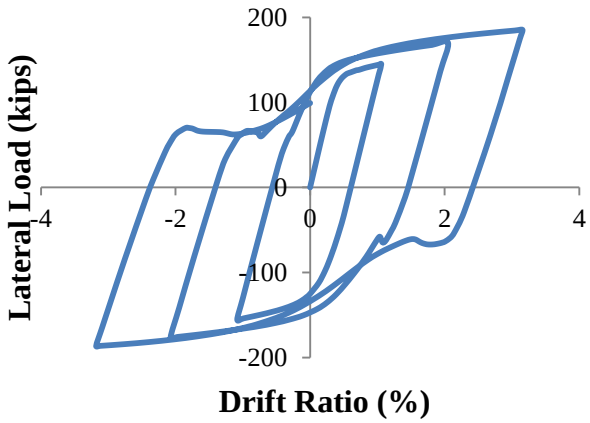

Figure 36: Load-drift plot for staggered full-size panel

As clear from Figure 36, the staggered alignment results in a lower strength as compared the aligned-ring configuration (refer Figure 24). This is due to the fact that the 45^{o} stagger creates larger distances between the rings. The lesser number of rings in the panel, results in lower strength. Also, this leads to decrease in the initial stiffness of the staggered panel. The strength and the stiffness of this configuration can thus be tuned by changing the distance between the adjacent ring units. However, the panel still shows a full hysteresis with almost no pinching. The prominent mode of buckling in this panel was global tension field buckling.

Although the staggered ring model is a potentially attractive variation of BR-SPSW, there are certain challenges associated with it. For a given outer dimension of the shear plate (length and height of the wall), laying out the rings in 45° staggered configurations is a challenging task without making the links too long or short. Due to this reason, this configuration was not further investigated. The parametric study only consists of aligned-ring models

4.6. SUMMARY OF ANALYSIS RESULTS

Table 4 and Table 5 and summarize the analysis results of the ring units and the full panel for the models in which the ring unit had the outer radius (R_o) of 10 in. and the ring width (R_c) of 3 in. The table mainly focuses on the strength and stiffness of the models.

The strength of the unconstrained ring models (both shell and beam) has to be resolved at 45^{o} because in the full panel they would be placed at an inclination of 45^{o}. Thus the table summarizes both the strength and the resolved strength (referred to as the effective shear strength in Table 4

and Table 5) of the unconstrained models. Note that in the constrained model, the links are already at a 45^{o} angle and thus no resolution of strength is required. The stiffness of the ring models shown in Table 4 is not the resolved shear stiffness, but the actual stiffness of the ring in the direction of the applied load.

As anticipated, the strength of the full panel is in between the strength of the constrained and the unconstrained ring models. This is shown from the extrapolated strength (effective strength) of the full panel which is calculated by multiplying the strength of one ring unit by the number of rings in one row of the full panel (nine in case of aligned rings and six in case of staggered rings). Also, it is demonstrated that the beam model with identical boundary conditions and dimensions as the shell model, exhibited lower strength. This difference in strength can be attributed to difference in plastic hinging mechanism, as discussed in later section.

Table 5 shows a comparison between the results obtained by extrapolating the strength from the ring models to the strength of the full walls. This exercise was done to figure out the ring model that best represents the full wall. Although the strength of the full wall lies between the extrapolated strength obtained the constrained and the unconstrained ring model, the former seems to better represent the strength of the full wall. Note that these ring models will be used in Chapter 5 and 6 to calculate strength and stiffness of the full wall models.

Table 4: Comparison of analysis results of the rings units

	Unconstrained Shell Model	**Unconstrained Beam Model**	**Constrained Shell Model**
Total Strength (Kips)	27	21.5	23
Effective Shear Strength (Kips)	19.1	15.2	23
Stiffness (Kips/in.)	391	282	243

Table 5: Comparison of analysis results of the full panel

	Full Panel (Aligned-Rings)	Full Panel (Staggered Rings)	
Effective Strength of the Full Panel (Kips)	204	129	**Full Panel**
	172	114.6	**Unconstrained Shell Model**
	137	91.2	**Unconstrained Beam Model**
	207	138	**Constrained Shell Model**
Stiffness (Kips/in)	459	235	

CHAPTER 5

STRENGTH CALCULATION: DISCUSSION OF MECHANISMS

In this section, equations will be derived using plastic mechanism analysis (Chen and Han, 2007) to predict the strength of SPSW using rings. Four potential plastic mechanisms (with or without axial effects) have been explored. For each mechanism, an upper bound solution on the plastic capacity using equilibrium of forces and a lower bound on the capacity using virtual work principles has been computed. If the two are equal, the plastic capacity for that mechanism is a single solution. If they are not equal, there is a potential range for plastic capacity described by the upper and lower bounds. The predicted strengths will then be compared to the results from the finite element analysis to determine which mechanism is most appropriate for strength calculation. Note that all the derivations in this section have been done assuming that the connecting links experience negligible yielding and thus do not control the strength of the wall panel.

5.1. MECHANISM-I

This mechanism was initially developed to explain the behavior of the un-constrained ring model. This mechanism is shown in Figure 37. There were, however, a few issues with this mechanism not being able to closely represent the shell element model. These issues are discussed in Section 5.2 and 5.3.

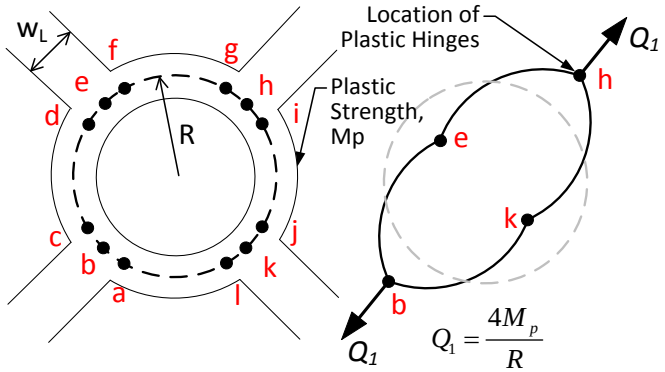

Figure 37: Pictorial Representation of Mechanism I

5.1.1. Plastic mechanism (without axial effects)

It was hypothesized that the inelastic behavior of a single narrow-ring subjected to a tension force could be predicted by this mechanism, wherein the axial effects at the plastic hinge can be neglected.

5.1.1.1. Lower-bound solution

The lower bound solution is derived by finding a set of forces and moments that satisfy equilibrium, balance the applied load, and do not exceed the plastic moment anywhere. The actual collapse load cannot be smaller than the resulting collapse load, so the calculated collapse load is a lower bound on the actual solution.

To derive the lower-bound solution, equilibrium of moments and forces are taken for one quarter of a ring of radius R, as shown in Figure 38.

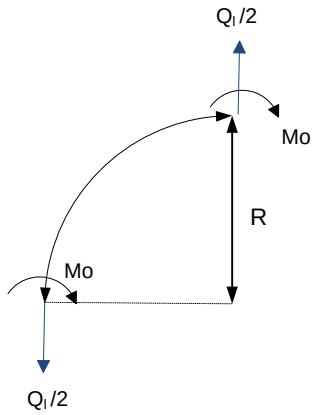

Figure 38: Free body diagram of quarter of a ring with radius R

$$2M_o = \frac{Q_l}{2}R \tag{5.1}$$

$$\Rightarrow Q_l = \frac{4M_p}{R} \tag{5.2}$$

Where, M_p is the plastic yield moment and is given by,

$$M_p = F_y\left(\frac{{w_c}^2 t}{4}\right) \tag{5.3}$$

In the above equation, F_y is the yield stress of the material, w_c is the width of the ring and t is the thickness of the steel plate used.

5.1.1.2. Upper-bound solution

The upper-bound solution is derived based on a compatible pattern of plastic deformations. The associated collapse load is computed using virtual work whereby the rate of work done by the external forces equals the rate of internal energy dissipation. Since the actual collapse load cannot be lower than the collapse load calculated in this way, the computed collapse load is an upper bound on the actual collapse load.

Consider the centerline of the ring with plastic hinges as shown in Figure 39.

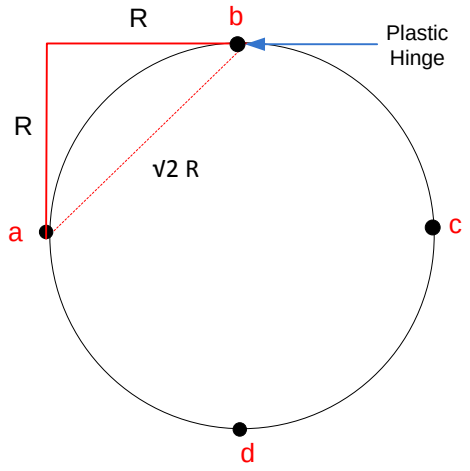

Figure 39: Plastic Hinge mechanism without axial effects

After the formation of plastic hinges, the arcs *ab*, *bc*, *cd* and *da* will rotate about the plastic hinges as shown in the Figure 40.

External work done, W_e, by load Q is given by:

$$We = Q \times x \tag{5.4}$$

Where x is the displacement of the point "*c*". Note that Point "*a*" is fixed.

Internal work, W_i, done by the plastic moment at the plastic hinges is given by:

$$Wi = M_p \times (8\theta) \tag{5.5}$$

Where, M_p is the plastic moment of the section and θ is the rotation of each arc about the plastic hinge.

Using the virtual work principle, the collapse load is obtained as follows,

$$Wi = We \tag{5.6}$$

$$\Rightarrow Q_u = \frac{Mp \times (8\theta)}{x} \tag{5.7}$$

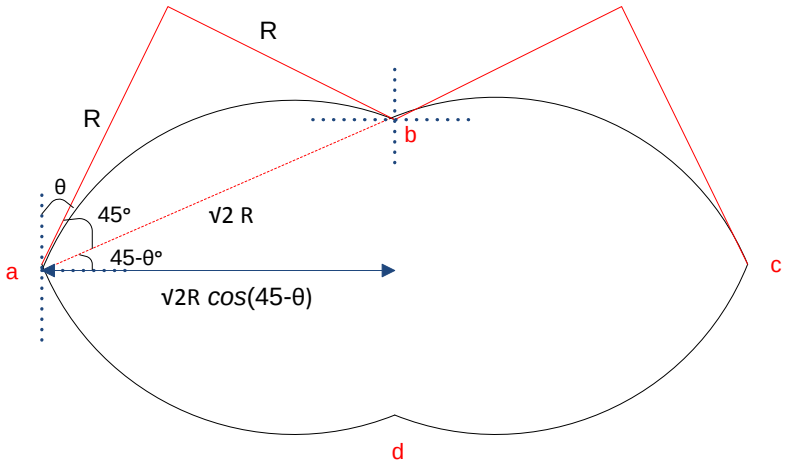

Figure 40: Deformation of the ring as governed by Mechanism-I without considering axial effects

Displacement of Point "*c*" is given by:

$$x = 2\sqrt{2}R\cos(45 - \theta) - 2R \tag{5.8}$$

Using trigonometric identities the dimension x can be written as,

$$x = 2R[cos\theta + sin\theta - 1] \tag{5.9}$$

Assuming small rotation angle, θ and using Taylor series expansion to the following expression was obtained,

$$x = 2R\theta \tag{5.10}$$

Substituting the value of x in the expression for$Q$, results in

$$Q_u = \frac{4M_p}{R} \tag{5.11}$$

Since the lower-bound solution is the same as upper-bound solution, the collapse load is obtained as,

$$Q = \frac{4M_p}{R} \tag{5.12}$$

5.1.2. Plastic mechanism with axial effects

In this mechanism the inelastic axial deformations are considered. This mechanism was examined to explain the behavior of the wide-ring unconstrained model as the axial effects are significant and cannot be neglected in wider rings. The concept is shown in the deformed ring shown in Figure 41.

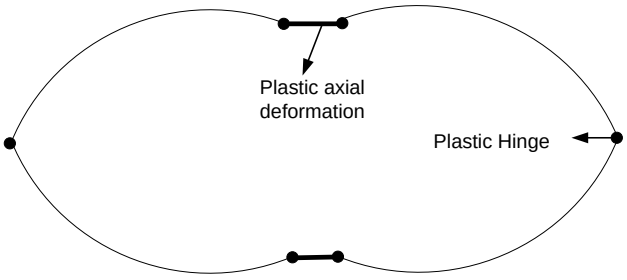

Figure 41: Plastic mechanism with axial effects

The cross-section used for the ring is a rectangular section. Thus the axial-bending interaction curve is approximately shown in Figure 42:

Mathematically, the curve can be expressed as follows:

$$f = \frac{M}{M_o} + \left(\frac{N}{N_o}\right)^2 - 1 \tag{5.13}$$

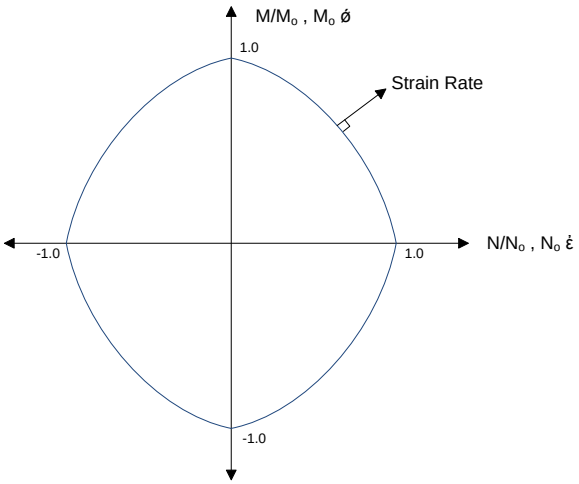

Figure 42: axial-bending interaction curve for rectangular cross-section [from (Chen and Han 2007)]

The plastic flow rule requires the generalized plastic strain rate vector to be normal to the plastic potential surface (assumed to be the same as the yield surface) at all points where the normal is uniquely defined. Thus,

$$\acute{\phi} = \mu \frac{df}{dM} = \frac{\mu}{M_0} \tag{5.14}$$

$$\acute{\varepsilon} = \mu \frac{df}{dN} = \frac{\mu N}{{N_0}^2} \tag{5.15}$$

Going back to the geometry of the deformed circle, and relating it to the axial-bending interaction curve it is noted that energy dissipation/unit length at Points *a* and *b* is given by:

$$D_a = M_o \acute{\phi} \tag{5.16}$$

$$D_b = M\acute{\phi} + N\acute{\varepsilon} \tag{5.17}$$

5.1.2.1. Upper-bound solution

As mentioned in the discussion for the previous mechanism, the solution for the collapse load will be done in the form of lower-bound and upper-bound. Starting with the upper-bound solution, the internal work done by the plastic moment and the external work done by the applied force has been evaluated as follows.

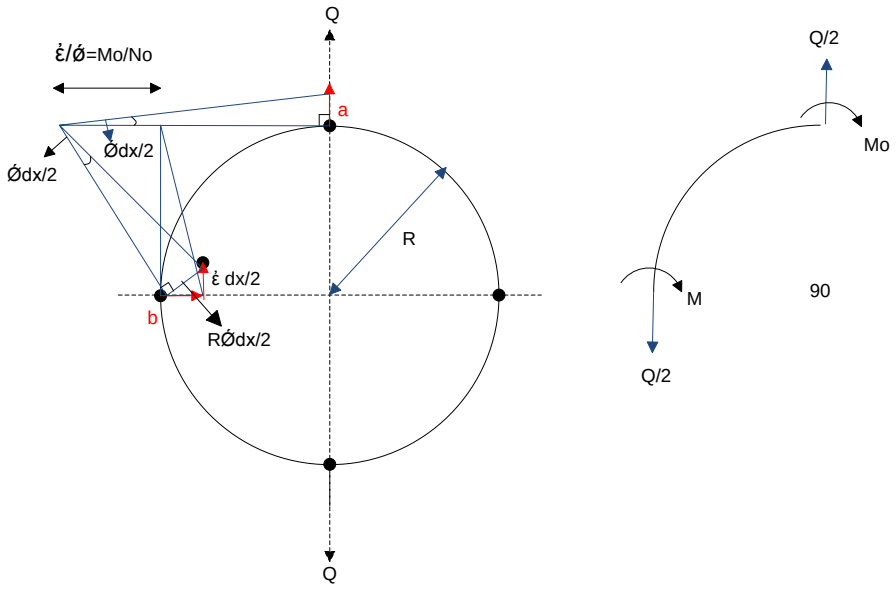

Figure 43: Elaborate analysis of the ring considering axial affects

As shown in Figure 43, *ø̇dx* is the rate of relative rotation of the element *dx* at the plastic hinge location.

Total internal work done at the location of the plastic hinges is given by:

$$W_i = 2D_a + 2D_b \tag{5.18}$$

$$\Rightarrow W_i = 2M_o\dot{\phi} + 2(M\dot{\phi} + N\dot{\varepsilon}) \tag{5.19}$$

Substituting the values of $\dot{\phi}$ and $\dot{\varepsilon}$evaluated earlier and using the axial-bending relationship results in,

$$W_i = 2M_o\dot{\phi} + \mu\left[\frac{M}{M_0} + 2\frac{N^2}{N_o^2}\right] = 2M_o\dot{\phi} + \mu\left[1 + \left(\frac{N}{N_o}\right)^2\right] \tag{5.20}$$

Further simplifying the equation,

$$W_i = 2M_o\dot{\phi} + 2M_o\dot{\phi}\left[1 + \frac{1}{4}\left(\frac{\dot{\varepsilon}M_o}{\dot{\phi}N_o}\right)^2\right] \tag{5.21}$$

The external work done by the applied force *Q* is given by:

$$W_e = 2Q\left[R + \frac{2M_oN}{{N_0}^2}\right]\dot{\phi}\frac{dx}{2} \tag{5.22}$$

Using the virtual work Principle,

$$W_i = W_e \tag{5.23}$$

On simplifying the equation,

$$Q = \frac{2M_o\left[2+\frac{1}{4}\left(\frac{N_O}{M_O}\right)^2\left(\frac{\dot{\varepsilon}}{\dot{\phi}}\right)^2\right]}{R+\frac{\dot{\varepsilon}}{\dot{\phi}}} \tag{5.24}$$

To obtain maximum Q for a given ratio of $\dot{\varepsilon}/\dot{\phi}$, differentiate Q with respect to $\dot{\varepsilon}/\dot{\phi}$

$$\frac{dQ}{d\left(\frac{\dot{\varepsilon}}{\dot{\phi}}\right)} = 0 \tag{5..25}$$

On differentiating and simplifying a quadratic equation in $\dot{\varepsilon}/\dot{\phi}$ is obtained.

$$\left(\frac{\dot{\varepsilon}}{\dot{\phi}}\right)^2 + 2R\left(\frac{\dot{\varepsilon}}{\dot{\phi}}\right) - 8\left(\frac{M_0}{N_0}\right)^2 = 0 \tag{5.26}$$

Solving the quadratic equation,

$$\frac{\dot{\varepsilon}}{\dot{\phi}} = \left[-1 + \sqrt{1 + \frac{8}{R^2}\left(\frac{M_0}{N_0}\right)^2}\right] \tag{5.27}$$

The resulting upper bound plastic capacity is given by Equation 5.24 with the value for strain rate ratio from Equation 5.27 substituted in.

5.1.2.2. Lower-Bound Solution

For lower-bound solution, the equilibrium of moments and forces was considered as shown in Figure 43.

$$M + M_o = \frac{Q_l}{2}R \tag{5.28}$$

Since axial-bending interaction curve for a rectangular cross-section has been used,

$$\frac{M}{M_o} + \left(\frac{N}{N_o}\right)^2 = 1 \tag{5.29}$$

Here,

$$N = \frac{Q_l}{2} \tag{5.30}$$

Hence,

$$\frac{M}{M_o} + \left(\frac{Q_l}{2N_o}\right)^2 = 1 \tag{5.31}$$

The two equations were combined to get a quadratic in *Q*,

$$Q_l{}^2 \left(\frac{1}{2N_o}\right)^2 + Q_l \left(\frac{R}{2M_o}\right) - 2 = 0 \tag{5.32}$$

Solving for *Q*,

$$Q_l = -\frac{2N_o{}^2 R}{M_o} + \sqrt{\left(\frac{N_o{}^2 R}{M_o}\right)^2 + 8N_o{}^2} \tag{5.33}$$

On comparing the upper and the lower bounds of the collapse load, it was found that they do not give the same result. Thus, the collapse load for this mechanism is found to be within the range between the upper and lower bounds. Note that for comparison of results from ABAQUS and predicted strength from equations later in this section, the upper-bound solution of this mechanism has been used for simplicity.

5.2. MECHANISM-II

Note that the plastic mechanisms in the previous two sections assumed the ring as a circle using the centerline radius R with four plastic hinges. The unconstrained ring in the ABAQUS model however has a link width w_c which spreads out the plastic hinge at the locations of the load application. The spread of plasticity at the points of load application is not captured in the previous two mechanisms. To account for the width of the link at the location of load application, a slight modification to Mechanism I, was devised in an attempt to better simulate the behavior of the unconstrained ring model.

For this mechanism, the position of the plastic hinges was represented as shown in the Figure 44. Note that radius of the circle represented by R_c is the centerline radius of the ring model and that axial yielding is neglected for this mechanism

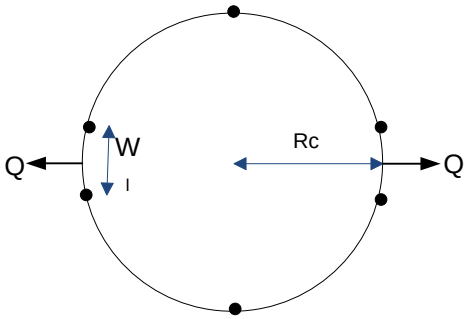

Figure 44: Line diagram for Mechanism -II

This mechanism better represents the plastic hinging in the un-constrained ring model as is clear from its stress distribution diagram shown in Figure 45. As previously described in Chapter 4, the Von Mises stress distribution in an unconstrained ring model reflects a certain pattern of plastic yielding. Note that the red and the orange region represent the yielded region and the blue region represents the zones with less than 13 ksi stress.

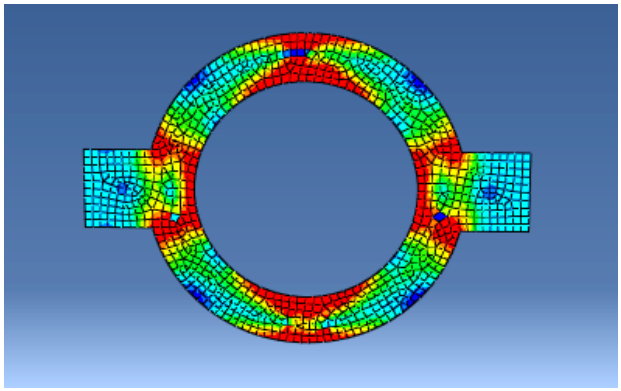

Figure 45: Stress distribution in an un-constrained ring (red and orange regions are yielded)

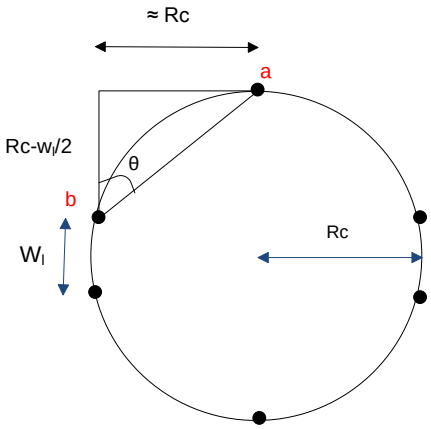

Figure 46: Dimensional features of Mechanism-II

As observed from the figure, instead of one plastic hinge at the joint of the ring and link, the stress pattern shows two distinct plastic hinges at each side of the link. Thus, Figure 44 and Figure 46 better simulates the behavior of the unconstrained ring model.

5.2.1. Lower-Bound Solution

Consider the equilibrium of forces and moments in the arc *"ab"* about point *"b"* as shown in Figure 47. The lower bound plastic capacity is computed as follows.

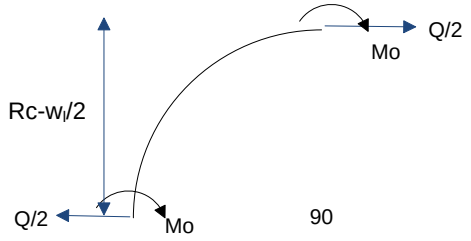

Figure 47: Free body diagram of quarter of a ring (Mechanism-II)

$$2M_p = Q_L(R_c - w_l) \tag{5.34}$$

$$\Rightarrow Q_L = \frac{4M_p}{(R_c - w_l)} \tag{5.35}$$

5.2.2. Upper-Bound Solution

After the formation of plastic hinge, the arcs *ab*, *bc*, *cd* and *da* will rotate about the plastic hinges as shown in Figure 48:

External work, W_e, done by load Q is given by:

$$We = Q \times x \tag{5.36}$$

Where x is the displacement of the point "*c*". Note that Point "*a*" is fixed.

Internal work, W_i, done by the plastic moment at the plastic hinges is given by:

$$Wi = M_p \times (8\emptyset) \tag{5.37}$$

Where, M_p is the plastic moment of the section and θ is the rotation of each arc about the plastic hinge.

Using the virtual work principle,

$$Wi = We \tag{5.38}$$

$$\Rightarrow Q_u = \frac{Mp \times (8\emptyset)}{x} \tag{5.39}$$

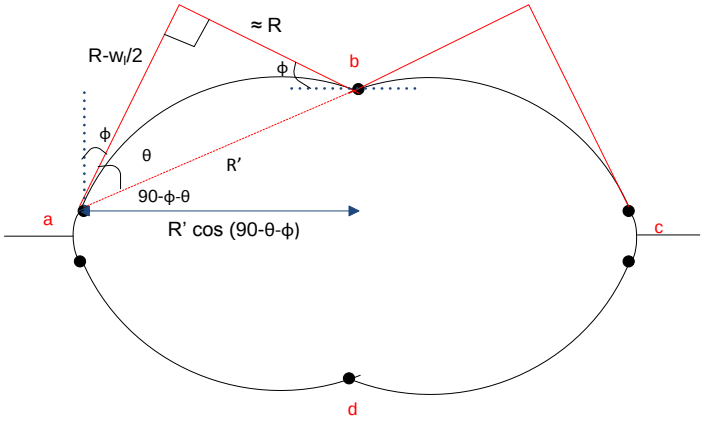

Figure 48: Development of plastic hinge in the ring as governed by Mechanism-II

In Figure 48,

$$R' = \frac{R_c}{sin\theta} \tag{5.40}$$

and

$$\theta = \tan^{-1}\left(\frac{R_c}{R_c - {}^{w_l}/_2}\right) \tag{5.41}$$

The total displacement of the ring, x at point "c" is given by:

$$x = 2R' \cos(90 - \theta - \emptyset) - 2R_c \tag{5.42}$$

$$x = 2R' \sin(\theta + \emptyset) - 2R_c \tag{5.43}$$

Using trigonometric identities and assuming a small φ,

$$x = 2R'(\theta \cos \emptyset + \sin \emptyset) - 2R_c \tag{5.44}$$

Substituting the value of R' and simplifying to the total displacement,

$$R' = \frac{2R_c\emptyset}{\tan\theta} \tag{5.45}$$

$$R' = 2\emptyset(R_c - w_l/2) \tag{5.46}$$

Substituting this value of x in the expression for $Q_u$results in,

$$Q_u = \frac{4Mp}{(R_c - w_l/2)} \tag{5.47}$$

Since the lower-bound solution is the same as upper-bound solution, the collapse load is obtained as,

$$Q = \frac{4M_p}{(R_c - w_l/2)} \tag{5.48}$$

$$Q = \frac{4M_p}{R_{eff}} \tag{5.49}$$

where,

$$R_{eff} = R_c - w_l/2 \tag{5.50}$$

Thus, it can be concluded that a better prediction of the strength of the unconstrained ring can be made by slightly modifying the effective radius of the ring.

5.3. MECHANISM-III

Another mechanism was developed on observing the deformation of individual ring units in the full-size panel wall. The magnified deformed ring and the mechanism are shown in Figure 49.

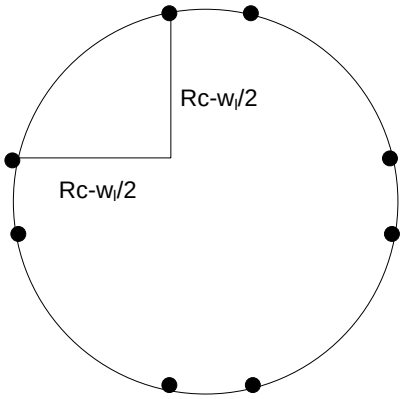

Figure 49: idealized line-diagram for Mechanism-III

It can be proved that the strength predicted by this mechanism is identical to that predicted by Mechanism II.

The total displacement of the ring (x) at point "*d*" shown in Figure 50 is given by:

$$= 2R' \cos(45 - \theta) + w_l - 2R_c \tag{5.51}$$

$$= 2\sqrt{2}\left(R_c - {}^{w_l}/_{2}\right)\cos(45 - \theta) + w_l - 2R_c \tag{5.52}$$

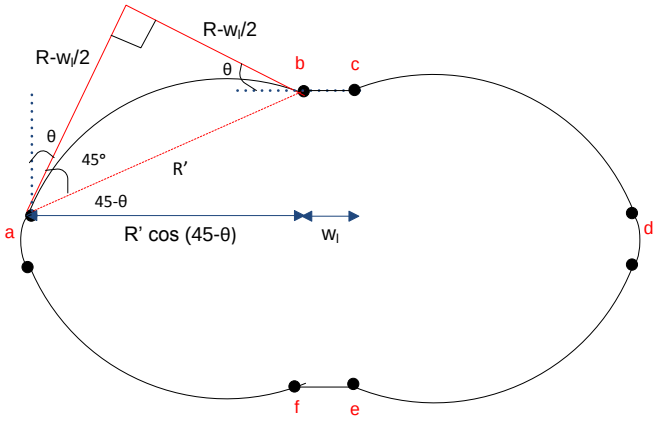

Figure 50: Deformation of the ring as governed by Mechanism-III

Using trigonometric identities the total displacement of the ring x at point "*d*" can be calculated as:

$$x = 2\left(R_c - {}^{w_l}/_2\right)[cos\theta + sin\theta] + w_l - 2R_c \tag{5.53}$$

Assuming θ is small and using Taylor series expansion,

$$x = 2\left(R_c - {}^{w_l}/_2\right)[1 + \theta] + w_l - 2R_c \tag{5.54}$$

$$x = 2(R_c - {}^{w_l}/_2)\theta \tag{5.55}$$

Computing the internal work done by the plastic moment to the external work done by the applied force, as done in all the previous derivations, results in external work done by load *Q* is given by:

$$We = Q \times x \tag{5.56}$$

Where x is the displacement of the point "*d*". Note that Point "*a*" is fixed.

Internal work done by the plastic moment at the plastic hinges is given by:

$$Wi = M_p \times (8\emptyset) \tag{5.57}$$

Where, M_p is the plastic moment of the section and θ is the rotation of each arc about the plastic hinge.

Using the virtual work principle,

$$Wi = We \tag{5.58}$$

$$\Rightarrow Q_u = \frac{Mp \times (8\emptyset)}{x} \tag{5.59}$$

Substituting this value of x in the expression for Q_u,

$$Q_u = \frac{4Mp}{(R_c - w_l/2)} \tag{5.60}$$

The same solution can be obtained for the lower-bound by taking the equilibrium of moments and forces for quarter of the ring (between two plastic hinges).

Thus, the collapse load for this mechanism is identical to that of Mechanism-II and is given by:

$$Q = \frac{4Mp}{(R_c - w_l/2)} \tag{5.61}$$

5.4. MECHANISM-IV

This mechanism was developed to explain the behavior of the constrained ring model.

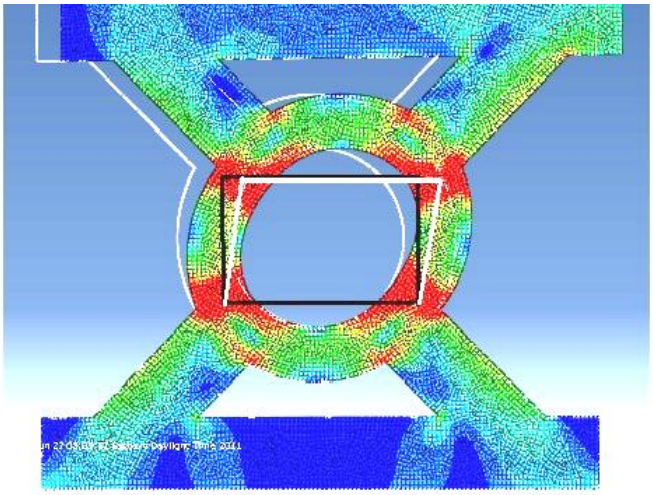

Figure 51: Deformed shape and the stress distribution of the constrained ring ABAQUS model

Figure 51 displays the deformation of the constrained ring with plastic hinges around the link-ring joints. The deformation can be approximated by a quadrilateral with plastic hinges at each vertex.

The rotation of the quadrilateral (θ) is the rotation of the single arc about the plastic hinge.

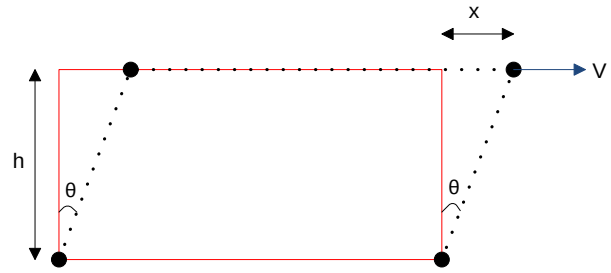

Figure 52: Deformed constrained ring represented by a quadrilateral

According to Figure 52,

External work, W_e, done by the shear force (V) is given by:

$$We = V \times x \tag{5.62}$$

Internal work, W_i, done by the plastic moment at the hinges is given by:

$$Wi = 4M_p \times \theta \tag{5.63}$$

Using the virtual work principle,

$$We = Wi \tag{5.64}$$

$$\Rightarrow V = \frac{4M_p \times \theta}{x} \tag{5.65}$$

Assuming θ is small,

$$h = x \times \theta \tag{5.66}$$

$$\Rightarrow V = \frac{4M_p}{h} \tag{5.67}$$

The value of h is the shorter distance between the two plastic hinges. To compute its value the constrained ring is redrawn as shown in Figure 53.

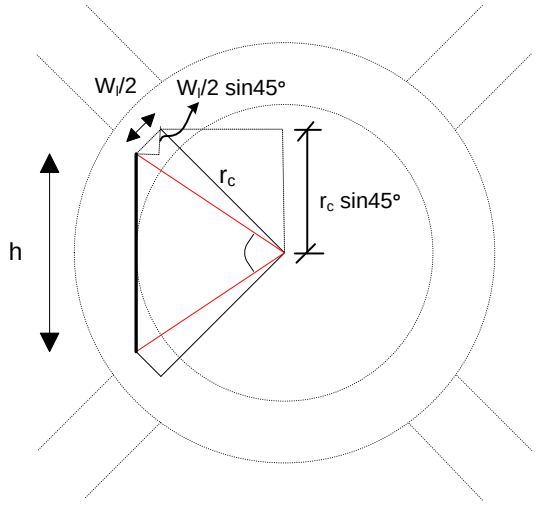

Figure 53: The constrained ring represented in the form of a line diagram

Here,

$$h = 2(r_c \sin 45 - \frac{w_l}{2} \sin 45) \tag{5.68}$$

$$\Rightarrow h = \sqrt{2}(r_c - \frac{w_l}{2}) \tag{5.69}$$

Where, r_c is the center-line radius of the ring and w_l is the centerline radius of the ring.

Using this value of h to compute *V*,

$$V = \frac{4M_p}{\sqrt{2}(r_c - \frac{w_l}{2})} \tag{5.70}$$

5.5. COMPARISON OF RESULTS

This section focuses on investigating the effectiveness of the derived equations in predicting the strength of ring models and the full panels from the preliminary study. Thus, this section is an extension to the comparison of analysis results of the various ABAQUS models done in Chapter 4. The results from ABAQUS analysis done for the preliminary study have been compared to the predicted strength in a set of tables presented below.

For extrapolating the plastic capacity of the ring to the capacity of the full panel, strength/ring is multiplied by the number of rings in a row to get the approximate strength of the full wall. An important thing to be pointed out in the table is the fact that for the unconstrained ring model, the strength has been calculated along the connecting links. When these rings become a part of the full panel the links are aligned at 45^o and thus the total strength of the rings is required to be resolved in the horizontal direction to get the effective strength of the panel.

Comparing the results in Table 6 and Table 7, it was observed that Mechanism-II/III and IV very well predict the strength of the unconstrained and constrained shell model respectively.

However, the main conclusion that can be drawn from Table 8 and Table 9 is that the strength of the full-panel is very well predicted by the constrained shell model as the average strength of the ring in the full panel is almost equal to the constrained ring model. The unconstrained models also give good results but they are not as close to the predicted results as the constrained model.

Another point to be noticed from the comparison is that in most of the cases axial effects do not have a significant influence in the strength of the models (refer Table 6).

Thus, based on the previous conclusion, Mechanism IV (constrained ring model) has been used for BR-SPSW strength calculation from this point onwards. The accuracy of the analytical solution (Mechanism-IV) in predicting the strength of the full wall specimens analyzed in the parametric study is investigated in Chapter 8.

Table 6: Comparison of computational and analytical results for unconstrained models

	Calculated Plastic Capacity (kips)			Observed Strength From FEM Model	
	Mechanism I	**Mechanism II**	**Mechanism III**	**Shell Model**	**Beam Model**
No Axial Effects	21.2	29.8	29.8	27.0 kips	23.0 kips
Axial Effects Included	21.1	28.4	28.4		

Table 7: Comparison of computational and analytical results for constrained model

Constrained Ring	**Calculated Plastic Capacity Mechanism IV**	**Observed Strength From FEM Model Shell Elements**
	22.3 kips	23.0 kips

Table 8: Comparison of computational and analytical results for full wall models

	Calculated Plastic Capacity (kips)			Observed Strength from full wall (FEM Model)
	Mechanism II	**Mechanism III**	**Mechanism IV**	
Single Story Panel	172	172	201	204 kips

Table 9: Comparison of results obtained from Mechanism-IV to computational results

	Calculated Plastic Cap.	Observed Strength From FEM Model (kips)			
	Mechanism IV	**Unconstrained Ring with Shell Elements**	**Unconstrained Ring Frame Elements**	**Constrained Ring**	**Full Panel / Number of Rings**
Shear Strength /Ring	22.3	19.1	15.2	23.0	22.6

CHAPTER 6

STIFFNESS CALCULATION: DISCUSSION OF MECHANISMS

This section develops the analytical solution for the stiffness of the full wall panel. The geometry of the BR-SPSW makes the derivation for stiffness quite challenging. To simplify the problem, a single ring unit and its deformation mechanics was considered to derive the analytical solution. The problem has been solved using two types of single ring unit models. A detailed derivation of stiffness using both these models and the assumptions associated with them is presented in the subsequent paragraphs.

6.1. UNCONSTRAINED RING MODEL

Consider the unconstrained ring model subjected to a point load *P* as shown in Figure 54. Note that since the axial stiffness of the connecting links (transferring the load P to the ring) is much larger than the total stiffness of the ring, link stiffness was ignored while deriving the stiffness of the unconstrained ring model.

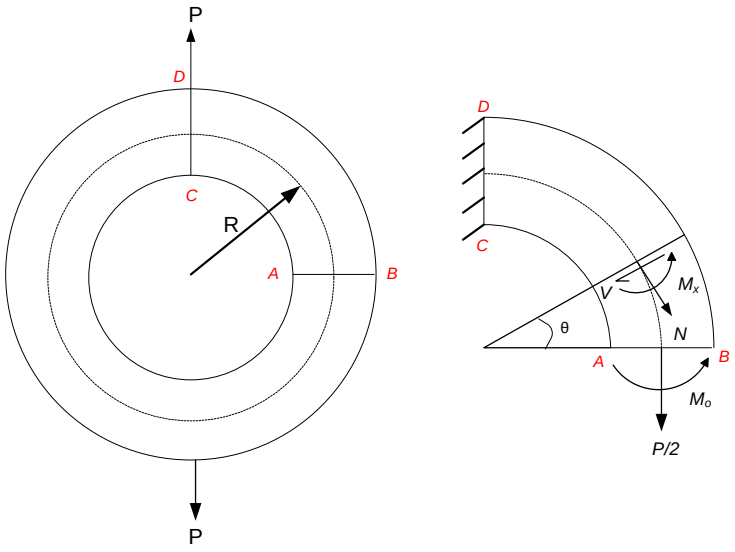

Figure 54: Unconstrained ring model

From symmetry, the deformations of each quadrant of the ring are identical. Hence, only one quadrant, *ABCD*, has been considered. The quadrant has been considered fixed at the section *DC* with a load *P/2* and moment M_o at section *AB*. Because of the symmetry of the ring and ring

deformations, section *AB* always remains perpendicular to section *DC*. Thus, the rotation of face *AB* is zero. Using Castigliano's Theorem it can be proved that (Boresi and Schmidt, 2003).

$$M_0 = \frac{PR}{2}\left(1 - \frac{2A}{RA_m\pi}\right) \tag{6.1}$$

where, R is the centerline radius of the ring; A is the cross sectional area and A_m for the ring cross-section is given by:

$$A_m = t \ln\frac{R_o}{R_i} \tag{6.2}$$

where, t is the thickness of the ring; R_o and R_i are the outer and the inner radius of the ring respectively.

For quadrant ABCD, the shear force (V), normal force (N_x) and bending moment (M_x) acting on a section at an angle θ can be expressed as:

$$V = \frac{P}{2}\sin\theta \tag{6.3}$$

$$N = \frac{P}{2}\cos\theta \tag{6.4}$$

$$M = M_o - \frac{PR}{2}(1 - \cos\theta) \tag{6.5}$$

$$\Rightarrow M = \frac{PR}{2}\left(\cos\theta - \frac{2A}{RA_m\pi}\right) \tag{6.6}$$

Castigliano's Theorem was used to find the vertical deflection (δ) of the quadrant *ABCD*, due to applied load *P/2*.

$$\delta = \frac{\partial U}{\partial(P/2)} \tag{6.7}$$

$$\delta = \int \frac{N}{EA}\frac{\partial N}{\partial(P/2)}dz + \int \frac{\kappa V}{GA}\frac{\partial V}{\partial(P/2)}dz + \int \frac{M}{EI}\frac{\partial M}{\partial(P/2)}dz \tag{6.8}$$

where, *E,I,G and* κ are the material and geometric properties of the ring and *dz* is an infinitesimal section of the ring and can be expressed as $Rd\theta$. Substituting the expression for *dz* integrating the expression from 0 to $\pi/2$,

$$\delta = \frac{P}{2}\left(\frac{\kappa R\pi}{4GA} + \frac{R\pi}{4EA} + \frac{R^3}{EI}\left\{\frac{c^2\pi}{2} - 2c + \frac{\pi}{4}\right\}\right) \tag{6.9}$$

The stiffness of the quadrant *ABCD,* is thus given by the expression,

$$k_u = \left(\frac{\kappa R\pi}{4GA} + \frac{R\pi}{4EA} + \frac{R^3}{EI}\left\{\frac{c^2\pi}{2} - 2c + \frac{\pi}{4}\right\}\right)^{-1} \tag{6.10}$$

where,

$$c = \frac{2A}{RA_m\pi} \tag{6.11}$$

Thus, the ring has four quadrants each with stiffness K_u as shown in the Figure 55. Effective stiffness of the ring can be calculated by considering the series and parallel stiffness combination of each quadrant as shown in figure. Thus, the resultant stiffness of the ring was obtained as K_u.

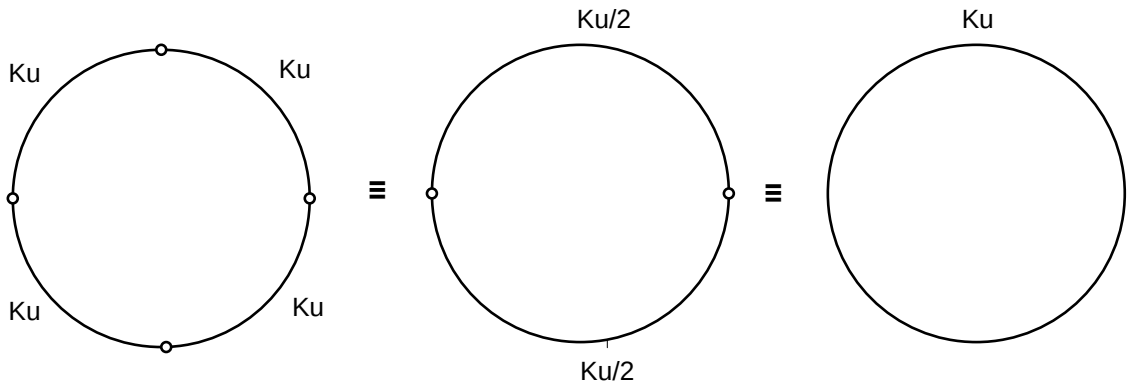

Figure 55: Resultant stiffness of the ring

As mentioned previously, the axial stiffness of the links is believed to have negligible effect on the stiffness of the ring model. As shown in Figure 55, the stiffness of the links will act in series with the stiffness of the ring. Since the axial stiffness of the link is very large as compared to the stiffness of the ring, the resultant stiffness (K) is almost equal to the stiffness of the ring by itself.

$$K = K_u \tag{6.11}$$

Based on the stiffness of the unconstrained ring model, the stiffness of the full wall has been calculated. The stiffness of full wall (K_w) has been expressed in terms of number of rings in a column (N_c), number of rings in a row (N_r) and stiffness of one ring based on unconstrained ring model (k_u).

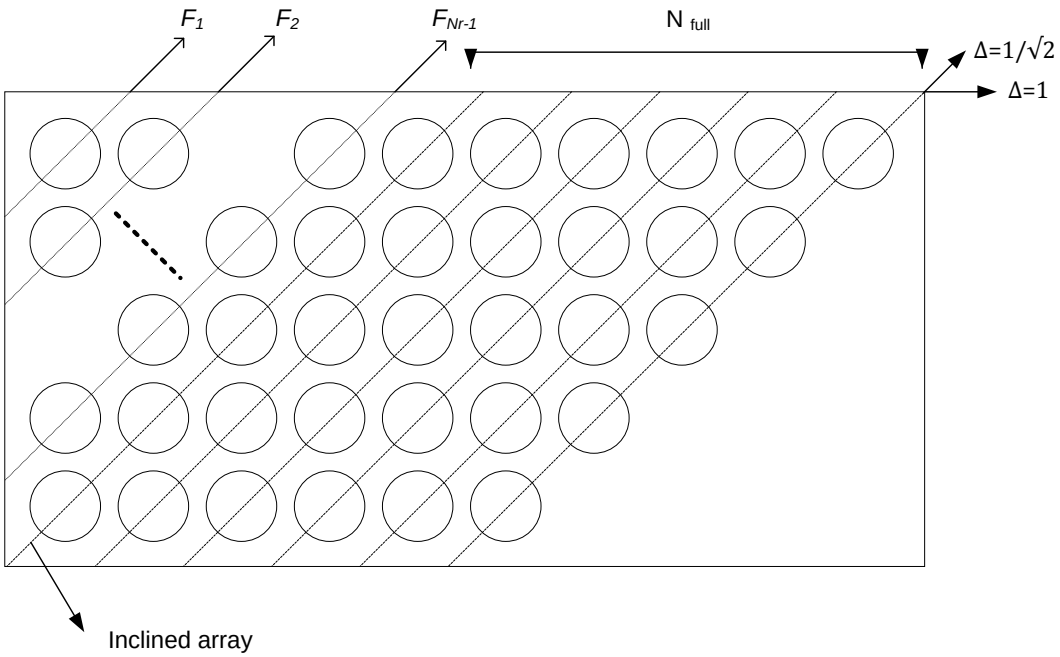

Figure 56: Stiffness of the full wall

From Figure 56,

Number of inclined arrays (N) = $N_c + N_r - 1$

Number of inclined arrays with maximum number of rings (N_{full}) = $N - 2(N_r - 1) = N_c - N_r + 1$

Resultant stiffness of the inclined array (k_c') along its length is given by,

$$k_u' = \frac{k_u}{number of\ rings\ in\ the\ array} \tag{6.12}$$

To calculate the stiffness of the full panel, it was subjected to a unit horizontal displacement as shown in Figure 56. Force experienced by each inclined array along its length due to this horizontal displacement is given by $F_1, F_2, \ldots F_N$. Firstly, the forces experienced by the partial arrays (denoted by dotted lines in the Figure 56) have been considered.

When the panel is being subjected to a unit displacement in the horizontal direction, each array is only experiencing a fraction of the displacement. As shown in the Figure 57, array *AB* is only experiencing a displacement equal to the difference of the horizontal displacement of its top and bottom end (*A* and *B*) which is given by,

$$\Delta ab = 1 - \frac{N_r - 1}{N_r} = \frac{1}{N_r} \tag{6.13}$$

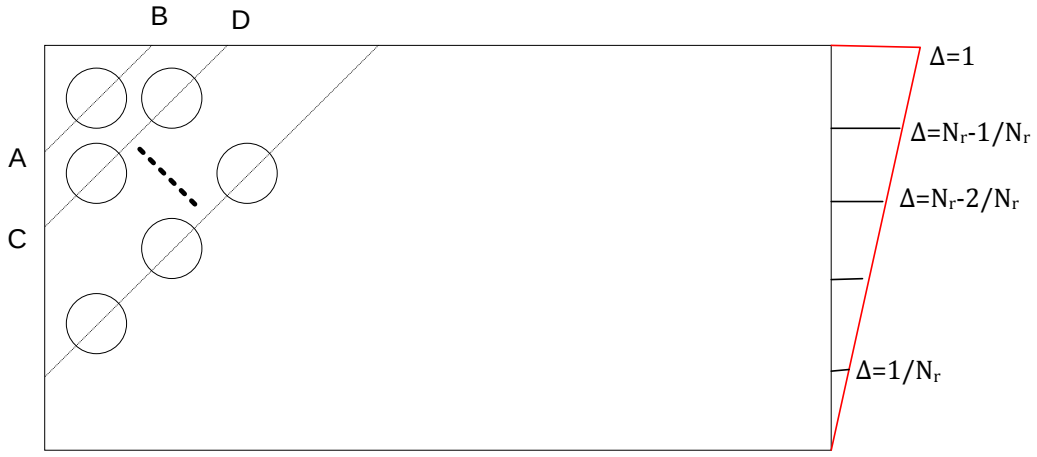

Figure 57: Displacement of inclined arrays

This horizontal displacement is then resolved along the array length to calculate the force in the array along its length.

$$F_{1=}2K_u{}' \times \frac{\Delta ab}{\sqrt{2}} \tag{6.14}$$

$$\Rightarrow F_1 = 2K_u^{'} \times \frac{1}{\sqrt{2}N_r} = \sqrt{2}K_u \times \frac{1}{N_r} \tag{6.15}$$

Similarly for other arrays,

$$F_2 = 2K_u^{'} \times \frac{2}{\sqrt{2}N_r} = \sqrt{2}\frac{K_u}{2} \times \frac{2}{N_r} = \sqrt{2}K_u \times \frac{1}{N_r} \tag{6.16 a}$$

.

.

.

.

$$F_{Nr-1} = 2K_u^{'} \times \frac{N_r - 1}{\sqrt{2}N_r} = \sqrt{2}\frac{K_u}{N_r - 1} \times \frac{N_r - 1}{N_r} = \sqrt{2}K_u \times \frac{1}{N_r} \tag{6.16 i}$$

Note that each force has been multiplied by a factor of 2 to account for an identical array positioned in the opposite corner of the full panel.

Thus, the total force due to partial arrays along the length is given by,

$$= \sqrt{2}K_u \frac{N_r - 1}{N_r} \tag{6.17}$$

The force contribution due to full arrays (denoted by dashed lines in the Figure 56) is given by,

$$= N_{full} K_u^{'} \times \frac{N_r}{\sqrt{2}N_r} = N_{full} \frac{K_u}{\sqrt{2}N_r} \tag{6.18}$$

Thus, total force along the length of the arrays if given by,

$$F = \sqrt{2}K_u \frac{N_r - 1}{N_r} + N_{full} \frac{K_u}{\sqrt{2}N_r} \tag{6.19}$$

The horizontal component of the total force was then taken to obtain the stiffness of the full panel.

$$F = K_u \frac{N_r - 1}{N_r} + N_{full} \frac{K_u}{2N_r} \tag{6.20}$$

The stiffness of the full panel is thus equal to the force due to unit displacement.

$$K_w = K_u \frac{N_r - 1}{N_r} + N_{full} \frac{K_u}{2N_r} \tag{6.21}$$

The expression was further simplified to get,

$$K_w = \frac{K_u}{2N_r}(N_r + N_c - 1) \tag{6.22}$$

Note that for panels in which $N_r > N_c$, the expression for the stiffness of the full wall can be modified to,

$$K_w = \frac{K_u}{2N_c}(N_r + N_c - 1) \tag{6.23}$$

While deriving the stiffness of the unconstrained ring model, a number of assumptions were made to simplify the analytical solution. First, the axial stiffnesses of the links has been assumed to be infinite and thus do not contribute to the stiffness of the model. Second, the joint of a link and ring is assumed to be a point assumed to be rigid with no rotations. Moreover, the derivation for the full wall stiffness assumes that the ring units experience perfect axial deformation (as a spring in series/parallel) with no transverse deflections. Additionally, the derivation is based on

the Castigliano's theorem as the initial premise which implies that it is only valid in the linear elastic region for a material. The comparison of the predicted stiffness with the results obtained from FE modeling is done in Chapter 8.

6.2. CONSTRAINED RING MODEL

Consider the constrained ring model with a shear force *V*. The line diagram of the model is shown in Figure 58.

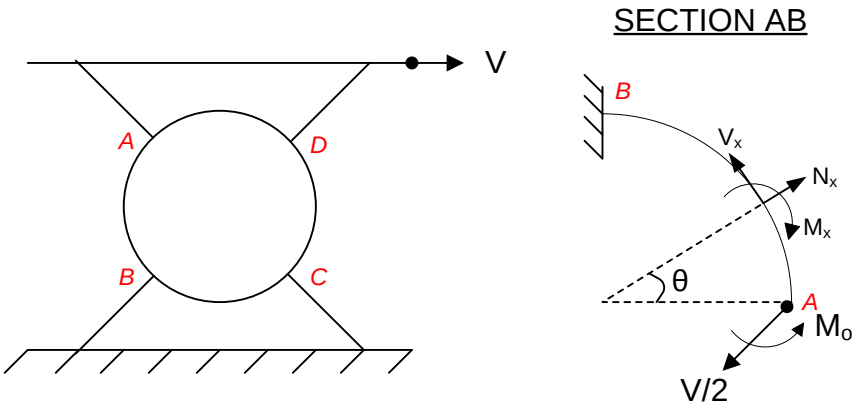

Figure 58: Line diagram of the constrained ring model

From Figure 58

$$Nx = \frac{V}{2}\cos(45 - \theta) \tag{6.24}$$

$$Vx = \frac{V}{2}\sin(45 - \theta) \tag{6.25}$$

$$Mx = M_o - \frac{VR}{2\sqrt{2}}(\sin\theta - \cos\theta + 1) \tag{6.26}$$

To find an expression for M_o, the rotation at end *A* was assumed to be zero. Therefore, by Castigliano's theorem, the rotation of end *A* is given by,

$$\emptyset_A = \frac{\partial U}{\partial M_o} = 0 \tag{6.27}$$

where, the total strain energy *U* is obtained in the form

$$U = \int \frac{\kappa V^2 R}{2AG} d\theta + \int \frac{N^2}{2AE} d\theta + \int \frac{A_m M_x^2}{2A(RA_m - A)E} d\theta - \int \frac{M_x N}{EA} d\theta \tag{6.28}$$

Taking the derivative of strain energy *U*, with respect to *Mo* and setting it to zero,

$$\int_0^{\frac{\pi}{2}} \frac{A_m}{A(RA_m - A)E} \left[M_o - \frac{VR}{2\sqrt{2}} (\sin\theta - \cos\theta + 1) \right] d\theta - \int_0^{\frac{\pi}{2}} \frac{V}{2EA} \cos(45 - \theta)\, d\theta = 0 \tag{6.29}$$

$$\Rightarrow M_0 = \frac{\sqrt{2}V}{\pi} \left(\frac{RA_m - A}{A_m} \right) + \frac{VR}{2\sqrt{2}} \tag{6.30}$$

The expression for moment at an angle θ from the horizontal (M_x) can be given by,

$$M_x = \frac{V}{2} \left[\frac{2\sqrt{2}}{\pi} \left(\frac{RA_m - A}{A_m} \right) - \frac{R}{\sqrt{2}} (\sin\theta - \cos\theta) \right] \tag{6.31}$$

Castigliano's Theorem was used to find the deflection (δ) of the section *AB* along the direction of the applied load *V/2*.

$$\delta = \frac{\partial U}{\partial (V/2)} \tag{6.32}$$

$$\delta = \int \frac{Nx}{EA} \frac{\partial Nx}{\partial (V/2)} dz + \int \frac{\kappa Vx}{GA} \frac{\partial Vx}{\partial (V/2)} dz + \int \frac{M}{EI} \frac{\partial Mx}{\partial (V/2)} dz \tag{6.33}$$

$$\delta = \frac{V}{2} \left[\frac{2\kappa R}{7GA} + \frac{9R}{7EA} + \frac{R}{EI} \left(\frac{\pi}{2} (a^2 + b^2) - b^2 \right) \right] \tag{6.34}$$

where,

$$a = \frac{2\sqrt{2}}{\pi} \left(\frac{RA_m - A}{A_m} \right) \tag{6.35}$$

and

$$b = \frac{R}{\sqrt{2}} \tag{6.36}$$

Thus the stiffness of section AB is given by,

$$k = \left[\frac{2\kappa R}{7GA} + \frac{9R}{7EA} + \frac{R}{EI} \left(\frac{\pi}{2} (a^2 + b^2) - b^2 \right) \right]^{-1} \tag{6.37}$$

To derive the expression for stiffness of the constrained ring model, it was assumed that Sections *AD* and *BC* are totally rigid and experience no axial or flexural deformation. The stiffness of the constrained model is thus given by,

$$K_c = 2k \tag{6.38}$$

$$\Rightarrow K_c = 2\left[\frac{2\kappa R}{7GA} + \frac{9R}{7EA} + \frac{R}{EI}\left(\frac{\pi}{2}(a^2 + b^2) - b^2\right)\right]^{-1} \tag{6.39}$$

The stiffness of the full wall was derived based on the stiffness of the constrained model (K_c). The arrangement of the rings in the full wall is shown in Figure 59.

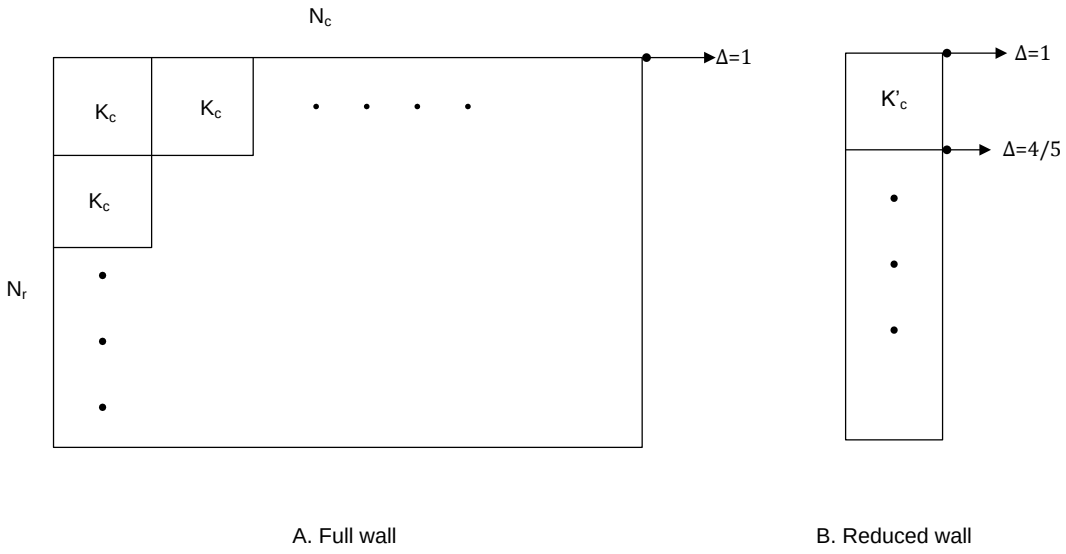

Figure 59: Arrangement of constrained ring models in the full panel

The ring units in one row are in parallel because each unit in experiencing the same displacement. Thus, the full wall can be represented as part b of Figure 59, where,

$$K_c^{'} = N_c K_c \tag{6.40}$$

Now in the resultant system, the ring units are in series because they resist the same shear force. Thus, the stiffness of the full wall is given by,

$$K_w = \frac{K_c^{'}}{N_r} = \frac{N_c}{N_r} K_c \tag{6.41}$$

While deriving the equation for the stiffness using the constrained ring model, a number of assumptions were made. First, the stiffness of the sections *AD* and *BC* and the links have been assumed to be infinite. Also, rotation of the section *AB* at both the ends is assumed to be zero. Additionally, assumptions made while deriving the stiffness for the unconstrained ring model are also valid in this case.

It was reasoned that since the unconstrained model was restricted by fewer assumptions, it would yield results that would approximate the mechanics of the plate more closely. Thus, the unconstrained model was used to predict the stiffness of the BR-SPSW specimens and for comparison of the analytical solution to the computational results obtained from the parametric study in Chapter 8.

CHAPTER 7
EFFECT OF INITIAL IMPERFECTIONS

Initial imperfections may have a major impact on the buckling behavior of a thin steel plate shear wall and the finite element model results attempting to simulate their behavior. Thus, to investigate the effect of imperfections on the BR-SPSW, a small parametric study was performed. The main aim of this study was to investigate the sensitivity of the plate to the shape and magnitude of initial imperfection. The effect of the initial imperfections in the shape of buckling modes on the system behavior was investigated. As a part of this study, eigen buckling analysis was performed on an ideal BR-SPSW specimen to identify the first five buckling modes. These buckling modes are shown in Section 7.2. Subsequently, two separate sets of analyses were performed to determine the effect of magnitude and shape of initial imperfection respectively. These simulations are briefly explained below.

7.1. EFFECT OF MAGNITUDE OF INITIAL IMPERFECTION

In this set of simulations, an initial imperfection in the shape of first buckling mode was induced in the specimen scaled to varying amplitudes of *L*/25, *L*/50, *L*/100, *L*/1000 where L is the height of the panel. The behavior of the specimen was then compared to a perfect plate and a plate with random initial imperfections. This comparison was done because using random out-of-plane loads on the web-plate is a much easier way to model some minimal amount of initial imperfections. If the behavior of the wall is not significantly dependent of the method of modeling initial imperfections, then performing an eigen buckling analysis can be avoided.

For the purpose of this study, two plates were chosen. Both the plates were ¼ in. thick but with varying outer ring radius. A thinner plate was chosen for the study because it was concluded from a short preliminary analysis that thicker plates displayed almost negligible sensitivity towards the shape or magnitude of initial imperfection when kept within normal fabrication tolerance. In general, the modeling features for the finite element model were identical to the ones used for the preliminary study (refer Section 4.1.1.). These models are a part of the parametric study and referred to as model A4 (smaller radii) and B11 (larger radii). For further description of these models refer Chapter 8. The first buckling mode of specimens A4 and B11 are shown in Table 11. The geometric features of the two plates are presented in Table 10.

Table 10: Geometric features of A4 and B11

	t (in.)	R_o (in.)	R_o/w_c	R_o/w_1
A4	0.25	10	3.33	2
B11	0.25	24	3.33	2

The pushover behavior for models A4 and B11 with varying levels of initial imperfection is shown in Figure 60 and Figure 61. From the figure it was concluded that as long as the imperfections are included in the model and are less that *L*/100, the effect of the magnitude of imperfection is small and can be neglected. For imperfections larger than *L*/100, the stiffness of the panel reduces. For example, an imperfection of *L*/50 resulted in the reduction of the initial stiffness by 30% for A4 and 43% for B11. In most cases higher imperfections also led to model instability. Thus it seems reasonable to limit the initial imperfections of the BR-SPSW to *L*/100 for practical purposes (about 1.44 inches for this plate).

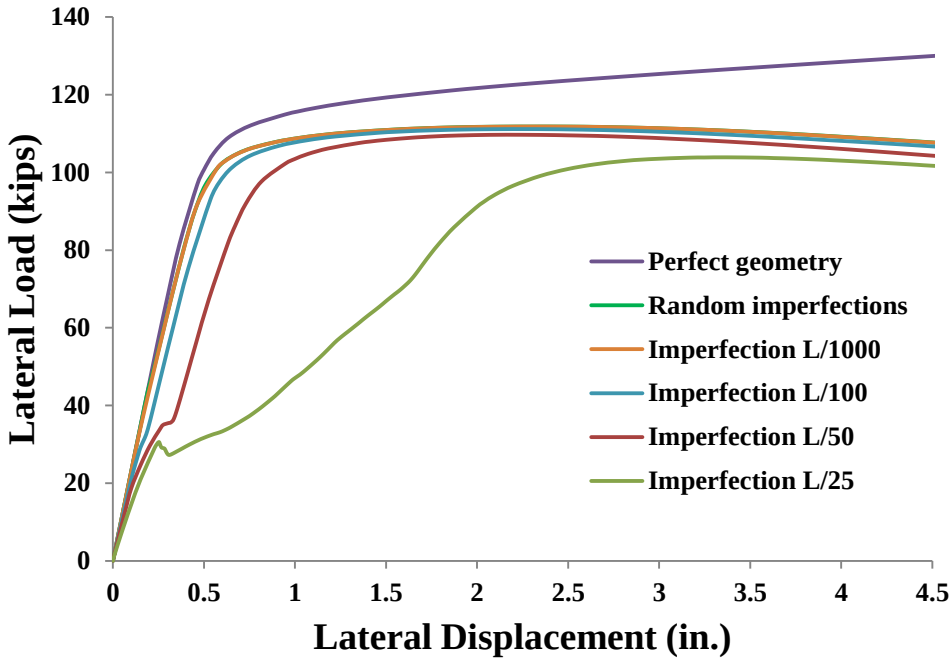

Figure 60: Effect of the magnitude of initial imperfections for plate A4

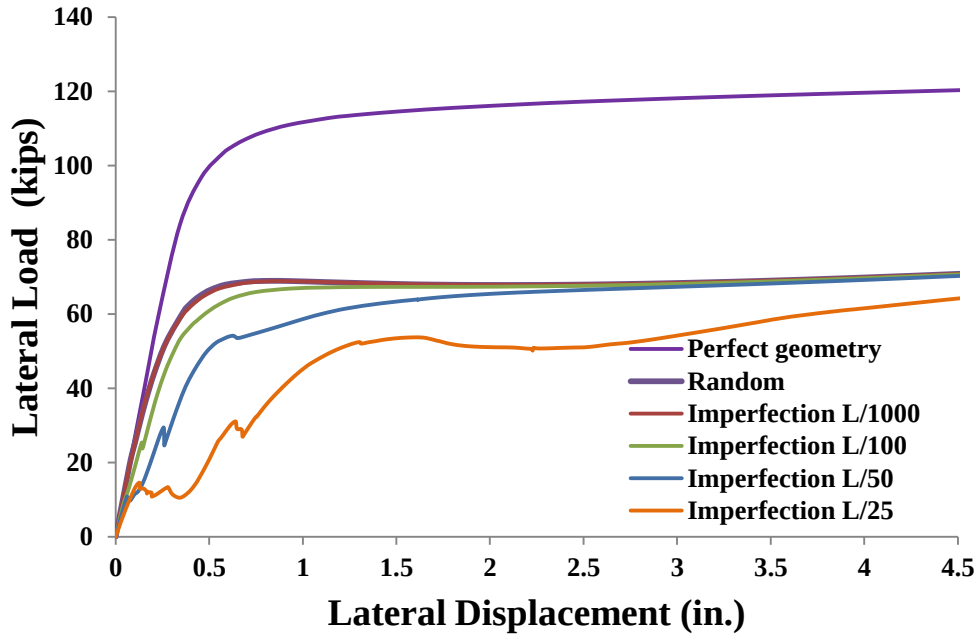

Figure 61: Effect of initial imperfection for plate B11

It was also concluded that using random imperfections for modeling the plates is acceptable since there was only a small difference in the capacity and stiffness of the plates as compared to the models with initial imperfections in the shape of the first eigen-mode. Another point that should be noted here is that large initial imperfections result in reduced strength and stiffness, especially in model B11 which had larger radii rings. Thus, it is very important to make initial imperfections in a model to simulate its actual behavior.

7.2. EFFECT OF THE SHAPE OF INITIAL IMPERFECTION

In this set of tests, initial imperfection in the shape of first five eigen buckling modes was used for both plates A4 and B11. These modes are shown in Table 11. The magnitude of the imperfection was scaled to $L/100$ for each case. The results were then compared to the behavior of the plate with random imperfections. Figure 62 and Figure 63 shows the effect of the shape of initial imperfection on the plate behavior. The mode shape clearly does not have major effect on the stiffness and strength of the plate.

The final conclusion that was drawn from this chapter was that the use of random out-of-plane imperfections to simulate initial imperfections is acceptable. Also, it saves computational time

and effort that would be required to perform eigen buckling analysis for each plate before running the main analysis.

Table 11: Table showing the eigen buckling modes of specimen A4 and B11

	Specimen A4	Specimen B11
Mode 1	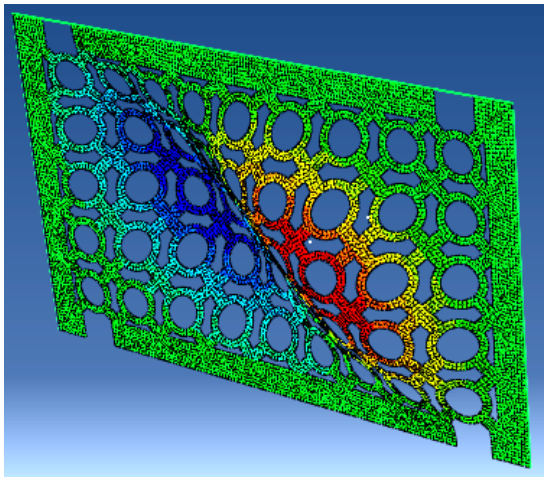	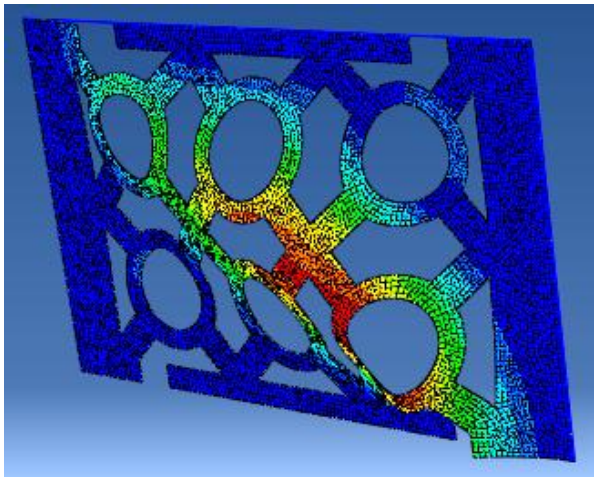
Mode 2	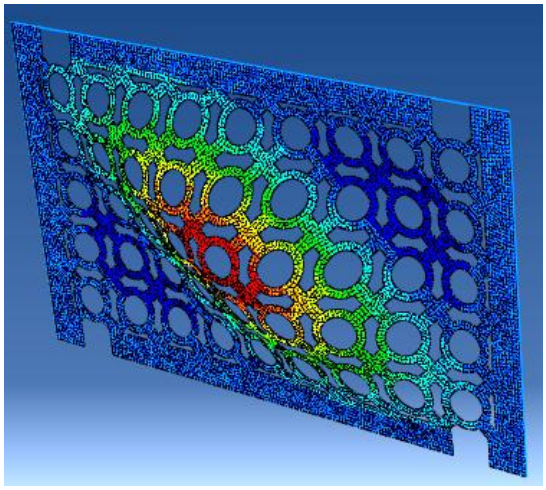	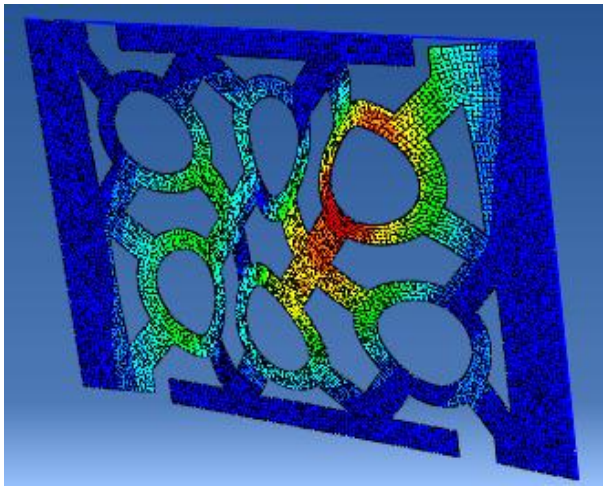

Mode 5

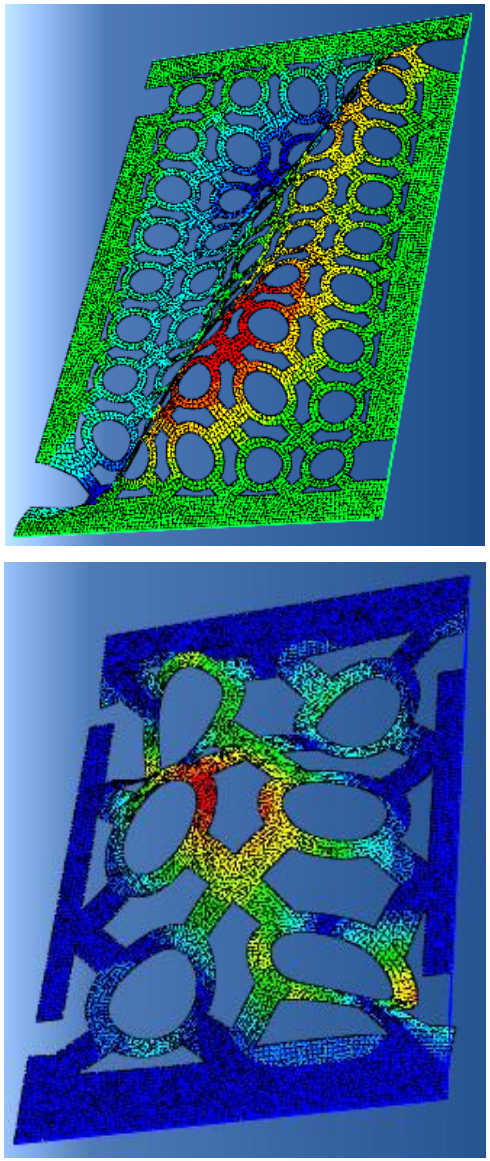

Mode 4

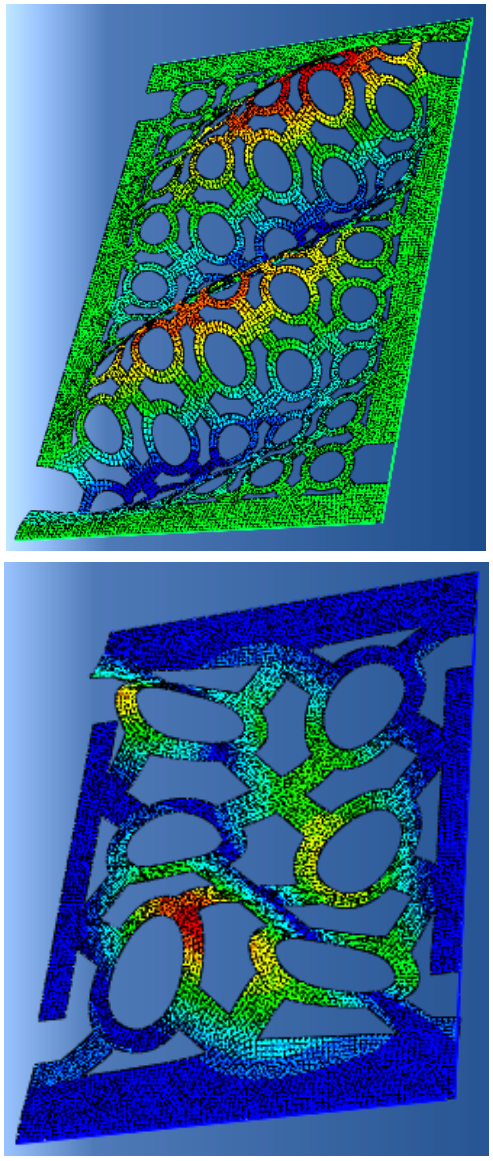

Mode 3

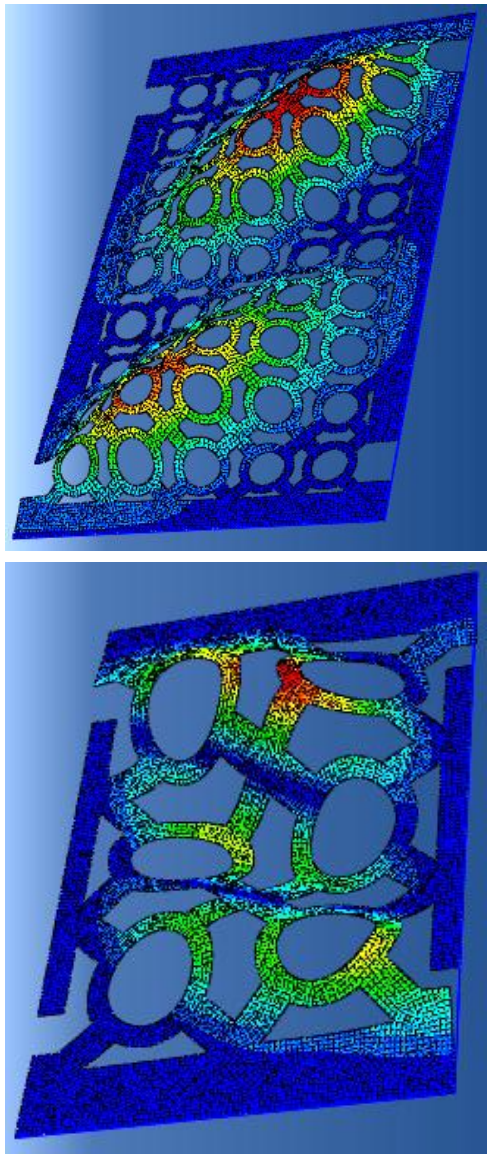

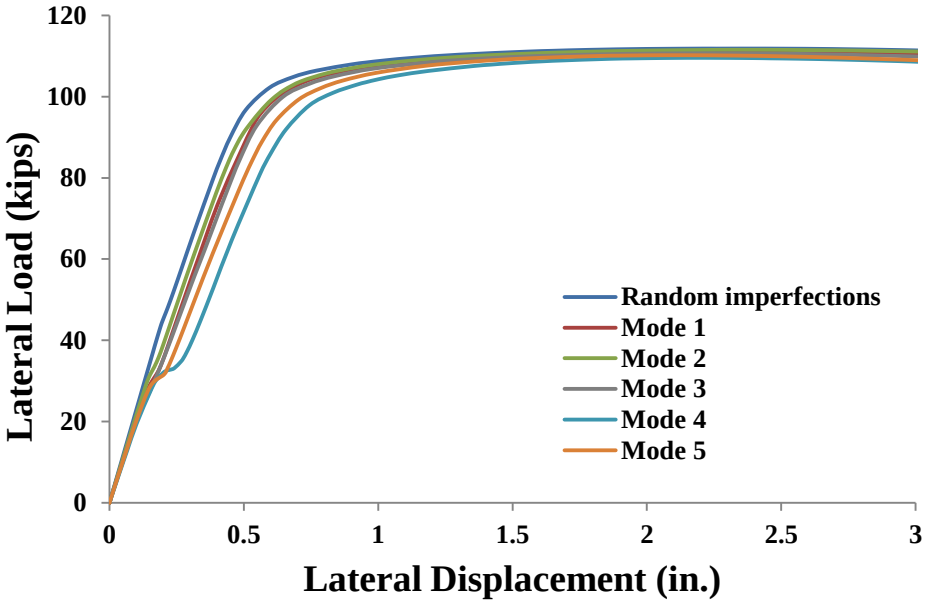

Figure 62: Effect of shape of initial imperfection on plate A4

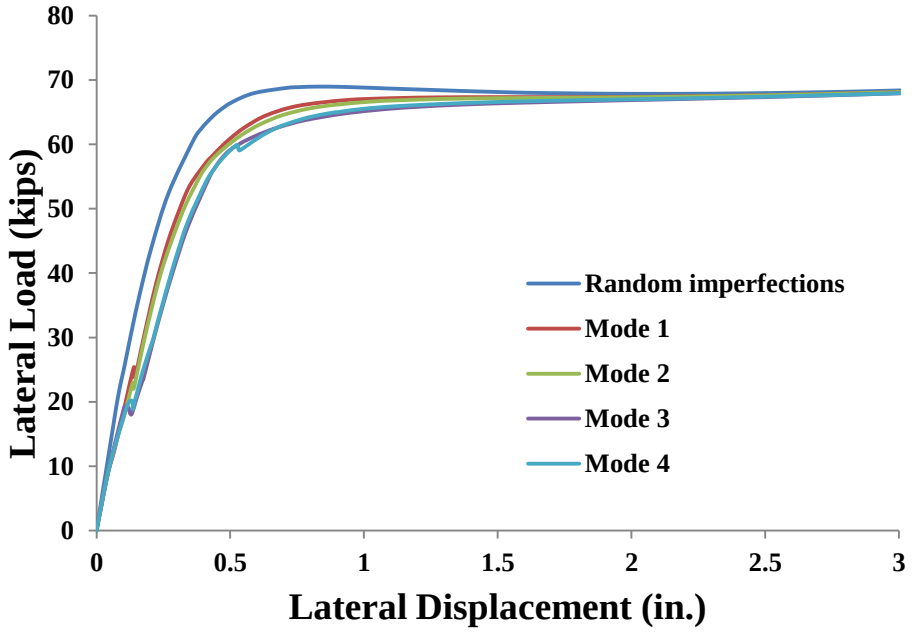

Figure 63: effect of shape of initial imperfection on plate B11

CHAPTER 8
PARAMETERIC STUDY

The preliminary analyses presented in Chapter 4 were done to validate the idea behind the BR-SPSW. The study showed that this proposed alternative to a typical shear wall reduced bucking, exhibited higher resistance to lateral loading during load reversals, and produced much less pinching of the hysteresis loops. Moreover, the system works well without moment connections (i.e. has sufficient stiffness, energy dissipation, and resists force during load reversals).

To build on the preliminary work presented in previous sections, there was a need to perform more rigorous and methodical computational study of the full-size panel with varying parameters to better understand the behavior of this system. The parametric computational study was performed using ABAQUS (Version 6.11 Documentation) as the main tool. 2D modeling with shells elements was used to model the plate. Geometric non-linearities were included to capture of the web plate. Boundary elements were modeled near rigid to isolate the behavior of the web plate. All the other modeling parameters were identical to the preliminary studies presented in Chapter 4. The loading protocol was however changed to a more standard protocol used for beam-to-column moment connections. The protocol was adopted from AISC seismic provisions (Appendix S6.2) but was modified such that only one cycle per story drift level was used as shown in Figure 64.

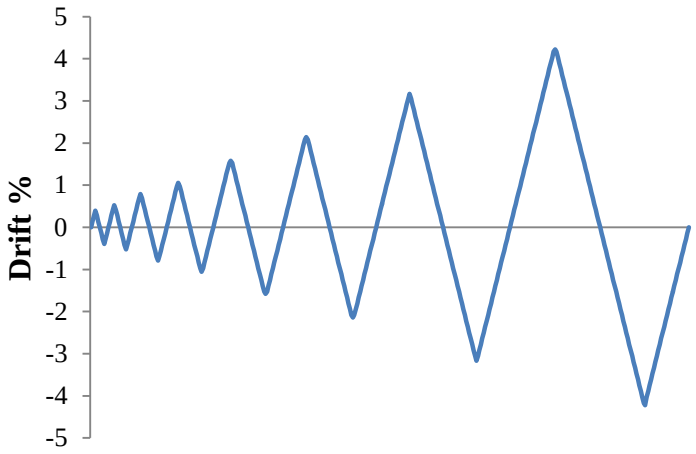

Figure 64: Loading protocol used for the parametric study

For the parametric study, the boundary elements (beam and columns) are assumed to be perfectly rigid so as to isolate the behavior of the panel. All the output data from ABAQUS was recorded at the middle layer of the shell elements. This was done to get axial stresses only and to avoid getting the high bending stresses associated with out of plane buckling.

The most critical parameters identified for the computational study, the range in which they are varied and related issues are discussed in the next section.

8.1. INPUT PARAMETERS

8.1.1. Thickness of steel plate used (t)

The web plate thicknesses to be used in the study are: 5/8 inches, 1/2 inches, 5/16 inches and 1/4 inches. These values were chosen for the steel plates so they can be used in large range of stories with varying load demand. The initial capacity prediction shows that using these thicknesses can result in strength in the range 50-550 kips. These values can be further increased or decreased by changing other dimensional parameters of the panel.

8.1.2. Outer radius of the rings (R_o)

The radius of the rings has been varied in the range: 8 inches, 10 inches, 16 inches and 24 inches. The lower bound of this range was chosen keeping in mind the fact the decreasing the diameter of the rings increases the cutting length exponentially, thus increasing the cutting cost. The upper bound of the range was chosen as 24 inches to further explore the design space to figure out what combinations of design parameters result in local lateral torsional buckling in the rings.

8.1.3. Width of the rings (W_c)

The width of the rings has been varied in the form of variation in the R_o/w_c ratio. This ratio is the slenderness ratio of the ring and is expected that it may influence the buckling behavior of the full wall. The ratio chosen for this ratio for the study are: 2, 2.5 and 3.33 and 5.These values were chosen keeping in mind two important facts. First, very wide rings may not yield easily and thus, reducing the dissipation energy. Second, a very narrow ring may experience local lateral torsional buckling, both of which can have adverse effects on the performance of the wall.

8.1.4. Width of the connecting link (W_l)

This parameter is expected to affect the amount of inelastic axial deformations of the link thus contributing to the amount of lag and pinching of the hysteretic behavior. Again, the parameter here has been varied in the form of R_o/w_lratio. The lower bound for the parameter was set

keeping in mind the fact that if the connecting link is too narrow, it will yield, causing an adverse effect on the wall behavior.

Apart from the independent variables mentioned above, a few dependent and dimensionless variables were studied to better understand the system behavior. R_o/t and w_c/t also referred in this text as the ring slenderness ratio were used to understand the local buckling of the rings which have a major impact on the overall energy dissipation of BR-SPSW.

8.2. OUTPUT PARAMETERS

To thoroughly study the behavior of the BR-SPSW a comprehensive list of output parameters was prepared as shown below.

- Strength of the shear wall system
- Stiffness of the shear wall system
- Yield drift % of the shear wall system
- Total energy dissipation
- Energy dissipation ratio
- Buckling Ratio
- Length of the cut
- Openness of the wall
- Peak strength
- Weight ratio

These output parameters were recorded for each specimen of the parametric study. This section briefly describes each of these parameters and the methods used to record them.

8.2.1. Strength, stiffness and yield drift

Strength, stiffness and the yield drift of a shear wall system were recorded by subjecting every specimen to a monotonic loading. The force-displacement plot was then generated as shown in Figure 65. For stiffness, the initial slope of the curve taking the origin (0,0) and the point on the curve which corresponds to the half of the maximum strength achieved (point-b) was recorded. Another line was constructed taking the points corresponding to 0.75% and 1% drift on the force-displacement plot. The intersection point of both the lines (point-a) was noted. The x-

coordinate of point was recorded as the strength of the shear panel and the y-coordinate as the yield drift. Similar plots showing the calculation of strength for all the specimens are compiled as a part of Appendix D. Each curve was examined individually to ensure that this method produced seemingly reasonable results.

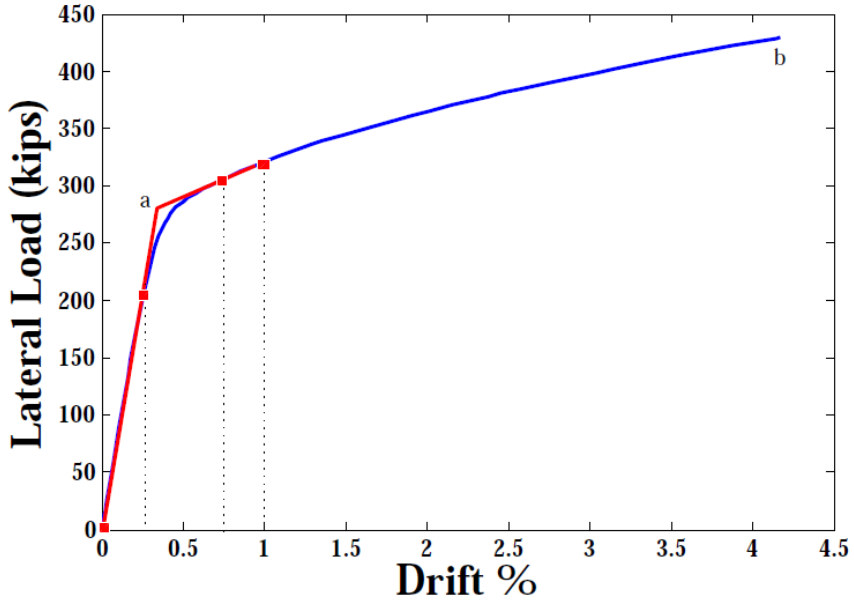

Figure 65: Strength, Stiffness and Yield Drift calculation from force-displacement plot

8.2.2. Total energy dissipation

Energy dissipation in a BR-SPSW takes places due to the yielding of the ring-link system. The efficiency of this unique geometrical feature would therefore be reflected in the total dissipated energy. This output parameter was recorded by taking the total area under the last hysteresis loop. The hysteresis curve for all the specimens is recorded in Appendix B.

8.2.3. Energy Dissipation Ratio

Energy dissipation ratio is a measure of how close a specimen is to an ideal specimen which displays full hysteretic behavior with no pinching. It is the ratio of the actual energy dissipated by a specimen to the ideal energy dissipated, if there were not strength degradation or pinching. Thus a higher energy dissipation ratio would indicate relatively higher energy dissipation.

To record this ratio, a parallelogram was constructed around the last cycle of a hysteresis curve as shown in Figure 66. The area under the dashed parallelogram represents the energy dissipated by an ideal specimen exhibiting full hysteretic behavior. The energy dissipation ratio is calculated as the ratio of the area of the last cycle of the hysteresis curve to the area under the parallelogram. To construct the parallelogram, the slopes of the adjacent edges of the parallelogram were first determined. One of the slopes was taken as the slope of the hysteresis curve in the last cycle right after it attains its peak strength (in the last cycle). The second slope was slope of the hysteresis curve right before it achieves its global peak strength. The plots for all the specimens showing the calculation of the energy dissipation ratio are attached in Appendix C.

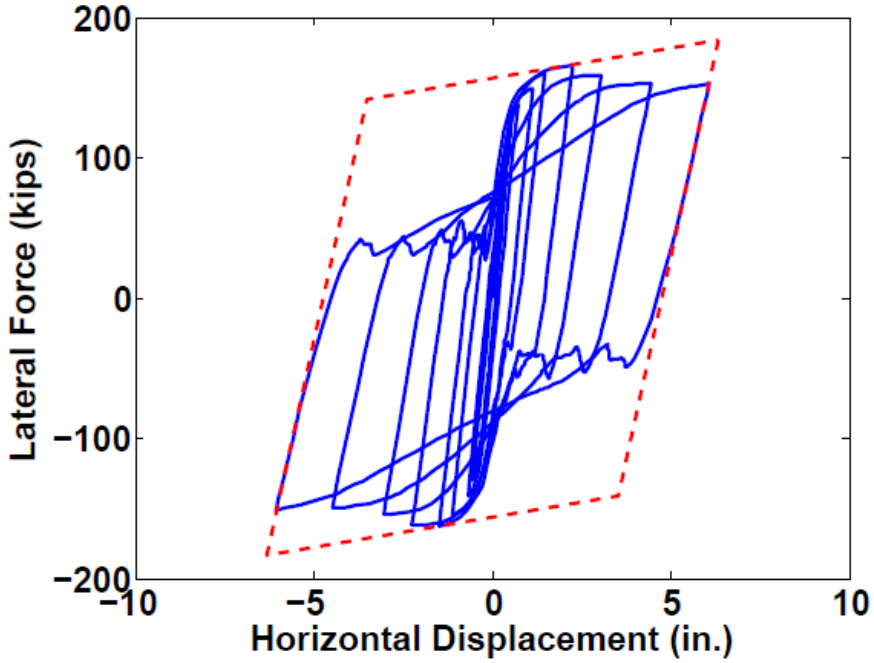

Figure 66: Plot showing the method for calculating the energy dissipation ratio

8.2.4 Buckling Ratio

This output parameter indicates the relative percentage of global tension buckling and lateral torsional bucking of the rings. A higher ratio implies relatively higher percentage of global tension field buckling. Note that this output parameter is important because the type of buckling modes (global tension field buckling or lateral torsional bucking of the rings) has an impact on the total energy dissipation of the shear wall. This will be elaborated in a Section 8.4.2.

Each specimen displayed a combination of both buckling modes and therefore, it was challenging to quantify their relative percentage. The procedure adopted to calculate the buckling ratio is elaborated in the next paragraph.

The first step towards calculating the buckling ratio was to record the out-of-plane displacement across the width of the web plate. The variation of the out-of-plane displacement was then plotted as shown in Figure 67.

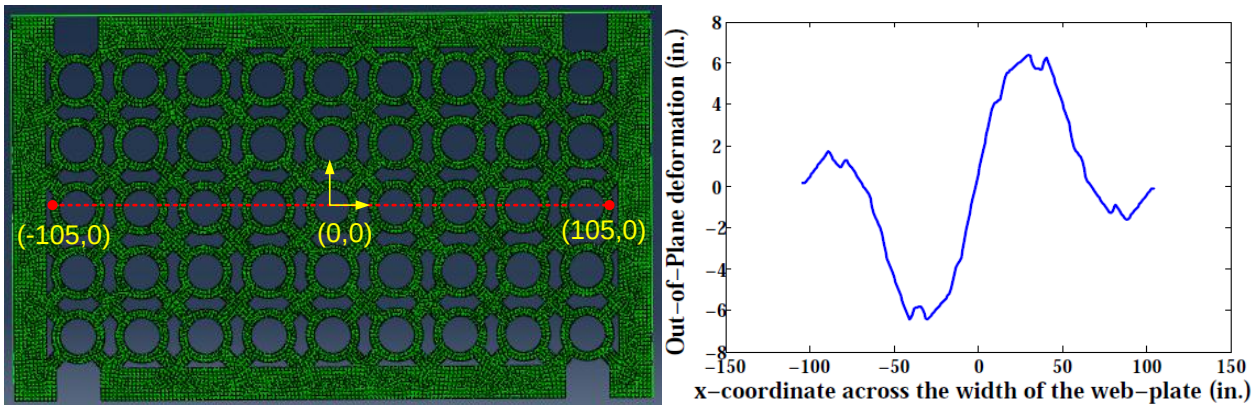

Figure 67: Plot showing the variation of out-of-plane displacement across the width of the web plate

This data was then run through a discrete Fourier transform function to separate the different wavelengths of the input signal (in this case the variation of out-of-plane deformation). The absolute value of the FFT was recorded. The idea was to separate out the higher wavelength corresponding to the global tension field buckling from the shorter wavelength (disturbances in the otherwise smooth wave, caused by the torsional buckling of the rings). The FFT plot for the out-of-plane displacement data in Figure 67 is shown in Figure 68. Note that only the first half of the FFT plot is shown in the figure as the second half is merely a mirror image of the first half.

The FFT plot clearly shows a dominant wavelength which corresponds to the global tension field buckling. The next peak is relatively much smaller indicating that the lateral torsional buckling of the rings which caused disturbance in the smooth wave-like curve is very minor (refer to the plot in Figure 67). The buckling ratio for the specimen was calculated by taking the ratio of the magnitude of the most prominent peak and the peak with the next highest magnitude. Although, this is a very crude method, it proved to be quite effective in determining the relative percentage

of local and global buckling. The efficacy of this approach is discussed in detail in the Section 8.4.2. Note that a similar approach is used by Zeinoddini-Meiman (2011) wherein power spectral density (PSD) plots were used to simulate imperfections in cold-form steel members.

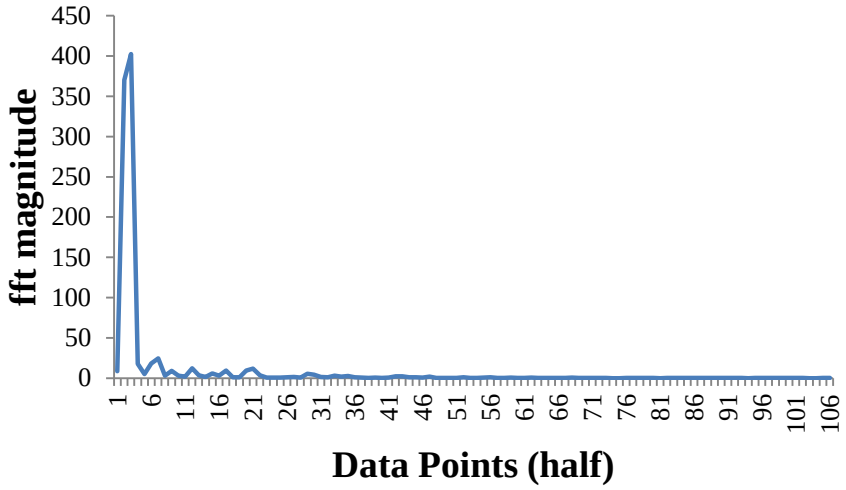

Figure 68: FFT plot for a specimen

8.2.5. Length of the cut

Length of the cut made on the BR-SPSW is an important output parameter because the cost of cutting directly depends on it. The length of the cut was determined by using the formula,

$$L_c = \left((2\pi(R_o + R_i) - 4w_l + 8L_l)N_r N_c\right) + 4R_o(N_c + N_r) \quad (8.1)$$

Refer Table 1 for the notations used in the equation.

8.2.6. Openness of the wall

This parameter is important with respect to the air flow and allowing daylight in the building. The approximate openness of the wall was determined by using the formula,

$$Openness = 2(R_o + L_l)^2 - 4L_l w_l - \pi(R_o^2 - R_i^2) \quad (8.2)$$

Refer Table 1 for the notations used in the equation.

8.2.7. Peak strength

The peak strength attained by the specimen through the entire course of loading was recorded.

8.2.8. Weight ratio

The weight ratio was defined as the ratio of the weight of BR-SPSW (considering the cut-out pattern) specimen to the weight of a solid panel having the same strength as the BR-SPSW specimen.

The expression used for the strength of the solid panel is given by (Berman and Bruneau, 2007),

$$V = 0.5tWF_y \sin 2\alpha \tag{8.3}$$

where, t is the thickness of the plate, W is the width of the plate and α is the angle of inclination of tension field (taken as 40° in this report). For calculating the strength of BR-SPSW, equation 5.70 was used.

8.3. TEST SETS

A detailed summary of all the analyses to be performed as a part of the computational study is presented in

Table 12-15. Each series of tests is designed to study the influence of a specific parameter on the overall behavior of the panel. Refer to Section 8.1 for the definition of the input parameters used in the parametric study.

Note the staggered configuration, which was analyzed as a part of the preliminary study was excluded from the main parametric study. The reason behind this decision was the difficulty in the ring arrangement for a given web-plate dimension.

Meshing the models with appropriate mesh size is quite essential for obtaining accurate results from FE analysis. However, too much mesh refinement is computationally expensive. Thus, before starting the parametric study, two mesh sizes (seed size 0.75 and 1.5) were used for specimen A1. Note that an element seed size of 1.5 was used for preliminary study.

It was observed that the difference in the major output parameters (strength, stiffness, yield drift %, energy dissipation) for the two models was less than 9%. The use of element seed size of 1.5 was thus justified and was used for the parametric study.

Table 12: Table showing the tests done as a part of SERIES A of the parametric study

SERIES A: To determine the influence of thickness(t_w)							
	t_w	Ro	Ro/w_c	w_c	Ro/w_L	w_L	Ro/t_w
A1	5/8"	10"	3.33	3"	2	5"	16
A2	1/2"	10"	3.33	3"	2	5"	20
A3	5/16"	10"	3.33	3"	2	5"	32
A4	1/4"	10"	3.33	3"	2	5"	40

Table 13: Table showing the tests done as a part of SERIES B of the parametric study

SERIES B: To determine the influence of outer radius Ro							
	t_w	Ro	Ro/w_c	w_c	Ro/w_L	w_L	Ro/t_w
B1	1/2"	24"	3.33	7.2"	2	12"	48
B2	5/8"	16"	3.33	4.8"	2	8"	25.6
B3	5/16"	8"	3.33	2.4"	2	4"	25.6
B4	5/8"	24"	3.33	7.2"	2	12"	38.4
B5	1/2 "	16"	3.33	4.8"	2	8"	32
B6	1/4"	16"	3.33	4.8"	2	8"	64
B7	5/8"	8"	3.33	2.4"	2	4"	12.8
B8	1/4"	8"	3.33	2.4"	2	4"	32
B9	1/2"	8"	3.33	2.4"	2	4"	16
B10	5/16"	16"	3.33	4.8"	2	8"	51.2
B11	1/4"	24"	3.33	7.2"	2	12"	96
B12	5/16"	24"	3.33	7.2"	2	12"	76.8

Table 14: Table showing the tests done as a part of SERIES C of the parametric study

SERIES C :To determine the influence of Ro/w_c and Ro/w_l ratio							
	t_w	Ro	Ro/w_c	wc	Ro/w_L	w_L	Ro/t_w
C1	1/2"	10"	5	2"	2	5"	20
C2	5/8"	16"	2.5	6.4"	2	8"	16
C3	5/16"	8"	5	1.6"	2	4"	32
C4	5/8"	10"	2.5	4"	2	5"	16
C5	1/2 "	16"	5	3.2"	2	8"	20
C7	1/2"	10"	2.5	4"	2	5"	20
C8	5/8"	8"	2.5	3.2"	2	4"	12.8
C9	1/2"	8"	2.5	3.2"	2	4"	16
C10	5/16"	10"	2.5	4"	2	5"	32
C11	5/8"	10"	5	2"	2	5"	16
C12	5/16"	10"	2	5"	2	5"	32
C13	1/2"	10"	2	5"	2	5"	20
C14	5/8"	10"	2	5"	2	5"	16
C15	5/8"	10"	3.33	3"	1.5	6.667"	16
C16	1/2"	10"	3.33	3"	1.5	6.667"	20
C17	5/16"	10"	3.33	3"	1.5	6.667"	32
C18	5/8"	10"	3.33	3"	2.5	4"	16
C19	1/2"	10"	3.33	3"	2.5	4"	20
C20	5/16"	10"	3.33	3"	2.5	4"	32
C21	5/8"	10"	3.33	3"	3	3.33"	16
C22	1/2"	10"	3.33	3"	3	3.33"	20
C23	5/16"	10"	3.33	3"	3	3.33"	32

Table 15: Table showing the tests done as a part of SERIES D of the parametric study

SERIES D: To determine the influence of Ro/w_l and Ro/w_c ratio							
	t_w	Ro	Ro/w_c	wc	Ro/w_L	w_L	Ro/t_w
D1	5/8"	10"	3.33	3"	3	3.33"	16
D2	5/8"	16"	2.5	6.4"	1.5	10.67"	16
D3	1/2"	10"	5	2"	3	3.33"	20
D4	5/16"	8"	2.5	3.2	3	2.67"	25.6
D5	1/2"	8"	3.33	2.4"	1.5	5.33"	20
D6	1/2"	24"	3.33	7.2"	1.5	16"	20
D7	1/2"	8"	2.5	3.2	3	2.67"	16
D8	1/2"	10"	2.5	4"	3	3.33"	20
D9	1/2"	10"	2.5	4"	2.5	4"	20
D10	1/2"	8"	2.5	3.2"	2.5	3.2	16
D11	1/2"	16"	2.5	6.4"	2	8"	32
D12	1/2"	16"	2.5	6.4"	2.5	6.4"	32
D13	1/2"	16"	2.5	6.4"	3	5.33"	32

8.4. RESULTS AND DISCUSSION

This section discusses the results of the parametric study. Conclusions related to the behavior of BR-SPSW have been drawn and recommendations have been made for optimum design.

8.4.1. Hysteretic behavior

As previously mentioned, hysteresis plots for each specimen in the parametric study was generated. The hysteresis plot reflects the behavior of a specimen under cyclic loading, specifically its energy dissipation capability. As highlighted previously, the main purpose of the parametric study was to investigate the sensitivity of the system behavior on the input parameters. The hysteresis plot of all the test specimens was keenly observed to derive appropriate conclusion.

One of the major input parameter for the parametric study was the thickness of the steel plate used. It was observed as the plate thickness decreases, the energy dissipation capacity of the specimen decreases as is clear from the shrinking area under the curve in Figure 69. This observation can be attributed to the fact that thinner plates buckle faster and hence experience

significant strength and stiffness degradation. For example, specimen A4 with thinnest web plate suffered a reduction in stiffness of about 66% in the last cycle as compared to the first cycle. This decrease was comparatively less (52%) for specimen A2. A much detailed and quantitative analysis of the dependence of system behavior on the thickness of the web plate is presented in Section 8.4.3.

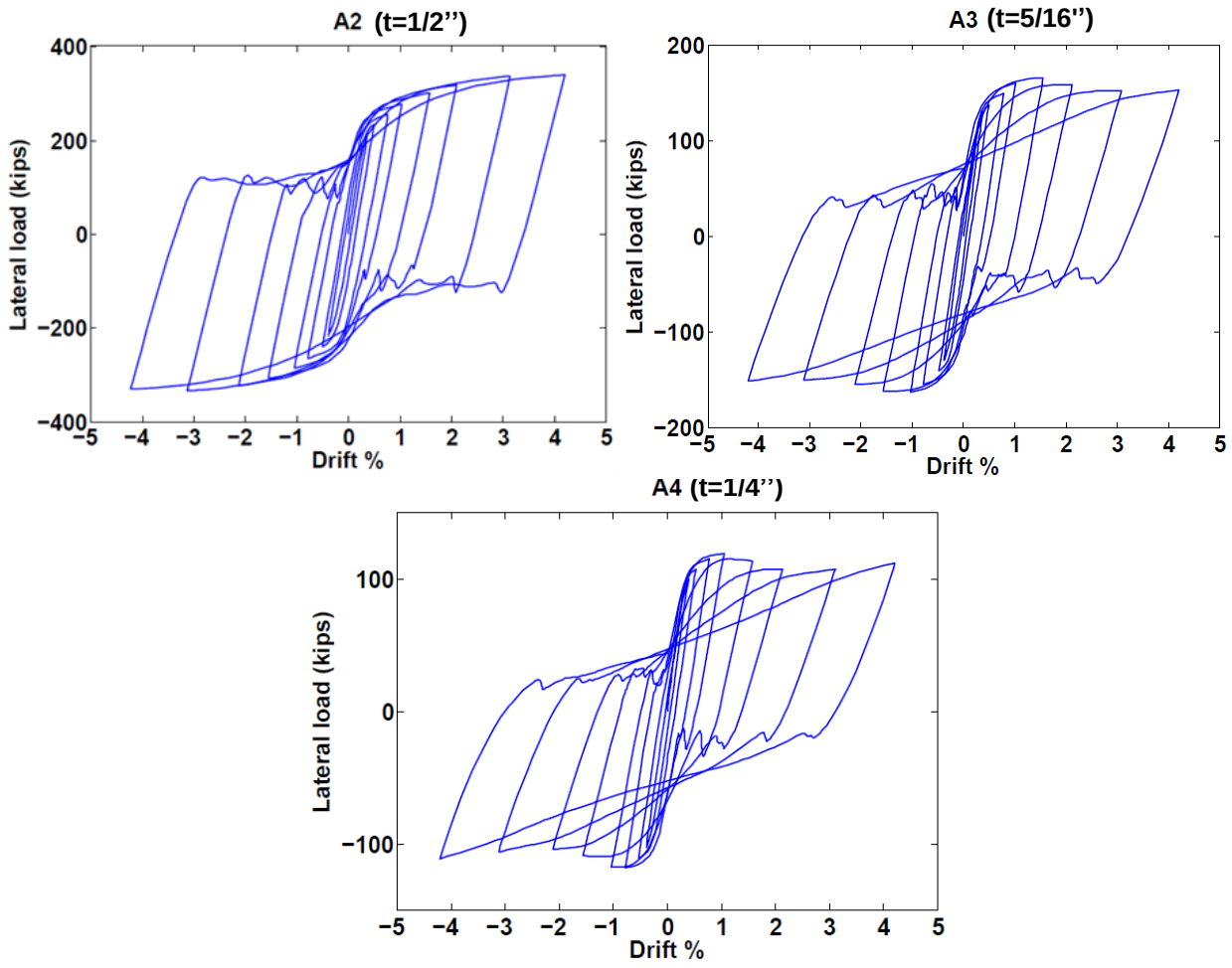

Figure 69: Figure showing the dependence of hysteretic behavior on thickness for 10'' outer ring radius

Next, the dependence of the hysteretic behavior on the ring radius was investigated. It was observed that increase in the outer ring radius resulted in lower energy dissipation as shown in Figure 70. The FE analysis results showed that specimens with larger ring radius (B5 and B1) exhibited severe lateral torsional buckling of the rings as opposed to their smaller radii

counterparts (A2 and B9), which majorly experiences global tension field buckling. The figure also shows that for specimen B1 and B5, with the large ring radii, the lateral load resistance is small during load reversal until the system reaches its previous peak displacement. This results in the pinching of the hysteretic behavior. Additionally, these specimens also exhibit substantially reduced stiffness and capacity in the last few cycles. For example, specimen B1 exhibited a 67% decrease in stiffness in the last cycle, as compared to a 28% decrease in B9. Thus, it can be concluded that for the same plate thickness, the specimens with smaller ring radius would dissipate more energy.

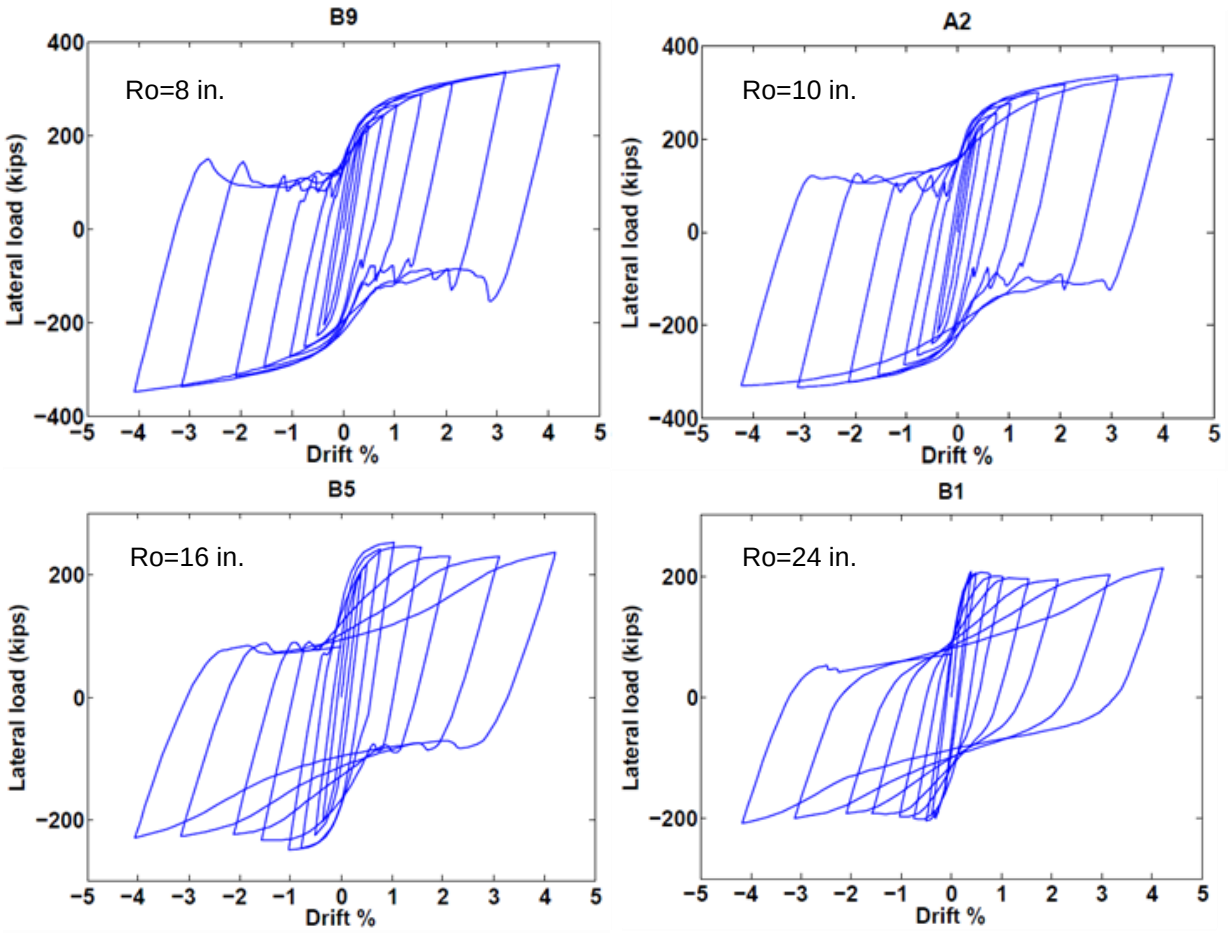

Figure 70: Figure showing the dependence of the hysteretic behavior on the ring radius (t=1/2'')

Another important parameter was the width of the ring. It was expected that the width of the ring would govern the lateral torsional buckling of the rings and hence the hysteretic behavior of the shear wall. From Figure 71, it was observed that a very narrow ring (specimen C1) results in

very small stiffness and negligible energy dissipation. Negligible yielding at the link-ring joint was observed. In all the other specimens with R_o/w_c ratio of 5, similar results were obtained. Thus, specimen design employing a R_o/w_c ratio as high as 5 is not advisable. Note that for the purpose of parametric study all the input variables were chosen in a wide range so as to capture the extreme behavior of the BR-SPSW. However, it is important to recognize that not all the test specimens would result in a practical design.

From Figure 71, it was also observed that very wide rings increase the strength of the shear wall, but this advantage is marred by the increase in the lateral torsional buckling of the rings which in turn results in pinched hysteretic behavior (specimen C13). Keeping R_o/w_c ratio in the range of 2.5-3.33, results in fuller hysteretic behavior and higher energy dissipation.

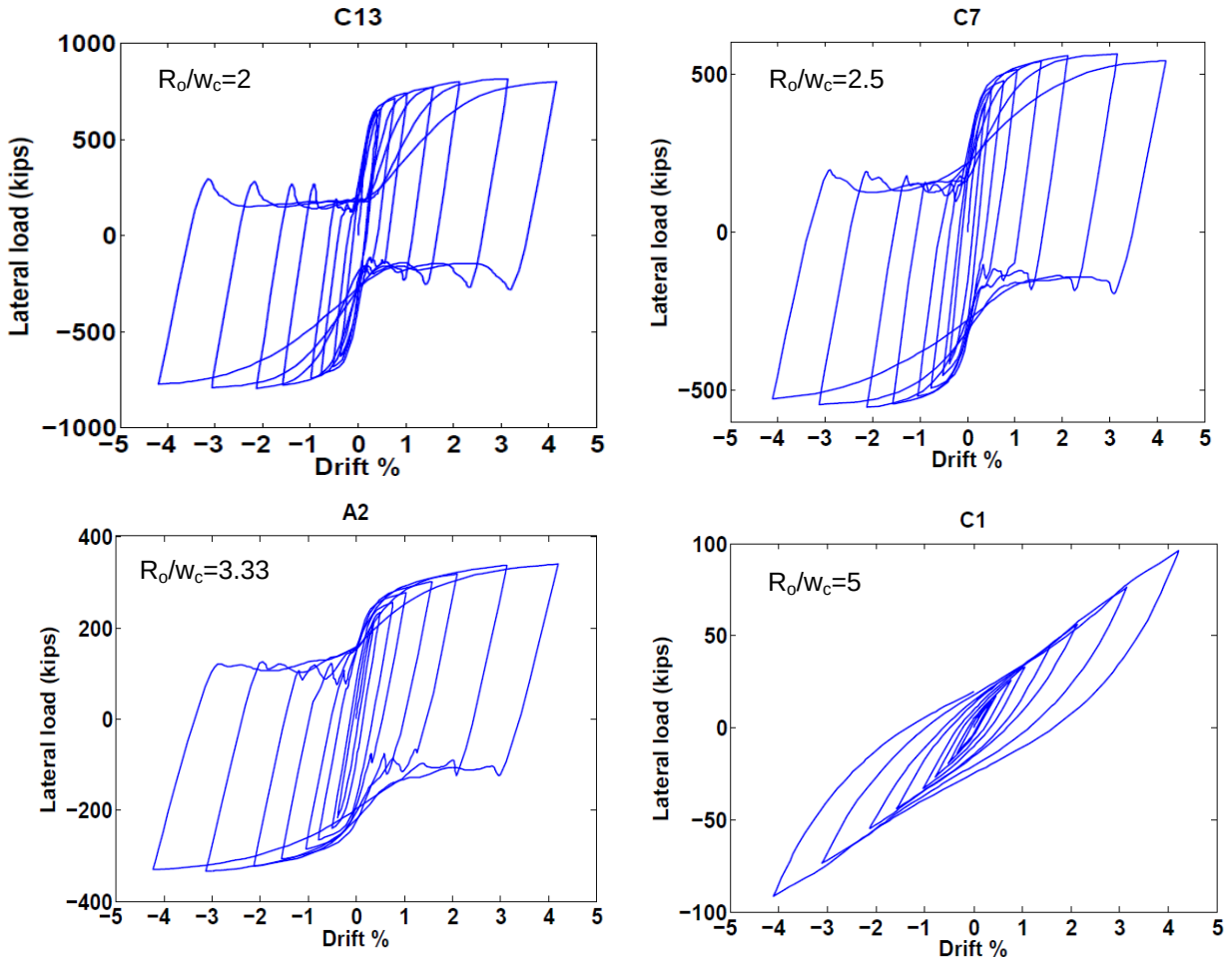

Figure 71: Figure showing the dependence of the hysteretic behavior on the ring width

The dependence of other input parameters on the system response will be further investigated in Section 8.4.3. with the help of trend plots.

8.4.2. Buckling ratio

As mentioned in Section 8.2.4, the buckling ratio of each specimen was derived from the discrete Fourier transform of the out-of-plane deformation data. The main goal of this exercise was to quantify the relative percentage of local torsional buckling and global tension field buckling in a BR-SPSW. The next paragraph presents the effectiveness of the method in decomposing the buckling modes.

Using the procedure mentioned in Section 8.2.4, the variation of out-of-plane deformation for Specimen A1 and A4 was generated as shown in Figure 72. The screen shot of the specimens show the out-of-plane deformation (U3) wherein blue and red color represents its maximum value in the positive and negative direction. Figure 72 shows the smooth wave-like variation of out-of-plane deformation in specimen A1 which is a result of global tension field buckling. In specimen A4, however, this variation sees minor disturbances as a result of lateral torsional buckling of the ring.

This difference in the variation of out-of-plane deformation is reflected in the FFT plots generated for the two sets of data as shown in Figure 73. The smooth variation with little or no disturbance (specimen A1) translates to Fourier transform with a prominent wavelength of high magnitude. Major disturbances in this curve would result in more than one prominent peak in the FFT plots corresponding to the major wavelengths forming the curve. The ratio of the magnitudes of the first peak and the second peak is thus a crude, albeit effective way of measuring the deviation from the smooth wave-like variation of out-of-plane deformation. This ratio, referred to as the buckling ratio in this text, is thus indicative of the relative percentage of the global and local buckling in BR-SPSW.

As indicated in the Figure 73, the buckling ratio for specimen A1 is much higher (33.3) as compared to its thinner counterpart A4 with a buckling ratio of 8.5. This is expected because the ring units in A4 have a much higher R_o/t (ring slenderness ratio). This results in local torsional buckling of the rings. Another important observation that can be made from Figure 73 is that the

most prominent wavelength obtained from the FFT plots is almost of the order of the width of the plate. Similarly, the second prominent wavelength is of the order of the ring diameter.

The dependence of the buckling ratio on other input parameters has been discussed in detail in the Section 8.4.3.

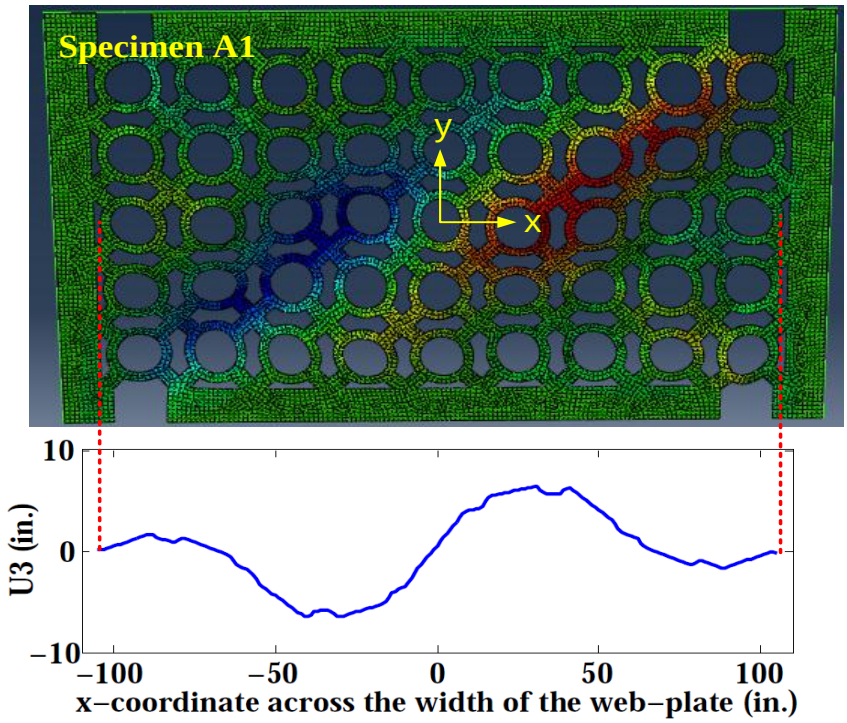

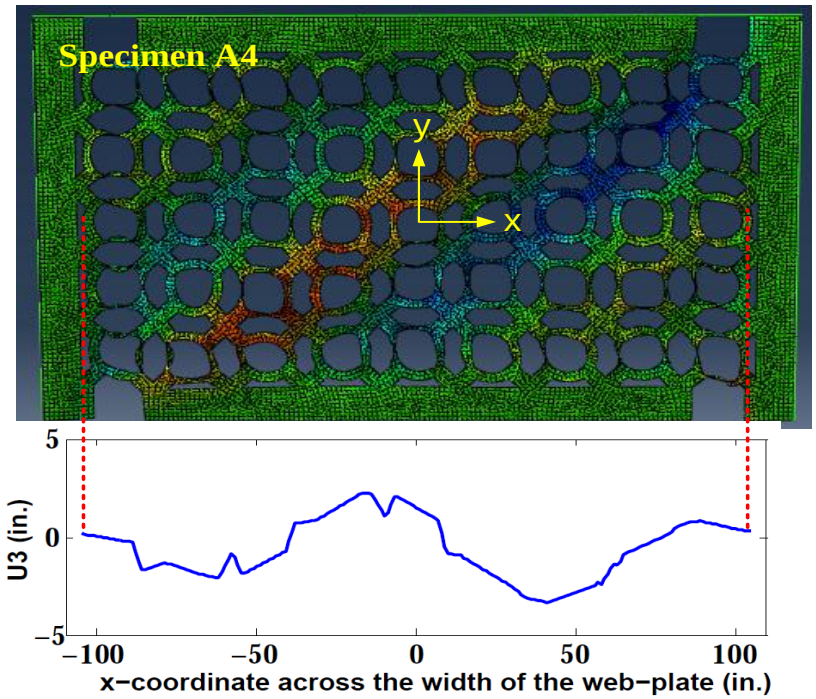

Figure 72: Variation of out-of-plane deformation across the width of the web-plate

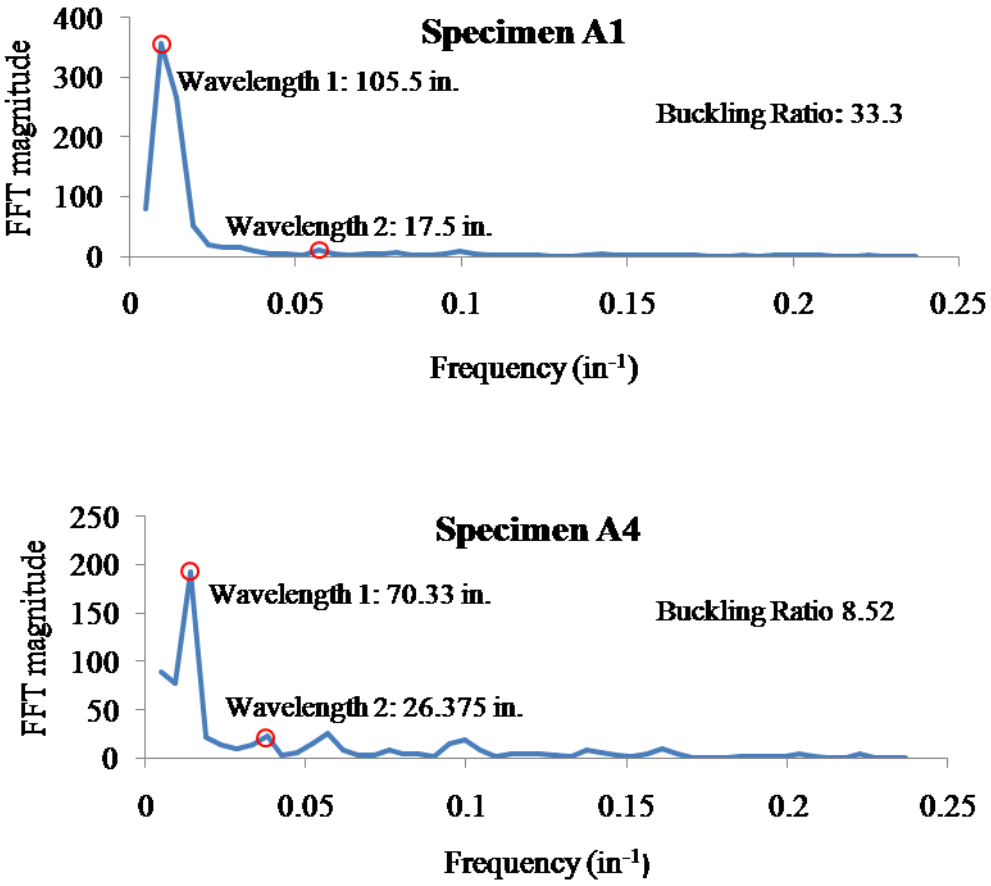

Figure 73: Discrete Fourier Transform for Specimen A1 and A4

8.4.3. Trend plots

Based on the output parameters recorded for each specimen in the parametric study, a set of trend plots were generated. These plots captured the behavioral trends of each output parameter with respect to the pre-defined set of input parameters. The following section discusses the major trend plots and draws conclusions associated with each output parameter individually. All the trend plots are compiled in Appendix A.

8.4.3.1. Strength

Figure 74, Figure 75 and Figure 76 demonstrate the influence of various geometric features on the strength of the full wall.

- For a fixed R_o/w_c and R_o/w_l ratios, the strength per ring (strength of the full wall divided by the number of rings in a horizontal row increases significantly with the increase in the

plate thickness. This effect slowly decreases as the radius of the ring decreases. This is evident from Figure 74, where a 5/16th inch increase in the plate thickness (from 5/16th in. to 5/8th in.), results in 175% increases in the strength/ring for a 24 inch radius shear plate. This increase is, however relatively small for an 8 inch radius (110%).

- For a given ring radius and link width, it was concluded that both R_o/t and R_o/w_c ratios affect the strength/ ring significantly. From Figure 75, it was concluded that increase in both R_o/t and R_o/w_c ratios have depreciating effect on the strength of a unit ring. Since the radius is fixed here, the decreasing strength of the ring with the R_o/w_c merely suggest that decreasing the width of the ring will result in lower strength/unit ring
- For a fixed ring radius and ring width, the strength/ring slightly decreases with the width of the link. This is due to the slight shift in the position of the plastic hinges. This dependence of the width of the link on strength is reflected in Equation 5.70. This effect is negligible as the thickness of the plate decreases. Also, comparing Figure 75 and Figure 76 it can be concluded that as compared to the width of the link, width of the ring has a larger influence on the ring unit strength. For example, for a R_o/t of 20, a 0.5 increase in R_o/w_c results in 31% decrease in strength. A similar increase in R_o/w_l, results in only 16% decrease in strength/ring unit.

From design point of view, the trend charts presented below could act as a tool for designing plates with desired strength. Typically, higher strength can be obtained by using thicker web plates. While this is still true, the biggest advantage of BR-SPSW is that higher strength can still be achieved by varying other geometric parameters. Conversely, if a thicker plate is easily available, it can still be used in cases of lower load demands by altering other geometrical features.

For example, as shown in Figure 74, a strength of 25 kips / ring can be achieved using R_o=24" &t=1/4", R_o=24" & t=0.5", or R_o=8" & t=5/8" along with fixed values of R_o/w_c=3.33 and R_o/w_l=2.0. The choice between these configurations might be based on stiffness or hysteretic energy absorption. However, since this is stated in strength per ring, the size of the full panel and number of rings in the full panel must also be considered.

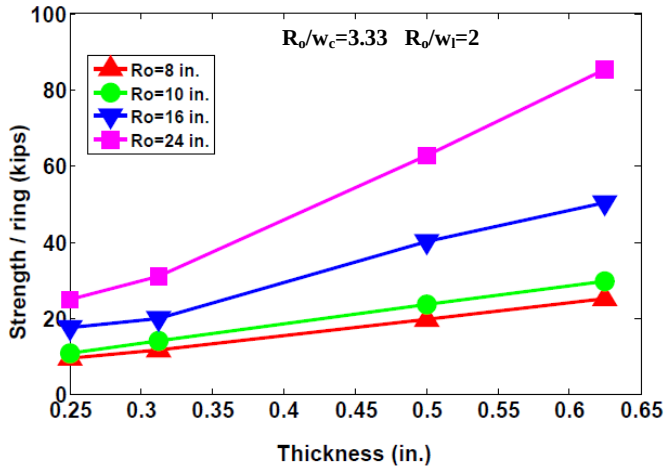

Figure 74: Effect of web plate thickness and radius on strength/ring

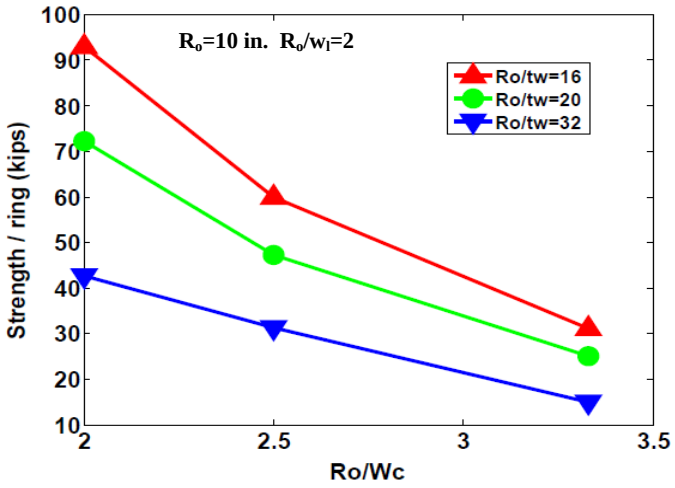

Figure 75: Effect of R_o/w_c and R_o/t ratios on strength/ring unit

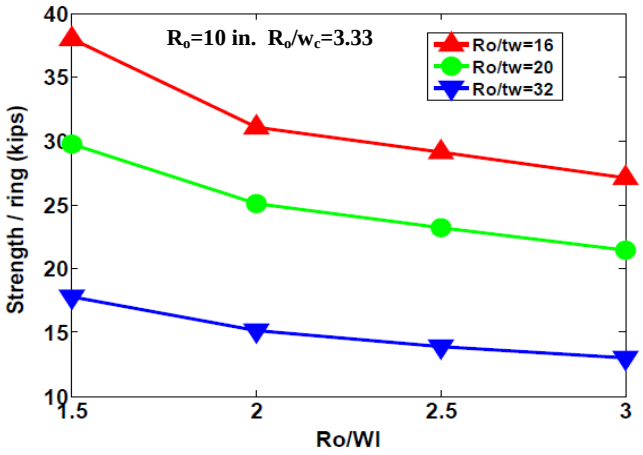

Figure 76: Effect of R_o/w_l and R_o/t ratios on strength/ring unit

8.4.3.2. Stiffness

Figure 77, Figure 78 and Figure 79 demonstrate the influence of various geometric features on the strength of the full wall.

- For a fixed R_o/w_c and R_o/w_l ratios, the stiffness per ring increases linearly with the increase in the plate thickness. As shown in Figure 77. An increase of 3/8th inch in the plate thickness results in about 150% increase in the stiffness/ring. For smaller radii, the stiffness/ring does not change much with thickness.
- As previously concluded in the case of strength, for a given ring radius and link width, both R_o/t and R_o/w_c ratios affect the strength/ ring significantly. From Figure 78, it was concluded that increase in both R_o/t and R_o/w_c ratios have depreciating effect on the stiffness of a unit ring. Since the radius is fixed here, the decreasing stiffness of the ring with the R_o/w_c merely suggest that decreasing the width of the ring will result in lower stiffness/unit ring

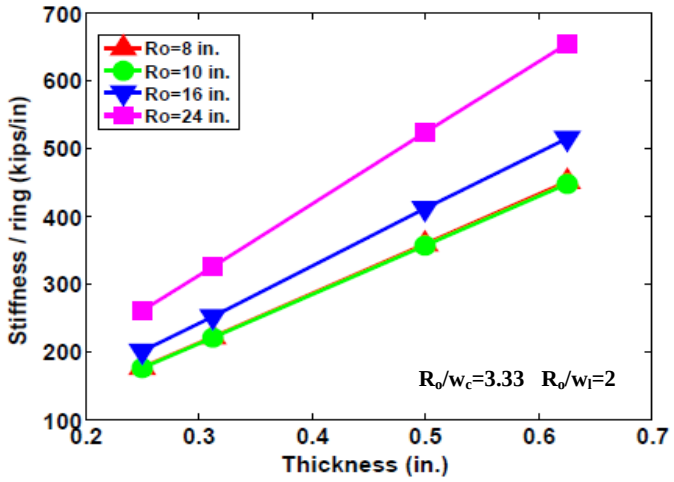

Figure 77: Effect of web plate thickness and radius on stiffness/ring

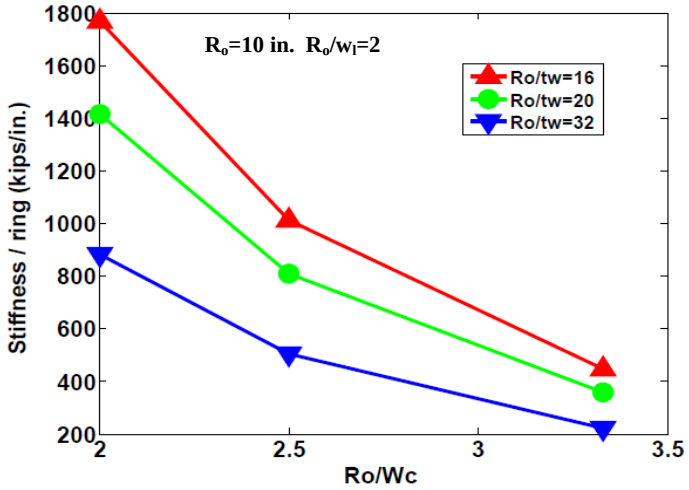

Figure 78: Effect of R_o/w_c and R_o/t ratios on the stiffness/ring

- For a fixed ring radius and ring width, the stiffness/ring slightly decreases with the width of the link. This effect is decreases as the thickness of the plate decreases. Also, comparing Figure 78 and Figure 79, it can be concluded that as compared to the width of the link, width of the ring has a larger influence on the ring unit stiffness. For example, for a R_o/t of 20, a 0.5 increase in R_o/w_c results in 42% decrease in stiffness. A similar increase in R_o/w_l, results in only 26% decrease in stiffness/ring unit.

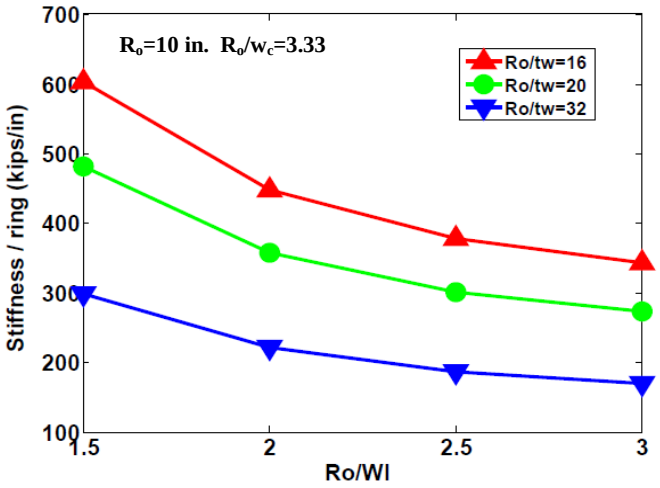

Figure 79: Effect of R_o/w_l and R_o/t on stiffness/ring

As observed from section 8.4.3.1 and 8.4.3.2, strength and stiffness per ring of BR-SPSW have similar behavioral trends with respect to the major input parameters. It is therefore difficult to separately tune strength and stiffness per ring. However, as per the analytical solutions derived for the strength and stiffness of the full wall, it can be concluded the number of rings in BR-SPSW does not have the same influence on the aforementioned output parameters (refer Eq. 5.70 and 6.22). Thus strength and stiffness of the full wall can be separately tuned by changing number of rings in rows and/or columns. This can be done either by using a specific shear wall outer dimension or by changing the length of the links.

8.4.3.3. Total energy dissipation

- In this section, Figure 80, Figure 81 and Figure 83 have been used to demonstrate the influence of various geometric features on the strength of the full wall. For fixed R_o/w_c and R_o/w_l ratios, total dissipated energy increases significantly with increase in thickness. In Figure 80, for a SPSW with a 10 inch outer radius, an increase of $3/8^{th}$ inch results in about 350% increase in the total dissipated energy. This is increase is due to the fact that increase in web plate thickness delays buckling and improves the hysteretic response of the BR-SPSW. Another conclusion that can be drawn from Figure 80 is that web plates with lower radii rings dissipate relatively more energy than the ones with larger radii. This phenomenon is explained in subsequent sections in detail.

- For a fixed R_o/w_l and R_o/w_c ratio, total dissipated energy drastically decreases with an increase in the ring slenderness ratio (R_o/t) as shown in Figure 81. The energy dissipation in thinner plates however does not exhibit much dependence on the slenderness ratio. This is because unlike in thin plates where buckling is majorly local in nature, in thicker plates, energy dissipation is governed by mode of buckling. A plate with larger radii exhibit lateral torsional buckling of the rings as opposed to the global tension field buckling. The former type of buckling has been shown to dissipate lower energy. This has been elaborated in Section 8.4.3.4.
- For a fixed ring radius and ring width, total energy dissipation gradually decreases with the width of the link as shown in Figure 82. However, for thinner plates, width of the link does not have much influence on energy dissipation.

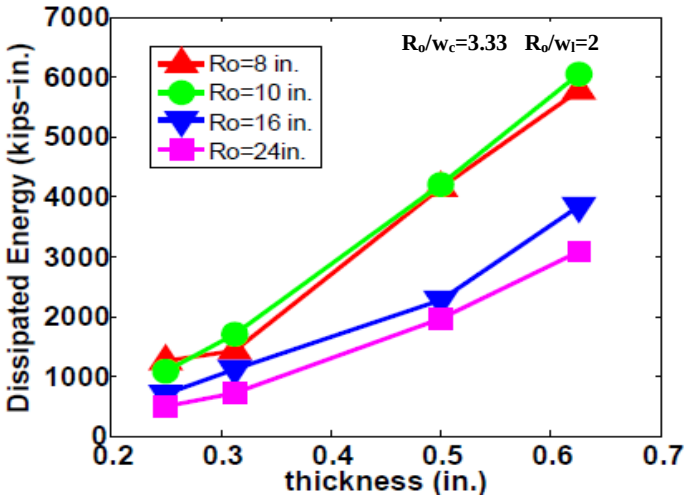

Figure 80: Effect of thickness and radius on total dissipated energy

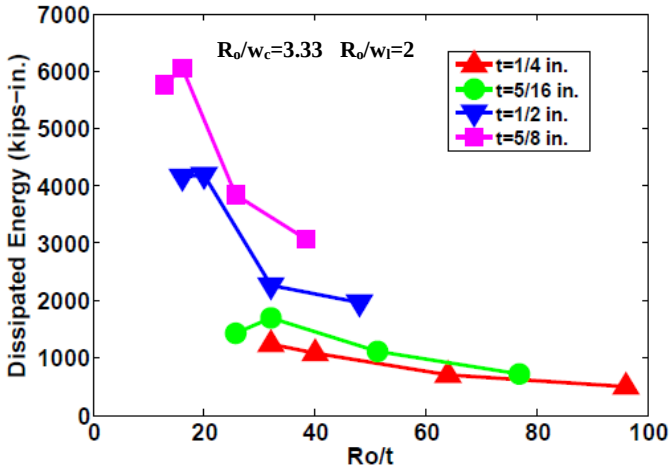

Figure 81: Effect of R_o/t on the total dissipated energy

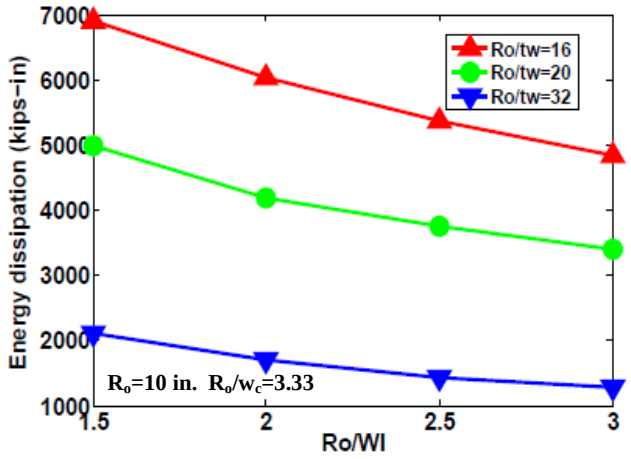

Figure 82: Effect of R_o/w_l on total dissipated energy

- Similarly, for a fixed ring radius and link width, total energy dissipation gradually decreases with the width of the ring as shown in Figure 83. However, for thinner plates, width of the ring does not have much influence on energy dissipation. However, as compared to the width of the link, width of the ring has a larger influence on the total dissipated energy. For example, for R_o/t of 16, a 0.5 increase in R_o/w_c resulted in 25% decrease in the total dissipated energy. A similar increase in R_o/w_l, results in only 15% decrease in total dissipated energy.

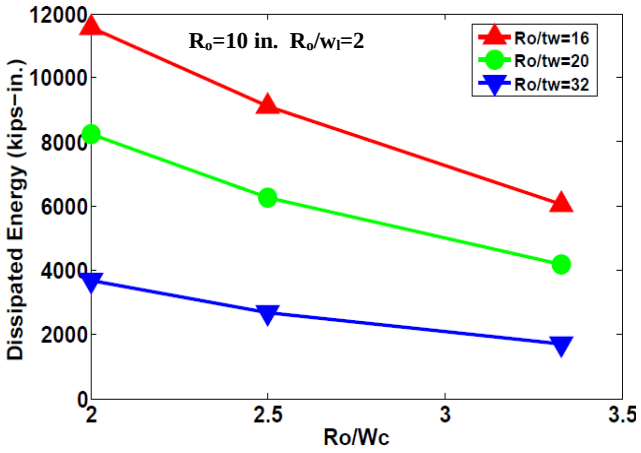

Figure 83: Effect of R_o/w_c on total dissipated energy

8.4.3.4. Energy dissipation ratio

This section highlights the influence of input parameters on the energy dissipation ratio with the help of Figure 84, Figure 85 and Figure 86.

- For a fixed R_o/w_c and Ro/w_l ratios, the trend plot shown in Figure 84 seems to form two separate groups, with the smaller radii plates having higher energy dissipation ratio and the larger radii plates having a much smaller energy dissipation ratio. This trend can be attributed to two different forms of buckling that the plates undergo to resist lateral loading. Plates with smaller radii ring units mostly exhibited global-tension field buckling whereas, the ones with larger radii rings exhibited lateral torsional buckling of the rings. On the ring level, onset of local torsional buckling results in reduction of load-carrying capacity and stiffness of a ring. Moreover, the ring does not properly elongate into an ellipse, which was the main concept behind the BR-SPSW. Needless to say, this deterioration of the ring behavior when translated to the full wall results in pinched hysteretic behavior. Therefore, separate two groups are observed in the trend plot.
- Figure 84 also shows that that increase in the web plate thickness results in higher energy dissipation ratio implying that thicker plates experience delayed buckling and thus exhibit relatively fuller hysteretic behavior. Thinner plates suffer from lateral torsional buckling of the rings, which results in slight pinching in the hysteresis curve.
- Both R_o/w_c and R_o/t ratios influence the energy dissipation ratio as shown in Figure 85. Increasing the ring slenderness ratio (R_o/t) decreases the energy dissipation ratio

considerably. It can also be concluded from Figure 85 that increasing the width of the ring reduces the energy dissipation ratio. This happens because a wider ring buckles in a lateral torsional mode, which results in a much lower energy dissipation than the specimen with narrow rings.

- For a fixed ring radius and ring width, width of the link has negligible effect on the energy dissipation ratio of the wall. This effect is clear from Figure 86. This result is extremely important because in Section 4.1, it was conjectured that the reducing the yielding of the link geometry result in increasing the fullness of the hysteretic behavior. Yet Figure 86 shows that link width doesn't have much influence on the hysteretic behavior.

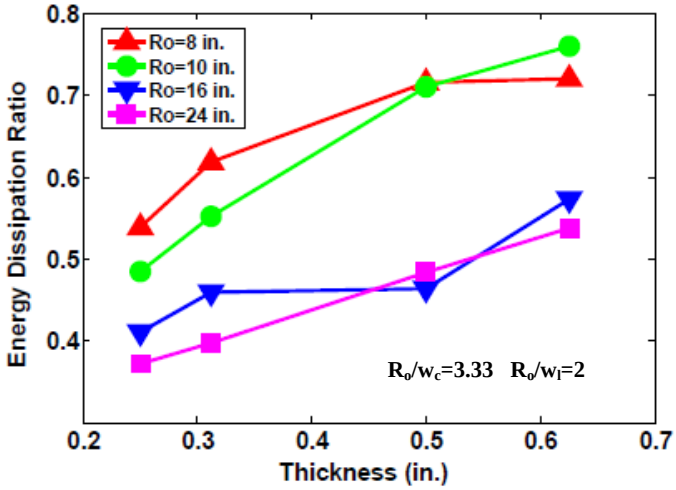

Figure 84: Effect of thickness and radius on energy dissipation ratio

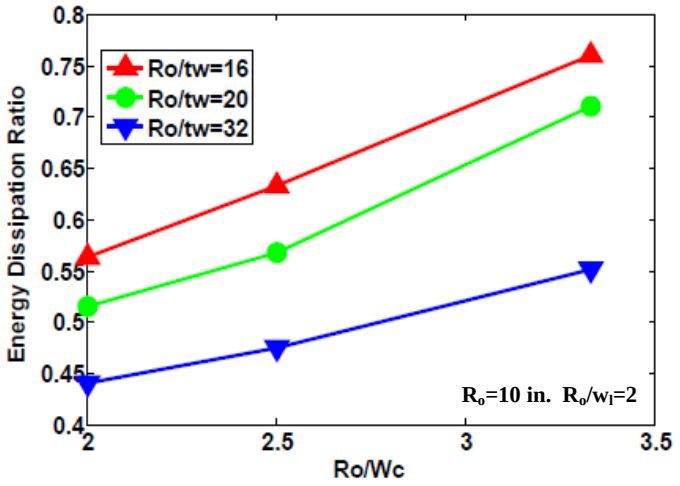

Figure 85: Effect of R_o/w_c and R_o/t on energy dissipation ratio

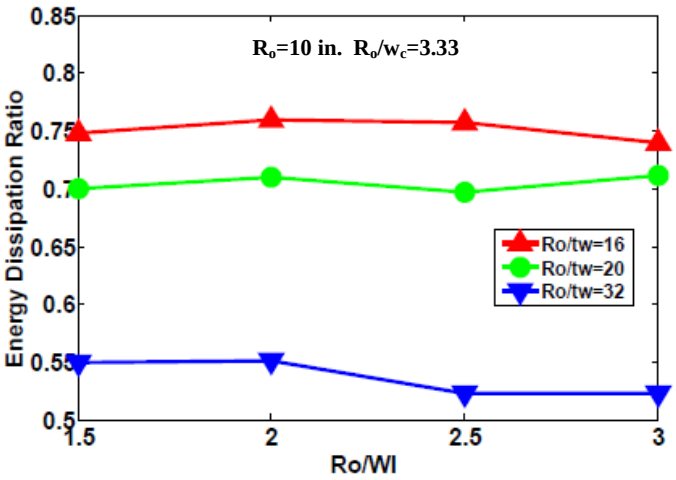

Figure 86: Effect of R_o/w_l on energy dissipation ratio

8.4.3.5. Buckling ratio

Figure 87, Figure 88 and Figure 89 demonstrate the influence of the major input parameters on the buckling ratio.

- For a fixed R_o/w_c and Ro/w_l ratios, buckling ratio increases with web plate thickness. This implies that thicker plates tend to exhibit global tension field buckling as opposed to lateral torsional buckling of the rings which is local in nature. For larger radii plates however, thickness has negligible influence on the buckling radii. This implies that irrespective of the thickness, these plates suffer from lateral torsional buckling of the rings and thus exhibit very low buckling ratio. This trend is shown in Figure 87.

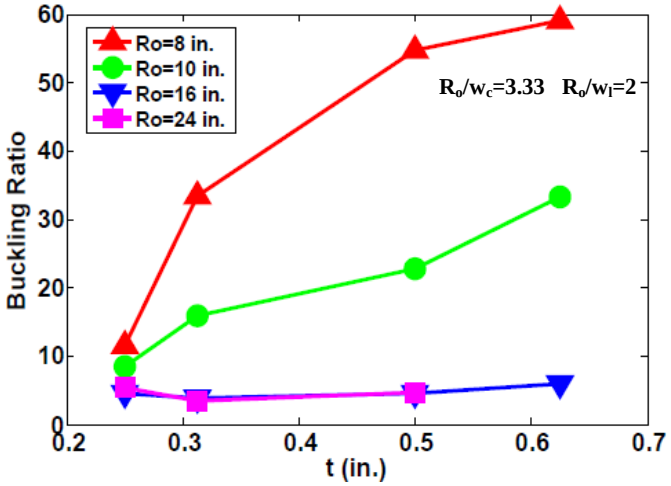

Figure 87: Effect of radius and thickness on buckling ratio

- For a fixed R_o/w_c and R_o/w_l ratios, buckling ratio decreases drastically with the slenderness ratios (w_c/t, R_o/t) as shown in Figure 88 and Figure 89.
- For a fixed ring radius and ring width, buckling ratio almost increases exponentially as the width of the ring decreases implying that wider rings can easily undergo lateral torsional buckling. This trend is shown in Figure 90.

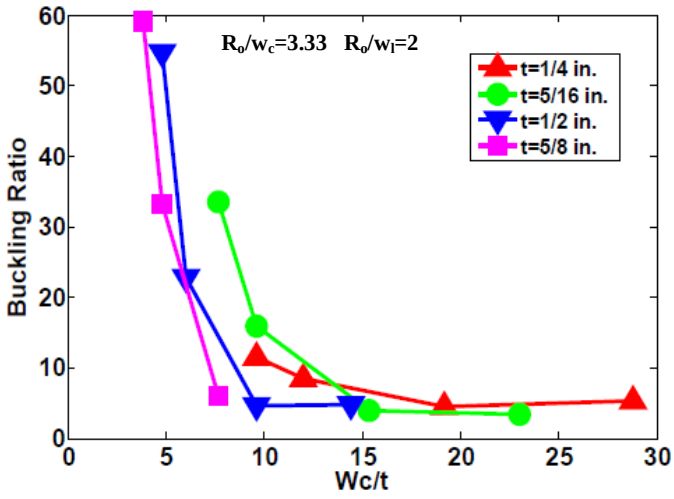

Figure 88: Effect of w_c/t on buckling ratio

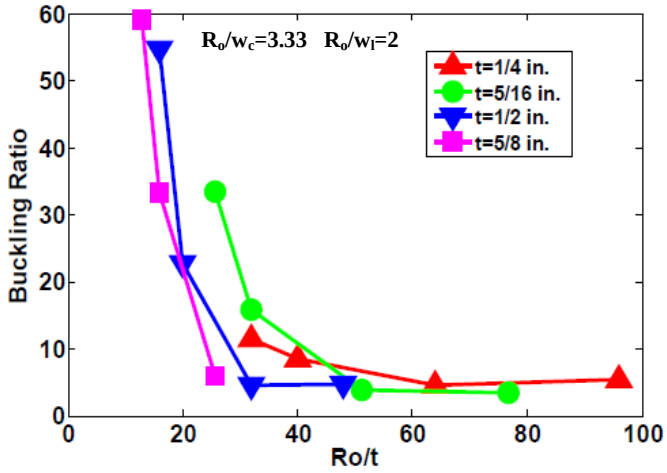

Figure 89: Effect of R_o/t on buckling ratio

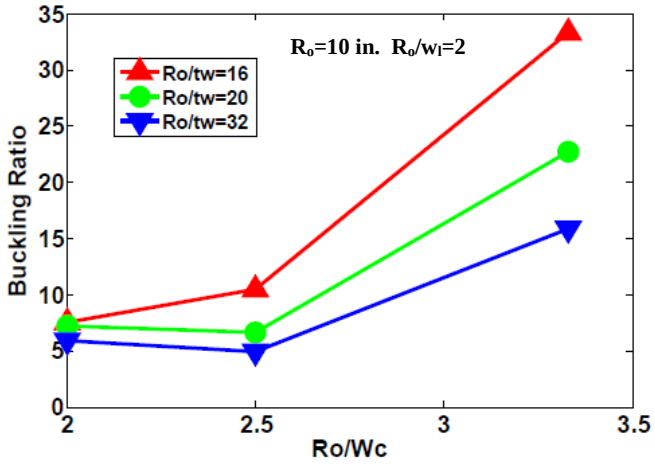

Figure 90: Effect of R_o/w_c and R_o/t on buckling ratio

8.4.3.6. Length of cut

- For a fixed R_o/w_c and R_o/w_l ratios, length of the cut exponentially decreases with an increase in the ring radius as shown in Figure 91. Since cost of cutting is directly proportional to the length of the cut, using a 16in. radius ring instead of 8 in. ring, for example, would result in about 45% reduction in the cutting cost.

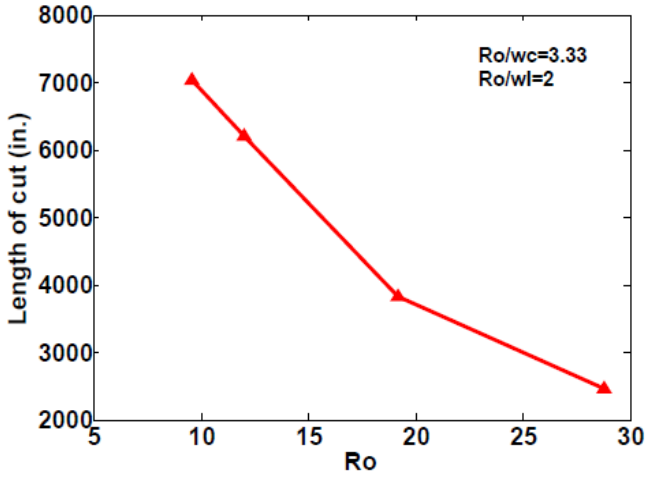

Figure 91: Effect of ring radius on the length of cut

- For a fixed ring radius and ring width, length of the cut exponentially increases as the width of the link decreases as a shown in Figure 92. However this increase is not substantial (a 0.5 increase in R_o/w_l only increases the cutting length by 5%).
- Similarly, for a fixed ring radius and link width, length of the cut exponentially increases as the width of the ring decreases as shown in Figure 93. However this increase is not substantial. (0.5 increase in R_o/w_c ratio increases the cutting length by less than 5%).

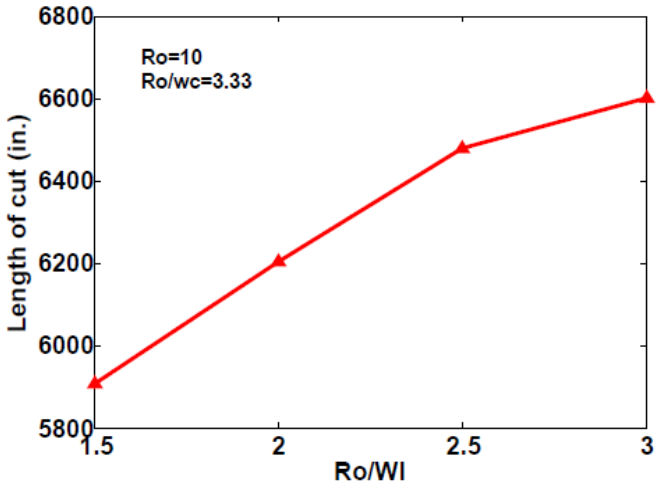

Figure 92: Effect of R_o/w_l on the length of cut

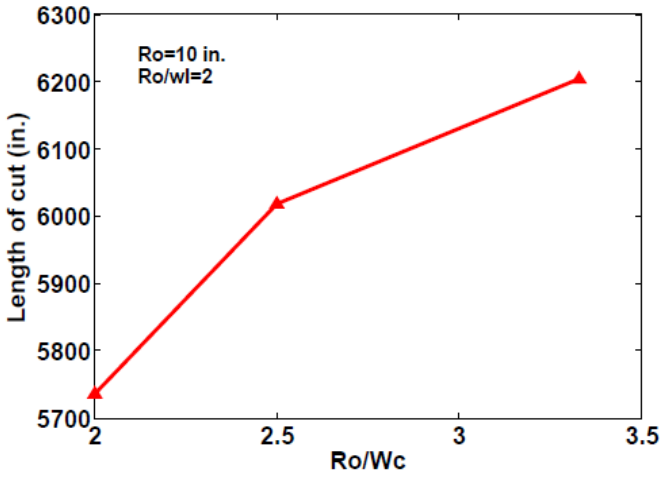

Figure 93: Effect of R_o/w_c on the length of cut

8.4.3.7. Yield drift

- For a fixed R_o/w_c and R_o/w_l ratios, yield drift of the shear wall increases with web plate thickness as shown in Figure 94. For a large radius, this increase can be as much as 50%, however, as the radius of the ring decreases, this increase is not significant (only 6% for 8 inch radius ring).
- For a given radius and link width, yield drift of the shear wall does not depend significantly on the slenderness ratio R_o/t. It, however, linearly increases as the width of the ring decreases. This trend is shown in Figure 95.
- For a fixed R_o/w_c and R_o/w_l ratios, yield drift drastically decreases with the slenderness ratio w_c/t and R_o/t as shown in Figure 96 and Figure 97.

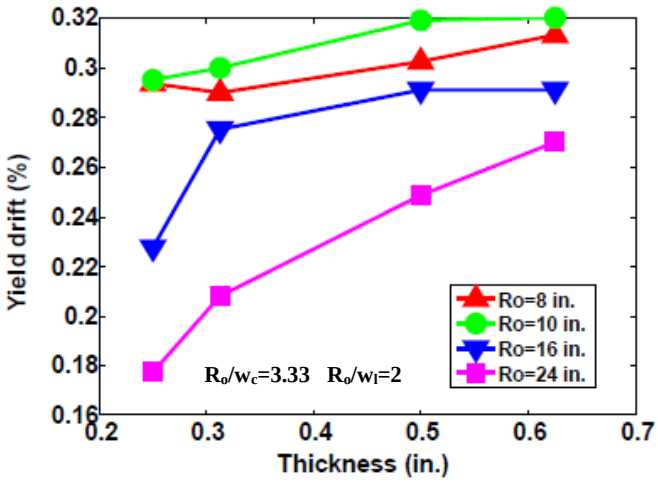

Figure 94: Effect of thickness and radius on yield drift

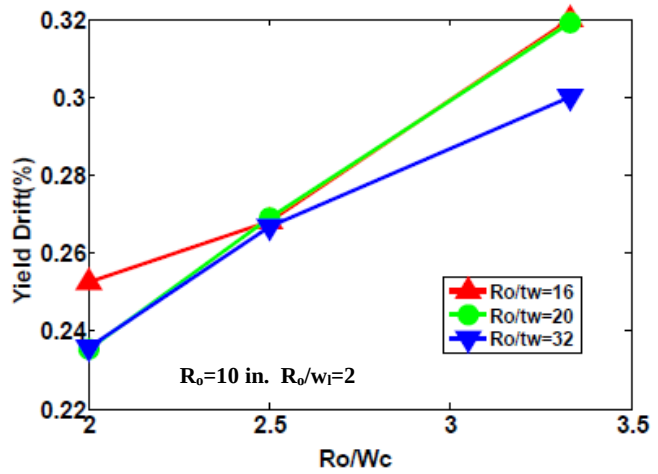

Figure 95: Effect of R_o/w_c and R_o/t on yield drift

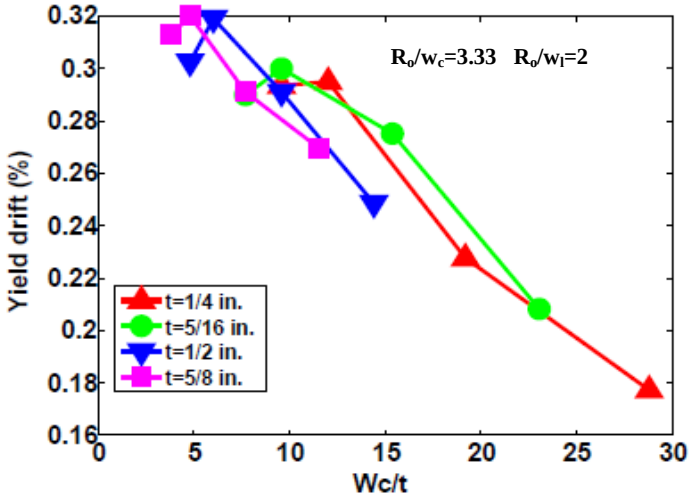

Figure 96: Effect of w_c/t on yield drift

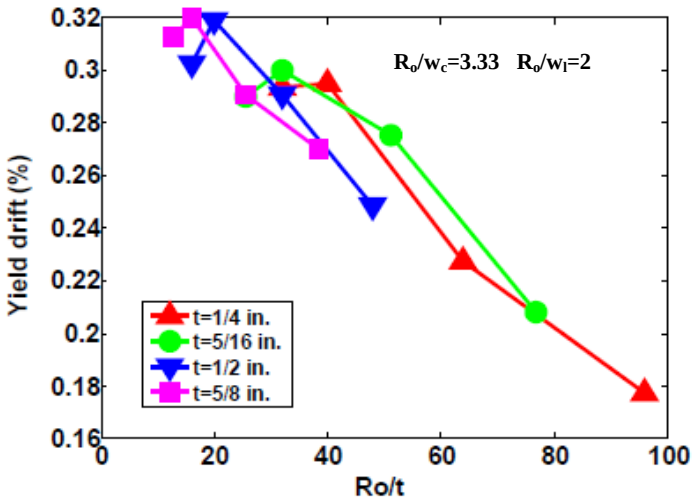

Figure 97: Effect of R_o/t on yield drift

The output parameters recorded for each specimen is summarized in Table 16. Note that some tests were deleted from the test matrix because the ABAQUS analysis for those specimens got aborted due to convergence issues.

Table 16: Output parameters for the test specimens of SERIES A

	Strength (kips)	Peak Strength (kips)	Stiffness (kips/in)	Yield Drift (%)	Length of cut (inches)	Open-ness of the wall (in^2)	Energy dissipation (kips-in)	Energy Dissipation Ratio	Weight Ratio	Buckling ratio
A1	280	465	582	0.32	6204	13327	6047	0.76	6.76	33.3
A2	226	339	464	0.319	6204	13327	4190	0.71	6.8	22.76
A3	136	166	288	0.3	6204	13327	1697	0.55	7.19	15.85
A4	110	119	230	0.295	6204	13327	1073	0.49	7.49	8.53

Table 17: Output parameters for the test specimens of SERIES B

	Strength (kips)	Peak Strength (kips)	Stiffness (kips/in)	Yield Drift (%)	Length of cut (inches)	Open-ness of the wall (in^2)	Energy dissipation (kips-in)	Energy Dissipation Ratio	Weight Ratio	Buckling ratio
B1	200	213	524	0.249	2464	13009	1960	0.48	7.849	4.68
B2	265	353	601	0.291	3818	14455	3835	0.57	6.81	5.93
B3	127	173	278	0.29	7124	14455	1420	0.62	7.315	33.49
B4	260	290	654	0.27	2464	13009	3070	0.54	7.18	3.78
B5	213	253	480	0.291	3818	14455	2268	0.46	6.82	4.55
B6	107	94	235	0.228	3818	14455	704	0.41	6.37	4.51
B7	267	465	565	0.313	7029	14647	5765	0.69	6.73	59.15
B8	100	123	222	0.294	7029	14647	1243	0.54	7.24	11.55
B9	213	350	450	0.303	7029	14647	4154	0.72	6.94	54.7
B10	123	126.41	294	0.275	3818	14455	1106	0.46	7.351	3.85
B11	68	87.78	261	0.177	2464	13009	493	0.37	11.06	5.36
B12	98	117	326	0.208	2464	13009	711	0.4	9.406	3.4

Table 18: Output parameters for the test specimens of SERIES C

	Strength (kips)	Peak Strength (kips)	Stiffness (kips/in)	Yield Drift (%)	Length of cut (inches)	Open-ness of the wall (in^2)	Energy dissipation (kips-in)	Energy Dissipation Ratio	Weight Ratio	Buckling ratio
C2	475	543	1258	0.253	3667	12887	5733	0.53	4.0399	4.95
C4	530	774	1318	0.268	6018	11162	9118	0.63	3.9	10.45
C5	93	103	168	0.339	3969	16263	1519	0.73	15.25	12.29
C7	426	561	1052	0.269	6017	11162	6254	0.57	3.91	6.65
C8	482	749	1207	0.251	6727	13079	8472	0.65	3.89	34.86
C9	377	556	963	0.264	6823	12887	6143	0.64	4.045	16.42
C10	259	283	655	0.267	6017	11162	2673	0.48	3.968	4.95
C12	384	410	1148	0.236	5735	9607	3691	0.44	2.73	5.95
C13	650	812	1841	0.235	5735	9607	8251	0.52	2.73	7.23
C14	837	1127	2302	0.253	5735	9607	11570	0.56	2.54	7.55
C15	342	558	784	0.303	5907	9956	6914	0.75	6.148	17.63
C16	268	417	625	0.298	5907	9956	4994	0.7	6.2743	15.23
C17	160	203	388	0.287	5907	9956	2107	0.55	6.5525	12.55
C18	262	418	491	0.37	6480	14322	5379	0.76	6.6058	48.15
C19	209	300	391	0.371	6480	14322	3756	0.7	6.6091	24.52
C20	125	149	242	0.358	6480	14322	1429	0.52	6.9245	7.83
C21	244	382	446	0.38	6601	15158	4842	0.74	6.7911	14.46
C22	193	275	355	0.377	6601	15158	3405	0.71	6.874	12.59
C23	117	135	220	0.369	6601	15158	1285	0.52	7.0767	9.54

Table 19: Output parameters for the test specimens of SERIES D

	Strength (kips)	Peak Strength (kips)	Stiffness (kips/in)	Yield Drift (%)	Length of cut (inches)	Open-ness of the wall (in^2)	Energy dissipation (kips-in)	Energy Dissipation Ratio	Weight Ratio	Buckling ratio
D1	244	383	445	0.345	6601	15158	4974	0.74	7.4	17.11
D2	561	647	1548	0.245	3545	10875	6854	0.53	3.7	21.38
D4	196	235	507	0.259	7046	15175	2339	0.5	4.41	8.97
D5	257	425	593	0.29	6709	12338	4956	0.69	6.119	22.64
D6	244	287	696	0.248	2367	10868	2473	0.47	6.5	11.68
D7	323	474	818	0.263	7046	15175	5061	0.6	3.94	20.28
D8	357	477	880	0.273	6318	13321	5222	0.57	4.2	20.12
D9	379	510	948	0.268	6197	12485	5762	0.59	4.12	6.09
D10	348	506	886	0.263	6919	14366	5561	0.63	4.1	20.13
D11	374	397	1006	0.259	3667	12887	4819	0.61	3.95	3.68
D12	331	362	885	0.264	3763	14212	3049	0.43	4.12	2.76
D13	319	345	833	0.268	3827	15055	3337	0.5	4.13	3.93

8.5. COMPARATIVE ANALYSIS: SPSW AND BR-SPSW

To compare the behavior of BR-SPSW with a typical steel plate shear wall, finite element analysis on a solid plate was performed. The boundary elements were identical to the ones used for the analysis of BR-SPSW. The thicknesses of the solid plates were chosen such that their strengths were comparable to one of the specimens from the parametric study. Note that the strength of the typical SPSW was calculated using Equation 8.3.

Figure 98 shows the comparison of hysteretic behavior of BR-SPSW (specimen C4 with 5/8'' thick web plate, 10'' outer radius, R_o/w_c ratio of 2.5 and R_o/w_l ratio of 2) and a typical SPSW with 0.12 in. thick web plate. BR-SPSW, very distinctly have much less pinching in the hysteresis curve as compared to the SPSW. This is indicative of the fact the there is a huge lag in the resistance of the web plate in SPSW when the tension field changes direction during the load reversals. This results in substantial decrease in the energy dissipation of the SPSW. As compared to an energy dissipation ratio of 0.63 for specimen C4, 0.12 in. web plate shear wall has an energy dissipation ratio of only 0.38 (refer Figure 99). In absolute terms, SPSW dissipates about 26% less energy than BR-SPSW but its efficiency as compared to an ideal specimen (full hysteresis curve), is 40% less than BR-SPSW.

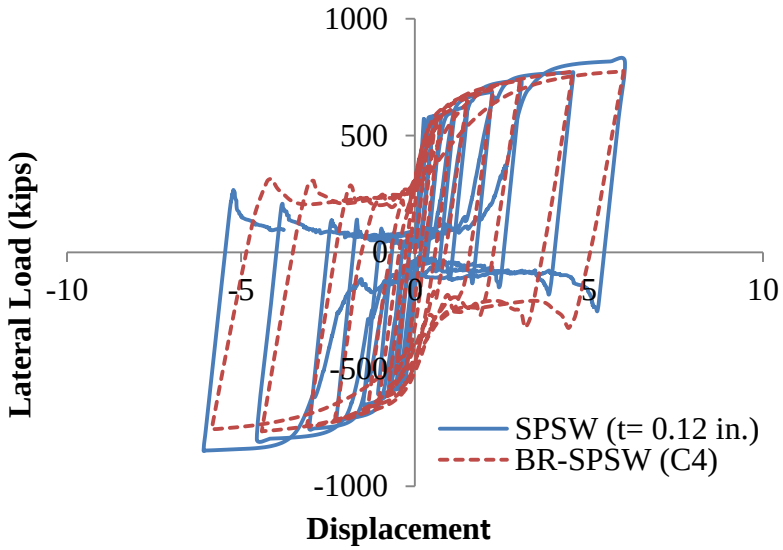

Figure 98: Comparison of hysteretic behavior of BR-SPSW and SPSW

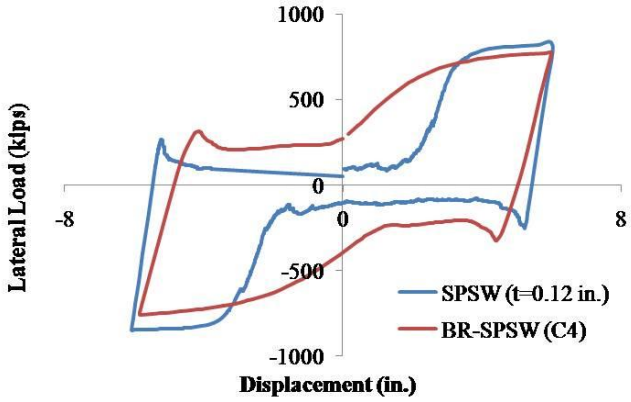

Figure 99: Last cycles comparing the total energy dissipation for BR-SPSW and SPSW

8.6. ANALYTICAL VS. COMPUTATIONAL RESULTS

This section focuses on the comparison of computational results obtained from the parametric study to the predicted results from the analytical solution. The equations derived in Chapter 6 and Chapter 7 was used to predict the strength and stiffness of BR-SPSW. The next two subsections highlight the comparison of the computational results to the predicted strength and stiffness of the full wall respectively.

8.6.1. Comparison of strength of the full wall

This section highlights the accuracy of the analytical model in predicting the strength of the specimens in parametric study. Recall that several mechanisms were investigated while deriving the equation for the strength of the full wall (refer Chapter 6). However, using the computational results from the preliminary investigations it was concluded that Mechanism-IV predicts the strength of full wall fairly accurately. Therefore, the equation for strength using Mechanism- IV has been used in this section (Equation 5.70) for comparison against the computational results.

Figure 100 shows the percent error in the predicted strength of the full wall as compared to the FE modeling results. For the majority of the specimens the error was within 18%. No prominent trends were observed in the error. Therefore, high percent of error (a maximum of 28%) in a few specimens may be due to the method used in recording the strength from the FE modeling results. Another source of error could be the assumption that the links do not experience inelastic deformation. While the links staying elastic is an ideal situation, yielding of the links is not highly improbable, especially in the specimens with very narrow links.

Figure 100 also shows that the proposed analytical solution provides a conservative estimate of the strength of the full wall. This implies that the prediction for strength will produce results that are on average 8% (with a standard deviation of 8.9%) less than the observed yield strength of BR-SPSW.

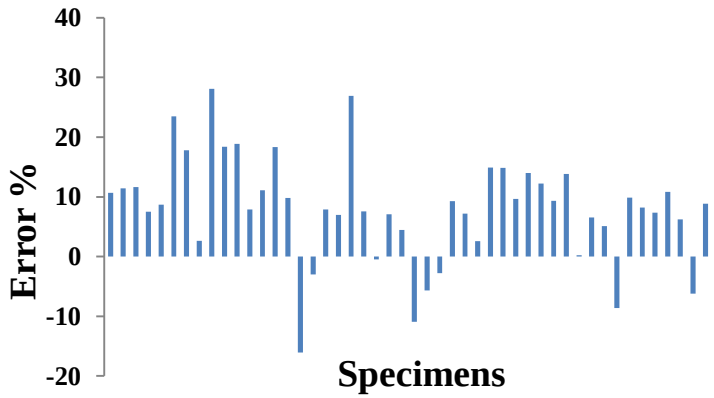

Figure 100: Percent error in the predicted strength as compared to the FE results

8.6.2. Comparison of stiffness of the full wall

This section highlights the accuracy of the analytical model in predicting the stiffness of the specimens in parametric study. The analytical model for the stiffness of the full wall was developed on the basis of two ring-unit models: constrained and unconstrained ting models. However, since the accuracy of the unconstrained ring model was restricted by fewer assumptions, it was decided that the solution based on unconstrained ring-model will be used for comparison to the computational results. The following paragraph discusses the accuracy of the analytical solution and the cases in which it fails to predict the stiffness of the full wall within a reasonable error limit.

Figure 101 shows that narrow links the predicted equation accurately predicts the stiffness of the full wall (within 15% error). However, as the R_o/w_l ratio decreases the percent error increases significantly. This major deviation from the FE results is due to the fact that the analytical solution ignores the width of the link and assumes the ring-link joint to be a point. Thus, wider the link gets, the more deviation is seen from the actual solution. It was also found that the proposed equation did not work well for very large radii plates (24 inches outer radius). Irrespective of the R_o/w_l ratio, all the specimens with 24 inches outer radius showed an error of more than 30%.Other geometrical parameters did not play a major role in the accuracy of the analytical model.

Additionally, it was also noted that the predicted stiffness was in most cases less than the actual stiffness of the wall. This observation can be attributed to the fact that the derived equation for stiffness does not include the stiffness of the links and the material at the boundary of the web plate. It was found that the analytical solution predicted the results which were on an average 17% less that the observed stiffness of the full wall.

The final conclusion drawn from this comparison was that the proposed analytical model can be used with good accuracy for R_o/w_l ratios less than 2 and for plates with ring radius of 16 inches or less.

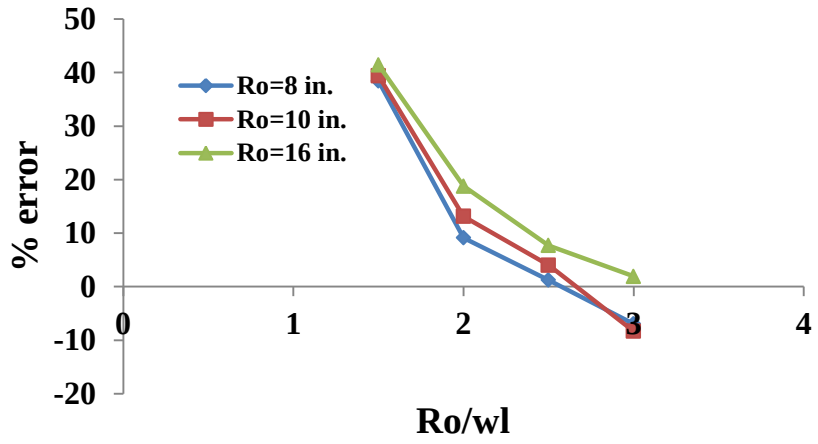

Figure 101: Plot showing the dependence of the accuracy of the analytical solution on Ro/wl ratio

Since the analytical solution for the stiffness of BR-SPSW presented earlier did not work well for some cases, an empirical equation was derived using the FE analysis data obtained from the parametric study. Stiffness data for a set of 47 specimens modeled in ABAQUS was used to derive this formula using multiple regression analysis.

$$K_{r,emp} = 15812.4 \times t^{1.3} \left(\frac{R_o}{w_l}\right)^{-3.4} \left(\frac{R_o}{t}\right)^{0.3} \left(\frac{w_c}{w_l}\right)^{2.7} \tag{8.1}$$

where, K_r is the stiffness per unit ring in kips/in. unit.

Stiffness of the full wall is given by,

$$K_{w,emp} = \frac{K_{r,emp}}{2N_c}(N_r + N_c - 1) \tag{8.2}$$

The regression model had R-squared value of 0.98 which is indicative of good fit to the data. The equation thus obtained predicted the full wall stiffness within 14% error. Note that this equation will work well for BR-SPSW with material properties similar to the one analyzed in the parametric study. Also, since the empirical equation is given in the form of stiffness per unit ring, it can be applied to shear walls of any dimension although the equation's accuracy has not yet been verified outside the range of variables included in this study.

CHAPTER 9
FRACTURE PREDICTION AND FUTURE WORK

This section details the various approaches used to predict failure of the BR-SPSW. Predicting fracture in the panel was challenging because of the complexity in the wall geometry and limitations in currently available fracture prediction capability. Two models based on the void growth mechanism which eventually leads to ductile fracture, have been discussed. Finally, a finite element analysis based method has been used to model cracks. Shortcoming and challenges of these approaches and recommendation for future work has been summarized.

9.1. SMCS MODEL

The initiation of ductile failure in steel is typically controlled by the growth and coalescence of microvoids that nucleate around secondary particles, such as carbides or sulfides in the steel matrix. Several models incorporate a combination of stress triaxiality and plastic strains to predict fracture. One such model, first proposed by Hancock and Mackenzie 1977, and further expanded by Panontin and Sheppard 1995, Rousselier 1987, Kanvinde and Deierlein 2006, and Chi, Kanvinde et al. 2006 predicts fracture when equivalent plastic strain at any continuum point exceeds a critical value. This failure criterion also referred stress modified critical strain (SMCS) criterion is given by Equation 9.1.

$$\bar{\varepsilon}^p > \bar{\varepsilon}^p{}_{critical} = \alpha . \exp(-1.5T) \tag{9.1}$$

In the above equation, T is the triaxiality ratio which is defined as the ratio of the equivalent or Von Mises stress to the mean stress and is given by:

$$T = \frac{Mean\ hydrostatic\ stresses}{Von\ Mises\ stress} = \frac{\sigma_m}{\bar{\sigma}} \tag{9.2}$$

α is a material parameter that quantifies a material's resistance to fracture. This parameter is calibrated based on circumferential notched tension (CNT) bars.

Another crude, albeit effective way for comparing the potential for ductile fracture for two configurations is to record their rupture index. The rupture index is defined as the ratio between the plastic equivalent strain index and the ductile fracture strain multiplied by the material constant α, such that,

$$RuptureIndex = \alpha \frac{PEEQ\ Index}{\varepsilon_f} = \frac{PEEQ\ Index}{\exp(-1.5\frac{\sigma_m}{\bar{\sigma}})} \tag{9.3}$$

PEEQ Index is defined as the equivalent plastic strain divided by the yield strain. This index is a measure for local ductility.

This model, however, was found to predict higher critical strains to failure (as compared to experimental results) at low stress triaxiality. This issue is further elaborated in the next section.

9.2. CVGM MODEL

The Cyclic Void Growth Model (CVGM) recently developed by Kanvinde and Deierlein (Kanvinde and Deierlein 2007), is a powerful tool for predicting fracture in ductile materials due to ULCF loading. Ultra Low Cycle fatigue (ULCF), defined as less than 20 cycles before fracture, is particularly important for earthquake structural engineering because the cyclic failure of steel structural components are often a result of fewer but severe loading cycles. Like monotonic ductile fracture, ULCF is caused by growth and coalescence of microscopic voids. However, the severe cyclic loading results in reversed plasticity which in turn degrades the fracture resistance of the material. CVGM extends upon a more widely used void growth model (VGM) developed by Rice and Tracey (Rice and Tracey 1969) and others (McClintock 1968) for monotonic ductile fracture.

The VGM uses a semi-empirical equation which predicts the growth rate of a single spherical void in an infinitely large, three-dimensional, and elastic perfectly plastic solid. This equation relates the growth rate of the void radius *dR/R*, to the triaxiality of the stress state (and the incremental equivalent plastic strain, $d\bar{\epsilon}^p = \sqrt{(2/3)\,.\,d\varepsilon_{ij}^{.p} d\varepsilon_{ij}^{.p}}$.*C* is a material parameter.

$$\frac{dR}{R} = C exp(1.5T)\, d\bar{\epsilon}^p \tag{9.4}$$

Based on this relationship, a monotonic failure condition was postulated.

$$\int \exp(1.5T)\, d\bar{\epsilon}^p = \frac{\ln(R_{critical}/R_o)}{C} \geq VGI_{monotonic}^{critical} \tag{9.5}$$

According to the VGM, the ductile fracture initiates when the right hand side of the equation, reaches a material specific critical value, $VGI_{monotonic}^{critical}$.

The CVGM extends the VGM so that the concepts used to develop it can be applied to ULCF loading. The CVGM can be summed up by two equations. The first one presented in Equation 9.6, characterizes the fracture demand imposed on a material by ULCF loads. This equation assumes that voids grow during tensile cycles and shrinks during compressive cycles. The nature of a cycle (tensile or compressive) is defined by the sign (positive or negative) of the mean stress at a material point.

$$VGI_{cyclic} = \sum_{\substack{tensile \\ cycles}} \int \exp(|1.5T|)\, d\bar{\epsilon}^p - \sum_{\substack{compressive \\ cycles}} \int \exp(|1.5T|)\, d\bar{\epsilon}^p \tag{9.6}$$

In short, VGI_{cyclic} quantifies the effects of void growth and shrinkage due to ULCF loading.

The second equation (Equation 9.7) characterizes the fracture toughness of a material under ULCF loads. It basically represents the capacity of material which decreases due to the strain accumulation at the material point in question.

$$VGI_{cyclic}^{critical} = \exp\left(-\lambda {\epsilon_p}^{accumulated}\right).VGI_{monotonic}^{critical} \tag{9.7}$$

Where λ is a material parameter that determines the rate at which ductile facture toughness degrades and ${\epsilon_p}^{accumulated}$ is the equivalent plastic strain that has accumulated up to the beginning of each "tensile" excursion of loading.

The fracture is said to initiate when the fracture demand exceeds the fracture toughness or capacity shown in Equation 9.8.

$$VGI_{cyclic} \geq VGI_{cyclic}^{critical} \tag{9.8}$$

Once the failure mechanism was established, the CVGM was calibrated to the material test data. This was done in two steps. First, $VGI_{monotonic}^{critical}$ was calibrated to monotonic noted bar tests followed by the calibration of λ parameter to characterize degradation of the critical void ratio as a function of accumulated strain. The calibration was done for seven different steel types. It was noted that the notched cylindrical bars used for calibration provided high stress triaxiality values (0.8-2.0).

The CVGM was found to predict the crack initiation due to ULCF with good accuracy (within about 25% error). The following paragraph describes an example of how the CVGM model may help in predicting fracture initiation for BR-SPSW.

To test the CVGM model, one of the fracture-prone locations (ring-link joint) on specimen A1 (refer Table 12) was chosen. Equivalent plastic strain and triaxiality ratio at the chosen location was recorded. Equations 9.3 and 9.4 were used to calculate the VGI demand and capacity, respectively, at the chosen location. The material constants λ and $VGI_{monotonic}^{critical}$ was taken as 1 and 2.6, respectively, for steel type SN 490B (Myers 2009). The growing demand and the reduction in the capacity of the material due to strain accumulation are clear from Figure 102.

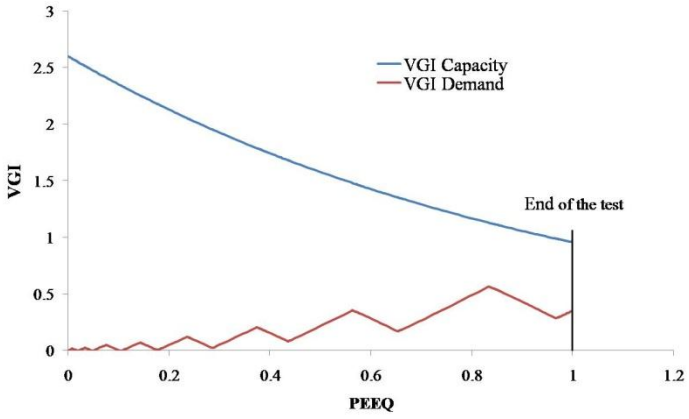

Figure 102: CVGM model example

According to the CVGM model, the specimen will not fracture since the demand never exceeds the capacity. However, it should be noted that the model parameters were not calibrated to be used for A36 steel in low triaxiality cases. Therefore, the results from obtained from this model may not be entirely accurate for this example. However, this example effectively demonstrates the use of the CVGM model in predicting fracture.

In order to use the CVGM model to predict the fracture initiation in BR-SPSW correctly, it would have to be calibrated for the material and stress triaxiality pertaining to the web plate of BR-SPSW specimen. This would mean calibrating the CVGM for the steel material type (A36 steel) using appropriate specimens which would potentially exhibit low state of triaxiality (0.3-0.6). Carefully designed experiments and extensive finite element analysis would be required to calibrate the CVGM to predict the fracture initiation.

As discussed previously in the case of SMCS model, the major challenge while dealing with the BR-SPSW would be the low triaxiality ratio it experiences. It has been identified (Fell 2008) that at lower triaxiality states (0.33-0.75), the fracture may initiate on the surface and move inwards. This is quite unlike the more constrained higher triaxiality cases where the fracture initiates internally and then propagates outward. This shift in initiation location may impact the mechanism of fracture. The research work by Bao and Wierzbicki (2004), lends an insight to the dependence of fracture strain on triaxiality ratio for monotonic loading case. The authors conducted a series of 11 tests on a particular aluminum alloy for which the triaxiality ratio ranged from -0.3 to 0.95. A fracture locus was then developed which is shown in Figure 103. A change in the fracture mechanism results in a slope discontinuity at triaxiality ratio of 0.4.

It is quite evident that there is a change in the fracture mechanism at lower state of triaxiality (around 0.4). Extensive study in conjunction with suitably designed experiments would be required to identify the different fracture mechanisms. This should eventually lead to the development of a unified model that can predict fracture initiation for structures experiencing any state of triaxiality.

Another challenge indirectly associated with these models is the high sensitivity of the equivalent plastic strain to the mesh size. Thus, to ensure accurate values for equivalent plastic strain, an appropriate mesh convergence analysis is highly recommended before settling on a specific mesh size to obtain this particular data accurately.

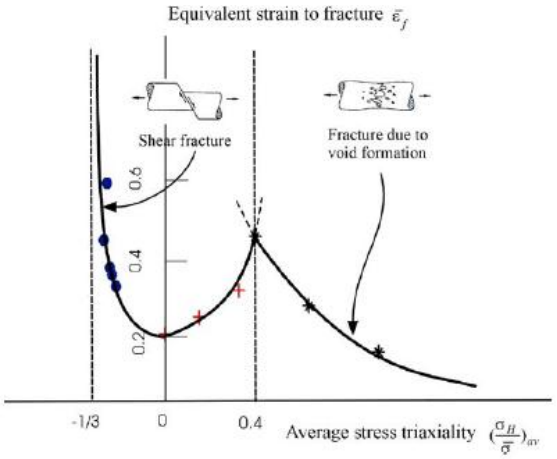

Figure 103: Dependence of the equivalent strain to fracture on the stress triaxiality [from (Bao and Wierzbicki 2004)]

9.3. EXTENDED FINITE ELEMENT MODELING (XFEM)

An extremely important aspect related to the fracture ductility of the BR-SPSW, which was slightly touched upon during the course of this work was modeling cracks in the web plate. Extended finite element method (XFEM) techniques were used to model cracks in single-ring unit specimens subjected to monotonic loading. A brief discussion of the XFEM concept is presented in the next paragraph followed by the results of crack modeling and how it can be implemented in the full-scale BR-SPSW model.

Modeling discontinuities has always been a major challenge in the field of computational mechanics. Cracks when modeled using standard finite element method (FEM) requires the FEM mesh to conform to the crack geometry. In case of static or quasi-static evolving cracks or dynamic crack propagation problems, a new mesh needs to be generated as the crack grows. Additionally heavy mesh refinement is required at the discontinuity. This method therefore proves to be computationally expensive. To ease difficulties in solving crack propagation problems, XFEM was developed by Belytschko and Black (1999). This method requires the application of an enrichment function in addition to the standard nodal DOF, to obtain displacement interpolation locally in the domain of interest. These enrichment functions represent the displacement jump across the crack face and the model singularity at the crack tip and are known as the Heaviside function and Crack tip enrichment function respectively. The XFEM displacement interpolation is represented by:

$$u^h(x) = \sum_I N_I(x)\left[u_I + \sum_J F_J(x) a_I^J\right] \tag{9.9}$$

In the above equation, u_I is the nodal DOF for conventional shape function N_I . $F_J(x)$ is the enrichment function and a_I^J is the nodal enriched DOF.

In terms of modeling in ABAQUS, the major advantage of this method is the ease of initial crack definition. First, the mesh generation is independent of the crack. Also, there is no need of partitioning the geometry as when a crack is represented explicitly. Secondly, XFEM allows solution dependent crack initiation and propagation path so the crack path need not have to be specified prior to the analysis. Moreover, the use of singular crack tip enrichment function results in a much improved convergence rate as compared to standard FEM techniques. ABAQUS also allows the damage modeling through predefined damage initiation and evolution criterion.

As mentioned in the beginning of the section, some basic ABAQUS analyses were done to understand crack propagation in a single-ring unit subjected to monotonic loading. A 50% maximum principal strain damage initiation criterion was used in the analyses. This was an arbitrary criterion with the sole purpose of determining and controlling the location of the fracture initiation. No pre-cracks were modeled. The initiation of the crack is shown in Figure 104. The crack initiates at joint of the link and the ring. This result was expected as the link-ring joint is sharp and therefore prone to fracture.

A parametric study was done to investigate the effect of fillet radius (at the link-ring joint) on the crack initiation and the behavior of the ring unit. The idea behind modeling crack in a single-ring unit was to understand the post-fracture behavior of the unit. Most of the ABAQUS analysis exhibited instability soon after the crack initiation. Several techniques were used to reduce this instability but none of them worked well. The plots shown in Figure 105 terminate at approximately the displacement at which the crack initiated.

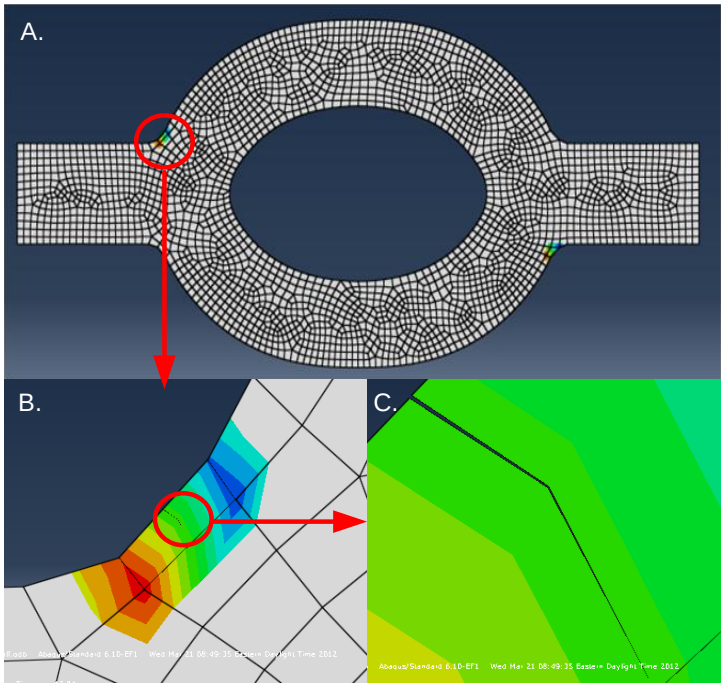

Figure 104: Initiation of crack in a single-ring model

A few observations can be made from the parametric study. First, very evident from the plots is the fact that with the increase in the fillet radius, the displacement at which cracks initiates increases. There is also a slight increase in the capacity of the ring unit. The parametric study

also included the fillet radius of 3 inches. The behavior of the ring was however quite different and hence the plot is separately shown in Figure 106. For this radius, the crack initiated at the inner edge of the ring as shown in Figure 106 but did not fully develop and the analysis could run without convergence issues. It was observed that once the crack started, the ring did not see any deformation and it was the link that contributed to the capacity of the system. This prevented the crack propagation. This kind of behavior is desirable for the ring-link system because the system almost fully yielded before the crack propagated and degraded the system capacity. However, it should be noted that this behavior is highly dependent on the damage initiation/evolution criteria used for the analysis. It is therefore very important to use the most suitable damage criteria. For this set of damage initiation/evolution criteria a fillet radius between 25-36% (2-3 in. for this model) of the outer ring radius is desirable.

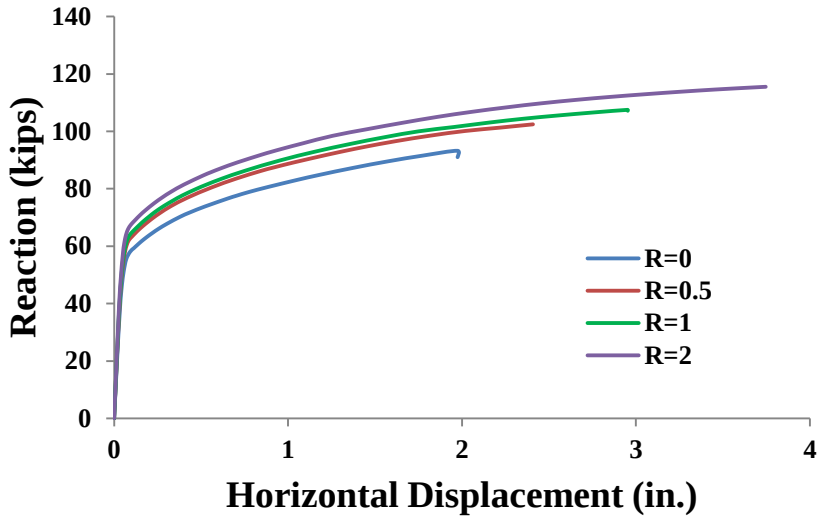

Figure 105: Plot showing the effect of fillet radius on crack initiation

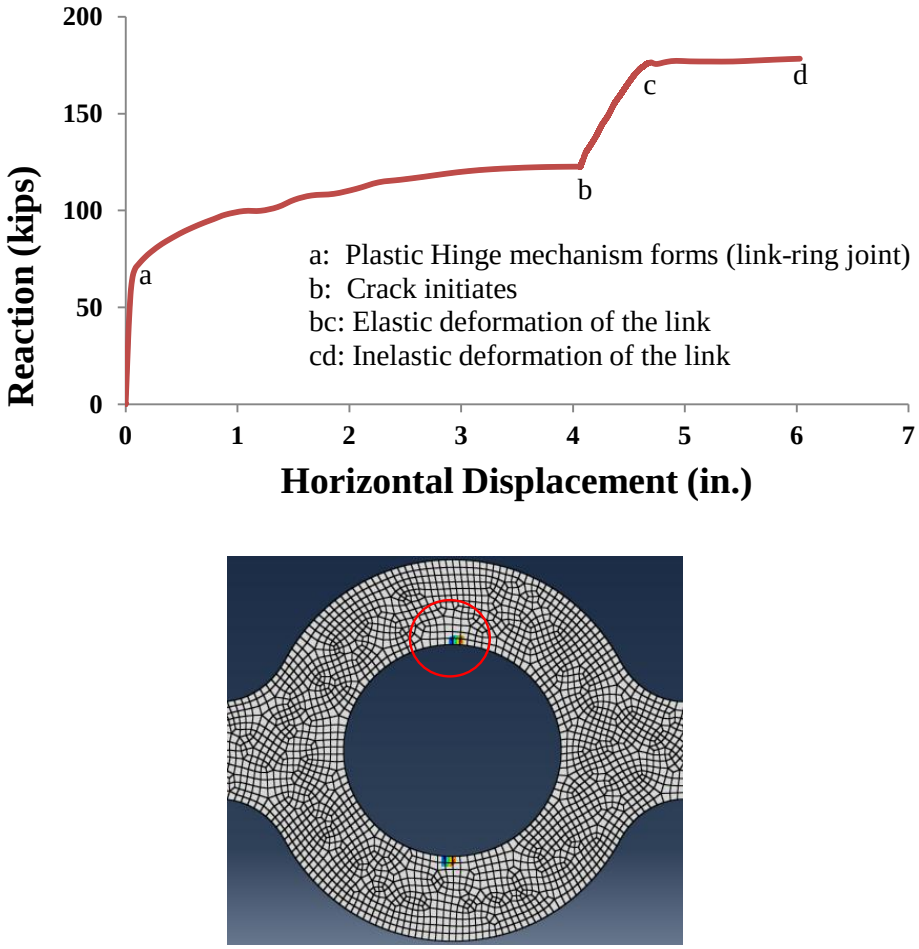

Figure 106: Force-displacement curve and crack initiation location for 3in. fillet model

The original intent was to use XFEM concepts on the full BR-SPSW wall to simulate the initiation and propagation of cracks. Since the full wall model consists of many rings, it was conjectured that this inherent redundancy would lead to good system behavior even if one ring fractures. However, the implementation of this technique on the full wall still requires a substantial amount of research work. First, the most appropriate damage initiation and evolution criterion needs to be identified for BR-SPSW. It might be a maximum principle stress criteria, principle strain criteria or a user-defined criteria formulated specifically for this geometry. This might require some experimentation in conjunction with FE analysis. Secondly, there is also a need for a more effective way of dealing with convergence problems.

CHAPTER 10

EXPERIMENTATIONAL STUDY DESIGN

A parallel experimental program is being conducted at Virginia Tech to further validate the concept behind BR-SPSW, investigate key parameters discussed in the previous section, and provide data to compare with computational and analytical predictions. The tests will be conducted on small-scale specimens and is expected to lend an insight to the ductility of the system and potential for web plate fracture.

The test specimens will be modeled using similar methods as the computational study. A few minor changes have been made in the geometry according to the test set-up. All sharp edges in the plate geometry have been rounded off to (fillet radius equal to 20% of the outer ring radius) reduce the potential of crack initiation. High quality water-jet cutting will be used to cut the specific pattern for each specimen. A typical test specimen is shown in The schematic test-setup for the experimental study is shown in Figure 108 .

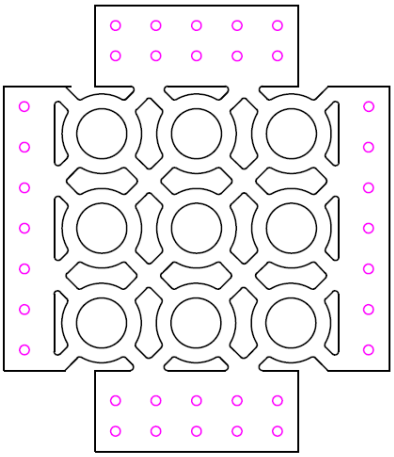

Figure 107: A typical test specimen to be tested as a part of experimental study

For the experiment, a total of eight specimens were designed. One of these specimens was chosen to be a solid plate with no perforations. This was done to compare the behavior of the BR-SPSW with a typical solid shear wall. A detailed description of these specimens and behavior related predictions associated with each of them is presented in Table 2027. Differences between the predicted behavior and the experimental results will be investigated.

Table 20: Predicted behavior of the experiment Specimen 1

Specimen 1	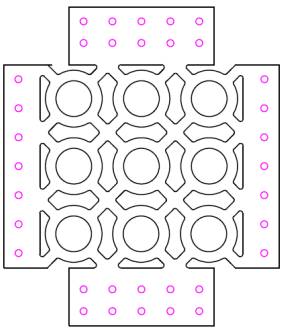 Plate thickness (t): 0.5 in. Outer Ring Radius (R_o): 3.9 in. Width of the link (w_c): 1.52 in.	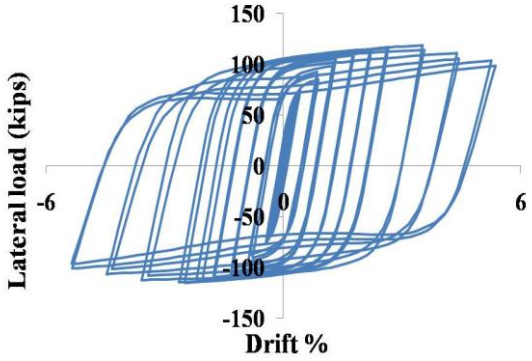 Predicted Strength:**69.7 kips** Predicted Stiffness: **584 kips/in.**

Table 21: Predicted behavior of the experiment Specimen 2

Specimen 2	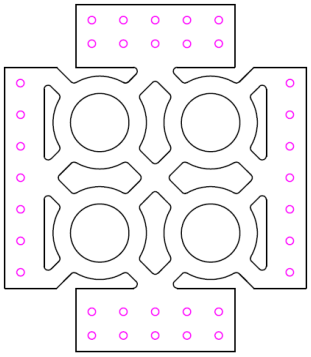 Plate thickness (t): 0.5 in. Outer Ring Radius (R_o): 5.89 in. Width of the link (w_c): 2.11 in.	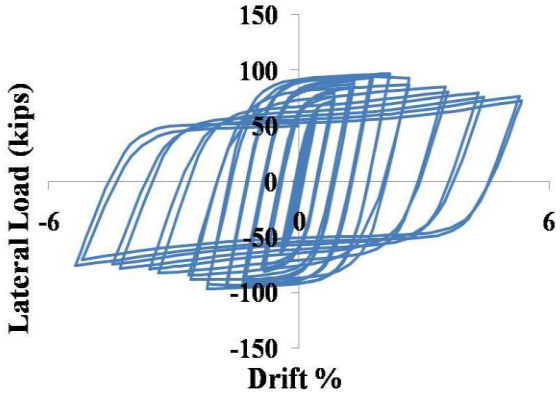 Predicted Strength:**64.3 kips** Predicted Stiffness: **491 kips/in.**

Table 22: Predicted behavior of the experiment Specimen 3

Specimen 3	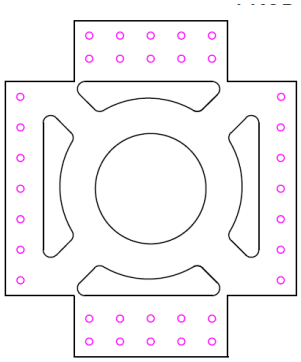	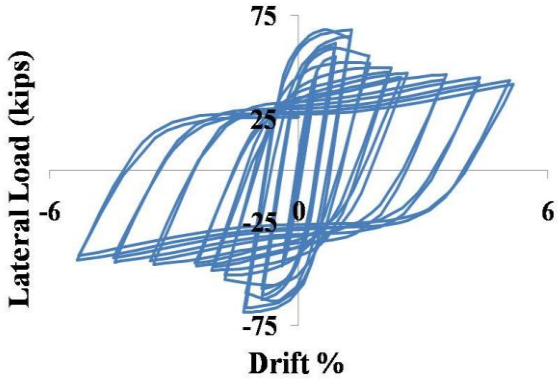
	Plate thickness (t): 0.5 in. Outer Ring Radius (R_o): 11.55 in. Width of the link (w_c): 4.88 in.	Predicted Strength:**50.7 kips** Predicted Stiffness: **349 kips/in.**

Table 23: Predicted behavior of the experiment Specimen 4

Specimen 4	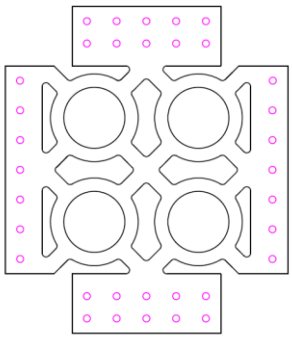	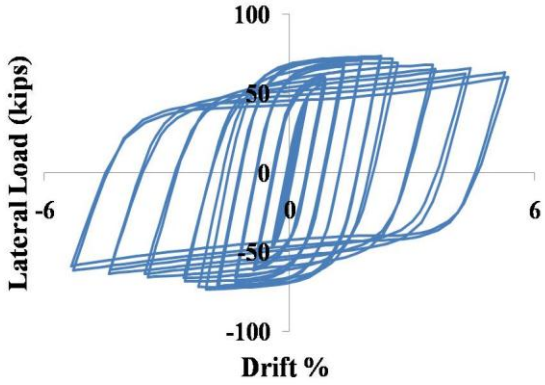
	Plate thickness (t): 0.25 in. Outer Ring Radius (R_o): 5.89 in. Width of the link (w_c): 1.74 in	Predicted Strength:**51 kips** Predicted Stiffness: **346 kips/in.**

Table 24: Predicted behavior of the experiment Specimen 5

Specimen 5	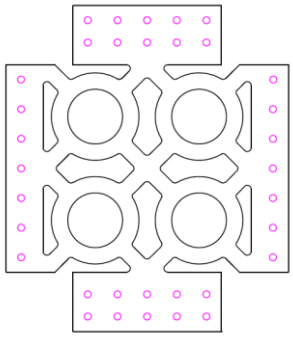 Plate thickness (t): 0.25 in. Outer Ring Radius (R_o): 5.89 in. Width of the link (w_c): 2.11 in.	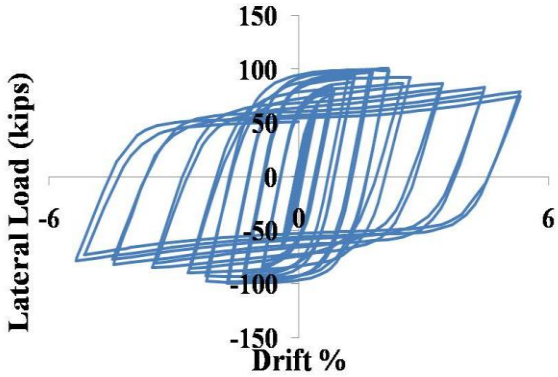 Predicted Strength:**71 kips** Predicted Stiffness: **507 kips/in.**

Table 25: Predicted behavior of the experiment Specimen 6

Specimen 6	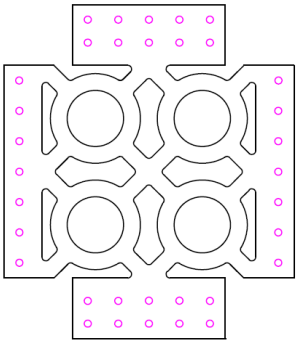 Plate thickness (t): 0.375 in. Outer Ring Radius (R_o): 5.89 in. Width of the link (w_c): 2.11 in.	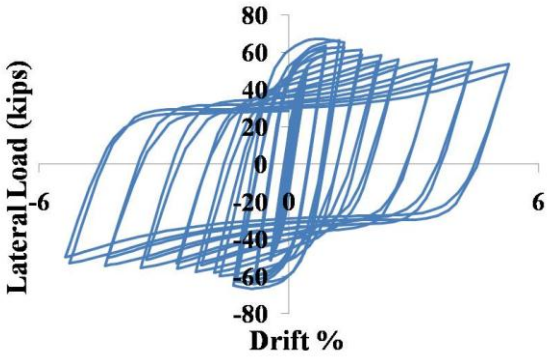 Predicted Strength:**51 kips** Predicted Stiffness: **390 kips/in.**

Table 26: Predicted behavior of the experiment Specimen 7

Specimen 7	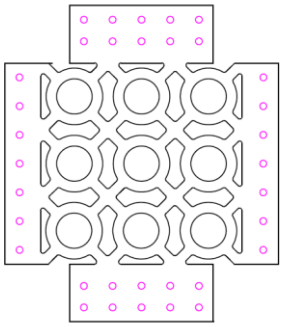 Plate thickness (t): 0.25 in. Outer Ring Radius (R_o): 3.9 in. Width of the link (w_c): 1.52 in	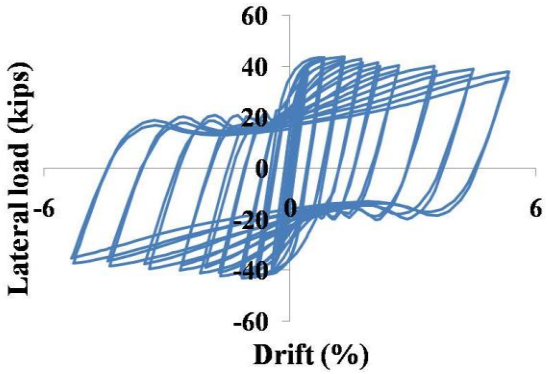 Predicted Strength:**37.5 kips** Predicted Stiffness: **320 kips/in.**

Table 27: Predicted behavior of the experiment Specimen 8

Specimen 8	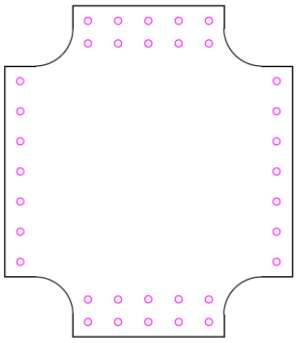 Plate thickness (t): 0.25 in.	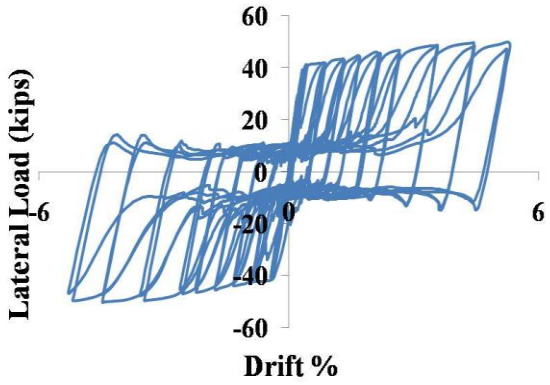 Predicted Strength:**42 kips** Predicted Stiffness: **346 kips/in.**

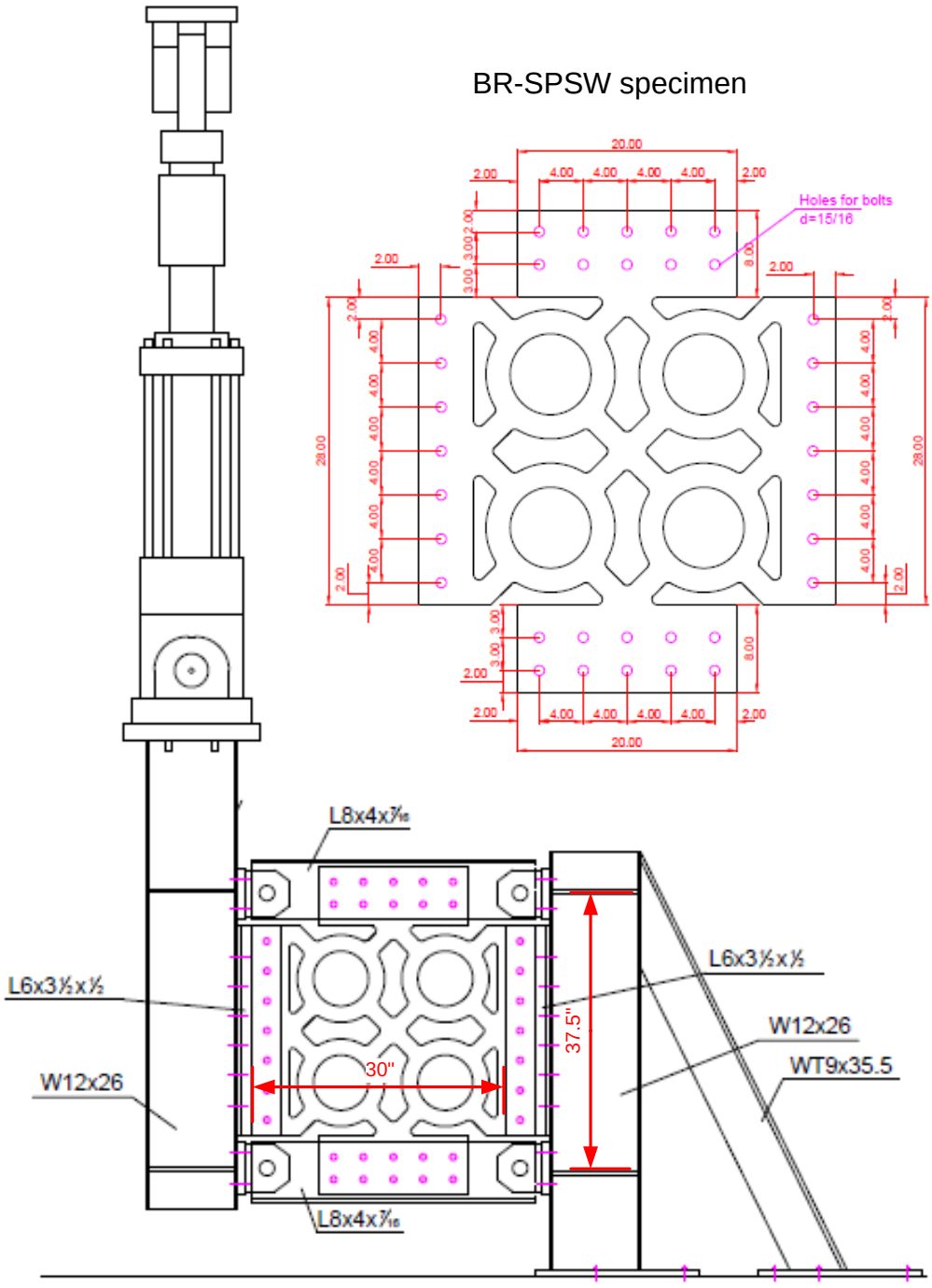

Figure 108: Experiment setup for small-scale BR-SPSW test

CHAPTER 11
SUMMARY AND CONCLUSIONS

This report includes the development of an efficient alternative to typical steel plate shear wall followed by a detailed analysis of the proposed system. It highlights the major behavioral aspects of the system and sensitivity of the system response to geometric features of the shear wall system. The conclusions made in this report include the understanding of BR-SPSW system and proposing analytical and computation models that can be used for the design of efficient and high performance shear wall systems.

BR-SPSW concept has been devised which builds on the advantages of a typical steel plate shear wall, but has improved seismic performance, reduced demands on the boundary elements and allows simple shear beam-to-column connections. It employs a unique ring like cut-outs which elongate into an ellipse when the shear plate is loaded laterally. This ring-effect reduces out-of-plane buckling and lends tunability to BR-SPSW system. A brief summary of the work done in developing this system and detailed conclusions drawn from this study of BR-SPSW is presented below.

11.1. PRELIMINARY INVESTIGATIONS

A preliminary study of the BR-SPSW was undertaken to prove that the concept behind the ring-like units in BR-SPSW would prevent excessive buckling of the web-plate and would resist substantial fraction of lateral load without the use of moment connections. The study was done by performing FE analysis on full wall and individual ring units using three dimensional finite element models with shell elements.

From the analysis result of the full wall, it was observed that BR-SPSW exhibited relatively fuller hysteresis as compared to the SPSW tested by Berman and Bruneau (2005). The pinching was much less as compared to the aforementioned experimental result. It was further concluded that BR-SPSW exhibits two modes of buckling. The specimens with larger rings exhibited a combination of global tension field buckling and lateral torsional buckling of the rings, while the specimens with smaller rings predominantly exhibit global tension field buckling.

Additionally, two single-ring models were devised in order to carefully capture the behavior of the ring units in the full wall. These models namely, constrained and unconstrained ring models were later used to understand the yielding mechanism of the rings in the full wall and for developing analytical solutions for the strength and stiffness of the full wall. The force deformation behavior of the unconstrained ring model also reinforced the fact that the when a ring deforms into an ellipse the longitudinal and transverse deformations are nearly same. It was found that up to an elongation of 20% of the ring diameter the effective Poisson's ratio of the ring is 1.0.

11.2. ANALYTICAL SOLUTION: STRENGTH OF THE FULL WALL

The analytical solution for the strength of the full wall was derived using the plastic mechanism analysis. Deformation mechanics of individual ring units with different level of constraints was studied. Four plastic mechanisms, some with and without plastic axial deformations, were proposed to explain the inelastic behavior of the ring in the full wall. The analytical solution was then compared to the preliminary finite element analysis results to establish the accuracy of the solution.

Out of the various mechanisms put forth, Mechanism IV which was developed to explain the mechanics of the constrained ring model agreed the best with the FE analysis results. This mechanism assumed the formation of plastic hinges at the link-ring joint and ignored the inelastic behavior of the links. It assumed that the top and bottom part of the rings act rigidly (Refer Figure 33). The derived equation for strength was thus given by Equation 11.1.

$$V = \frac{4M_p}{\sqrt{2}(r_c - \frac{w_l}{2})} \tag{11.1}$$

On comparison with the FE analysis results from the parametric study, it was observed that the proposed equation was conservative by an average of 8% with a standard deviation of 8.9%. As mentioned above, the major source of the error is believed to be due to the assumption that the links will remain fully elastic.

11.3. ANALYTICAL SOLUTION: STIFFNESS OF THE FULL WALL

The analytical solution for the stiffness of the full wall was developed along similar lines to the strength of the wall. Both the constrained and unconstrained ring model was considered to study

the deformation mechanism. Castigliano's Theorem was used for determining the displacements for linear-elastic system based on partial derivatives of the strain energy with respect to the generalized force in the direction of the displacement. The derived equation was then compared to the initial stiffness (recorded in linear elastic region) of the specimens tested as the part of the parametric study. While deriving the equation, the stiffness of the link was ignored to make the solution simple.

Out of the two, the unconstrained ring model was restricted by fewer assumptions. It was therefore used to predict the stiffness of BR-SPSW specimens. The stiffness of one ring unit obtained from this model is given by,

$$k_u = \left(\frac{\kappa R\pi}{4GA} + \frac{R\pi}{4EA} + \frac{R^3}{EI}\left\{\frac{c^2\pi}{2} - 2c + \frac{\pi}{4}\right\}\right)^{-1} \tag{11.2}$$

Refer to Section 6.2 for the definition of the variables used in the equation.

The expression for the full wall is then given by,

$$K_w = \frac{K_u}{2N_r}(N_r + N_c - 1) \tag{11.3}$$

On comparison to the FE analysis results, it was observed that the proposed equation works well for models with narrow links and smaller radii. It was finally concluded that the proposed analytical model can be used with good accuracy (within 15% error) for R_o/w_lratio less than 2 with 16 inches outer radii or less. Overall, the predicted stiffness of the full wall was observed to be on an average 17% less than the observed stiffness from the computational study.

Since the proposed analytical solution is complex and does not work for certain cases, an empirical equation was derived using the FE analysis data obtained from the parametric study. The empirical equation for the stiffness of a single ring unit is given by,

$$K_{r,emp} = 15812.4 \times t^{1.3}\left(\frac{R_o}{w_l}\right)^{-3.4}\left(\frac{R_o}{t}\right)^{0.3}\left(\frac{w_c}{w_l}\right)^{2.7} \tag{11.4}$$

where, K_r is the stiffness per unit ring in kips/in. unit.

The stiffness of the ring unit can be translated to the stiffness of the full wall by using the equation below.

$$K_{w,emp} = \frac{K_{r,emp}}{2N_c}(N_r + N_c - 1) \quad (11.5)$$

11.4. EFFECT OF INITIAL IMPERFECTIONS

A small parametric study was conducted to investigate the effect of initial imperfections on the performance of BR-SPSW when subjected to monotonic loading. In this study, specimens with random imperfections and imperfections corresponding to the eigen buckling modes of the plate were compared.

First, it was concluded that initial imperfections larger than L/100 result in significant reduction in strength and stiffness and thus it is advisable to limit the imperfections to L/100. Secondly, using random imperfections for modeling the plate was found to be acceptable. This was concluded based on the observation that when compared to the models where the model was built with an initial imperfection in the shape of the first eigen mode, the plates with random imperfections exhibited very minor difference in the capacity and stiffness. On comparing the effect of the shape of initial imperfections, it was found that the mode shape did not have a major effect on the strength and stiffness of the plate.

A more palpable conclusion of the study was that as compared to the perfect geometry, the specimens with any kind of initial imperfection exhibit reduced strength and stiffness. However, this reduction is more severe in the plates with larger ring radius. Moreover, the system strength and stiffness is not too sensitive to initial imperfections in the range of expected initial imperfections (L/1000 to L/100). Typically, the expected initial imperfections might be L/500 based on typical tolerances for out-of-straightness for a new construction. This lack of sensitivity is beneficial because the wall behavior won't change significantly if one of the web plates has more imperfections than another.

11.5. PARAMETRIC STUDY

The parametric study was done to build on the results of the preliminary study. It aimed at characterizing the influence of geometric features of the wall on the overall behavior of the system. A set of input and output parameters was defined for the parametric study. A set of behavioral trend plots were generated as an aid for the design process. Major conclusions drawn from these plots are summarized below.

- Thickness of the web plate plays an important role in all the behavioral aspects of BR-SPSW. A thicker plate exhibits a relatively fuller hysteretic behavior and does not experience substantial strength and stiffness reduction. This results in relatively much larger energy dissipation. A thinner plate experiences buckling at earlier stage and therefore exhibits a much smaller energy dissipation ratio. Moreover, thinner plates more often exhibit lateral torsional buckling of the rings in conjunction to the global tension field buckling which was shown to cause pinching in the hysteretic behavior of the shear wall. Needless to say, thicker web plates also result in higher strength and stiffness of the full wall. Additionally, it was observed that increase in thickness increases the drift at which the shear wall system yields globally.
- As expected, the behavior of BR-SPSW is highly sensitive to the size of the ring units. This is because the ring size is a major factor in determining the type of buckling the web-plate will experience. It was concluded that smaller radii rings resulted in global tension field buckling of the plate. On the contrary, BR-SPSW with larger radii experienced local torsional buckling of the rings in conjunction to the global tension field buckling. This difference in the buckling behavior of the wall influences the total energy dissipation and the energy dissipation ratio alike. It is hypothesized that lateral torsional buckling of the rings results in pinching of the hysteresis curve and thus reduces the energy dissipation capacity of the wall. This hypothesis was based on the idea that the distortion in the ring units caused by the local torsional buckling prevents the natural elongation of the rings into an ellipse, which was the basic idea behind BR-SPSW. This degrades the behavior of individual ring units and in turn the full wall.

  The parametric results also showed that although the strength per ring increases with increase in radius, the strength of the full wall with given dimensions may not necessarily be larger for larger radii ring models. The only major advantage of using a larger radius ring is the reduced cutting cost. It was observed that decreasing the ring radii exponentially increases the cutting cost of BR-SPSW. However, in all other aspects web-plates with smaller radii exhibit much better behavior.
- Another input parameter that had a major influence on the hysteretic behavior of the full wall was R_o/w_c ratio. Based on the FE analysis, it was observed that keeping R_o/w_c ratio in the range of 2.5-3.33, results in fuller hysteretic behavior and higher energy dissipation

ratio. An increase in the R_o/w_c ratio results in a tremendous increase in the buckling ratio, indicating that specimens with wider rings suffer from lateral torsional buckling of the rings which has been proved to be undesirable. An increase in the R_o/w_c ratio, however, also results in an exponential decrease in the strength and stiffness/ring. Additionally, the cost of cutting also increases slightly with the increase in this ratio. It can be concluded that keeping the ratio around 2.5-3.33 would result in an optimum design.

- R_o/w_l ratio has a similar influence on the strength and stiffness per ring as the R_o/w_c ratio. However, R_o/w_l ratio has a much less significant effect on the system behavior as compared to the R_o/w_c ratio. Increasing the R_o/w_l ratio slightly reduces the energy dissipation capacity of the full wall but has not major influence on the energy dissipation ratio. The cutting cost of the plate also slightly increases with an increase in the R_o/w_l ratio. Using a R_o/w_l ratio less than 3 is recommended since a very narrow link is prone to inelastic deformation which is undesirable.
- The ring slenderness ratio (R_o/t and w_c/t) has a major influence on the buckling behavior of the plate. It was observed that an increase in slenderness ratio results in a substantial decrease in the total dissipated energy and the buckling ratio. The slenderness ratio of the rings must be controlled for the design of more efficient BR-SPSW.

11.6. GENERAL OBESERVATIONS AND CONCLUSIONS

Some general conclusions drawn from the study are presented below.

- The concept of BR-SPSW was largely validated. The buckling of the web-plate was considerably reduced with substantial resistance during load reversals. A majority of the specimens tested in the parametric study exhibited relatively full hysteretic behavior. Energy dissipation ratio as high as 0.78 was observed, which indicates little pinching and high energy dissipation. The hypothesis regarding the ring deforming into an ellipse to reduce buckling works to a large extent. However, since this “ring effect” is an idealized concept, it was found to not to fully prevent buckling. The following paragraphs highlight the reasons for this deviation in the behavior of BR-SPSW.

  The major reason why BR-SPSW does not fully prevent buckling is due to the inelastic deformation of the links joining the rings. This results in non-uniform distribution of

stresses in a ring unit which hinders the perfect elongation of the ring. This problem gets severe when the links are narrow. Plastic axial deformation of the rings is another major reason why BR-SPSW does not work perfectly. Generally, at the site of plastic hinges, plastic axial deformation of the rings is observed. Comparing this to the ring-ellipse analogy, this would mean that the perimeter of the ring is expanding as it is elongated into an ellipse. This would be a violation of the assumption made while developing the idealized concept of BR-SPSW.

Additionally, lateral loading in the plates causes minor distortion in the rings, which is a deviation from the idealized behavior where the ring was always assumed to be deforming in a plane. This type of distortion reduces the strength of the individual ring and causes lag in the load resistance during load reversals which is evident from the pinching observed in the hysteretic behavior of BR-SPSW with large radii (refer Appendix B). Bending of frame elements, in cases where they are not totally rigid may also have adverse effect on the web-plate behavior.

The results from the preliminary investigation and parametric study were quite hopeful in terms of developing a high performance and more efficient alternative to a typical SPSW. The comparison of a typical steel plate shear wall to BR-SPSW (refer Section 8.5) showed that for a similar capacity wall, BR-SPSW exhibits substantially large resistance during load reversals which results in reduced pinching and much higher energy dissipation (about 26%).

Additionally, for achieving strength of about 250 kips with A36 steel plates, a typical SPSW may need to be as thin as 1/16'' and require moment connections between beams and columns. Thin web plate material creates challenges associated with constructability such as difficulty in welding and buckling of the web plate before construction (Eatherton 2006). This problem can be resolved by the use of BR-SPSW, where a 5/8'' thick A36 steel plate can be used to achieve strength of 250 kips (refer Table 16) with significantly improved stiffness and energy dissipation performance and simple shear beam to column connections.

Although not yet experimentally proven, another major advantage of BR-SPSW is expected to be the redundancy provided by the arrays of rings. This implies that if a one ring fracture during loading, the web plate is not expected to see major deterioration in its capacity. In a typical SPSW, fracture initiation generally leads to substantial decrease in the system capacity and in turn leads to the failure of the specimen (Berman and Bruneau, 2005).

- Analytical and empirical solutions for the strength and stiffness of BR-SPSW were derived. These solutions in conjunction with the trend plots presented in Section 8.4 provide a powerful tool that can be used for designing BR-SPSW.

- The study presented in this report is purely based on computational observations. Experiments are required and will be conducted in the near future to further validate the concept and the computational modeling. Good behavior is expected for the selected specimens as predicted by finite element models (Refer Table 20).

REFERENCES

ABAQUS Version 6.10 documentation, Dassault Systems, 10, Rue Marcel Dassault, 78140 Velizy-Villacoublay, France, 6th Edition.

Ahmed, A., Extended Finite Element Method(XFEM)- modeling arbitrary discontinuities and failure analysis, Master's thesis, The Institute for Advanced Study of Pavia, Pavia, Italy (April 2009).

American Institute of Steel Construction (AISC), Seismic Provisions for Structural Steel Buildings AISC 341-10, (2005).

Astaneh, A., Seismic behavior and design of steel shear walls, In proceedings of SEOANC Seminar, Structural Engineers Assoc. of Northern California, San Francisco, California, 2001.

Baldelli, J.A., Steel shear walls for existing buildings, Engineering Journal of the American Institute of Steel Construction 20 (1983) 70-77.

Bao, Y., Wierzbicki, T., On fracture locus in the equivalent strain and stress triaxiality space, International Journal of Mechanical Sciences 46 (1) (2004) 81-98.

Berman, J.W., Bruneau, M., Experimental investigation of light-gauge steel plate shear walls for the seismic retrofit of buildings, Technical Report MCEER-03-0001, Multidisciplinary Center for Earthquake Engineering Research, Buffalo, NY (May 2003).

Berman, J.W., Bruneau, M., Steel Plate Shear Walls are not plate girders, Engineering Journal of the American Institute of Steel Construction, Third Quarter, (2004) 95-106.

Berman, J.W., Celik, O.C., Bruneau, M., Comparing hysteretic behavior of light-gauge steel plate shear walls and braced frames, Engineering Structures 27 (3) (2005) 475-485.

Bruneau, M., Berman, J., Lopez-Garcia, D., Vian, D., A Review of Steel Plate Shear Wall Design Requirements and Research, Engineering Journal of the American Institute of Steel Construction, 44(1) 2007 27-34.

Berman, J.W., Seismic behavior of code designed steel plate shear walls, Journal of Engineering Structures 33 (2011) 230-244.

Caccese, V., Elgaaly, M., Du, C., Experimental study of thin steel plate shear walls under cyclic load, Journal of Structural Engineering (ASCE) 119 (2) (1983) 573-587.

Caccese, V., Elgaaly, M., Du, C., Postbuckling behavior of steel-plate shear walls under cyclic loads, Journal of Structural Engineering (ASCE) 119 (2) (1993) 588-605.

Chen, J.S., Jhang, C., Experimental study of low-yield-point steel plate shear wall under in-plane load, Journal of Constructional Steel Research 67 (2011) 977-985.

Chen, W.F., Han, D.J., Plasticity for Structural Engineers, J. Ross Publishing, 2007.

Chi, W. M., Kanvinde, A. M., Deierlein, G. G., Prediction of ductile fracture in steel connections using SMCS criterion, Journal of Structural Engineering 132 (2) (2006) 171-181.

Ciampi, V., Samuelli-Ferretti, A., Energy dissipation in buildings using special bracing systems, In proceedings of the 9th European Conference on Earthquake Engineering, Vol. 3 of 9-18, Moscow, Russia, 1990.

Ciampi, V., Arcangeli, M., Perno, S., Characterization of the low-cycle fatigue life of a class of energy dissipating devices, In proceedings of the 2nd European Conference on Structural Dynamics (EURODYN '93), Vol. 1 of 337-X, Trondheim, Norway, 1993, pp. 137-144.

Cortes, G., Liu, J., Steel slit panel configurations, In proceeding of the 14th World Conference on Earthquake Engineering, Beijing, China, 2008.

Driver, R.G., Kulak, G.L., Kennedy, D.J.L., Elwi, A.E., Seismic behavior of steel plate shear walls, Structural Engineering Report 215, Department of Civil and Environmental Engineering, University of Alberta, Edmonton, Alberta, Canada (February 1997).

Eatherton, M.R., Design and construction of steel plate shear walls, In proceedings of the 8th U.S. National Conference on Earthquake Engineering, San Francisco, California, 2006.

Elgaaly, M., Thin steel plate shear walls behavior and analysis, Thin Walled Structure 32 (1998) 151-180.

Fell, B. V., Large-scale testing and simulation of earthquake-induced ultra low cycle fatigue in bracing members subjected to cyclic inelastic buckling, Phd dissertation, University of California, Davis, CA (2008).

Hancock, J. W., Mackenzie, A. C., On the mechanics of ductile fracture in high strength steels subjected to multiaxial states of stress, Journal of mechanics and physics of solids 14 (1977) 147-169.

Hitaka, T. and Matsui, C., Experimental study on steel shear wall with slits, Journal of Structural Engineering (ASCE) 129 (5) (2003) 586-595.

Hitaka, T., Matsui, C., Tsuda, K., Sadakane, Y., Elastic-plastic behavior of buildings of steel frame with steel bearing wall with slits, In proceeding of the 12th World Conference on Earthquake Engineering, no. 0833, Auckland, New Zealand, 2000.

Hitaka, T., Matsui, S., Seismic performance of steel shear wall with slits integrated with multi-story composite moment frame, In proceedings of the 5th International Conference on Behaviour of Steel Structures in Seismic Areas, Yokohama, Japan, 2006.

Kanvinde, A. M., Deierlein, G. G., Cyclic void growth model to assess ductile fracture initiation in structural steels due to ultra low cycle fatigue, Journal of Engineering Mechanics 133(6) (2007) 701-712.

Lubell, A., Prion, H., Ventura, C., Rezai, M., Unstiffened steel plate shear wall performance under cyclic loading, Journal of Structural Engineering (ASCE) 126 (4) (2000) 453-460.

Ma, X., Borchers, E., Peña, A., Krawinkler, H., Deierlein, G., Design and behavior of steel shear plates with openings as energy-dissipating fuses, Internal report, Blume Earthquake Engineering Center, Stanford University, Stanford, California (2010).

Martinez-Rueda, J.E., On the evolution of energy dissipation devices for seismic design, Earthquake Spectra 18 (2) (2002) 309-346.

McCloskey, D.M., Steel slit panels for lateral resistance of steel frame buildings, MS thesis, Department of Civil Engineering, Purdue University, West Lafayette, Indiana. (2006).

Moes, N., DolBow, J., Belytschko, T. A finite element method for crack growth without remeshing, International Journal for Numerical Methods in Engineering, 46 (1999) 131-150.

Moghini, H., Driver, R.G., Effect of regular perforation patterns on steel plate shear wall column demands, In proceedings of Structures Congress (ASCE), Las Vegas, Nevada, United States, 2011, pp. 2917-2928.

Myers, A., Testing and probabilistic simulation of ductile fracture initiation in structural steel components and weldments, Phd dissertation, Stanford University, Stanford, CA (2009).

Panontin, T. L., Sheppard, S. D., An experimentally verified finite element study of the stress-strain response of crack geometries experiencing large-scale yielding, In proceedings of the 27th International Symposium on Fatigue and Fracture Mechanics, Vol. 27, ASTM Committee, Williamsburg, Virginia, 1995, pp. 216-242.

Rice, J. R., Tracey, D. M., On the ductile enlargement of voids in triaxial stress fields, Journal of Mechanics Physics Solids 17 (3) (1969) 201-217.

Roberts, T., Sabouri-Ghomi, S., Hysteretic characteristics of unstiffened perforated steel plate shear panels, Thin-Walled Structures 14 (2) (1992) 139-151.

Rogers, C., and Morrison, T., Ductile brace fuses for cost effective design of brace steel frames, In proceedings of North American Steel Construction Conference, Pittsburgh, Pennsylvania, 2011.

Rousselier, G., Ductile fracture models and their potential in local approach of fracture, Nuclear Engineering and Design 105 (1) (1987) 97-111.

Sabelli, R., Bruneau, M., Design Guide 20: Steel Plate Shear walls, American Institute of Steel Construction (2006).

Schumacher, A., Grondin, G.Y., Kulak, G.L., Connection of infill panels in steel plate shear Walls, Canadian Journal of Civil Engineering 26 (1992) 549-563.

Tanamal, A., Eatherton, M., Hajjar, J. F., Controlled rocking of steel-framed buildings with replaceable energy dissipating fuses fuse material coupons – tension tests, Tech. Rep. 61801, University of Illinois at Urbana-Champaign, Urbana, Illinois (March 2009).

Thorburn, L.J., Kulak, G.L., Montgomery, C.J., Analysis of steel plate shear walls., Structural Engineering Report 107, Department of Civil Engineering, University of Alberta, Edmonton, Alberta, Canada (May 1983).

Timler, P.A., Kulak, G.L., Experimental study of steel plate shear walls, Structural engineering report 114, Department of Civil Engineering, University of Alberta, Edmonton, Alberta, Canada (1983).

Timler, P.A., Design procedures development, analytical verification, and cost evaluation of steel plate shear wall structures, Technical report 98-01, Earthquake Engineering Research Facility, University of British Columbia, Vancouver, British Columbia, Canada (1998).

Tipping, S., B. Stojadinovic, S., Innovative corrugated steel shear walls for multi-story residential buildings, in: In proceedings of the 14th World Conference on Earthquake Engineering, 2008.

Tromposch, E.W., Kulak, G.L., Cyclic and static behavior of thin panel steel plate shear walls, Structural Engineer Report 145, Department of Civil Engineering, University of Alberta, Edmonton, Alberta, Canada (April 1987).

Tyler, R. G.,, Further notes on a steel energy-absorbing element for braced frameworks, Bulletin of the New Zealand National Society for Earthquake Engineering 18 (3) (1985) 270-279.

Vian, D., Bruneau, M., Steel plate shear wall for seismic design and retrofit of building structures, MCEER Technical Report 05-0010, Multidisciplinary Center for Earthquake Engineering Research, University at Buffalo (2005).

Vian, D., Bruneau, M.,, Testing of special LYS steel plate shear walls, In proceedings of the 13th World Conference on Earthquake Engineering, no. 978, Vancouver, B.C., Canada, 2004.

Wagner, H., Flat sheet metal girder with very thin metal web, Technical Memo 604-606, National Advisory Committee for Aeronautics (NACA), Washington, D.C. (1931).

Xue, M., Lu, L., Interaction of Infilled Steel Shear Wall Panels with Surrounding Frame Members. 1994 Annual Task Group Technical Session, Structural Stability Research Council report on current research activities, Lehigh University, Bethlehem, PA, June 1994.

Zeinoddini-Meimand, V., Geometric imperfections in cold-formed steel members, PhD dissertation, Johns Hopkins University (2011).

APPENDIX A: TREND PLOTS

This appendix compiles the trend plots generated for the output variables of the system with respect the geometrical features of the BR-SPSW system. These trend plots can be used for the design of BR-SPSW.

APPENDIX A1

BEHAVIOR TRENDS FOR FULL-WALL STRENGTH

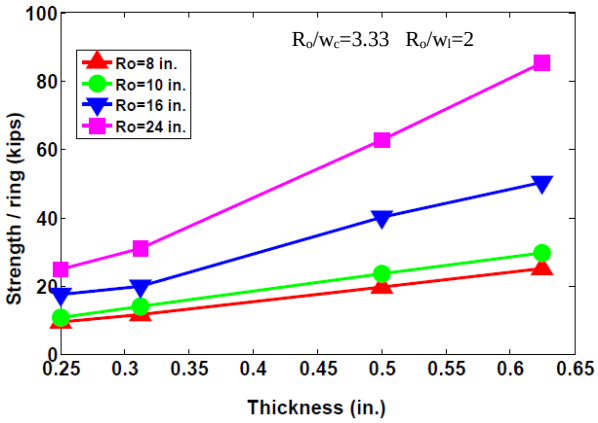

(a)

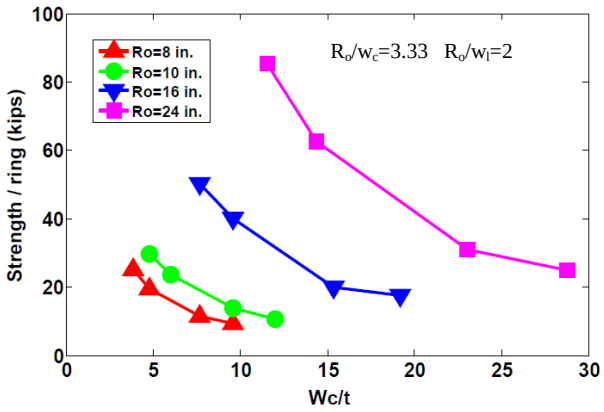

(b)

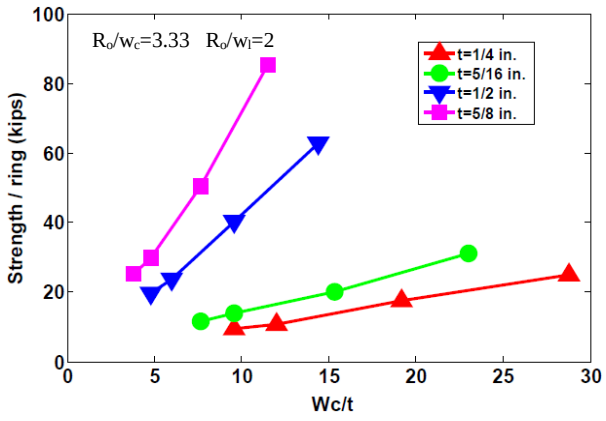

(c)

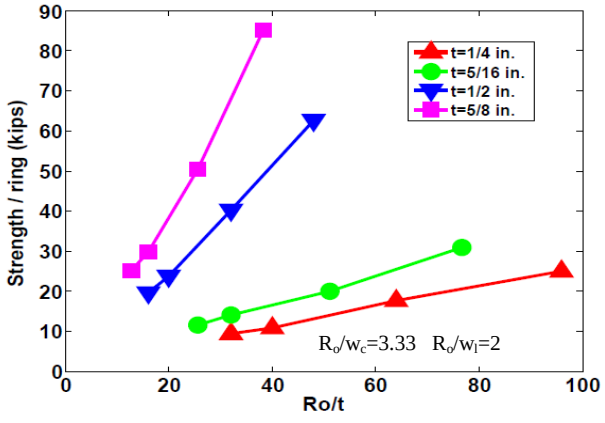

(d)

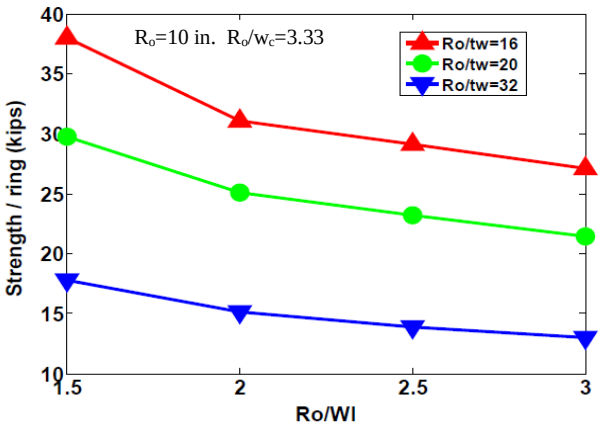

(e)

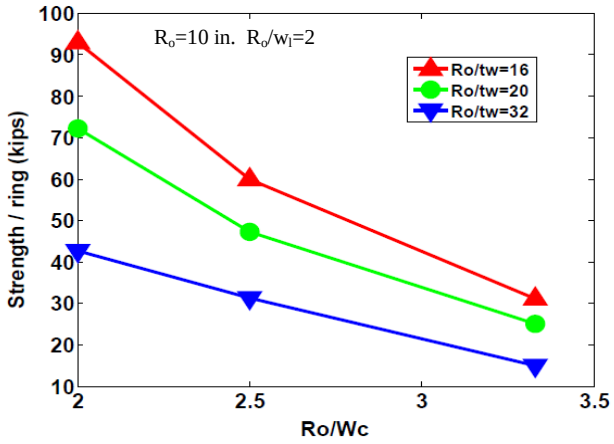

(f)

Figure A.109: Trend plots for strength per ring

APPENDIX A2

BEHAVIOR TRENDS FOR FULL-WALL STIFFNESS

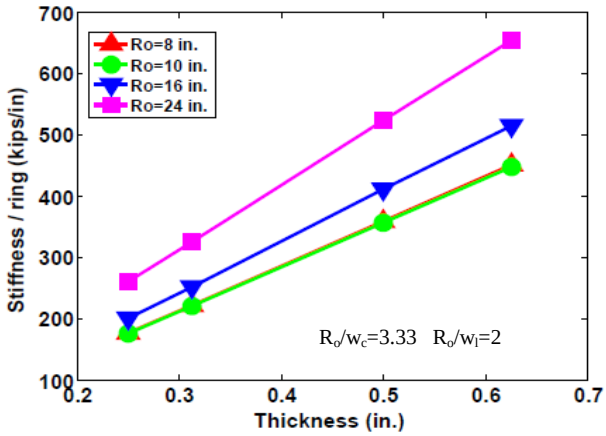

(a)

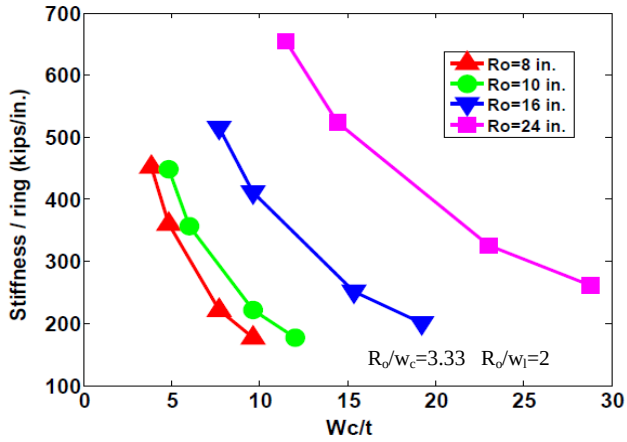

(b)

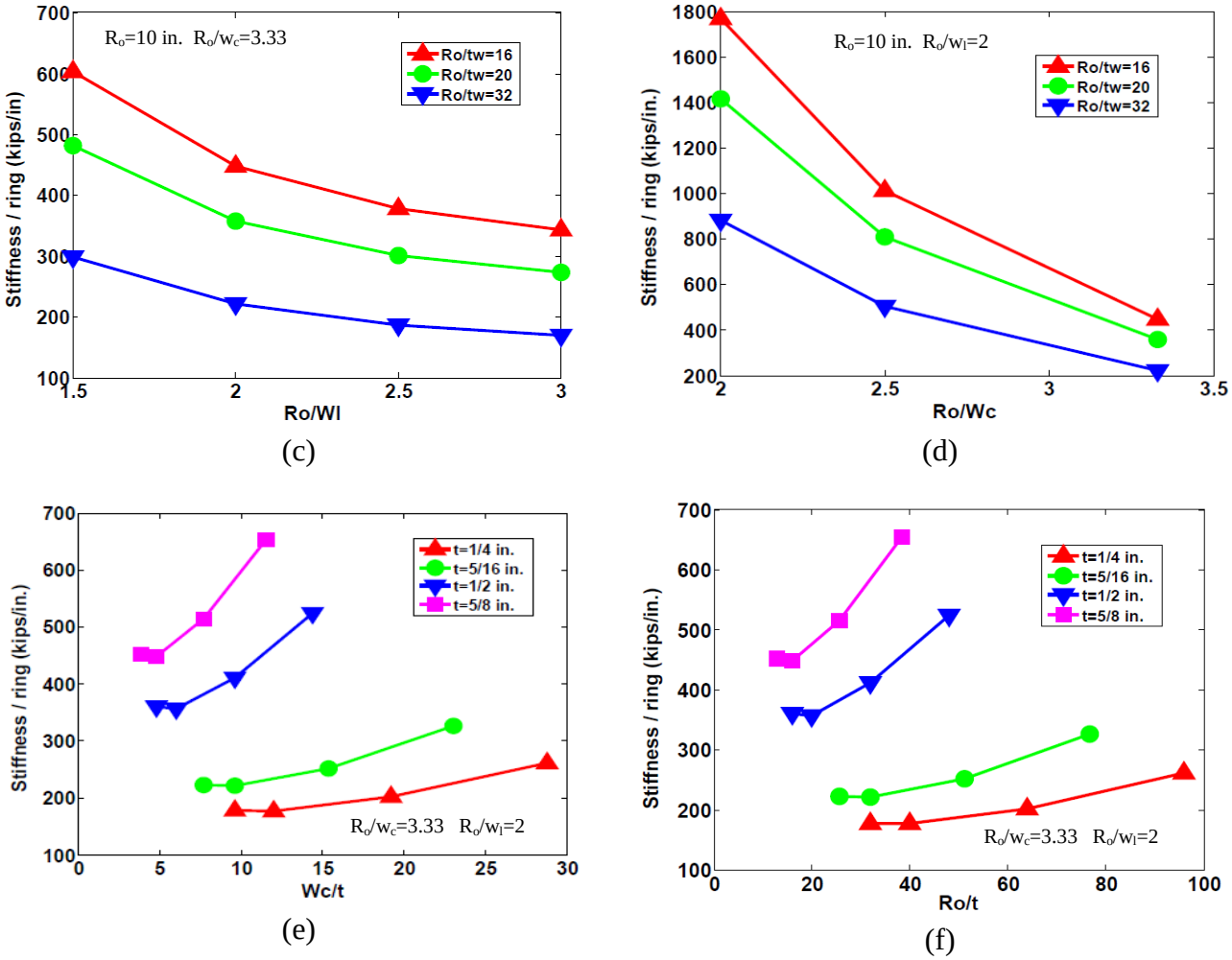

Figure A.110: Trend plots for stiffness per ring

APPENDIX A3

BEHAVIOR TRENDS FOR FULL-WALL YIELD DRIFT %

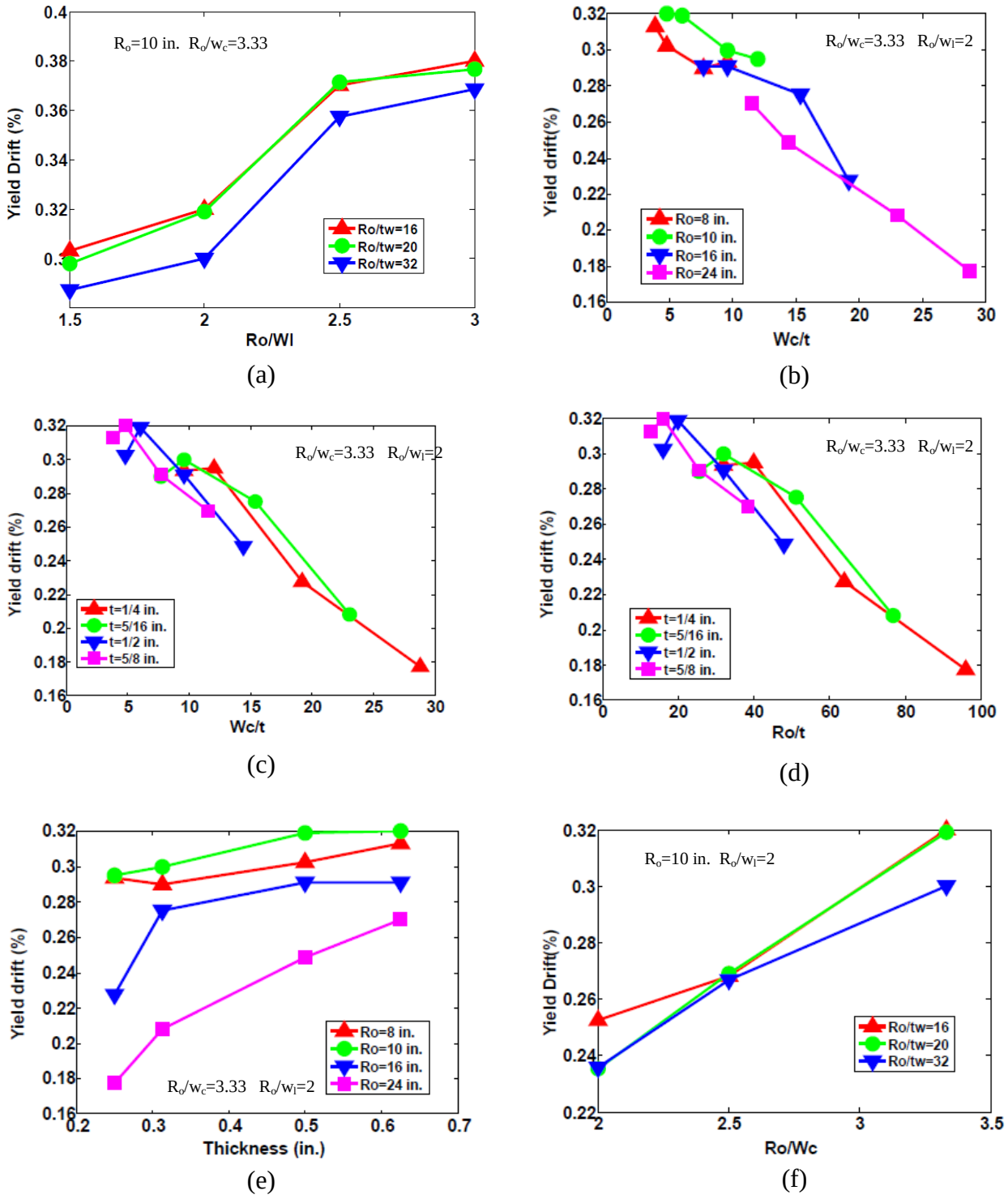

Figure A.111: Trend plots for yield drift %

APPENDIX A4

BEHAVIOR TRENDS FOR TOTAL DISSIPATED ENERGY

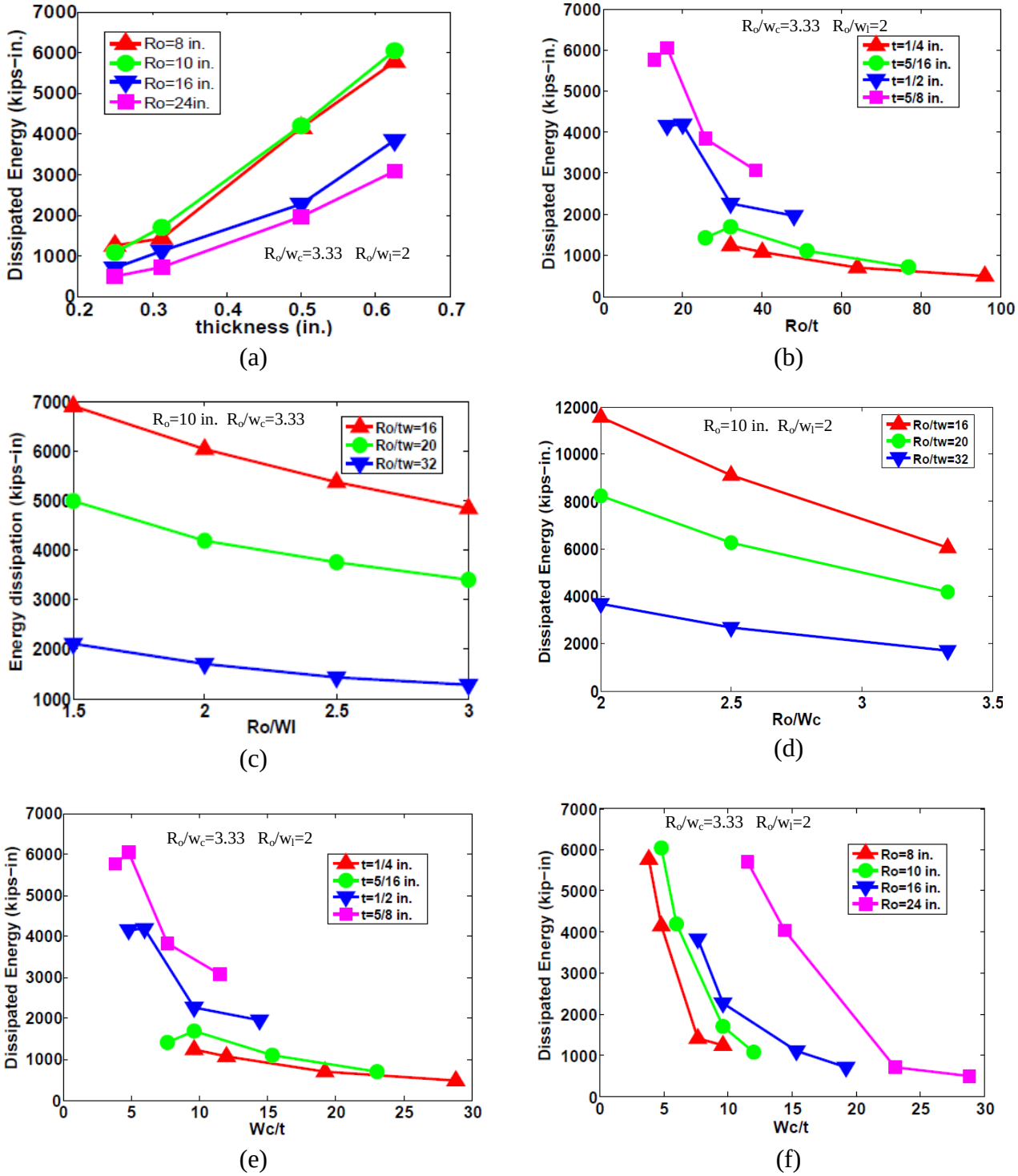

Figure A.112: Trend plots for total dissipated energy

APPENDIX A5

BEHAVIOR TRENDS FOR ENERGY DISSIPATION RATIO

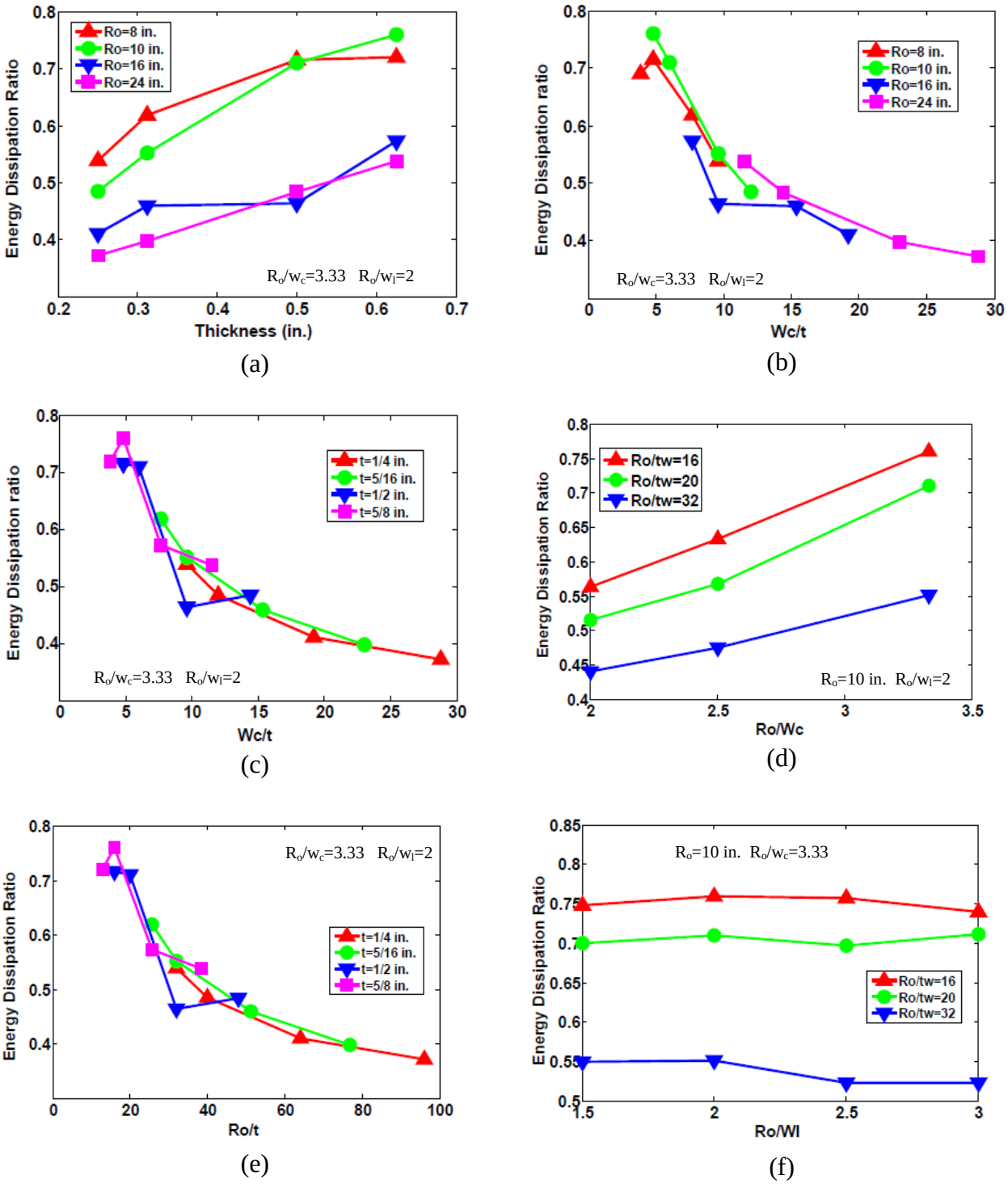

Figure A.113: Trend plots for energy dissipation ratio

APPENDIX A6

BEHAVIOR TRENDS FOR BUCKLING RATIO

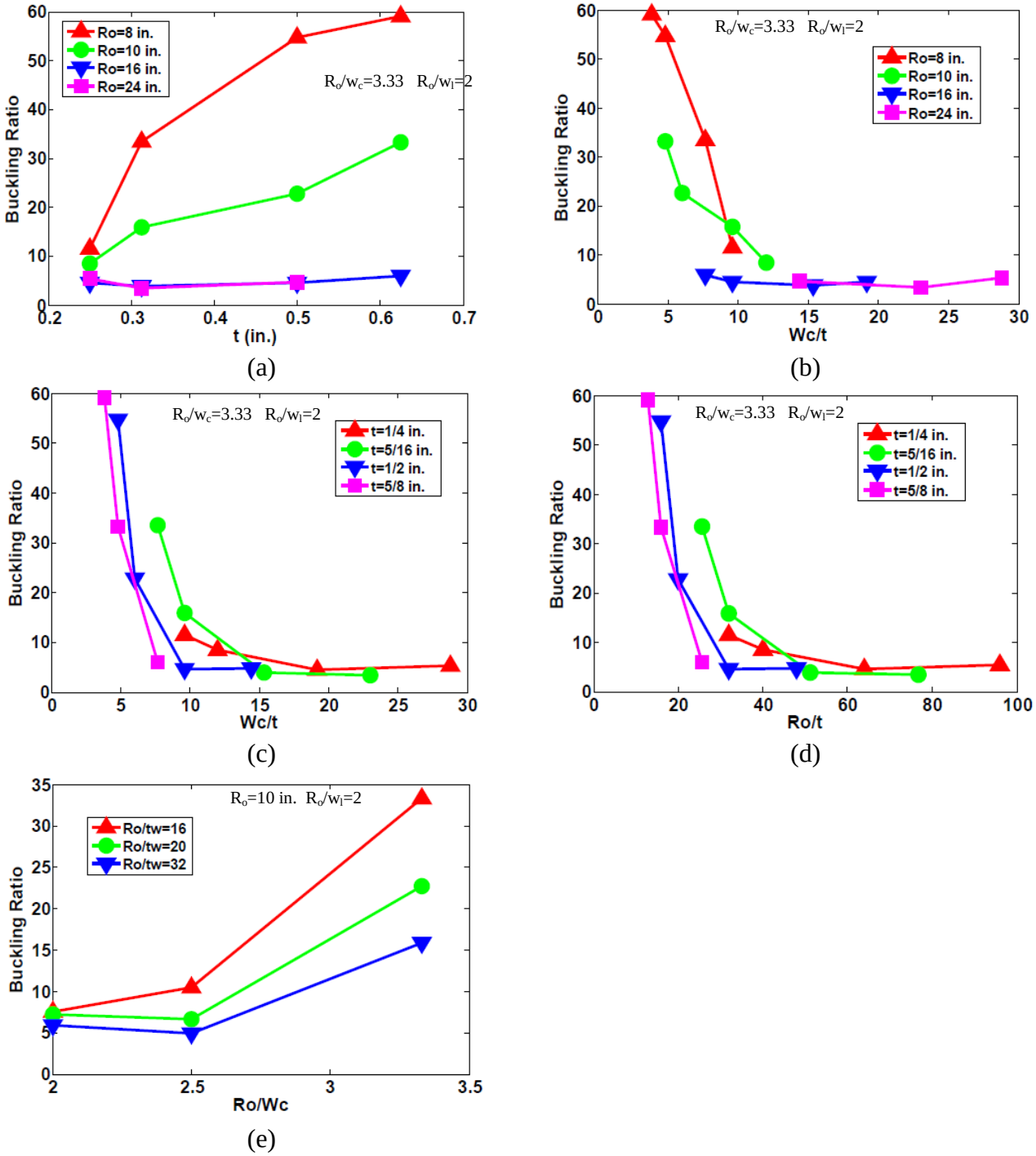

Figure A.114: Trend plots for buckling ratio

APPENDIX A7

BEHAVIOR TRENDS FOR LENGTH OF CUT

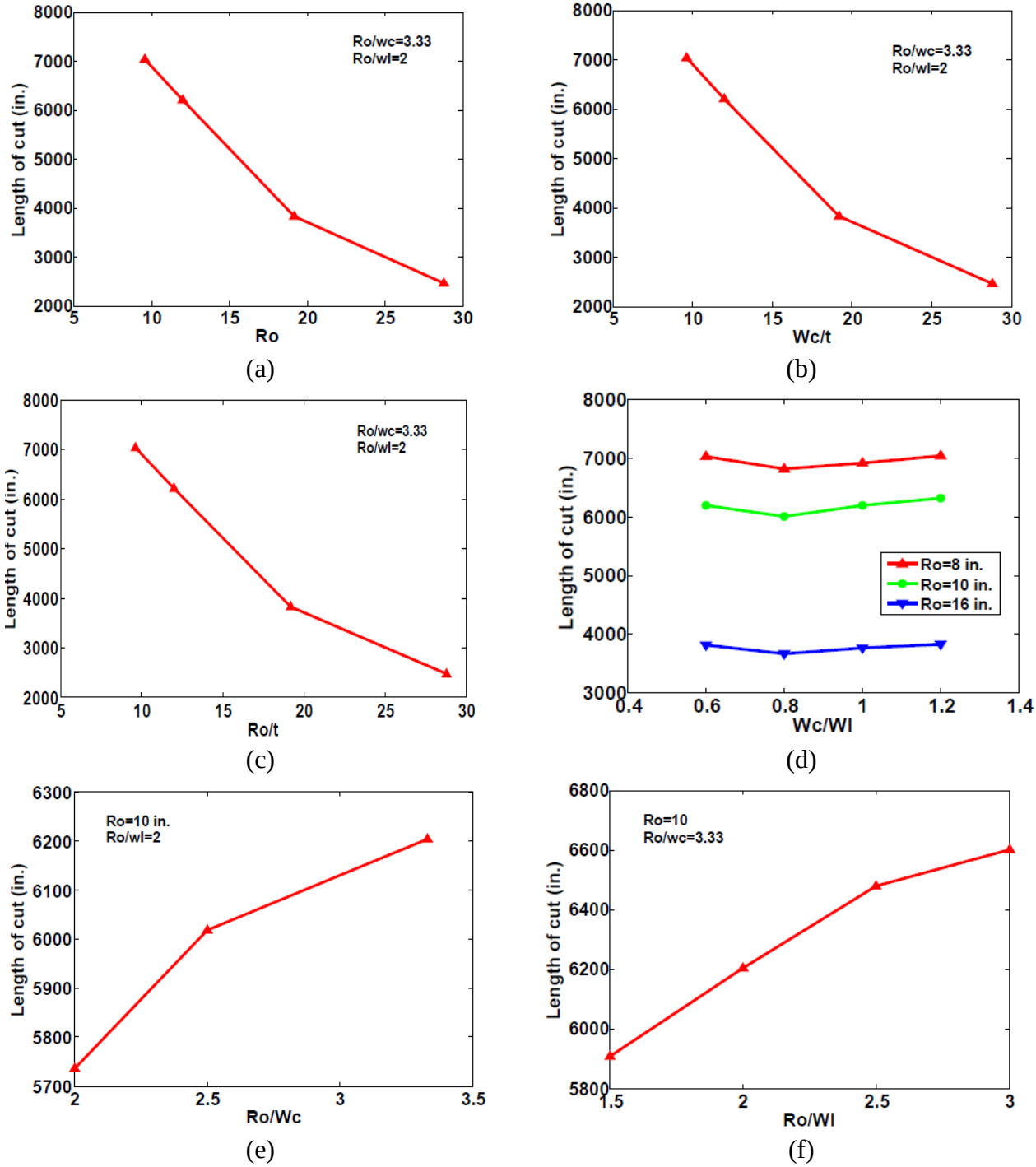

Figure A.115: Trend plots for cutting length

APPENDIX B: HYSTERETIC PLOTS

This appendix tabulates the hysteresis plots generated for each test specimen which was the part of the parametric study.

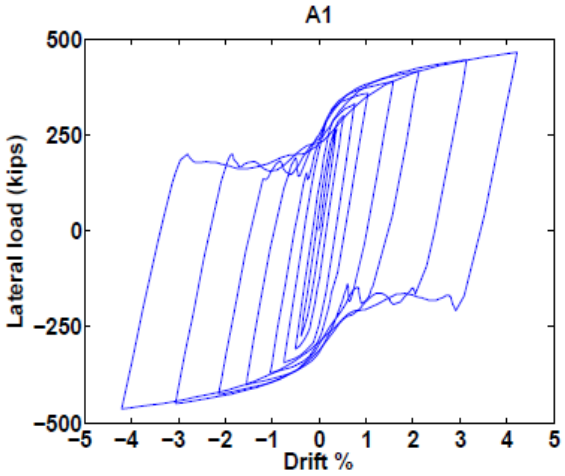

(a)

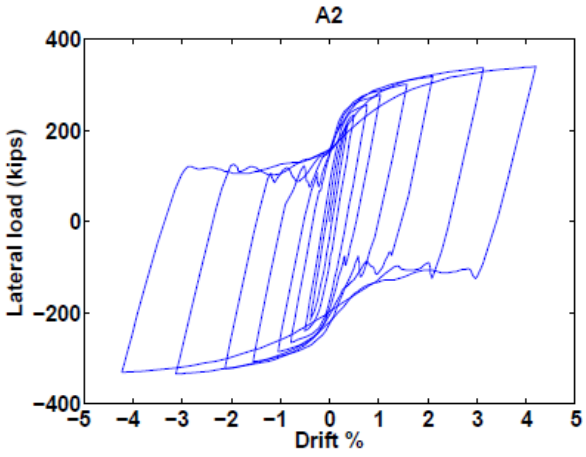

(b)

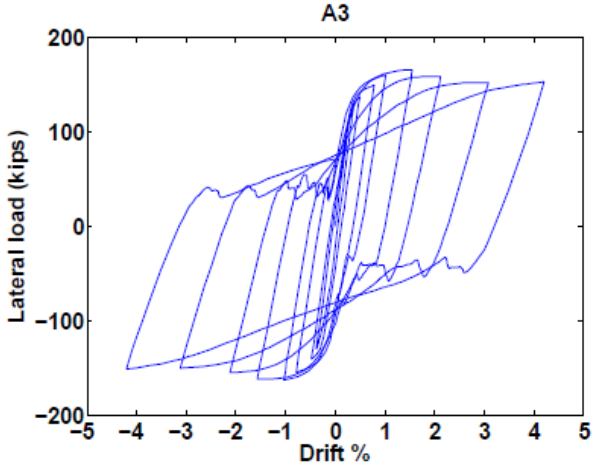

(c)

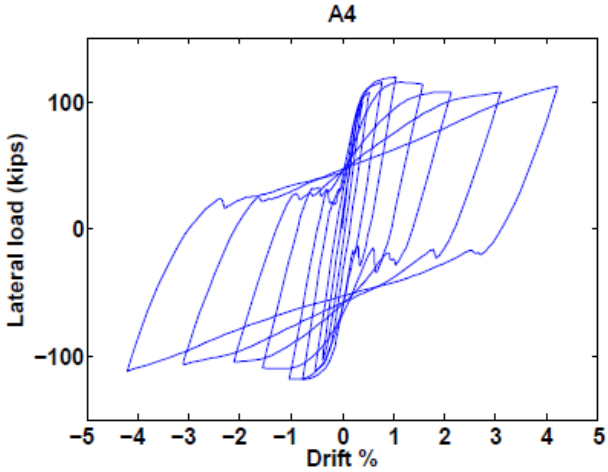

(d)

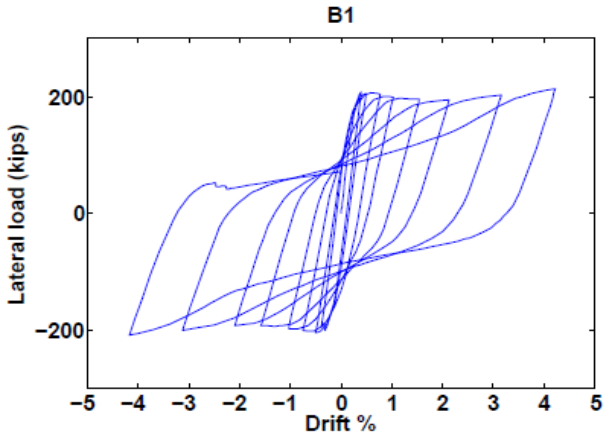
B1
Lateral load (kips)
Drift %

(e)

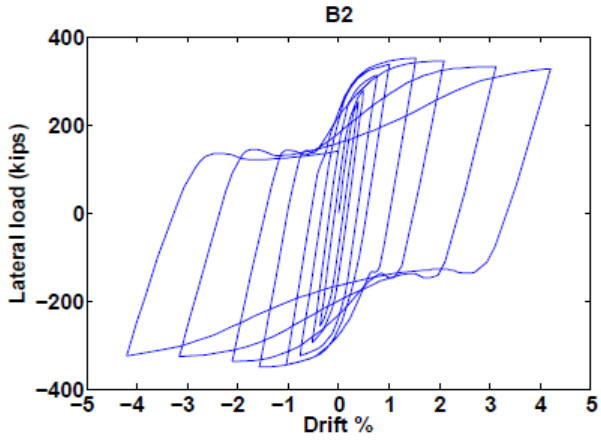
B2
Lateral load (kips)
Drift %

(f)

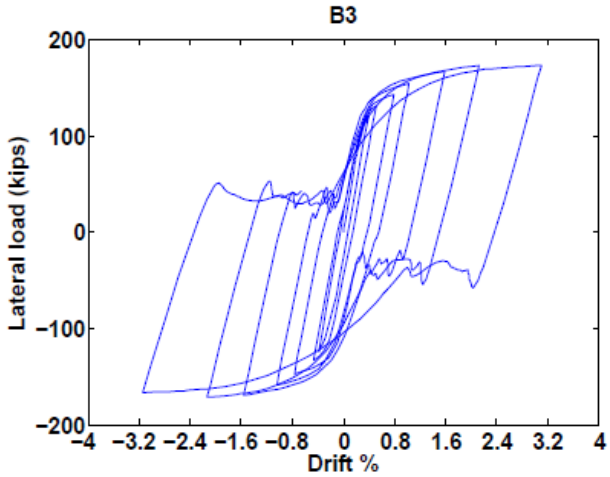
B3
Lateral load (kips)
Drift %

(g)

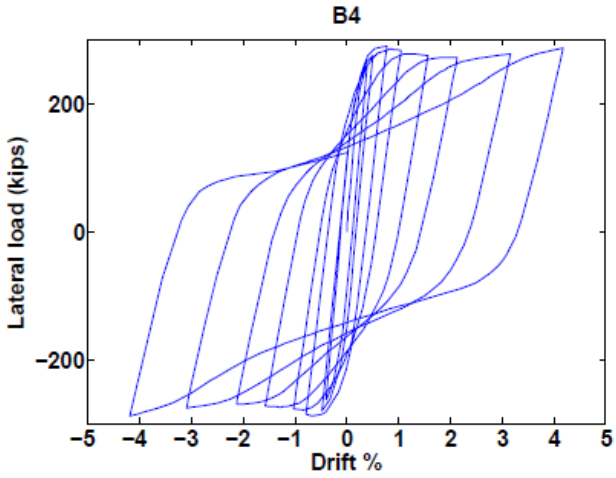
B4
Lateral load (kips)
Drift %

(h)

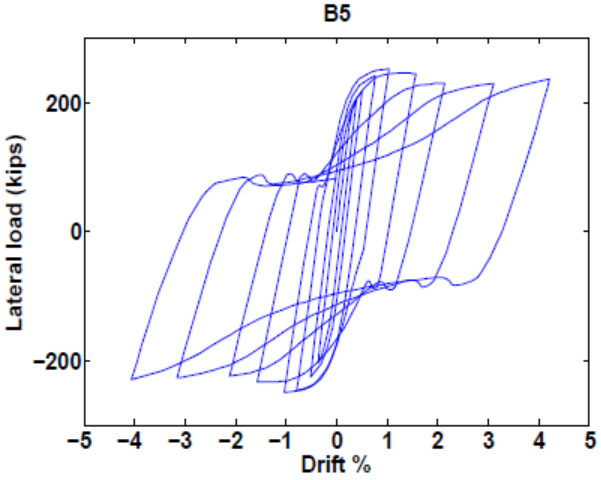
B5
Lateral load (kips)
Drift %

(i)

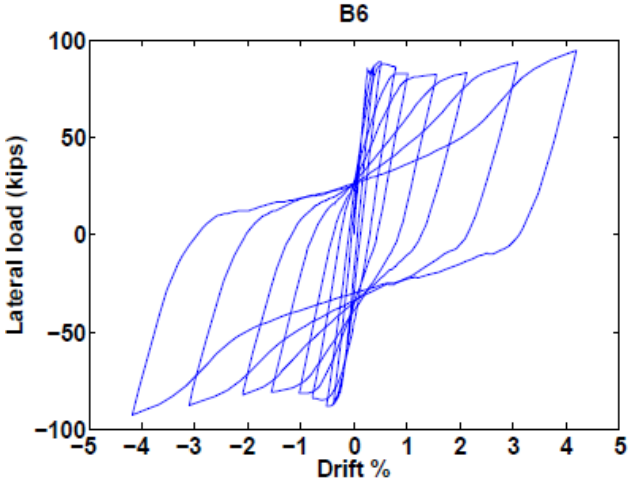
B6
Lateral load (kips)
Drift %

(j)

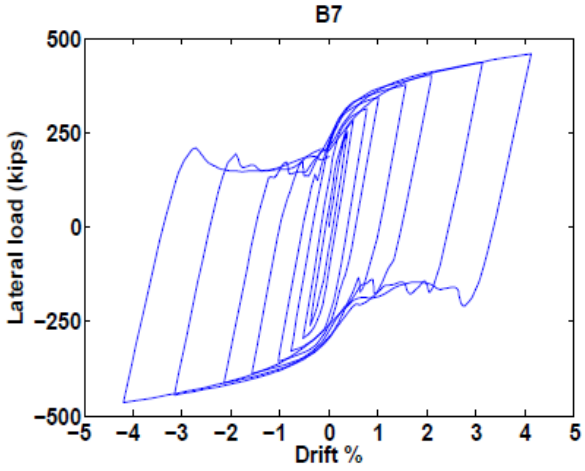
B7
Lateral load (kips)
Drift %

(k)

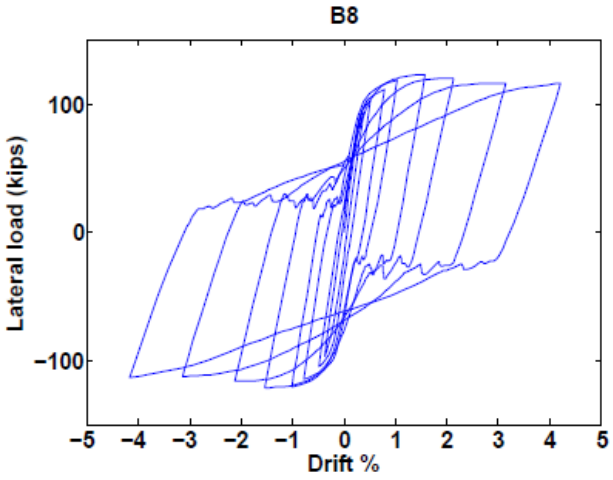
B8
Lateral load (kips)
Drift %

(l)

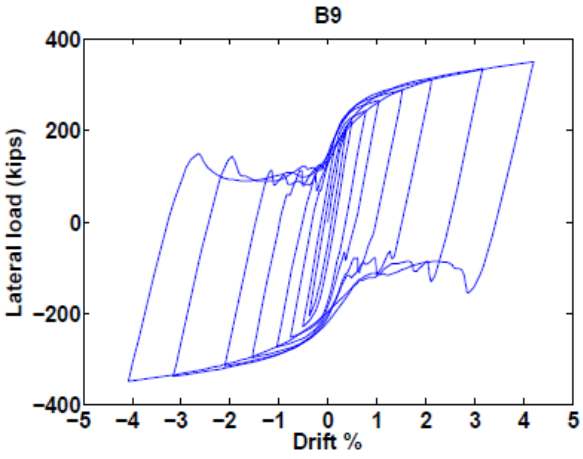
B9
Lateral load (kips)
Drift %

(m)

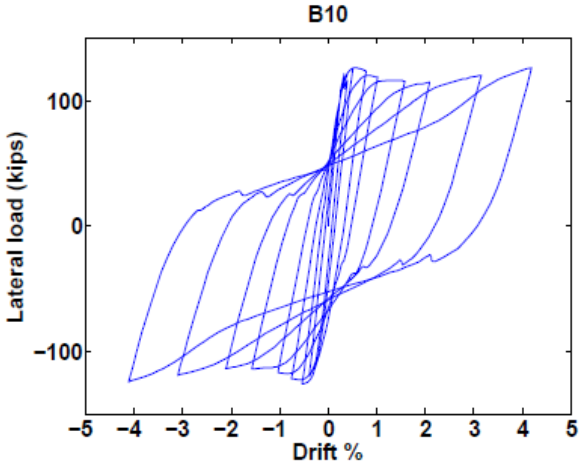
B10
Lateral load (kips)
Drift %

(n)

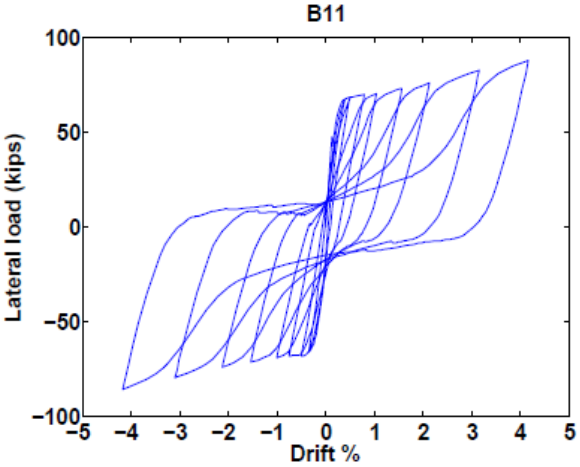
B11
Lateral load (kips)
Drift %

(o)

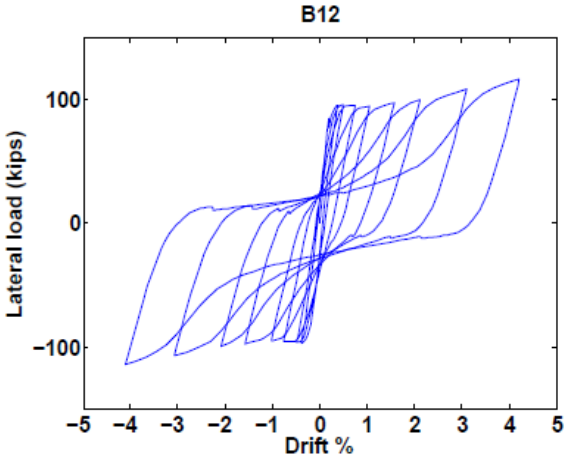
B12
Lateral load (kips)
Drift %

(p)

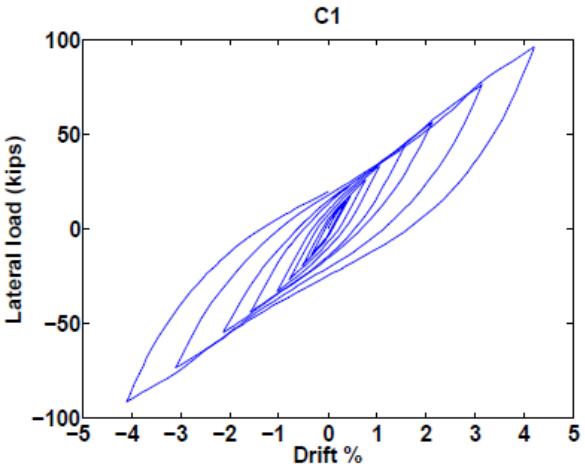
C1
Lateral load (kips)
Drift %

(q)

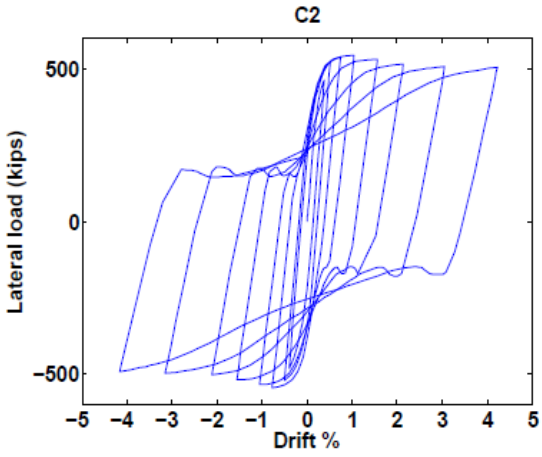
C2
Lateral load (kips)
Drift %

(r)

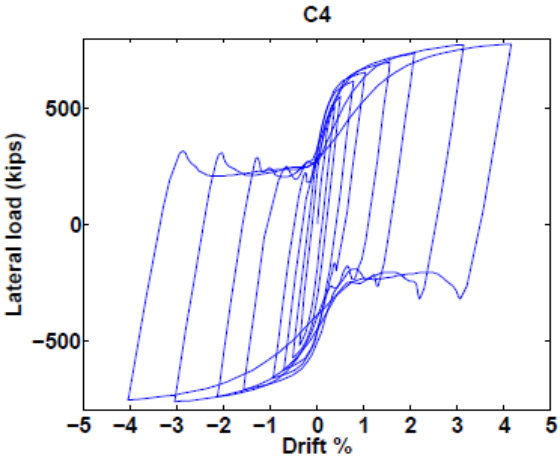
C4
Lateral load (kips)
Drift %

(s)

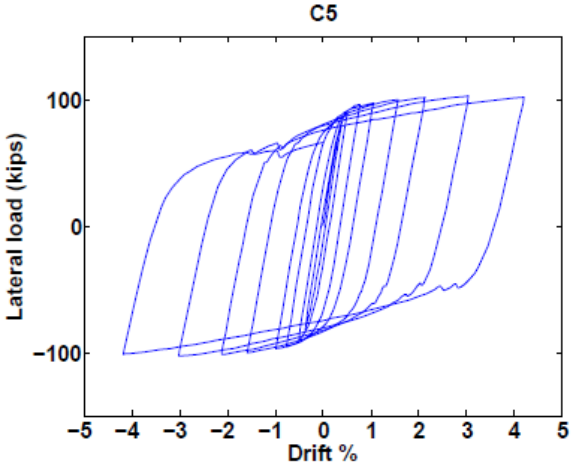
C5
Lateral load (kips)
Drift %

(t)

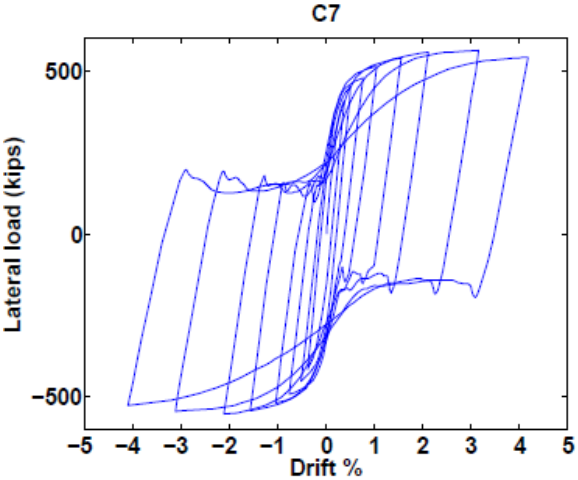
C7
Lateral load (kips)
Drift %

(u)

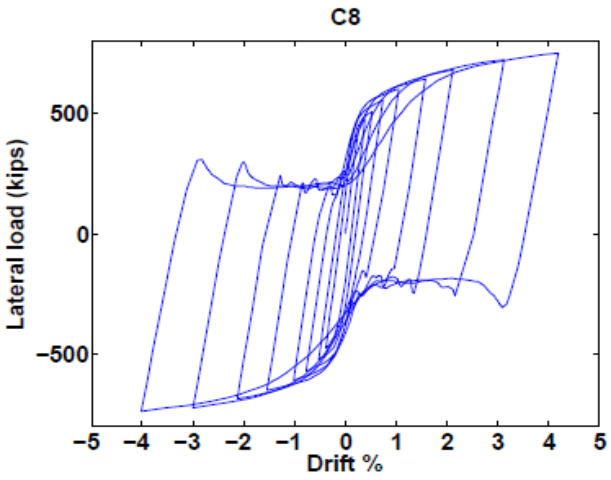
C8
Lateral load (kips)
Drift %

(v)

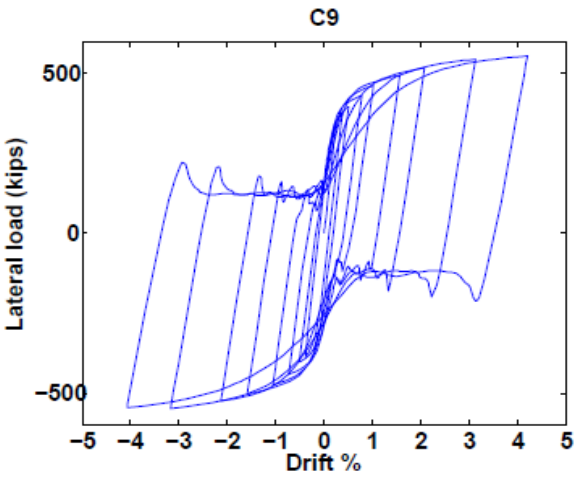
C9
Lateral load (kips)
Drift %

(w)

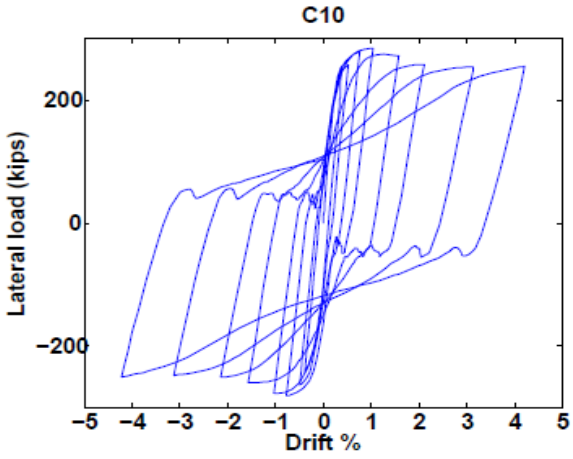
C10
Lateral load (kips)
Drift %

(x)

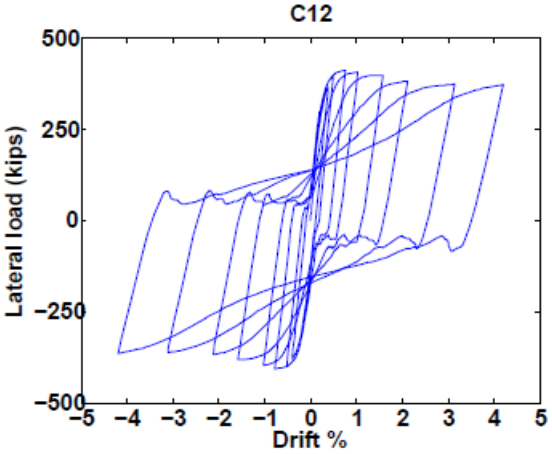
C12
Lateral load (kips)
Drift %

(y)

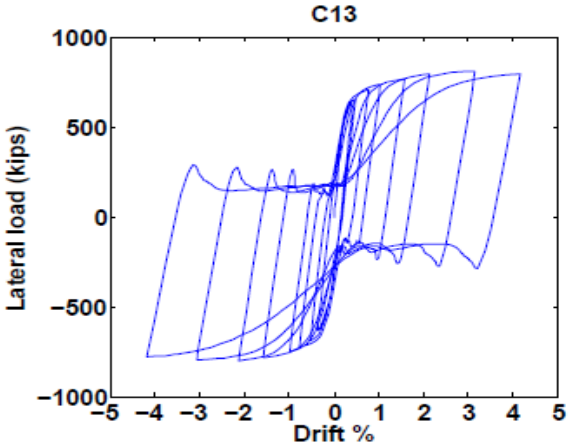
C13
Lateral load (kips)
Drift %

(z)

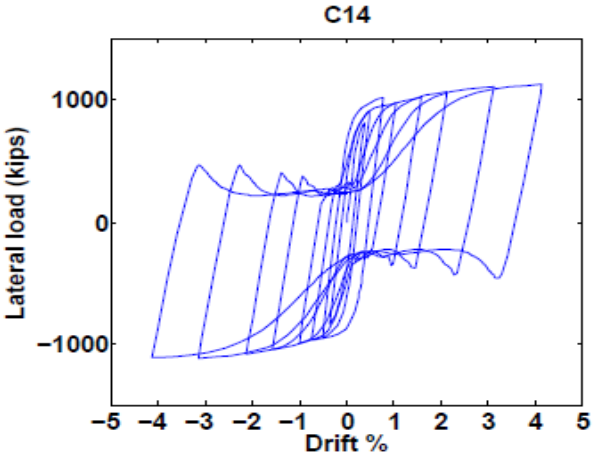
C14
Lateral load (kips)
Drift %

(aa)

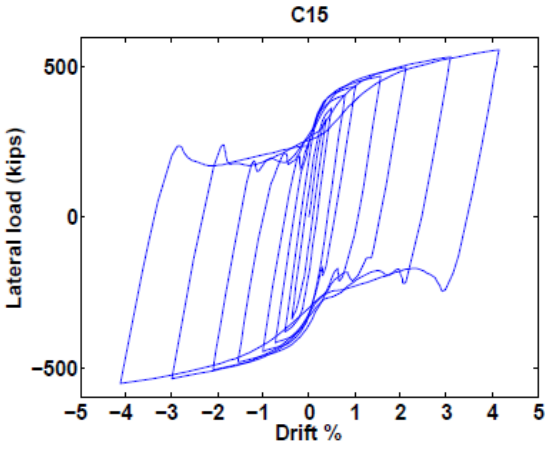
C15
Lateral load (kips)
Drift %

(ab)

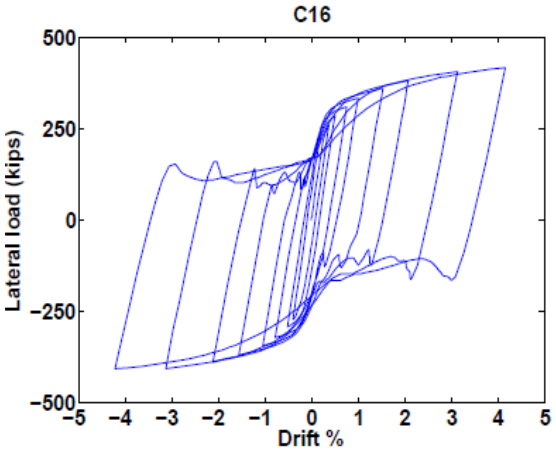

(ac)

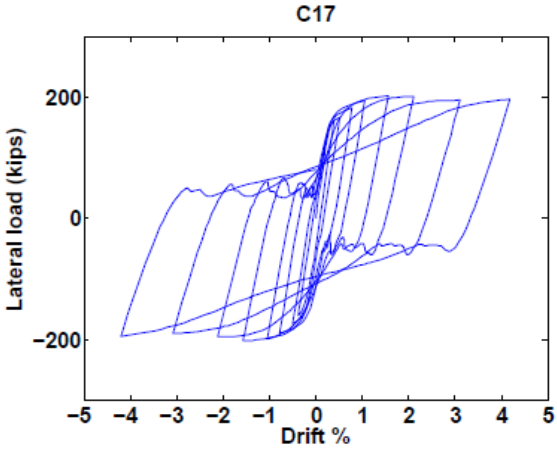

(ad)

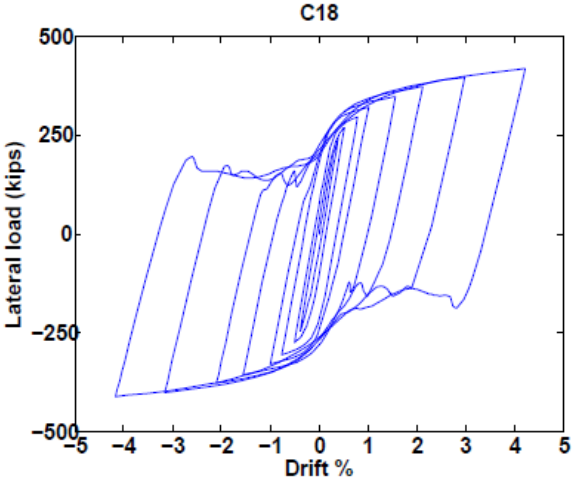

(ae)

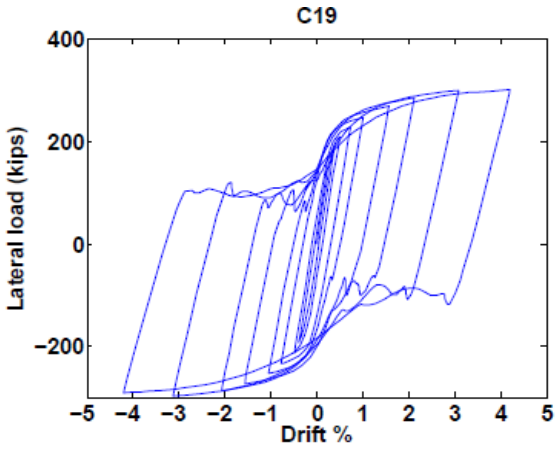

(af)

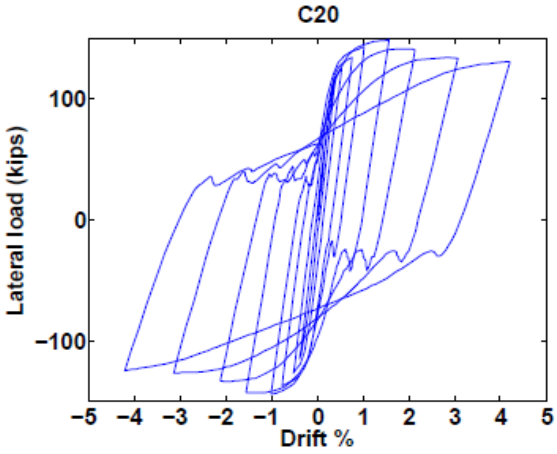

(ag)

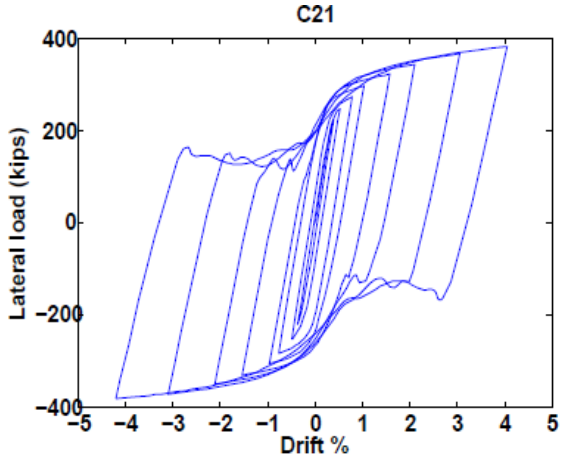

(ah)

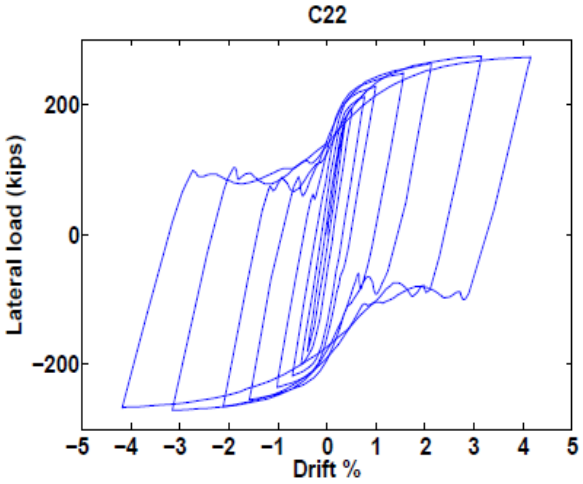

(ai)

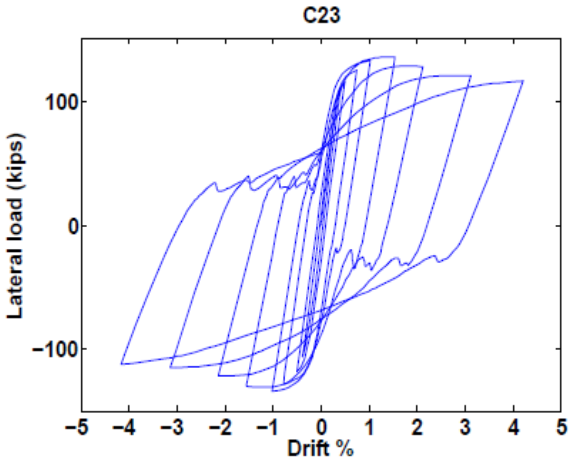

(aj)

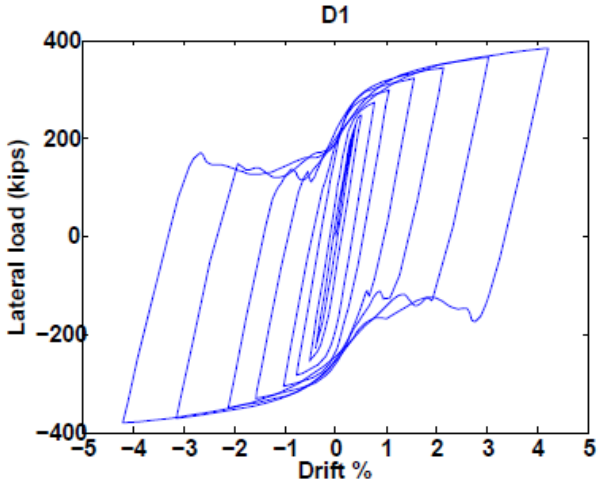

(ak)

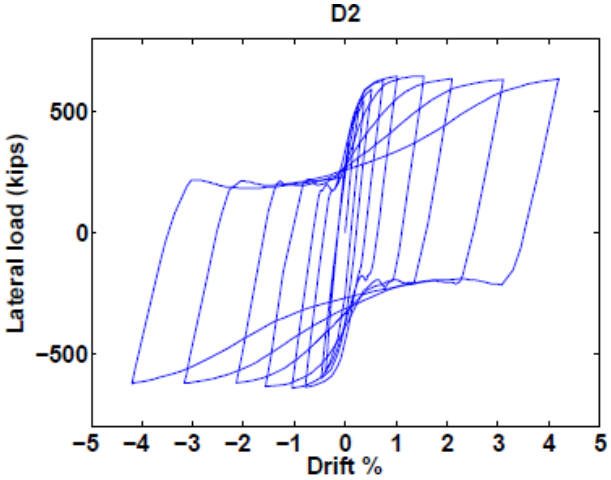

(al)

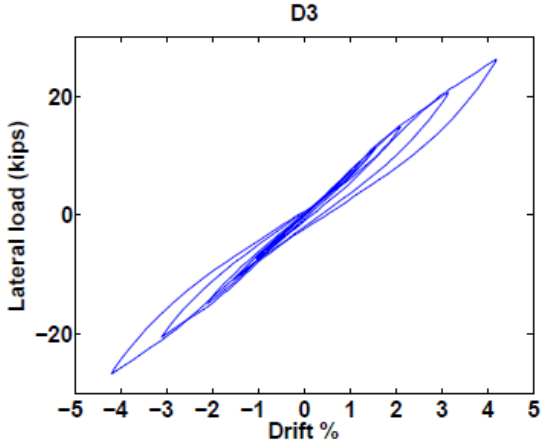

(am)

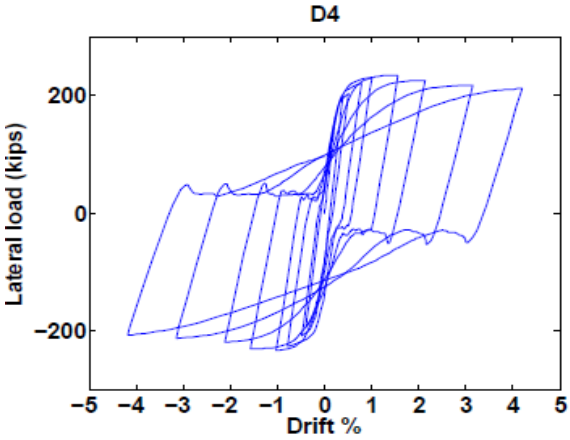

(an)

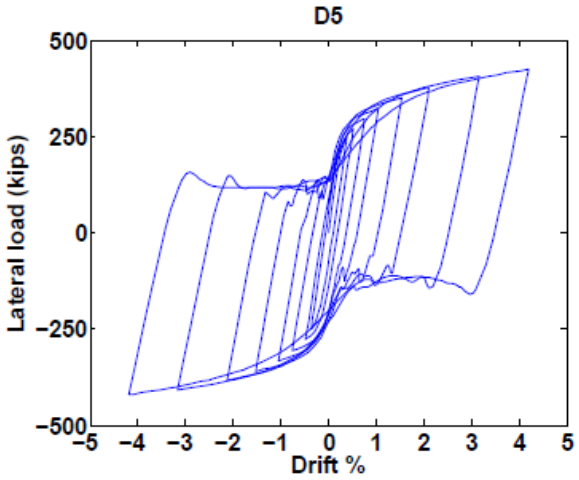

(ao)

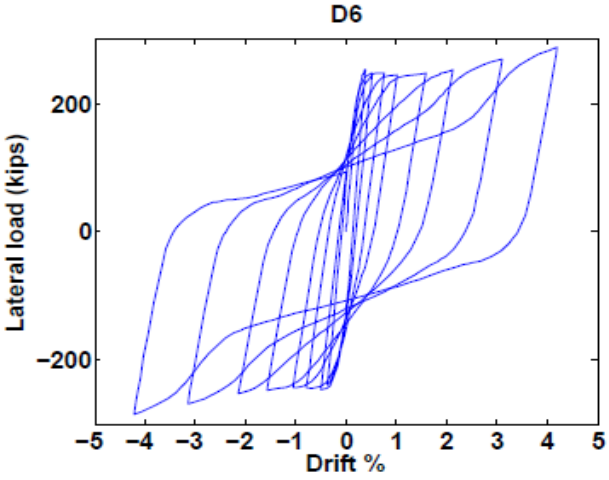

(ap)

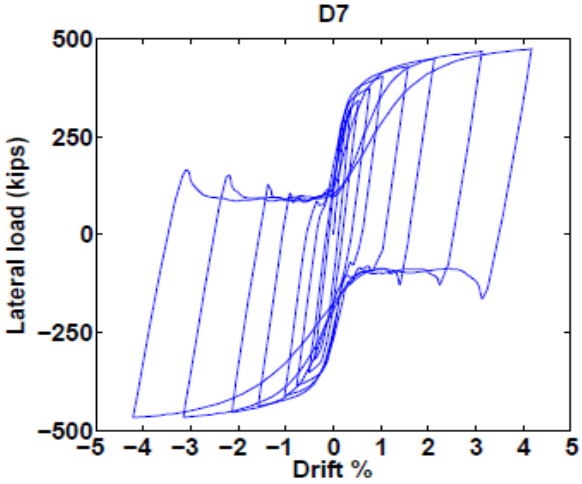

(aq)

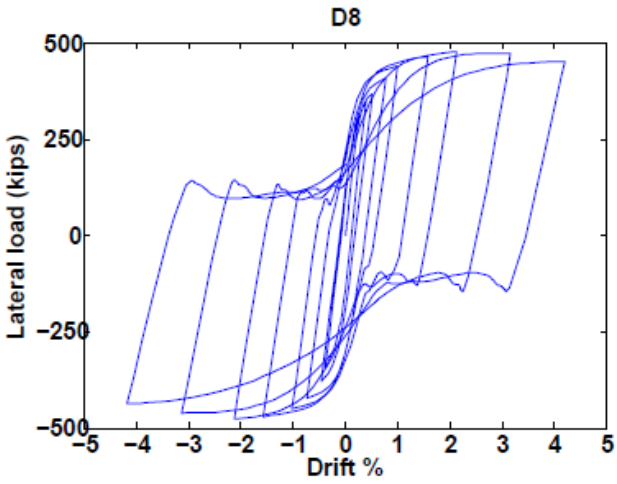

(ar)

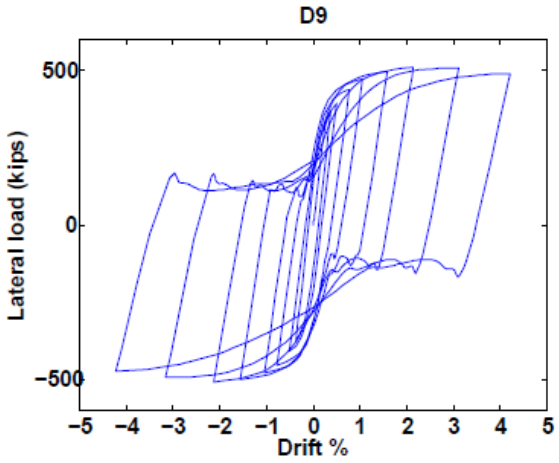

(as)

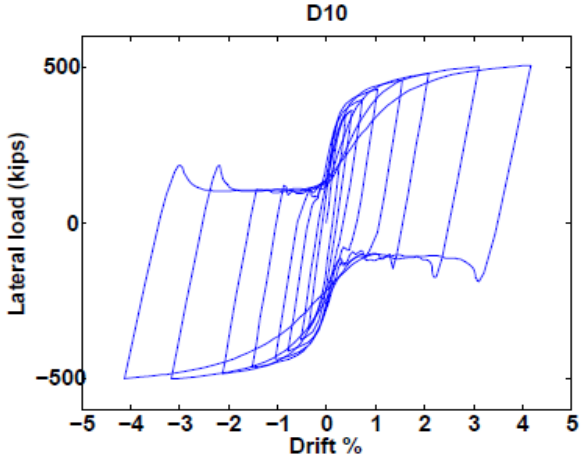

(at)

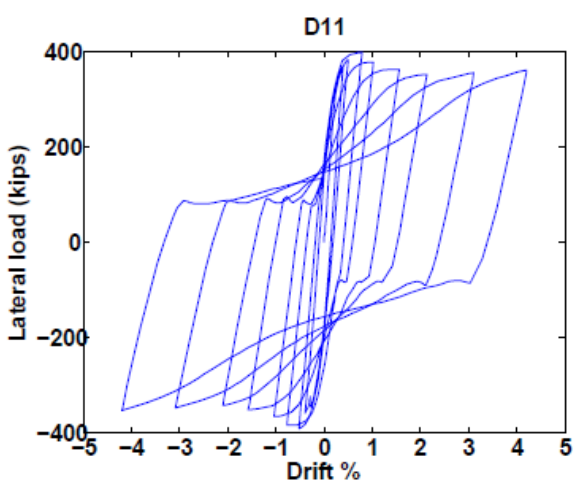

(au)

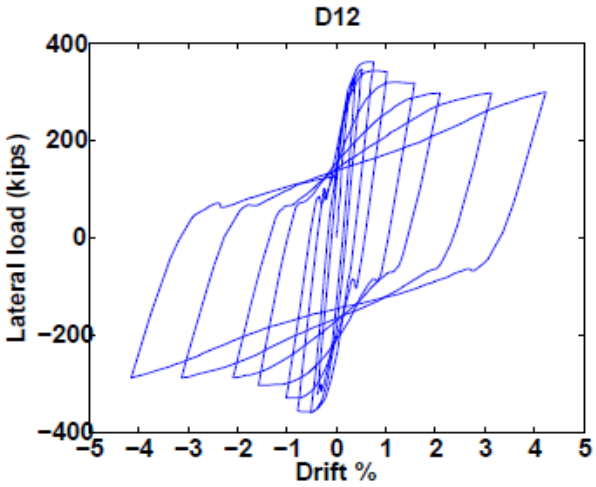

(av)

Figure A.116: Hysteresis plots for specimens

APPENDIX C: ENERGY DISSIPATION RATIO

This appendix tabulates the hysteresis behavior of an ideal specimen superimposed on the hysteresis behavior of BR-SPSW to calculate energy dissipation ratio.

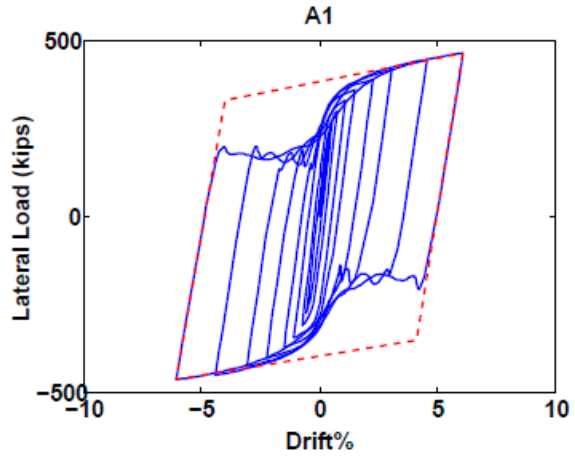

(a)

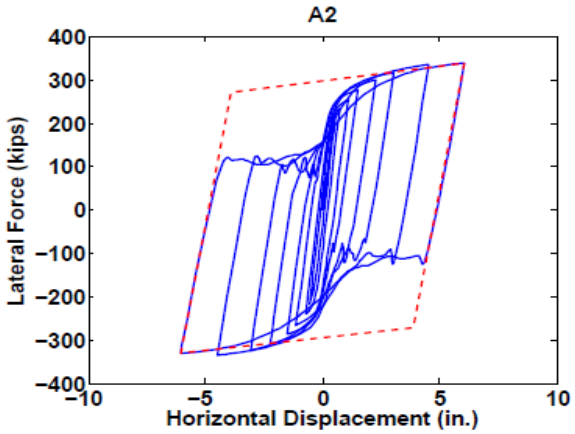

(b)

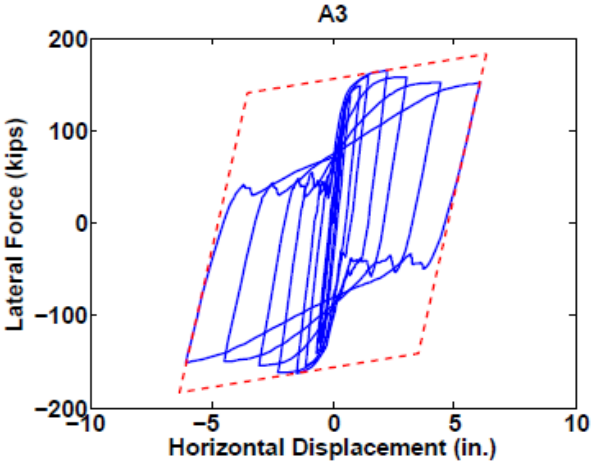

(c)

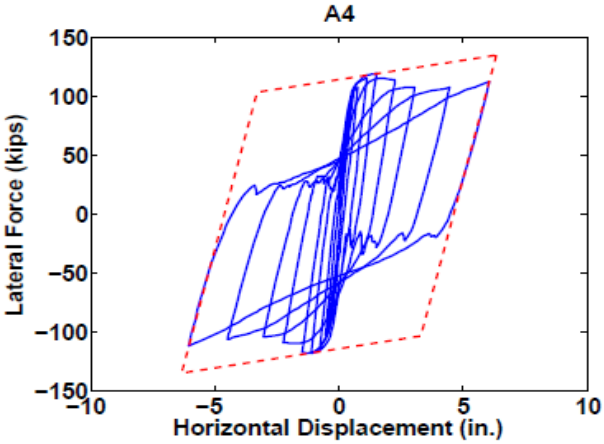

(d)

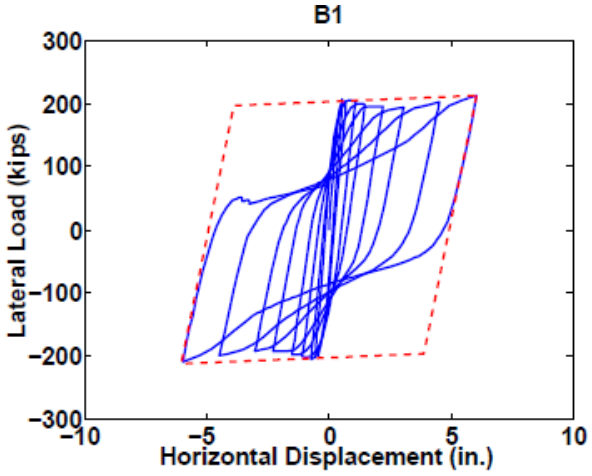
B1
Lateral Load (kips)
Horizontal Displacement (in.)

(e)

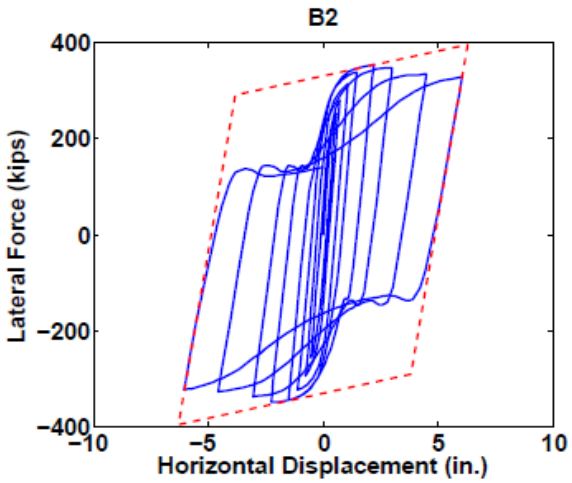
B2
Lateral Force (kips)
Horizontal Displacement (in.)

(f)

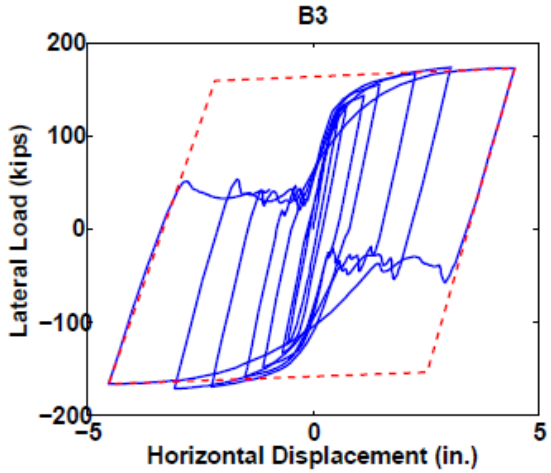
B3
Lateral Load (kips)
Horizontal Displacement (in.)

(g)

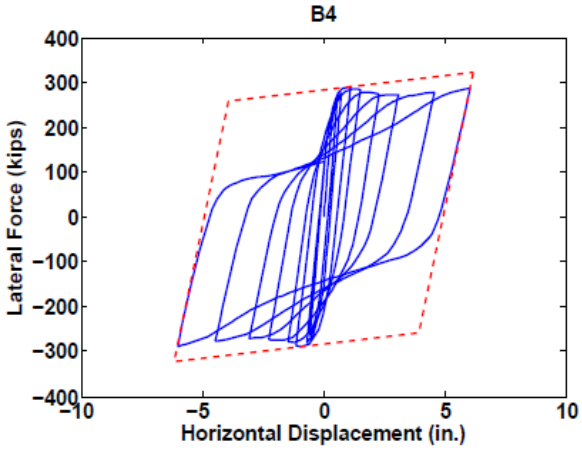
B4
Lateral Force (kips)
Horizontal Displacement (in.)

(h)

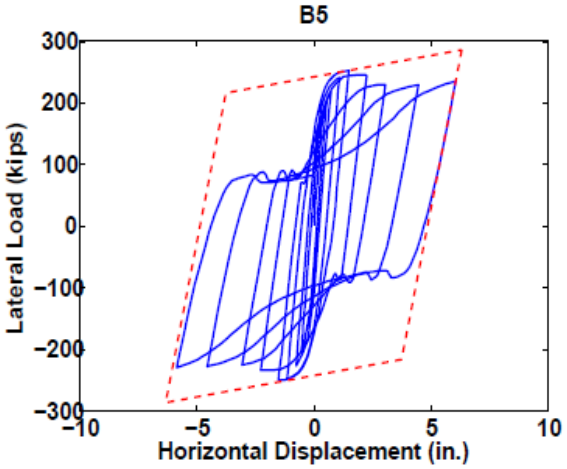
B5
Lateral Load (kips)
Horizontal Displacement (in.)

(i)

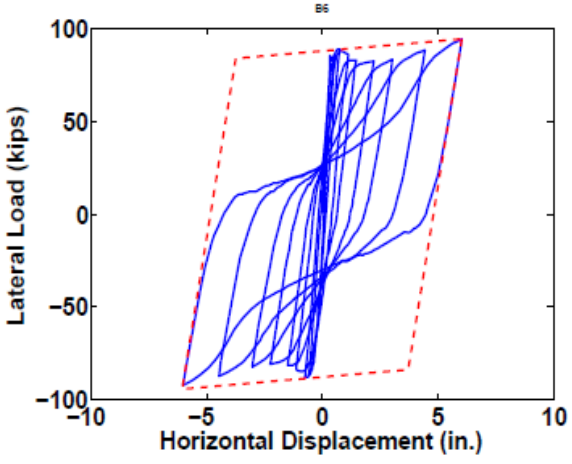
B6
Lateral Load (kips)
Horizontal Displacement (in.)

(j)

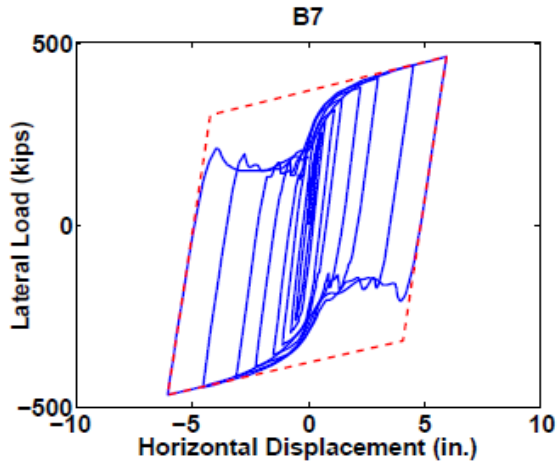
B7
Lateral Load (kips)
Horizontal Displacement (in.)

(k)

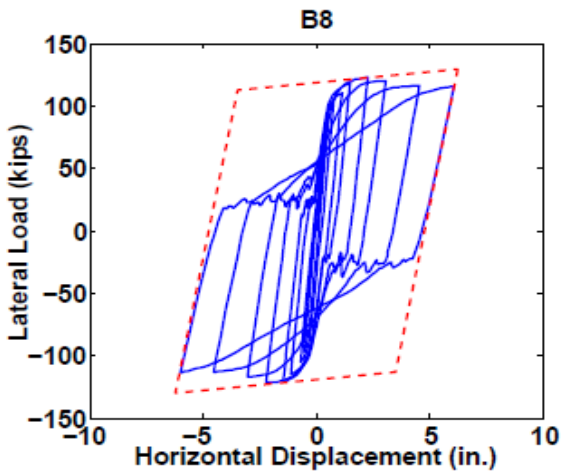
B8
Lateral Load (kips)
Horizontal Displacement (in.)

(l)

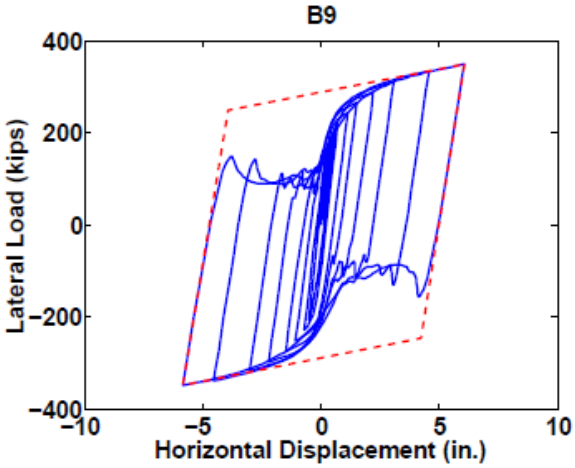
B9
Lateral Load (kips)
Horizontal Displacement (in.)

(m)

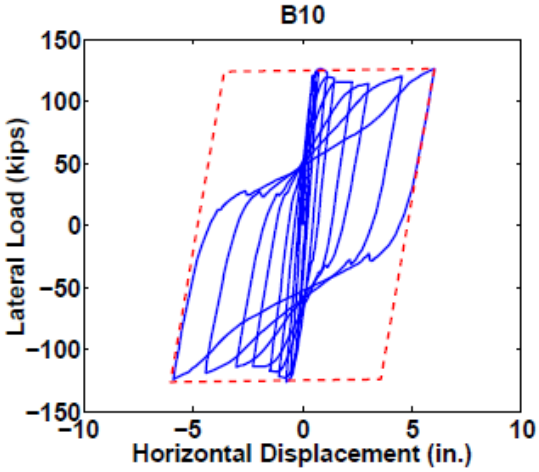
B10
Lateral Load (kips)
Horizontal Displacement (in.)

(o)

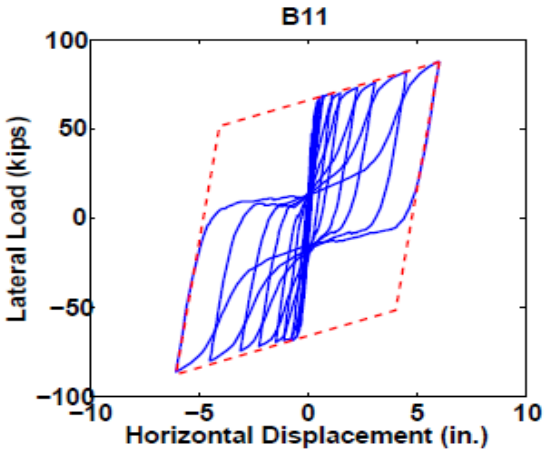
B11
Lateral Load (kips)
Horizontal Displacement (in.)

(p)

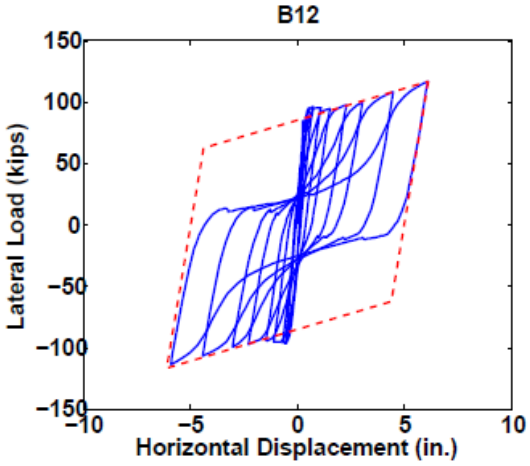
B12
Lateral Load (kips)
Horizontal Displacement (in.)

(q)

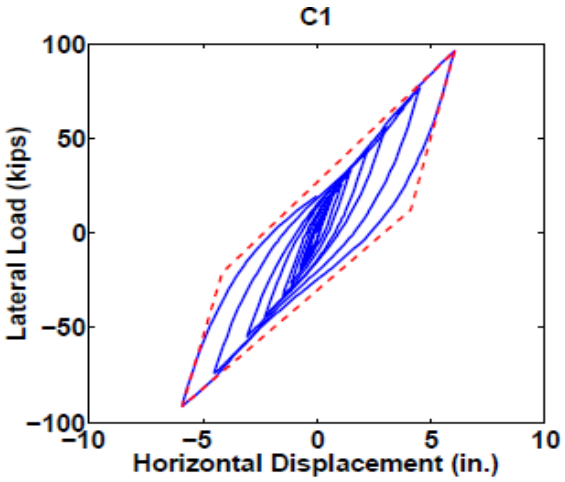
C1
Lateral Load (kips)
Horizontal Displacement (in.)

(r)

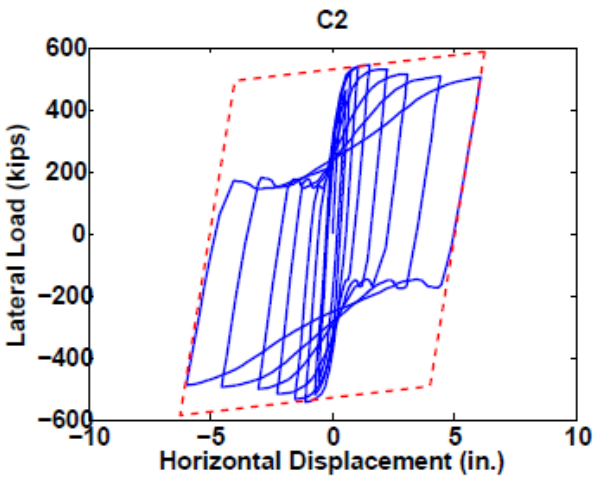
C2
Lateral Load (kips)
Horizontal Displacement (in.)

(s)

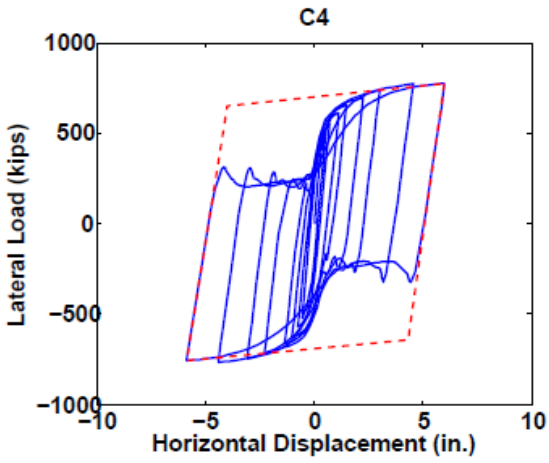
C4
Lateral Load (kips)
Horizontal Displacement (in.)

(t)

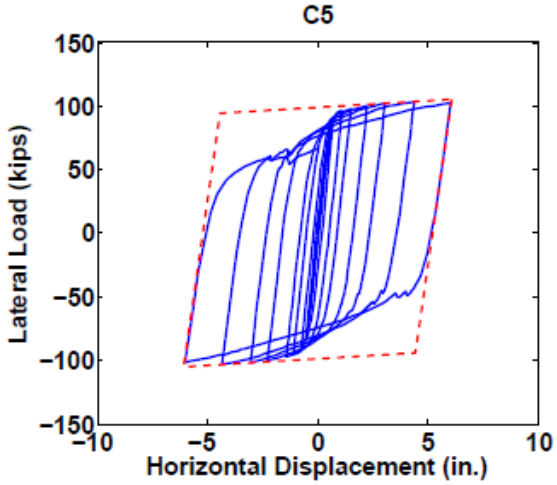
C5
Lateral Load (kips)
Horizontal Displacement (in.)

(u)

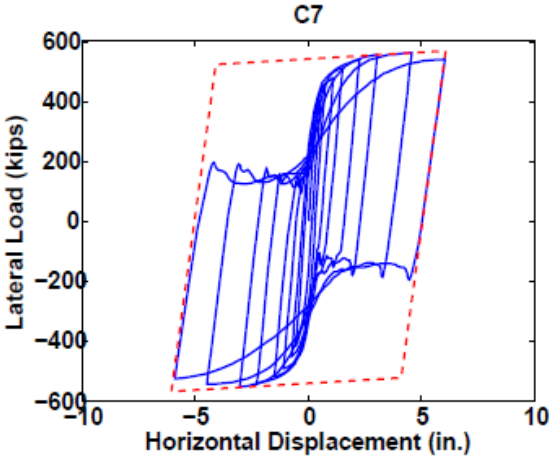
C7
Lateral Load (kips)
Horizontal Displacement (in.)

(v)

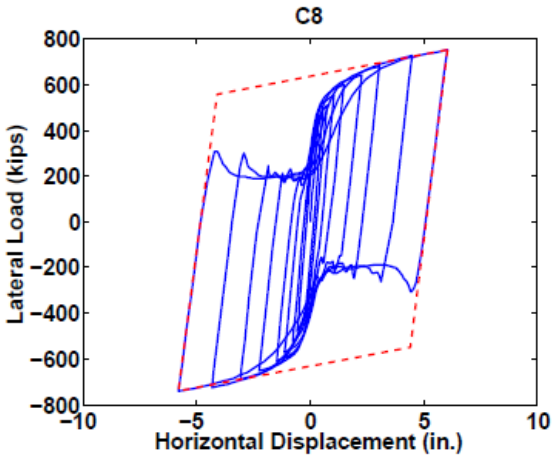
C8
Lateral Load (kips)
Horizontal Displacement (in.)

(w)

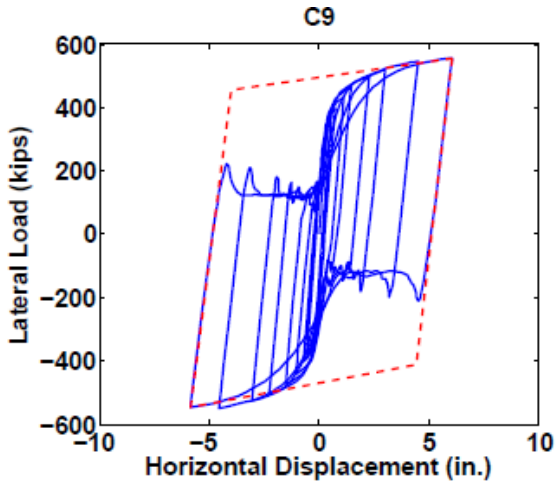
C9
Lateral Load (kips)
Horizontal Displacement (in.)

(x)

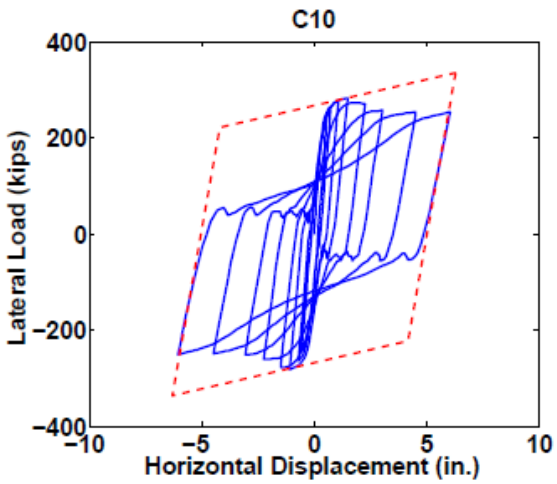
C10
Lateral Load (kips)
Horizontal Displacement (in.)

(y)

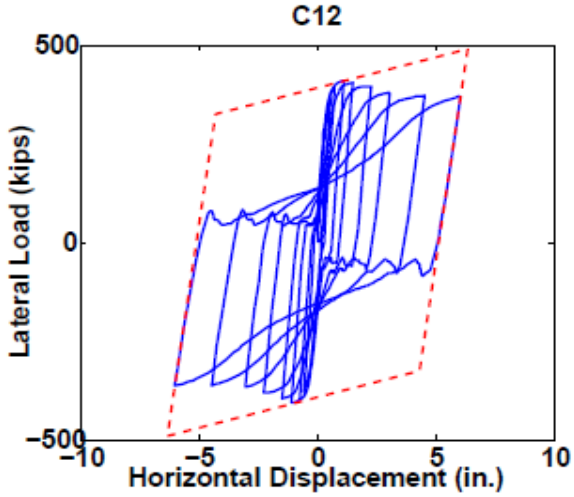
C12
Lateral Load (kips)
Horizontal Displacement (in.)

(z)

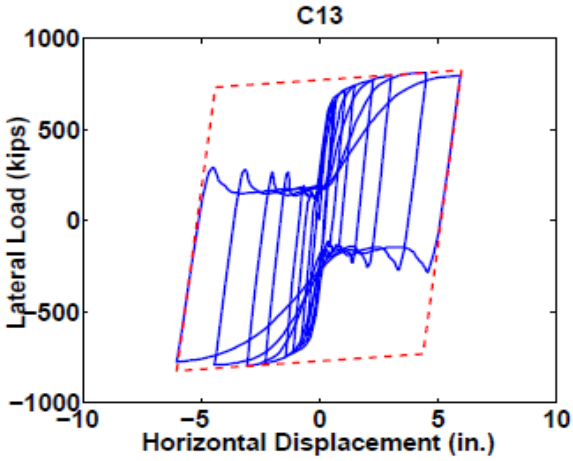
C13
Lateral Load (kips)
Horizontal Displacement (in.)

(aa)

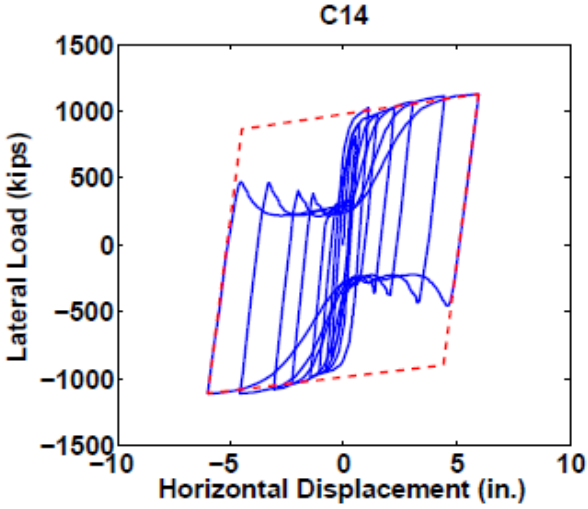
C14
Lateral Load (kips)
Horizontal Displacement (in.)

(ab)

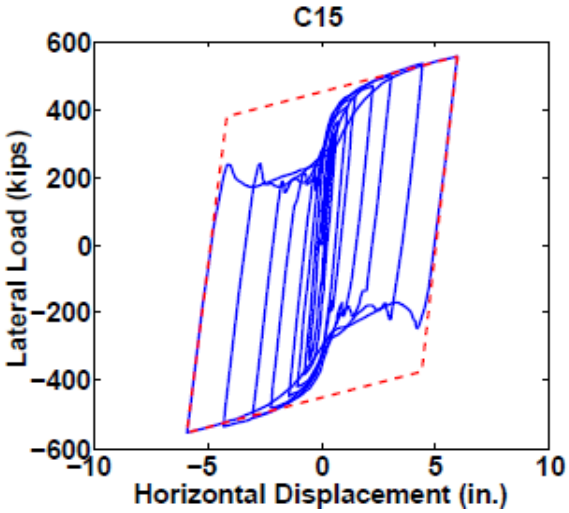
C15
Lateral Load (kips)
Horizontal Displacement (in.)

(ac)

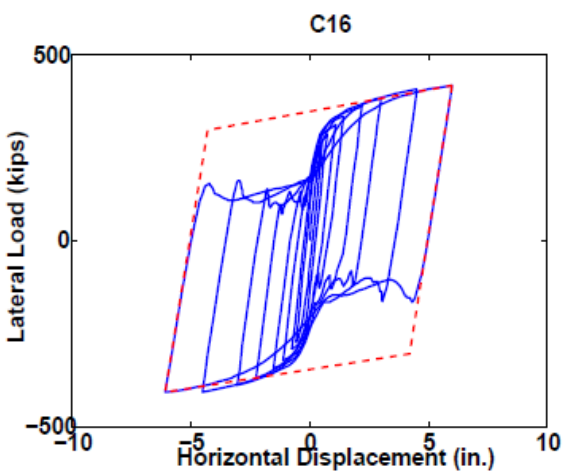

(ad)

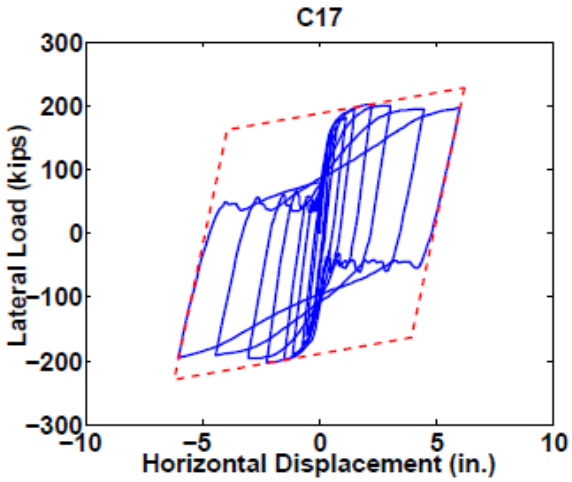

(ae)

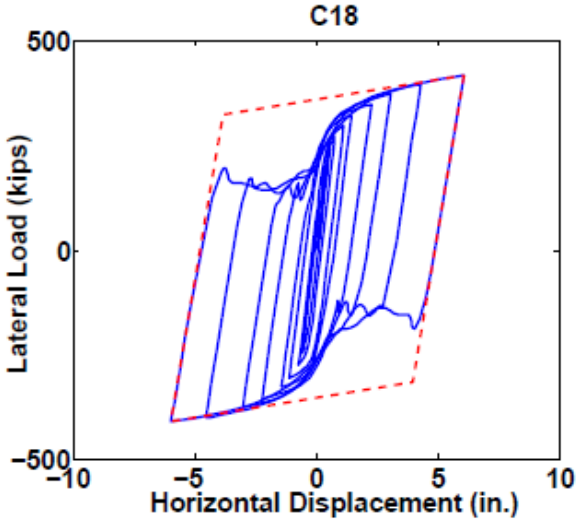

(af)

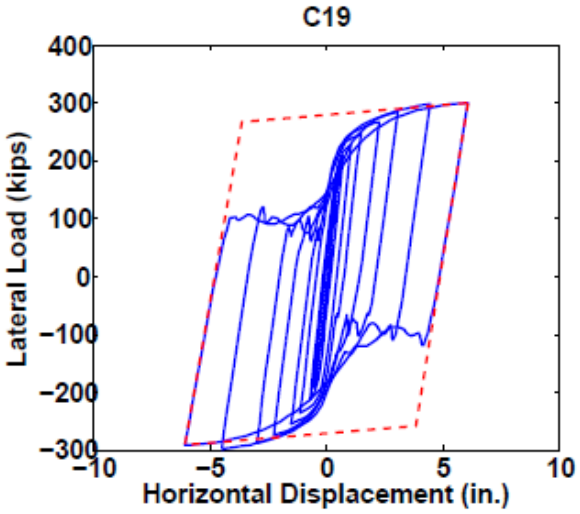

(ag)

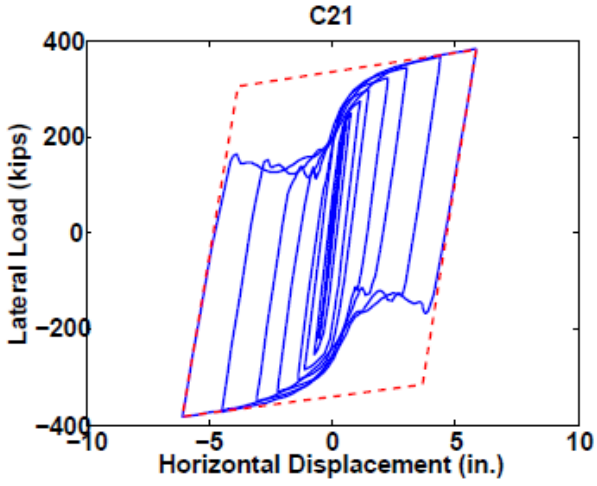

(ah)

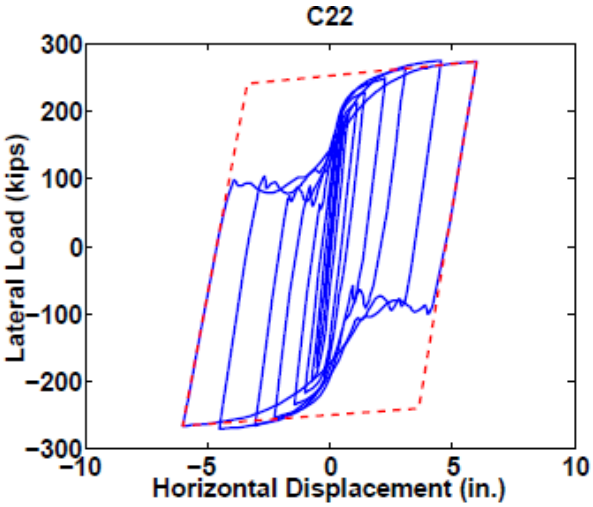

(ai)

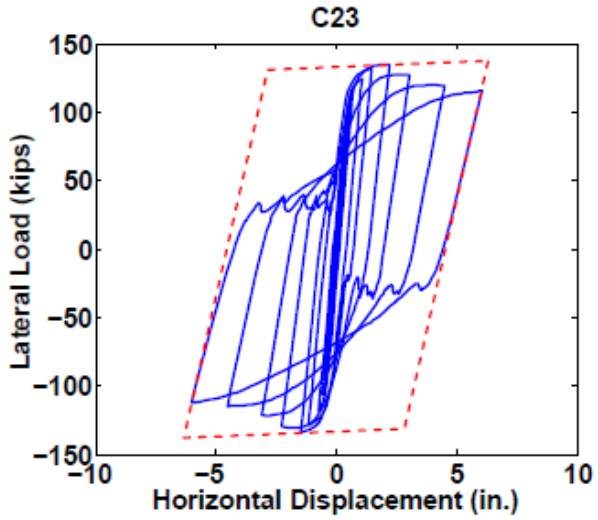

(aj)

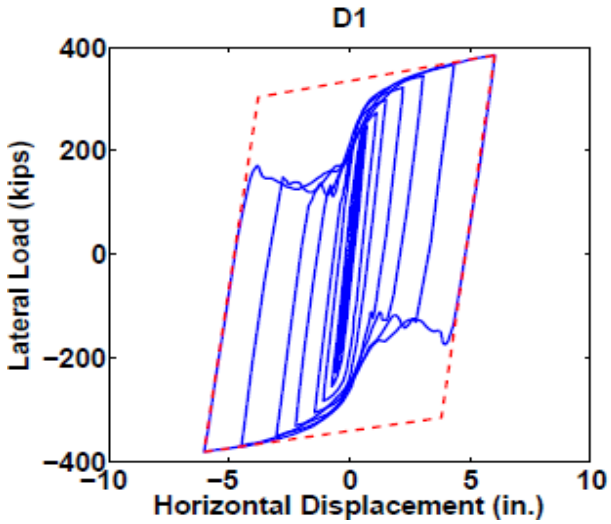

(ak)

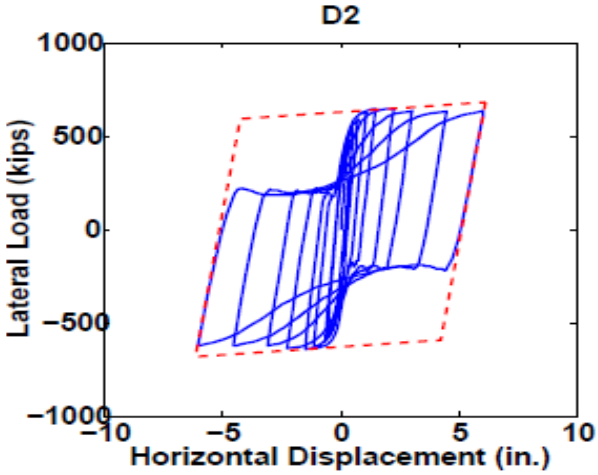

(al)

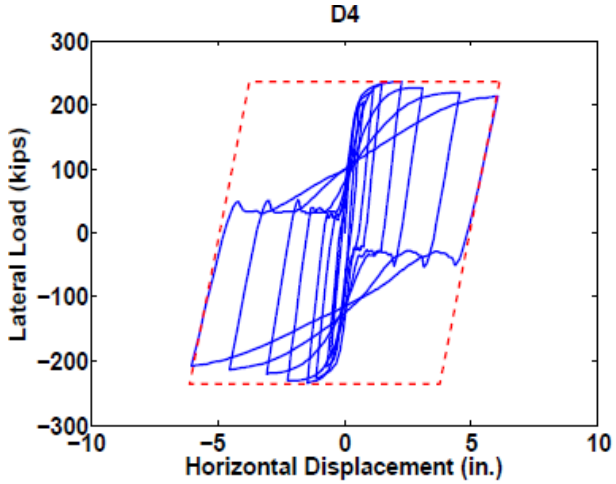

(am)

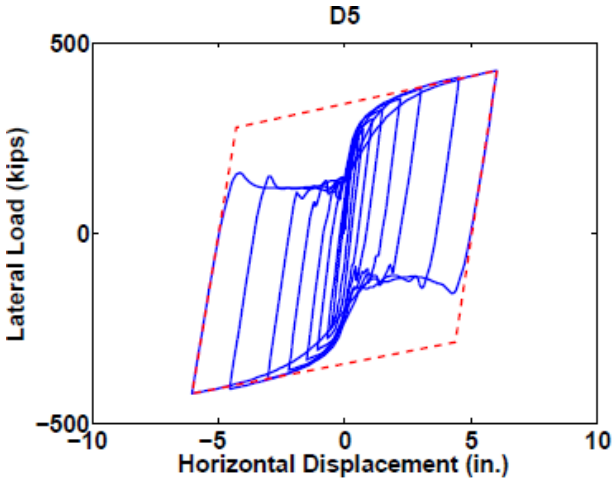

(an)

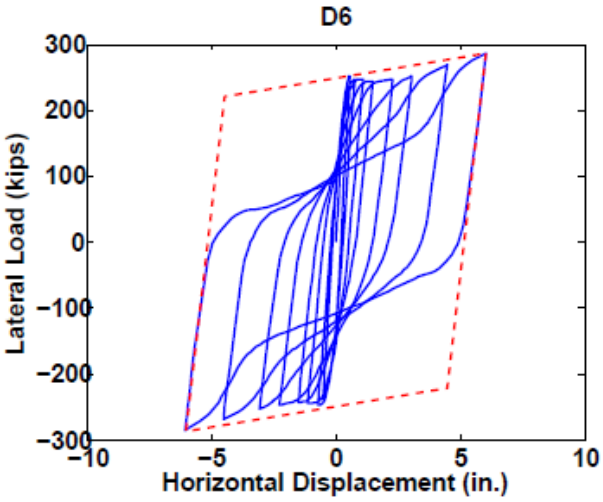

(ao)

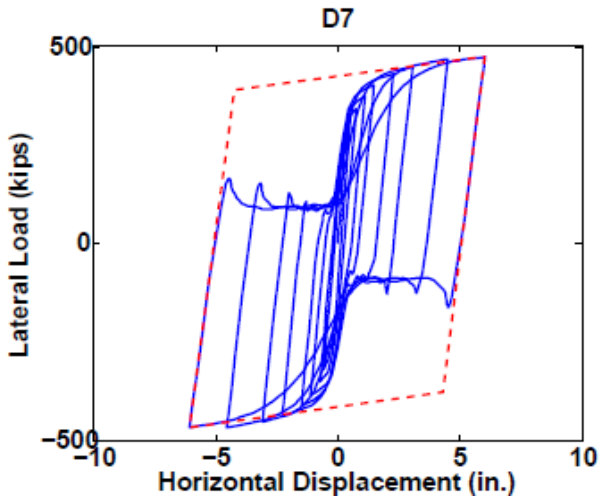

(ap)

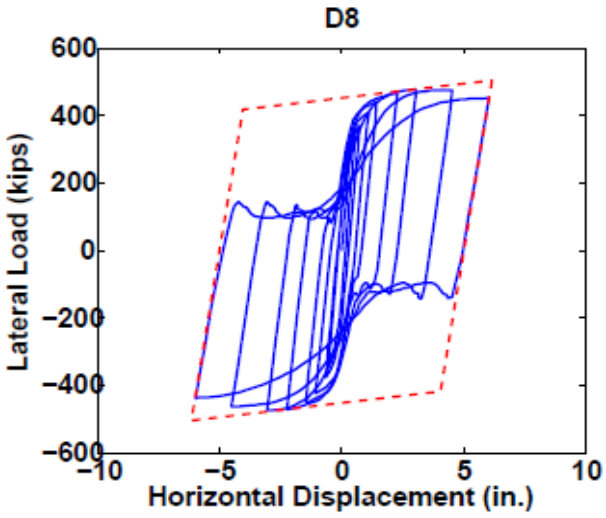

(aq)

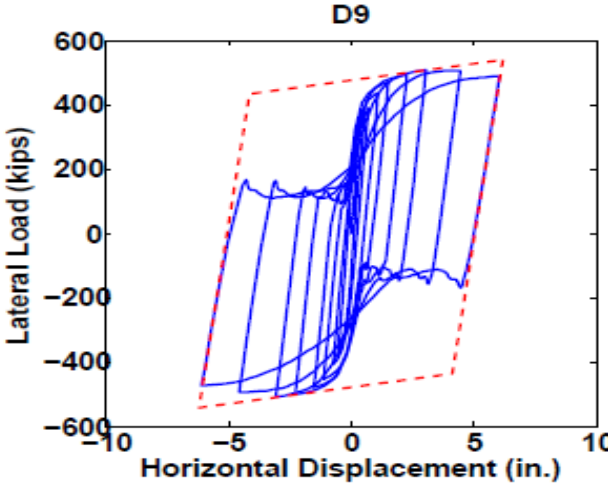

(ar)

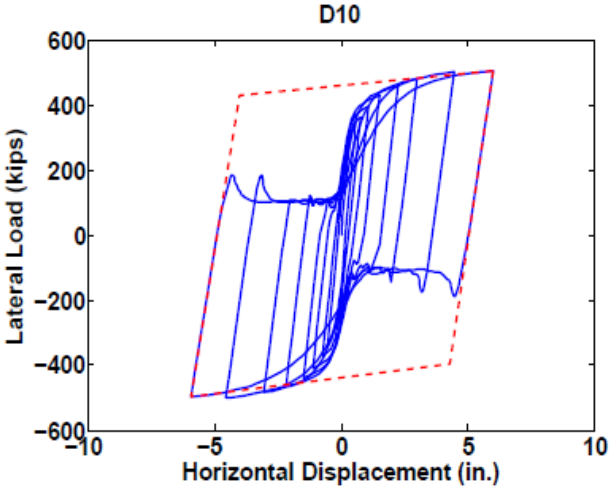

(as)

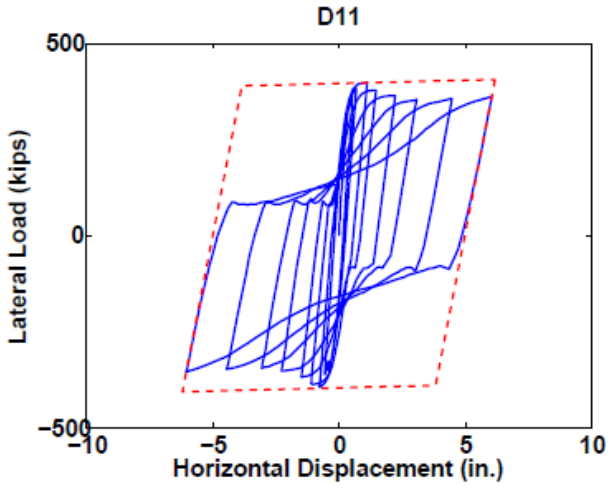

(at)

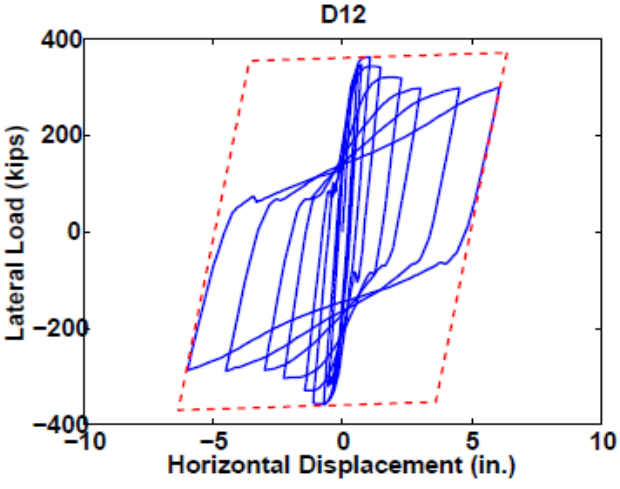

(au)

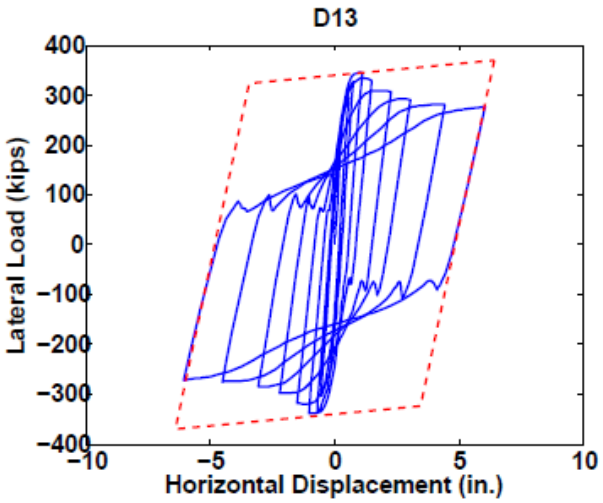

(av)

Figure A.117: Plots for the calculation of energy dissipation ratio

APPENDIX D: STRENGTH CALCULATION

This appendix tabulates the force-displacement plot for all the specimens generated for the purpose of strength calculation of the full wall**.**

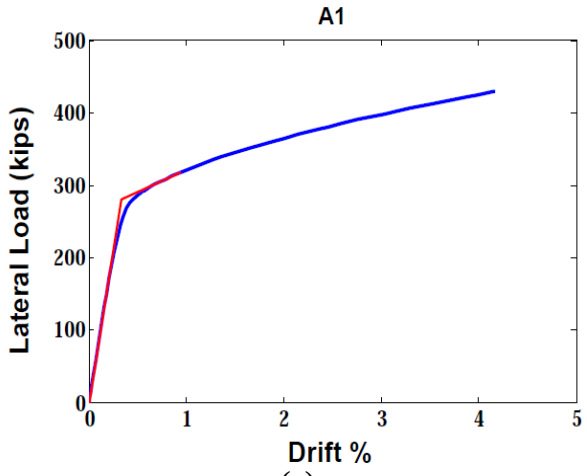

(a)

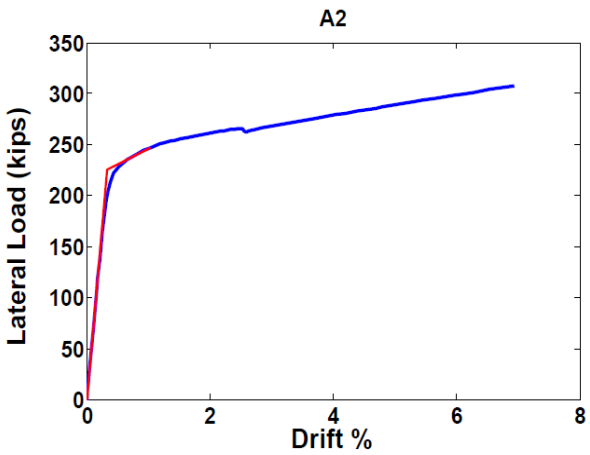

(b)

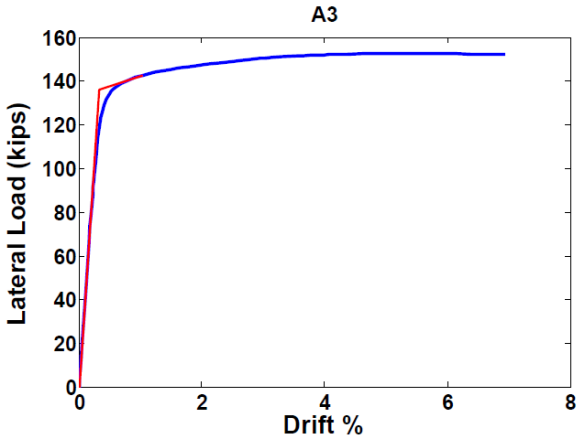

(c)

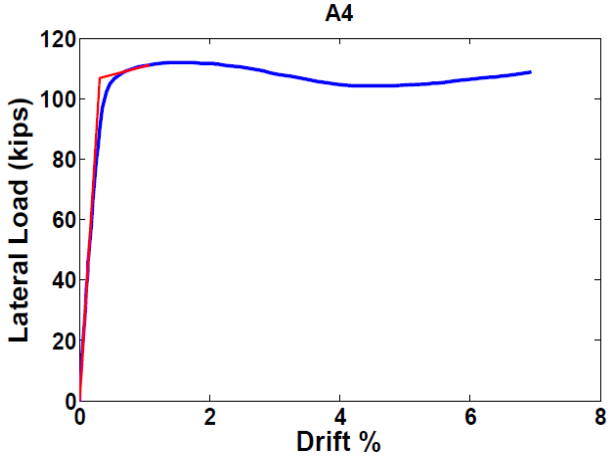

(d)

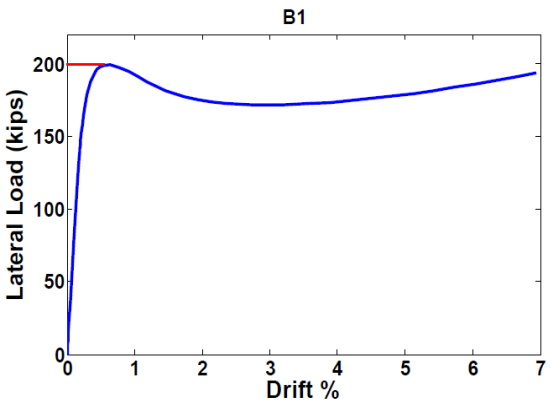

(e)

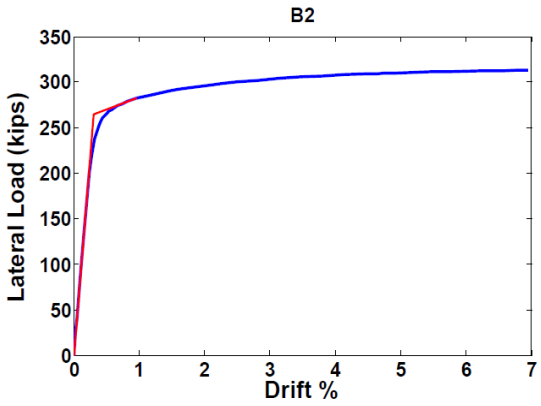

(f)

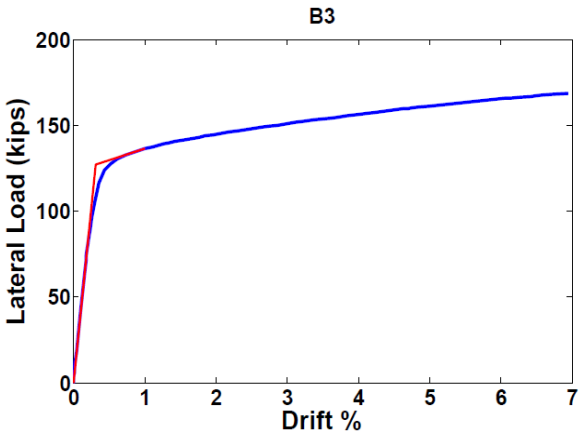
B3
Lateral Load (kips)
Drift %
0
50
100
150
200
0
1
2
3
4
5
6
7
(g)

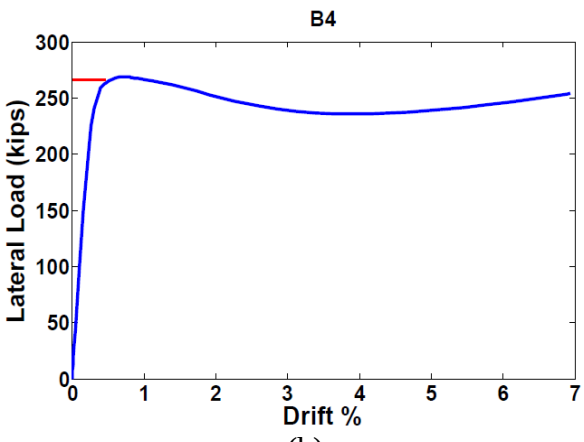
B4
Lateral Load (kips)
Drift %
0
50
100
150
200
250
300
0
1
2
3
4
5
6
7
(h)

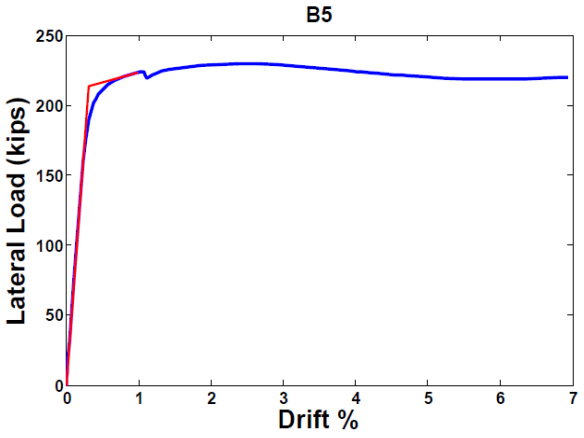
B5
Lateral Load (kips)
Drift %
0
50
100
150
200
250
0
1
2
3
4
5
6
7
(i)

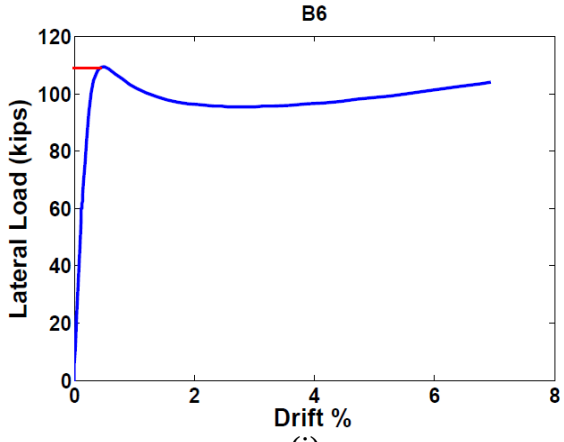
B6
Lateral Load (kips)
Drift %
0
20
40
60
80
100
120
0
2
4
6
8
(j)

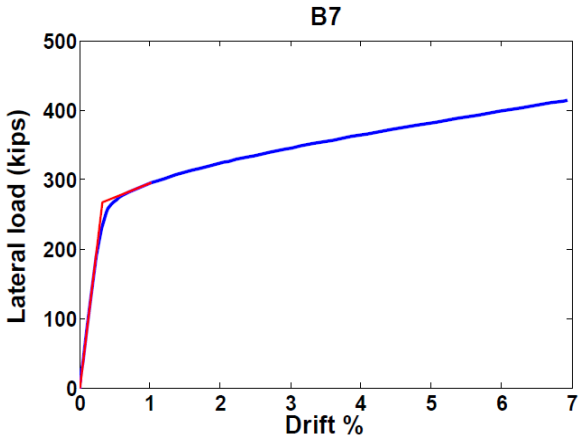
B7
Lateral load (kips)
Drift %
0
100
200
300
400
500
0
1
2
3
4
5
6
7
(k)

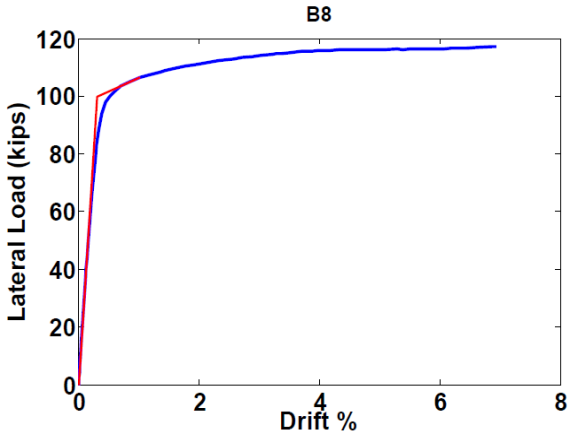
B8
Lateral Load (kips)
Drift %
0
20
40
60
80
100
120
0
2
4
6
8
(l)

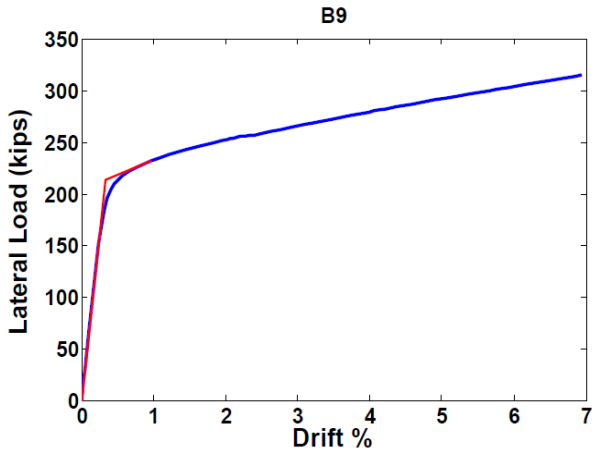
B9
Lateral Load (kips)
Drift %
0
50
100
150
200
250
300
350
0
1
2
3
4
5
6
7

(m)

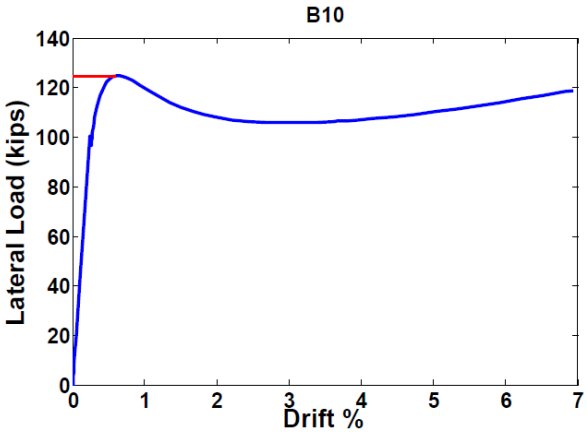
B10
Lateral Load (kips)
Drift %
0
20
40
60
80
100
120
140
0
1
2
3
4
5
6
7

(n)

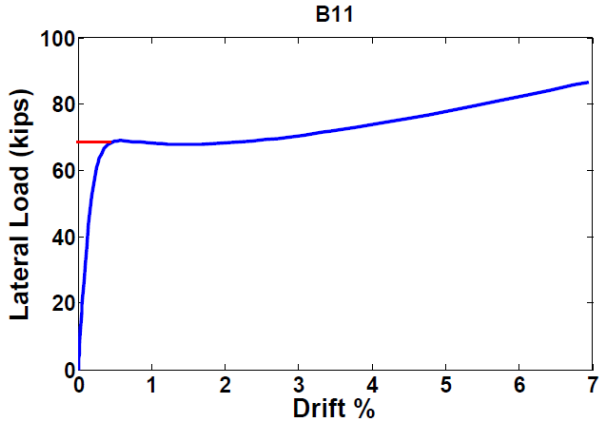
B11
Lateral Load (kips)
Drift %
0
20
40
60
80
100
0
1
2
3
4
5
6
7

(o)

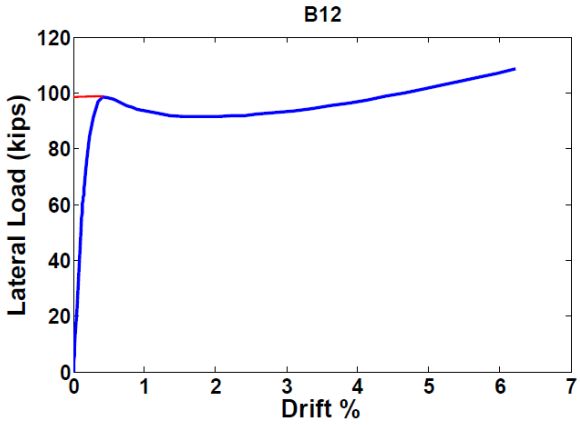
B12
Lateral Load (kips)
Drift %
0
20
40
60
80
100
120
0
1
2
3
4
5
6
7

(p)

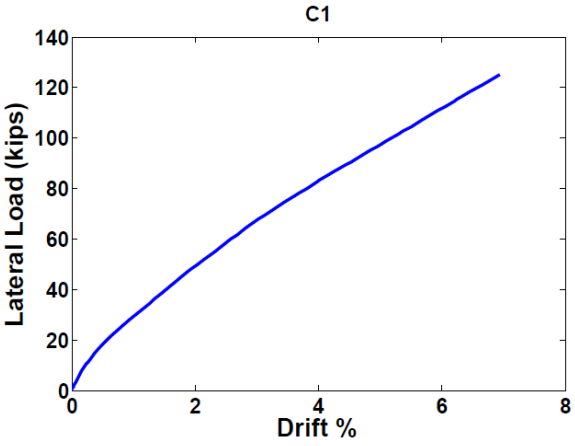
C1
Lateral Load (kips)
Drift %
0
20
40
60
80
100
120
140
0
2
4
6
8

(q)

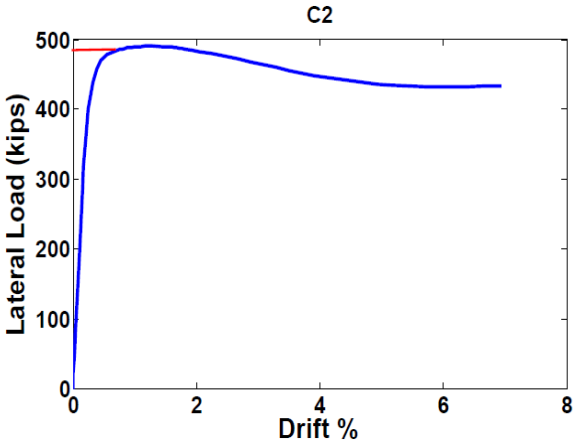
C2
Lateral Load (kips)
Drift %
0
100
200
300
400
500
0
2
4
6
8

(r)

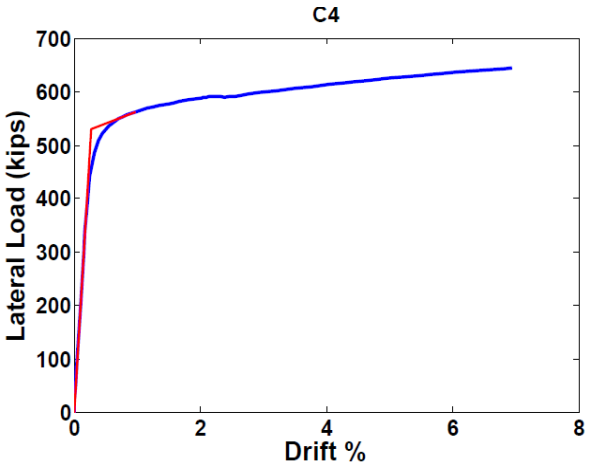
C4
Lateral Load (kips)
Drift %
0
100
200
300
400
500
600
700
0
2
4
6
8

(s)

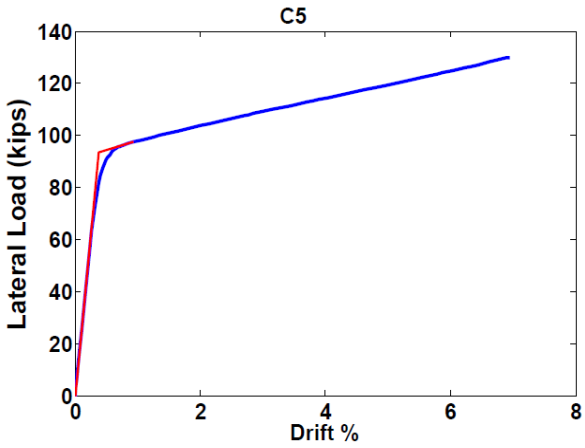
C5
Lateral Load (kips)
Drift %
0
20
40
60
80
100
120
140
0
2
4
6
8

(t)

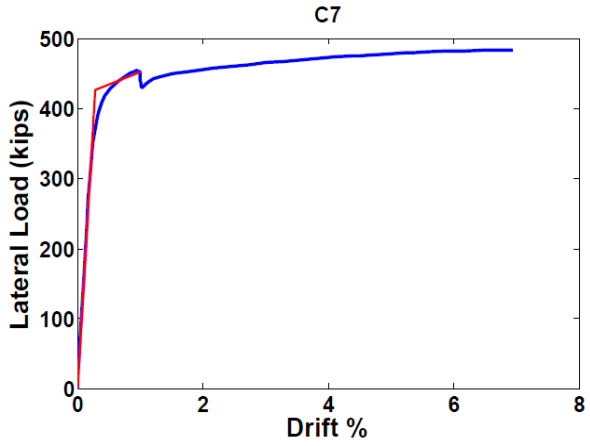
C7
Lateral Load (kips)
Drift %
0
100
200
300
400
500
0
2
4
6
8

(u)

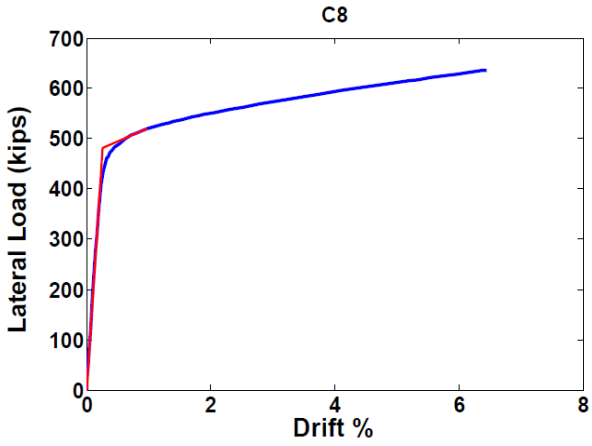
C8
Lateral Load (kips)
Drift %
0
100
200
300
400
500
600
700
0
2
4
6
8

(v)

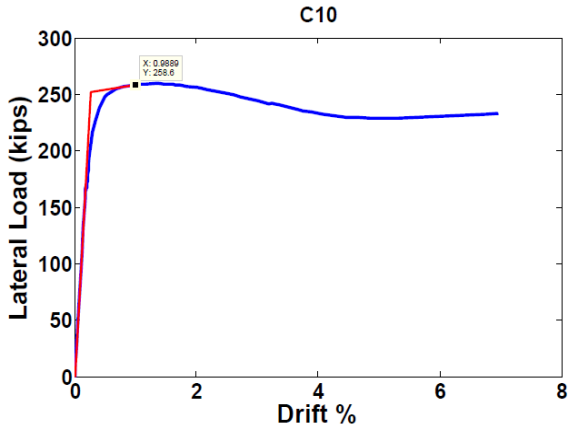
C10
Lateral Load (kips)
Drift %
0
50
100
150
200
250
300
0
2
4
6
8

(w)

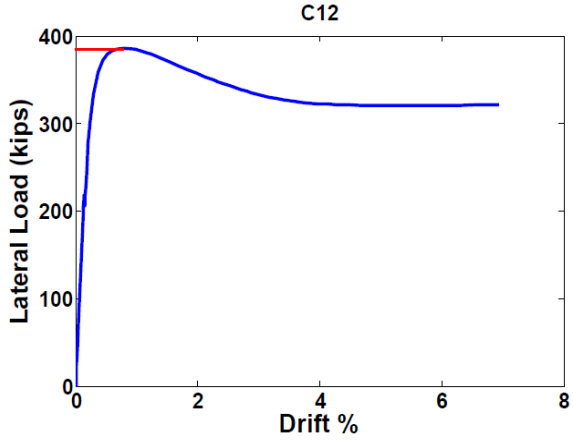
C12
Lateral Load (kips)
Drift %
0
100
200
300
400
0
2
4
6
8

(x)

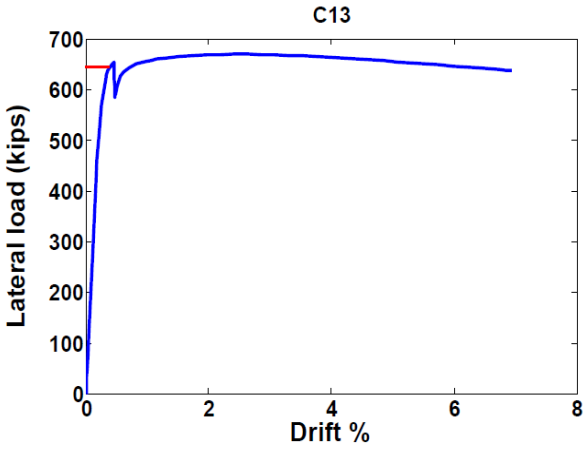
C13
Lateral load (kips)
Drift %

(y)

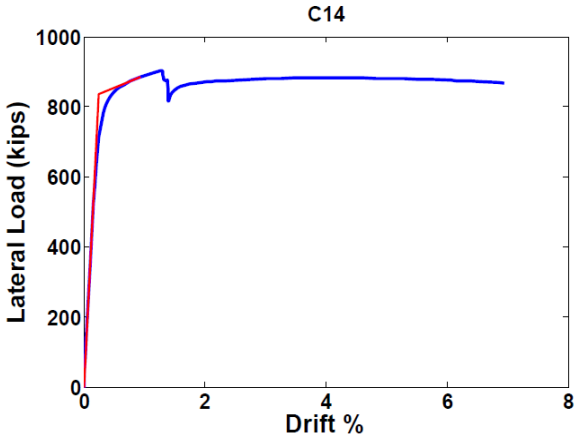
C14
Lateral Load (kips)
Drift %

(z)

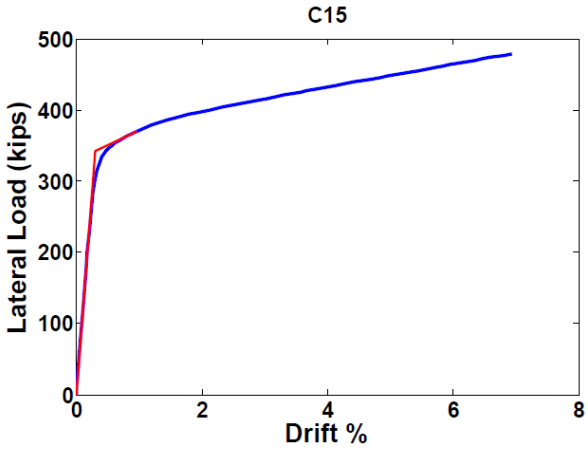
C15
Lateral Load (kips)
Drift %

(aa)

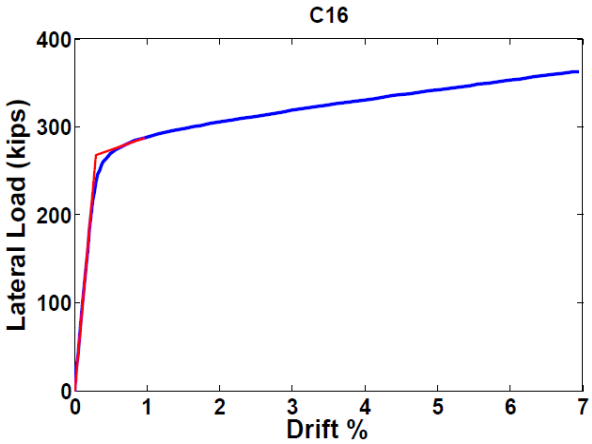
C16
Lateral Load (kips)
Drift %

(ab)

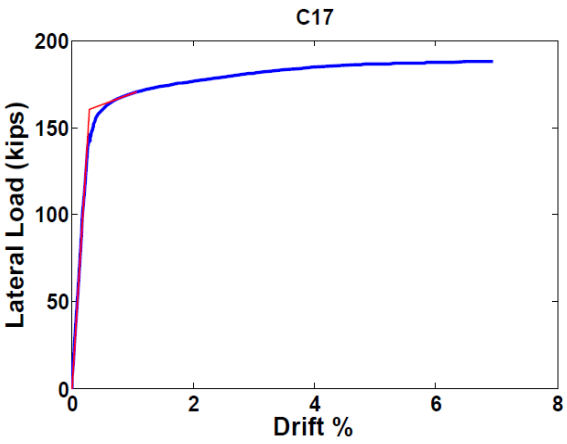
C17
Lateral Load (kips)
Drift %

(ac)

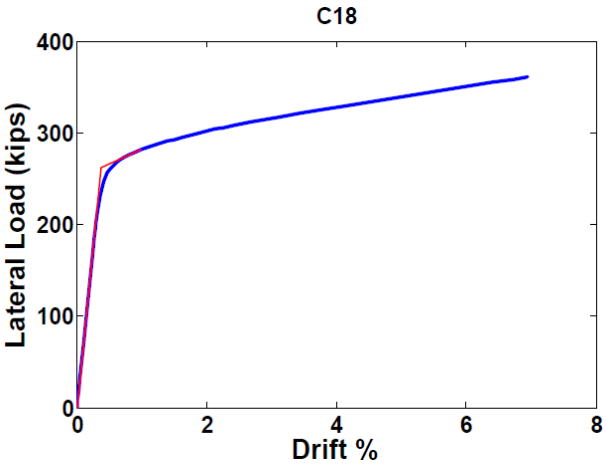
C18
Lateral Load (kips)
Drift %

(ad)

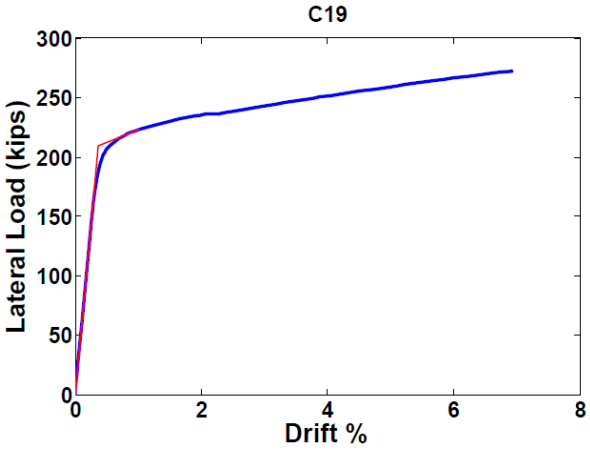

(ae)

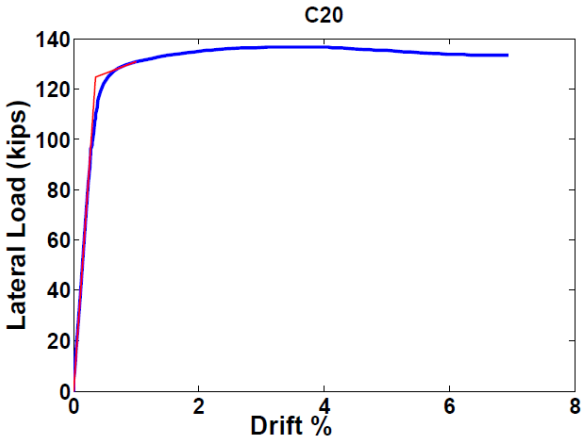

(af)

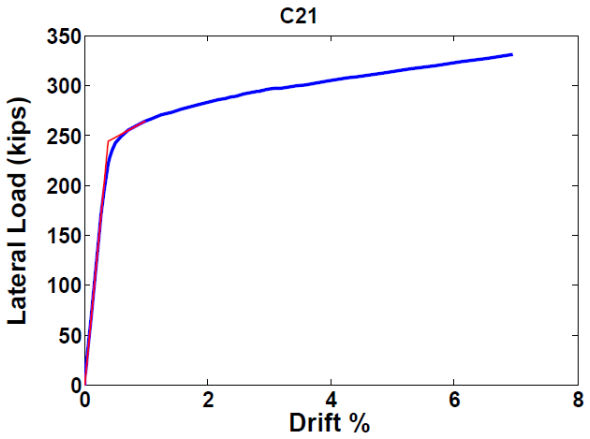

(ag)

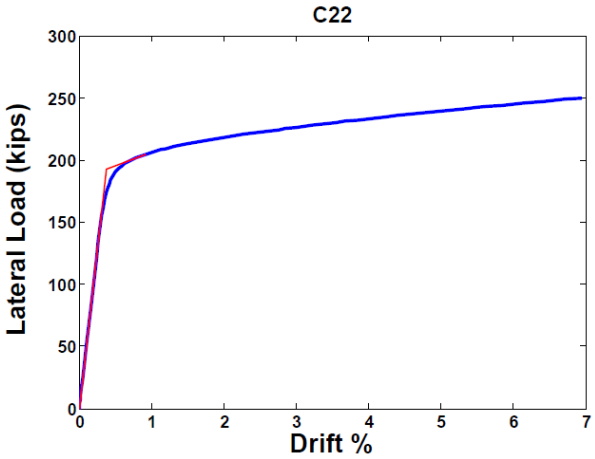

(ah)

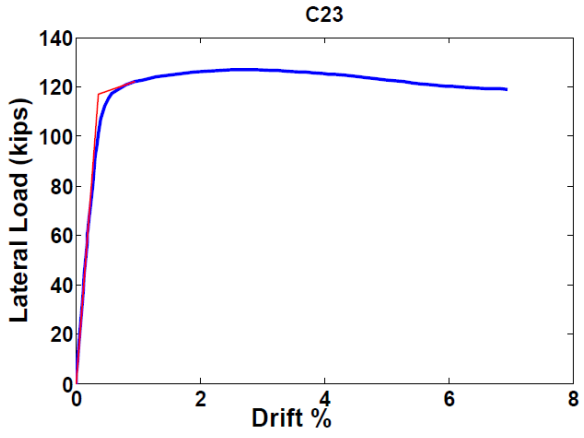

(ai)

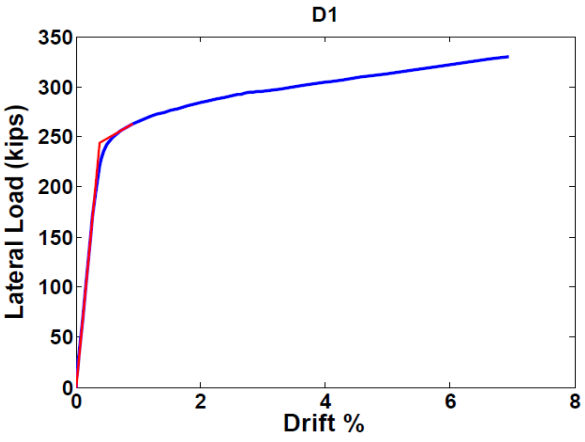

(aj)

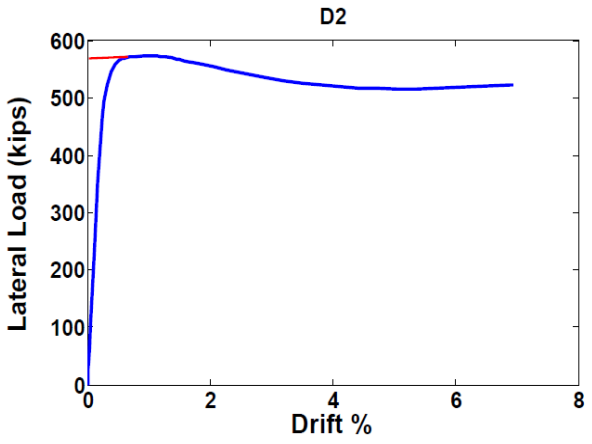

(ak)

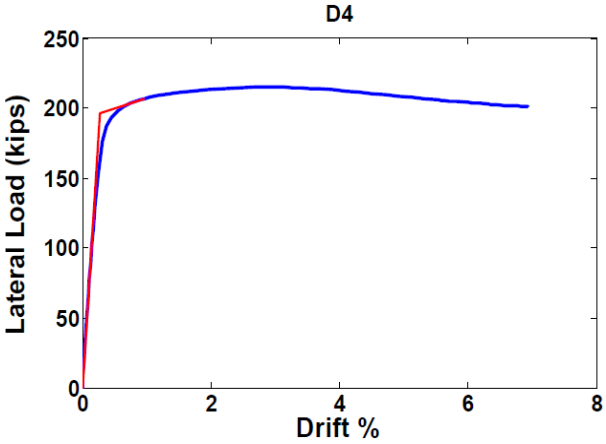

(al)

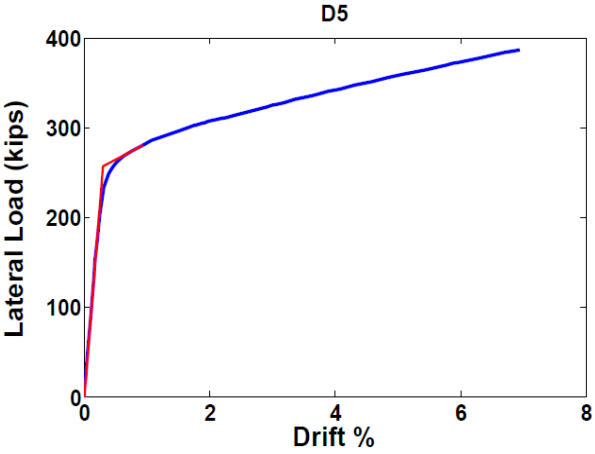

(am)

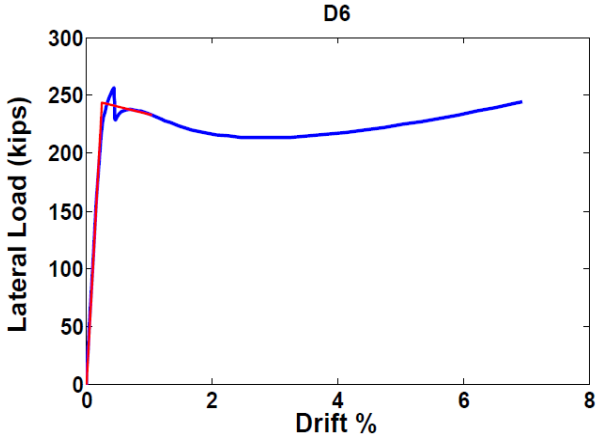

(an)

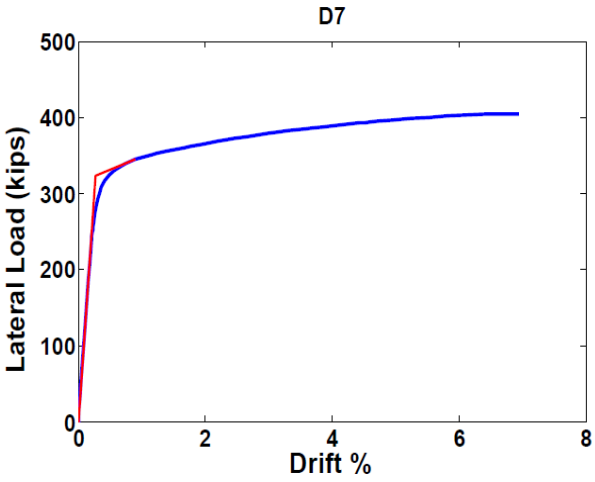

(ao)

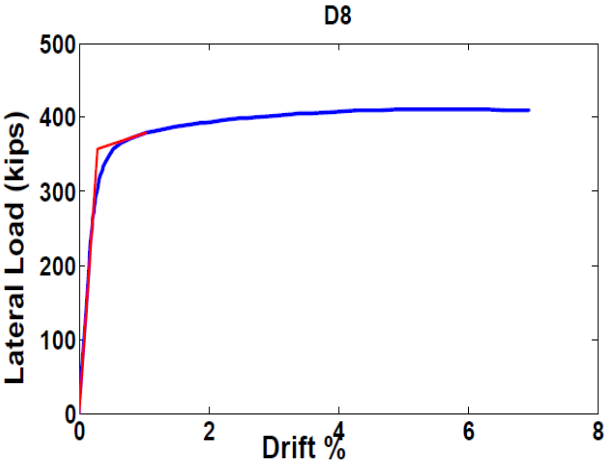

(ap)

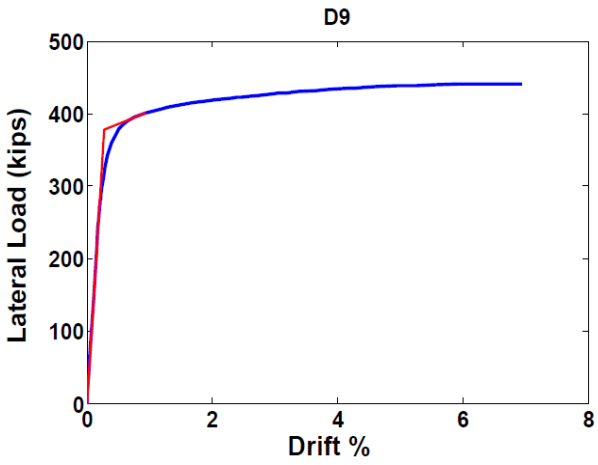

(aq)

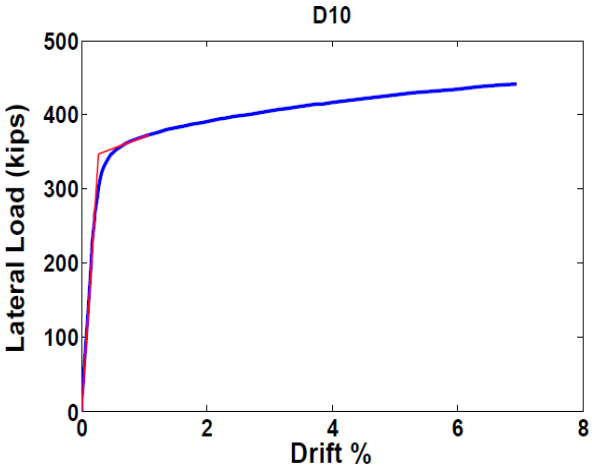

(ar)

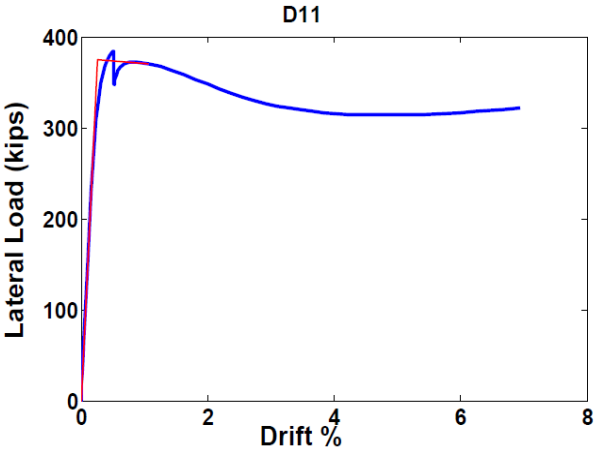

(as)

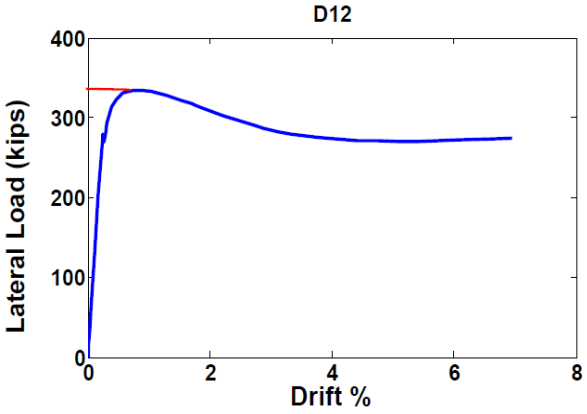

(at)

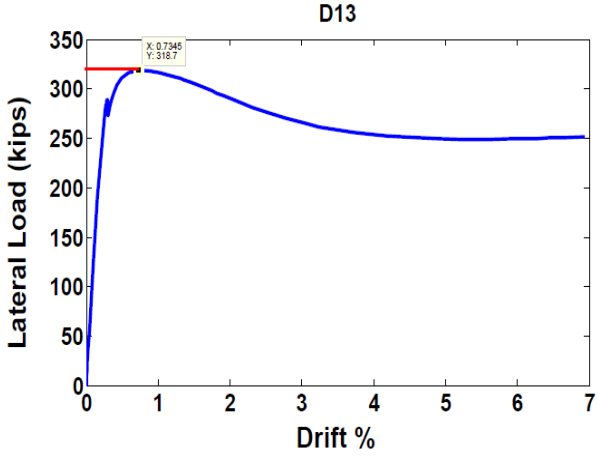

(au)

Figure A.118: Plots showing the method for calculation of full wall strength

APPENDIX E: COPYRIGHTED FIGURES

This appendix lists citations for copyrighted works (figures). Fair use determination for each figure is attached separately.

Figure 1: A four-story SPSW system [from (Berman and Bruneau 2004)]

Figure 2: Force-displacement plot for a typical steel plate shear wall system [from (Berman, Celik and Bruneau 2005)]

Figure 3: Force-displacement plot for a shear wall web plate [from (Berman, Celik and Bruneau 2005)]

Figure 5: Diagrammatic representation of Strip Model [from (Lubell et al. 2000)]

Figure 6: Diagrammatic representation of multi-angle strip model [from (Lubell et al. 2000)]

Figure 7: Infill panel connection details tested [from (Schumacher, Grondin and Kulak 1999)]

Figure 9: Perforated steel plate shear walls [from (Roberts et al. 1992 and Vian et al. 2005)]

Figure 10: Steel plate walls with rectangular slits [from (Hitaka et al. 2006)]

Figure 11: Panel with butterfly fuse [from (Borchers, Peña, Krawinkler, and Deierlein 2010)]

Figure 12: Yielding frame with constant cross-section [from (Tyler 1985)]

Figure 13: Yielding frame with varying width [from (Ciampi and Samuelli-Ferretti 1990)]

Figure 14: Yielding frame with varying depth [from (Ciampi and Samuelli-Ferretti 1990)]

Figure 15: Yielding frame with complementary plates [from (Ciampi and Samuelli-Ferretti 1990)]

Figure 16: Ring fuse [from (Rogers and Morrison 2011)]

Figure 42: axial-bending interaction curve for rectangular cross-section [from (Chen and Han 2007)]

Figure 103: Dependence of the equivalent strain to fracture on the stress triaxiality [from (Bao and Wierzbicki 2004)]